



City Research Online

City, University of London Institutional Repository

Citation: Robinson, Gordon M. (1995). Genetic algorithm optimisation of load cell geometry by finite element analysis. (Unpublished Doctoral thesis, City University London)

This is the accepted version of the paper.

This version of the publication may differ from the final published version.

Permanent repository link: <https://openaccess.city.ac.uk/id/eprint/13593/>

Link to published version:

Copyright: City Research Online aims to make research outputs of City, University of London available to a wider audience. Copyright and Moral Rights remain with the author(s) and/or copyright holders. URLs from City Research Online may be freely distributed and linked to.

Reuse: Copies of full items can be used for personal research or study, educational, or not-for-profit purposes without prior permission or charge. Provided that the authors, title and full bibliographic details are credited, a hyperlink and/or URL is given for the original metadata page and the content is not changed in any way.

**Genetic Algorithm Optimisation
of Load Cell Geometry
by Finite Element Analysis**

Gordon M. Robinson

**A thesis submitted for the degree of
Doctor of Philosophy**

**City University
Measurement and Instrumentation Centre
Department of Electrical, Electronic and Information Engineering
School of Engineering
Northampton Square
London EC1V 0HB**

August 1995

To
Alison
and
my Mum and Dad

CONTENTS

ABSTRACT	vii
ACKNOWLEDGEMENTS	viii
DECLARATION	viii
LIST OF TABLES	ix
LIST OF FIGURES	x
LIST OF PLATES	xvi
CHAPTER 1	
INTRODUCTION	1
1.1 General introduction to force measurement	1
1.1.1 Force standards	1
1.1.2 Transfer standards	2
1.2 Strain gauge load cells	3
1.2.1 Principle of operation	3
1.2.2 Sources of error	4
1.3 Sensitivity to end-loading conditions	5
1.3.1 Tension load cells	5
1.3.2 Compression load cells	6
1.3.3 End-loading sensitivity and standards	6
1.3.4 Load cells as stress integrators	7
1.4 Scope of this study	9
1.5 Column load cells	9
1.5.1 Requirement for low profile column load cells	9
1.5.2 Multi-column designs	10
1.6 An overview of this thesis	11
CHAPTER 2	
A REVIEW OF PREVIOUS WORK	13
2.1 Introduction	13
2.2 Analytic studies	13
2.2.1 Saint-Venant's Principle	13
2.2.2 Circular cylinders under axisymmetric loading	14
2.3 Experimental studies	15
2.3.1 The work of Rohrbach	16

2.3.2	The work of Feucht	17
2.3.3	The work of Debnam & Jenkins	19
2.3.4	The work of Bray	20
2.4	Numerical studies	21
2.4.1	The work of Mitchell et al.	21
2.4.2	The work of Sundin & Jonsson	23
2.4.3	The work of Williams	24
2.5	Conclusions	25
CHAPTER 3		
PRELIMINARY ANALYSIS OF COLUMN LOAD CELLS		
3.1	Introduction	27
3.2	Axisymmetric column load cells subject to general stress distributions	27
3.3	Bridge strain	31
3.4	Homogenous Solution Study	32
3.4.1	Introduction	32
3.4.2	The modelling of finite cylinders as semi-infinite	32
3.4.3	Analysis method	33
3.4.4	Approximation of an annular load	37
3.5	The analysis program	38
3.5.1	Overview	38
3.5.3	Optimum parameter values	38
3.6	Results from program CYSTRESS.FOR	39
3.6.1	Surface axial strain	40
3.6.2	Surface circumferential strain	40
3.6.3	Surface bridge strain	44
3.7	Conclusions	45
CHAPTER 4		
MEASUREMENT OF SURFACE STRAINS IN A CYLINDER		
4.1	INTRODUCTION	49
4.2	Strain gauged cylinder	49
4.2.1	Strain gauges	51
4.2.2	Instrumentation	51
4.2.3	Strain gauge bridge circuit	52
4.2.4	Thermal effects on bridge output	53
4.2.5	Creep of the strain gauge output	53
4.2.6	Control and data logging	53

4.2.7	Loading pads	54
4.2.8	Test method	56
4.2.9	Calculation of results	57
4.3	Results	58
4.3.1	Tests on plane, central disc, and ring pads	58
4.3.2	Tests on the concave and convex pads	65
4.4	Measurement of Young's modulus and Poisson's ratio	69
4.4.1	Strain gauge configuration	69
4.4.2	Results	70
4.5	Conclusions	71
CHAPTER 5		
DEVELOPMENT OF A SIMPLE FINITE ELEMENT ANALYSIS PROGRAM		72
5.1	Introduction	72
5.2	The finite element method	72
5.3	Choice of finite element software	73
5.4	The axisymmetric finite element program, axi.f	74
5.5	Tests on the simple finite element program	74
5.5.1	Infinite thick cylinder under internal pressure	75
5.5.2	Analysis of long cylinder subject to annular load	78
5.5.3	Conclusions from the 'benchmark' tests	79
5.6	Conclusions	80
CHAPTER 6		
MODELLING CONTACT		86
6.1	Introduction	86
6.2	Finite element analysis using infinite elements	86
6.2.1	Introduction to infinite elements	87
6.2.2	Two dimensional Zienkiewicz mapped infinite elements	88
6.2.3	Implementation of infinite elements	91
6.2.4	Test problems using infinite elements	91
6.3	Finite element analysis of contact problems	98
6.3.1	Introduction	98
6.3.2	The contact algorithm	100
6.3.3	Tests on contact algorithm	106
6.3.4	Conclusions from benchmark tests	107
6.4	Comparison between finite element model and experimental results	108
6.4.1	1.0 r_o pads	108

6.4.2	1.5 r_0 pads	111
6.5	Conclusions	111
CHAPTER 7		
AUTOMATION OF THE MODELLING PROCESS		116
7.1	Introduction	116
7.2	Parameterised representation of the load cell	116
7.2.1	Representation of the lateral surface	118
7.3	Automatic mesh generation	121
7.3.1	Requirements	121
7.3.2	The automatic meshing routine	121
7.4	Meshing of the contact pads	130
7.5	Measures of end-loading sensitivity	131
7.5.1	EN-immunity	131
7.5.2	PCCU-immunity	133
7.6	Reducing computation time	134
7.7	Conclusions	137
CHAPTER 8		
GENETIC ALGORITHM SHAPE OPTIMISATION		138
8.1	Introduction	138
8.2	Optimisation algorithms	139
8.2.1	Gradient methods	139
8.2.2	Gradientless methods	140
8.2.3	Choice of algorithm	141
8.3	The simple genetic algorithm	142
8.3.1	Introduction	142
8.3.2	String representation	142
8.4	Theory of the simple genetic algorithm	145
8.4.1	Schemas	145
8.4.2	Crossover	146
8.4.3	Reordering	147
8.4.4	Mutation	149
8.5	Choice of GA parameters	149
8.6	Performance of GA routines on trial problems	150
8.7	Conclusions	154

CHAPTER 9	
THE 'DARWIN' LOAD CELL	155
9.1 Introduction	155
9.1.2 The POGLE Program	155
9.2 Optimisation of 3 MN low-profile column load cell	156
9.2.1 Calibration of concrete-cube testing machines	156
9.2.2 Problem specification	156
9.3 Results from the GA optimisation	157
9.3.1 Optimisation of EN-immunity.	158
9.3.2 Optimisation of PCCU-immunity	159
9.4 End-loading sensitivity of 3 MN load cells with solid and hollow circular cylindrical elements	161
9.4.1 EN-immunity of circular cylinders	161
9.4.2 PCCU-immunity of circular cylinders	161
9.4.3 Comparison of Darwin design with cylindrical load cells	164
9.5 Conventional 3 MN low-profile load cell	164
9.5.1 Comparison of the Darwin and conventional designs	166
9.6 Manufacture of the Darwin prototype load cell	166
9.6.1 Machining	166
9.6.2 Strain gauging	172
9.7 Testing of the prototype load cell	172
9.7.1 Bearing pad test results	174
9.8 Conclusions	174
 CHAPTER 10	
CONCLUSIONS AND PROPOSALS FOR FURTHER WORK	176
10.1 Conclusions	176
10.2 Proposals for further work	177
 REFERENCES AND BIBLIOGRAPHY	180

ABSTRACT

The objective of the work described in this thesis was to numerically model the influence of end-loading conditions on column strain gauge load cells and to develop the model into a program for optimising the geometry of column load cells.

It is shown that, for most practical loading conditions, load cells with large numbers of equispaced strain gauges are only sensitive to the axisymmetric components of contact stress distribution. The problem of cylindrical load cells subject to frictionless equipollant annular loading is analysed by the method of superposition of the homogenous solutions. A plot of the relationship between sensitivity, load radius and cylinder aspect ratio is presented.

An experimental study using a strain gauged cylinder was then undertaken. The measured strains confirmed the results of the analytic solution and provided results for other loading conditions, more representative of those to which real load cells are subjected.

In order to extend the study to more typical contact conditions and to load cells of more complex shape, a simple finite element (FE) program incorporating contact analysis, automatic meshing, and infinite elements was developed. The results from the program are shown to be in good agreement with those from the analytic solution, from benchmark problems, and from the experiments. The FE program was used to predict the end-loading sensitivity of hollow and solid cylindrical load cells. Plots of their end-loading sensitivity against aspect ratio are presented.

The finite element routines were then used as the core of a Program for Optimising the Geometry of Load cell Elements (POGLE). This program combines genetic algorithm optimisation with finite element analysis to optimise a load cell's shape so as to minimise its end-loading sensitivity.

In order to test the capabilities of the POGLE program it was used to optimise the shape of a 3 MN low-profile load cell. A prototype with the predicted optimum shape was manufactured and tested. The tests confirmed the program's predictions that the new design would have much lower end-loading sensitivity than existing designs.

ACKNOWLEDGEMENTS

This work was carried out while the author was an employee of the National Physical Laboratory (NPL). I gratefully acknowledge the provision by NPL of the time, funding, and facilities required for this work.

I wish to thank my supervisor at City University, Dr Faruq Abdullah, for his inspiration, support and guidance throughout this Ph.D. study. I am especially grateful for his infectious enthusiasm. I always returned to the work with renewed vigour following our discussions.

I would also like to thank all my colleagues at NPL who have assisted in many ways. In particular I am grateful to Andy Knott for his friendship, assistance and helpful criticism.

I would also like to single out Ray Jenkins of NPL for particular thanks. Ray has the rare ability to be simultaneously boss, colleague, and friend. In his capacity as boss, it is thanks to him that this work was started, and without his personal support it could not have been finished. As a colleague he gave me guidance, helpful suggestions, and encouragement. However, it is for his friendship that I would like to express my greatest thanks.

DECLARATION

I hereby grant powers of discretion to the University Librarian to allow this thesis to be copied in whole or in part without further reference to me. This permission covers only single copies made for study purposes, subject to normal conditions of acknowledgement.

LIST OF TABLES

Table 1.1: Maximum departures from output on plane surface specified in EN10002-3	7
Table 2.1: Debnam & Jenkins' results for four load cells of different design	20
Table 3.1: Effect of parameter values on bridge strain values ($m=4$, $E=1$)	39
Table 4.1: Output from gauges at mid plane	69
Table 5.1: Percentage error of strains from finite element solution, with various mesh configurations	77
Table 6.1: Comparison of analyses of Boussinesq's problem	93
Table 6.2: Axial stress for frictionless contact of cylinder on elastic foundation	96
Table 6.3: Radial slip for frictionless contact of cylinder on elastic foundation	96
Table 6.4: Axial displacements for frictionless contact of cylinder on elastic foundation	97
Table 6.5: Contact stresses for cylinder on elastic foundation,	106
Table 6.6 Radial slip for contact of cylinder on elastic foundation,	107
Table 7.1: EN10002-3 bearing pad test load conditions	131
Table 7.2: EN-immunity values of EN 10002-3 classes	133
Table 8.1: Parameters governing GA optimisation algorithm	149
Table 9.1: Parameters specifying problem for 3 MN load cell	157
Table 9.2: Parameters specifying modelling of 3 MN load cell	157
Table 9.3: Comparison of designs optimised for EN-immunity and PCCU-immunity	159
Table 9.4: Bearing pad test results for Darwin cell design	174
Table 9.5: Relative deviation from output on plane pad	174

LIST OF FIGURES

Figure 1.1: A typical strain gauge circuit	3
Figure 1.2: Examples of variation in end-loading conditions	6
Figure 2.1: Transfer of force into a cylindrical load cell element (from figure 4 of Rohrbach [1970])	16
Figure 2.2: Errors due to radial restraint of cylindrical load cell (from figure 5 of Rohrbach [1970])	17
Figure 2.3: Effect of four different end-loading conditions on sensitivity, linearity, and hysteresis (from figure 2 of Feucht [1970])	18
Figure 2.4: The four load cell designs tested by Debnam & Jenkins [1972]	19
Figure 2.5: Load cell loading arrangement (from figure 6 of Mitchell et al. [1971])	21
Figure 2.6: Axial surface strains over central section (from figure 8 of Mitchell et al. [1971])	22
Figure 2.7: Variation of load cell sensitivity with step position (from figure 3 of Sundin & Jonsson [1985])	23
Figure 2.8: The problem analysed by Williams	24
Figure 2.9: Fractional difference in bridge output with load radius (from figure 3.3 of Williams)	25
Figure 3.1: Column load cell subject to general stress distribution	27
Figure 3.2 - Surface axial strain v distance from loaded end: Prokopov solution: $z=0.5r$ to $2.0r$	41
Figure 3.3 - Surface axial strain v distance from loaded end: Prokopov solution: $z=0.9r$ to $1.8r$	41
Figure 3.4 - Surface circumferential strain v distance from loaded end: Prokopov solution: $z=0.5r$ to $2.0r$	42
Figure 3.5 - Surface circumferential strain v distance from loaded end: Prokopov solution: $z=0.9r$ to $1.8r$	42
Figure 3.6: Surface bridge strain v distance from loaded end, $z=0.5r$ to $2.0r$: Prokopov solution:	43

Figure 3.7: Surface bridge strain v distance from loaded end: Prokopov solution: $z=0.9r$ to $1.8r$	43
Figure 3.8: Spread of bridge strain v aspect ratio	44
Figure 3.9: Contours of bridge strain due to equipollant annular load with $X_f=0.01$: Prokopov solution	46
Figure 3.10: Contours of bridge strain due to equipollant annular load with $X_f=0.2$: Prokopov solution	46
Figure 3.11: Contours of bridge strain due to equipollant annular load with $X_f=0.4$: Prokopov solution	47
Figure 3.12: Contours of bridge strain due to equipollant annular load with $X_f=0.6$: Prokopov solution	47
Figure 3.13: Contours of bridge strain due to equipollant annular load with $X_f=0.8$: Prokopov solution	48
Figure 3.14: Contours of bridge strain due to equipollant annular load with $X_f=1.0$: Prokopov solution	48
Figure 4.1: Circuit of strain gauged cylinder (only one gauge pair shown)	52
Figure 4.2: $1.0r_o$ loading pads (profiles exaggerated)	55
Figure 4.3: $1.5r_o$ loading pads (profiles exaggerated)	56
Figure 4.4: Axial strain v distance from loaded end: Prokopov solution: Annular loads at mean contact radii	60
Figure 4.5: Axial strain v distance from loaded end: Experimental results: $1.0r_o$ pads	60
Figure 4.6: Circumferential strain v distance from loaded end: Prokopov solution: Annular loads at mean contact radii	61
Figure 4.7: Circumferential strain v distance from loaded end: Experimental results: $1.0r_o$ pads	61
Figure 4.8: Bridge strain v distance from loaded end: Prokopov solution: Annular loads at mean contact radii	62
Figure 4.9: Bridge strain v distance from loaded end: Experimental results: $1.0r_o$ pads	62
Figure 4.10: Axial strain v distance from loaded end: Experimental results: $1.5r_o$ pads	63

Figure 4.11: Circumferential strain v distance from loaded end: Experimental results: $1.5r_o$ pads	63
Figure 4.12: Bridge strain v distance from loaded end: Experimental results: $1.5r_o$ pads	64
Figure 4.13: Axial strain v distance from loaded end: Experimental results: Concave/convex pads	66
Figure 4.14: Circumferential strain v distance from loaded end: Experimental results: Concave/convex pads	66
Figure 4.15: Bridge strain v distance from loaded end: Experimental results: Concave/convex pads	67
Figure 4.16: Bridge strain v distance from loaded end: Experimental results: Bearing pad test	67
Figure 4.17: Bridge strain v distance from loaded end: Experimental results: All pads	68
Figure 5.1: Mesh configurations used to analyse Lamé's problem	76
Figure 5.2: Mesh configurations used to analyse cylinder of aspect ratio 4.0	76
Figure 5.3: Bridge strain v distance from loaded end: 20x5 quad. mesh	81
Figure 5.4: Bridge strain v distance from loaded end: 40x10 quad. mesh	81
Figure 5.5: Bridge strain v distance from loaded end: 40x10 triangular mesh	82
Figure 5.6: Bridge strain v distance from loaded end: 80x20 triangular mesh	82
Figure 5.7: Contours of bridge strain due to equipollant annular load with $X_f=0.0$: FE analysis	83
Figure 5.8: Contours of bridge strain due to equipollant annular load with $X_f=0.2$: FE analysis	83
Figure 5.9: Contours of bridge strain due to equipollant annular load with $X_f=0.4$: FE analysis	84
Figure 5.10: Contours of bridge strain due to equipollant annular load with $X_f=0.6$: FE analysis	84
Figure 5.11: Contours of bridge strain due to equipollant annular load with $X_f=0.8$: FE analysis	85
Figure 5.12: Contours of bridge strain due to equipollant annular load with $X_f=1.0$: FE analysis	85
Figure 6.1: Mapping of infinite elements	88

Figure 6.2: Mesh used to analyse Boussinesq's problem: 16 finite elements	92
Figure 6.3: Mesh used to analyse Boussinesq's problem: 12 finite elements + 4 infinite elements	92
Figure 6.4: Graded mesh used for Olukoko benchmark	95
Figure 6.5: Uniform mesh used for Olukoko benchmark	95
Figure 6.6: Contact between two bodies	101
Figure 6.7: Matrix reduction: start of first elimination pass	104
Figure 6.8: Matrix reduction: end of first elimination pass	104
Figure 6.9: Matrix reduction: end of second elimination pass	105
Figure 6.10: Axial strain v distance from loaded end: FE contact analysis: $1.0r_o$ pads	109
Figure 6.11: Circumferential strain v distance from loaded end: FE contact analysis: $1.0r_o$ pads	109
Figure 6.12: Bridge strain v distance from loaded end: FE contact analysis: $1.0r_o$ pads	110
Figure 6.13: Axial strain v distance from loaded end: FE contact analysis: $1.5r_o$ pads	112
Figure 6.14: Circumferential strain v distance from loaded end: FE contact analysis: $1.5r_o$ pads	112
Figure 6.15: Bridge strain v distance from loaded end: FE contact analysis: $1.5r_o$ pads	113
Figure 6.16: Axial strain v distance from loaded end: FE contact analysis: concave/convex pads	113
Figure 6.17: Circumferential strain v distance from loaded end: FE contact analysis: concave/convex pads	114
Figure 6.18: Bridge strain v distance from loaded end: FE contact analysis: concave/convex pads	114
Figure 6.19: Bridge strain v distance from loaded end: FE contact analysis: bearing pad test	115
Figure 6.20: Bridge strain v distance from loaded end: FE contact analysis: all pads	115
Figure 7.1: Parameterised load cell geometry	117

Figure 7.2: Crude estimate of distance from boundary	122
Figure 7.3: Capture interval too wide resulting in very distorted elements.	123
Figure 7.4: Capture interval too wide resulting in near coincident vertices	124
Figure 7.5: Grid of vertices with vertical boundary	124
Figure 7.6: Element formed by capture of vertex A	125
Figure 7.7: Element formed by capture of vertex B	125
Figure 7.8: Grid of vertices with boundary inclined at 45° to the horizontal	126
Figure 7.9: Element formed by capture of vertex A	126
Figure 7.10: Element formed by capture of vertex B	126
Figure 7.11: Initial rows of vertices and shape boundary	129
Figure 7.12: After capture by boundary and elimination of external vertices	129
Figure 7.13: Mesh generated from vertices	130
Figure 8.1: Function used in first trial GA optimisation	150
Figure 8.2: Three runs on first trial problem - without reordering	151
Figure 8.3: Mean fitness, X, and Y for run on first trial problem - without reordering	152
Figure 8.4: Function used in second trial GA optimisation	153
Figure 8.5: Mean fitness and radius for run on second trial problem - without reordering	153
Figure 8.6: Mean fitness and radius for run on second trial problem - with reordering	154
Figure 9.1: Mean fitness v generation for PCCU-immunity optimisation	158
Figure 9.2: Mesh of load cell optimised for EN-immunity	160
Figure 9.3 Mesh of load cell optimised for PCCU-immunity	160
Figure 9.4: Comparison of EN-immunity of cylindrical, Darwin and conventional load cell designs	162
Figure 9.5: Comparison of PCCU-immunity of cylindrical, Darwin and conventional load cell designs	163
Figure 9.6: Mesh of low-profile load cell of conventional design	165
Figure 9.7: Bridge strain in conventional load cell: Uniform pressure: No friction	167

Figure 9.8: Bridge strain in conventional load cell: Plane pad: Friction=0.3	167
Figure 9.9: Bridge strain in conventional load cell: Convex pad: Friction=0.3	168
Figure 9.10: Bridge strain in conventional load cell: Concave pad: Friction=0.3	168
Figure 9.11: Bridge strain in GA optimised load cell: Uniform pressure: No friction	169
Figure 9.12 Bridge strain in GA optimised load cell: Plane pad: Friction=0.3	169
Figure 9.13: Bridge strain in GA optimised load cell: Convex pad: Friction=0.3	170
Figure 9.14: Bridge strain in GA optimised load cell: Concave pad: Friction=0.3	170
Figure 10.1: Comparison of PCCU-immunity of Darwin and solid cylindrical load cells	179

LIST OF PLATES

Plate 4.1: The strain gauged cylinder	50
Plate 9.1: The prototype Darwin load cell	173

CHAPTER 1

INTRODUCTION

1.1 General introduction to force measurement

Since the earliest days of metrology there has been a requirement to measure force. Until recent times, little distinction was made between force, weight and mass and almost all force measurement relied on the use of weights either directly or acting through levers. Towards the beginning of this century, the first practical force sensors became available. These early devices, such as Amsler boxes, Wasau loops and proving rings, provided acceptable accuracy using mechanical or optical displacement measurement techniques. However, the devices were usually fragile, extremely sensitive to temperature, and required a great deal of skill to use.

Electrical resistance strain gauge force transducers, commonly called load cells, were developed during the 1940s and became available commercially in the 1950s. They were more robust than their mechanical and optical predecessors but were initially more expensive and less accurate. While they rapidly gained acceptance in control applications, force standards work remained the province of the mechanical devices until the advent of the integrated circuit in the 1970s. The cheap integrated circuit resulted in both a drop in price and an improvement in the performance of strain gauge bridge instrumentation. The photo-lithography techniques used to produce integrated circuits were also adapted to the manufacture of thin film strain gauges resulting in both price and performance improvements. As a result resistance strain gauge load cells have now displaced mechanical devices in almost all force standards work.

1.1.1 Force standards

Forces are measured in virtually every field of commerce and engineering. The safety and reliability of many engineering products depends on the accuracy of these measurements. It is therefore essential that these measurements are traceable to national force standards. In the UK, the National Physical Laboratory (NPL) is responsible for realising and disseminating the SI unit of force, the newton. The newton is realised at NPL by building and maintaining both dead-weight and hydraulic force standard machines. These machines are used to calibrate the load cells and

other force measuring devices which are used by industry as secondary standards. The accuracy with which the newton is disseminated is determined by the accuracy of both the NPL force standard machines and these 'transfer standards'.

1.1.2 Transfer standards

The load cells calibrated in the NPL force standard machines are required to fulfil a variety of roles and to transfer the standard of force to various accuracies. The majority of load cells calibrated are used to verify the servo-hydraulic testing machines used in industry for materials and component testing. These calibrations are generally carried out to the requirements of European standard EN10002-2, the testing machine being classified as being of accuracy class 3, 2, 1, or 0.5.

Higher accuracy is required of those load cells used to verify industrial force standard machines including those machines accredited by the National Measurement Accreditation Service (NAMAS). These machines range in accuracy from 0.1% to 0.02%.

The highest accuracy is required of those force transfer standards used by NPL to verify and intercompare the primary force standard machines. These high accuracy strain gauge load cells are used to compare the NPL force standard machines with similar machines in other national standards laboratories, e.g. PTB in Germany, TNO-IWECO in the Netherlands, NIST in the USA etc. (Debnam & Weiringa [1974], Jenkins & Debnam [1982], Knott & Robinson [1990]).

High accuracy strain gauge load cells are also used to verify the NPL hydraulic amplification and strain gauge hydraulic force standard machines using the 'build up' procedure. This involves using three load cells loaded in parallel to calibrate a machine, each of the three load cells having been individually calibrated in a force standard machine of lower capacity. The standard of force is therefore multiplied by a factor of three. This procedure may be repeated with groups of progressively larger load cells to provide further multiplication. By this means the standard of force is transferred up to 30 MN (\approx 3000 tonnes), the capacity of NPL's largest strain gauge hydraulic force standard machine.

Force transfer standards are therefore used under a variety of conditions and provide accuracies ranging from a few percent up to 0.01%. Strain gauge load cells currently provide the most accurate and convenient force transfer standards. Other technologies under development, such as resonant, SAW, and optical fibre sensors,



IMAGING SERVICES NORTH

Boston Spa, Wetherby
West Yorkshire, LS23 7BQ
www.bl.uk

BEST COPY AVAILABLE.

VARIABLE PRINT QUALITY

show some promise for the future. However, none of these is likely to replace strain gauge technology in the near future.

1.2 Strain gauge load cells

1.2.1 Principle of operation

A strain gauge load cell consists of an elastic 'element', usually steel or aluminium, to which a number of etched foil electrical resistance strain gauges are bonded. The strain gauges are usually positioned such that half are subject to tensile strain and half compressive strain. In most commercial load cell designs four gauges (two tension, two compression) are used. However in more specialist high accuracy load cells, eight, sixteen or twenty four gauges are used.

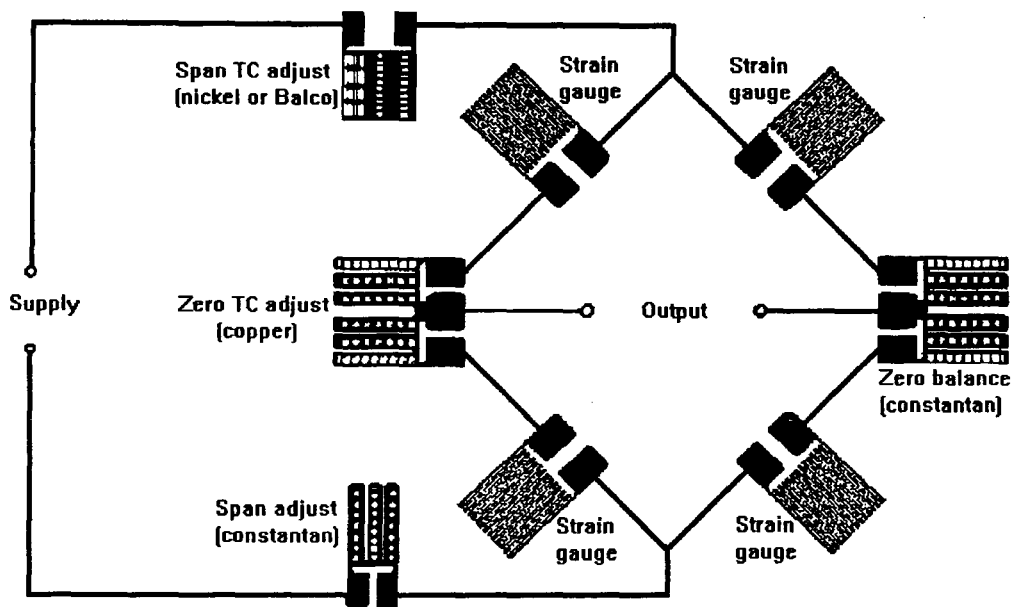


Figure 1.1: A typical strain gauge circuit

Figure 1.1 shows a typical load cell circuit diagram. The gauges are arranged in a Wheatstone bridge in order to combine the outputs from the tensile and compressive gauges. The bridge arrangement cancels out most of the temperature induced resistance changes in the strain gauges. The temperature dependence of the load cell output at zero load is further reduced by an abratable or ladder-type copper resistor in one of the bridge corners. This resistor is trimmed to balance the residual temperature induced zero shift of the circuit. The constantan resistor in the opposite bridge corner is used to adjust the initial zero balance of the circuit. Temperature changes also effect the transducer's span (output under load minus zero load output). This results from temperature dependence of both the Young's modulus of the elastic

element and the gauge factor of the strain gauges. Both of these can be compensated for by the inclusion of nickel or Balco resistors in the bridge excitation circuit.

1.2.2 Sources of error

If further improvements in the accuracy of strain gauge load cells are to be made the remaining sources of error must be addressed. These include:

Creep and Hysteresis:- Creep is a time-dependent change in the output of a load cell subject to constant force. Hysteresis is a dependence of bridge output on loading history. Two separate sources contribute to a load cell's creep and hysteresis. Firstly the material from which the load cell is manufactured may exhibit both creep and hysteresis. Although load cells are designed to be used well below their elastic limit, defects in the material microstructure may cause stress concentrations resulting in the elastic limit being locally exceeded, leading to plastic behaviour. Secondly the strain gauge glue layer and backing material are both visco-elastic and therefore contribute to creep and hysteresis in the load cell. Hysteresis may also result from variations in the frictional forces at internal and external interfaces in the load path.

Temperature sensitivity:- Although the compensation methods described above dramatically reduce the temperature sensitivity of load cells there is always some residual uncompensated sensitivity. In addition the compensation techniques rely on the load cell being at a uniform temperature. In practice load cells are often subject to temperature gradients which cause temperature errors that are uncompensated.

Sensitivity to parasitic forces:- Under ideal conditions, loads are applied along the axis of the load cell with no additional side loads or bending moments. In a deadweight machine, conditions close to this ideal may be achieved. However, in hydraulic machines the load cell is usually over constrained and small but significant side forces and bending moments may arise. The degree to which a load cell is sensitive to these side loads and bending moments is a function of its element geometry and gauge configuration.

Sensitivity to end loading conditions:- In order to measure a force a load cell must be introduced into the load path. Ideally the load cell should be insensitive to the mechanical arrangement by which this is done. In practice

both compression and tension load cells are sensitive to variations in the contact stress distribution.

NPL has several research programmes aimed at reducing the above errors. These include the investigation of alternative material types and alternative strain sensing technologies. In addition much work is being carried out on these problems by other national standards laboratories, load cell manufacturers, strain gauge manufacturers and academic institutions. The work described in this thesis involves the investigation of the errors that arise from the end-loading sensitivity of load cells

1.3 Sensitivity to end-loading conditions

Unfortunately, by their nature, errors due to sensitivity to end-loading conditions are often not so readily apparent as creep, hysteresis and temperature errors and as a result are sometimes overlooked by end users. Within calibration laboratories there is much qualitative experience of this problem. However, little work has been carried out to quantify and characterise the effects. The programme of research described here was aimed at gaining an improved understanding of the problem and using this to improve NPL's load cell designs. Due to their different methods of installation the nature of end loading condition errors are different for compression and tension load cells.

1.3.1 Tension load cells

Tension load cells are usually fastened into the machine by means of threaded adaptors, the ends of the load cell being provided with either an internal or external threaded area for this purpose. Tension load cells may be sensitive to some or all of the following:

The depth of thread engagement between the load cell and the adaptors.

The rotational alignment between the load cell and the adaptors.

Variations in thread pitch from adaptor to adaptor.

All of the above may cause errors if the load cell is used with adaptors other than those with which it was calibrated. Even when the same adaptors are used, errors may still arise unless great care is taken to ensure that each adaptor is screwed to the exact position used during the calibration. As yet EN10002-3 does not contain any test to determine the sensitivity of tension load cells to their end-loading conditions.

1.3.2 Compression load cells

Ideally, loads should be distributed uniformly over the loading surfaces of a compression load cell. However, in practice, non-uniform load distributions often arise due to combinations of the following (illustrated in figure 1.2):

The loading surfaces of the load cell and of the surfaces they contact may not be perfectly flat. Even if the platen of a materials testing machine is initially ground flat, subsequent use may cause pits, ridges and depressions. Similar problems may occur if the contact surfaces are not perfectly clean, particles of grit causing local areas of high contact stress.

The surfaces in contact with the load cell may deflect non-uniformly under load. Platens of different flexural stiffness undergo different deflections, resulting in variations in the contact stress distributions from platen to platen.

Surfaces the load cell contacts may vary in peripheral stiffness. The contact coefficient of friction may also vary from one surface to another. Both these may result in variations in the stresses present at the contact surfaces.

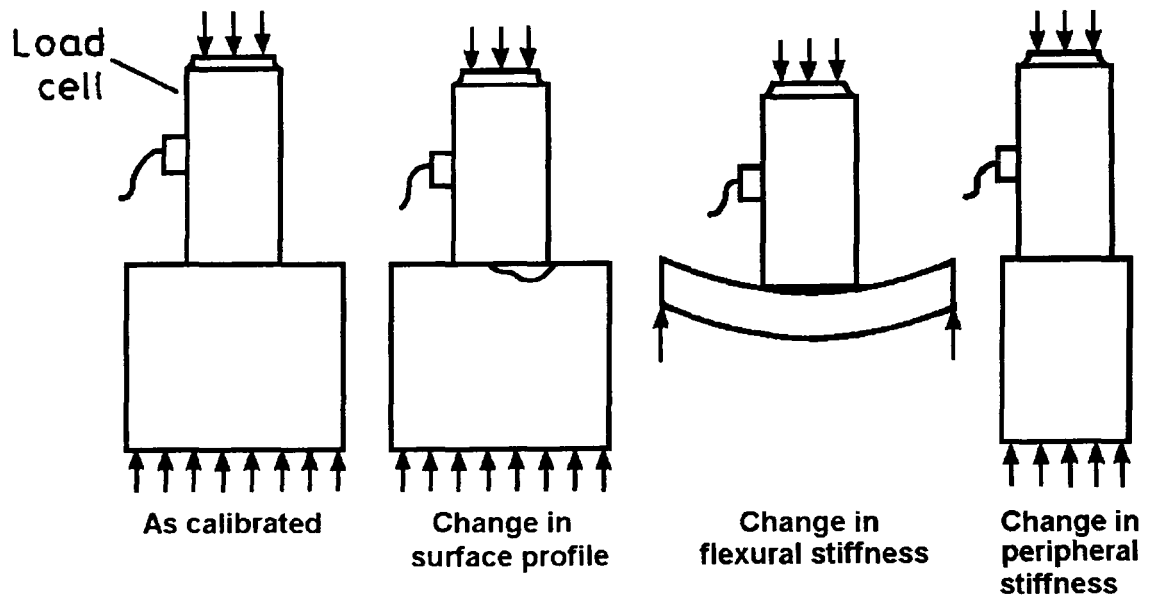


Figure 1.2: Examples of variation in end-loading conditions

1.3.3 End-loading sensitivity and standards

Since 1964 a test of the sensitivity of compression load cells to axisymmetric non-uniform loading, known as the bearing pad test, was required by the British Standard governing the calibration of load cells (BS1610:Part 2). This test was incorporated into EN10002-3, which recently superseded BS1610:Part 2. The test requires the load cell

to be loaded through bearing pads with plane, conically raised and conically depressed surfaces. The centres of the conical surfaces are respectively raised and depressed by $1/1000$ th of their radius, an angle of 0.06° . The standard sets limits for the maximum departure of the output on the depressed and raised surfaces from the output on the plane surface, at the maximum and minimum loads in its calibration range. The limits specified are given in Table 1.1.

Class	Maximum permissible difference	
	At minimum force	At maximum force
00	0.1 %	0.05%
0.5	0.2 %	0.1 %
1.0	0.4 %	0.2 %
2.0	0.8 %	0.4 %

Table 1.1: Maximum departures from output on plane surface specified in EN10002-3

An alternative method for testing the end-loading sensitivity of compression load cells is described in German standard, DIN 51301, which was also superseded by EN10002-3. This 'curvature test' requires the results obtained when loaded on a plane pad to be compared with those obtained when a paper ring or a paper disc are placed between the load cell contact surfaces. The outer diameter of the ring is equal to the diameter of the normal contact surface of the load cell. The inner diameter is 80% of this diameter. The diameter of the disc is 50% of the diameter of the normal contact surface. Paper thickness is to be chosen such that after loading its thickness is approximately 0.1% of the diameter of the normal contact surface, provided this is greater than 0.1 mm. No limits or guidance on the acceptable variation in sensitivity during this test are given in the standard. Instead the standard states that 'with the aid of the curvature test, statements can be made with regard to the quality of the force-proving device'. The related German standard, DIN 51233, covering the construction of compression testing machines, attempts to reduce end-loading errors by placing limits on the flatness and stiffness of machine platens. The standard states that platens must be flat to 0.03 mm and deflect less than 0.1 mm, both measured over 250 mm.

1.3.4 Load cells as stress integrators

The output ϕ of an ideal load cell should be a function of the measured force F only - i.e. proportional to the integral of a stress component over a cross-section of the load cell.

For column and bar cells this can be expressed:

$$\phi \propto F = \int_s \sigma_a \quad 1.1$$

where σ_a is the axial stress.

For shear load cells similar ideal behaviour can be expressed:

$$\phi \propto F = \int_s \sigma_s \quad 1.2$$

where σ_s is the shear stress.

For bending beam and ring load cells the applied force generates a bending moment M . This moment is measured and related to the applied force:

$$\phi \propto F = \frac{M}{c} = \frac{1}{c} \int_s y \sigma_b \quad 1.3$$

where c is the effective moment arm of the force, y is the distance from the neutral axis and σ_b is the bending stress.

In practice, the above equations do not describe the behaviour of real load cells. Load cell outputs are obtained, not from integrals of stress, but from the combined output of strain gauges mounted on the surface only. Ignoring strain gauge and instrumentation non-linearity, the output can be expressed:

$$\phi = \sum_{i=1}^n k_i \varepsilon_i \quad 1.4$$

where ε_i is the strain measured by the i th strain gauge and k_i is a factor dependant on the bridge configuration and the gauge factor. This output is a function not only of the axial force applied but also of the distribution of stress across the section where the strain gauges are applied. St Venant's principle states that the effects of changes in distribution of load over a contact surface diminish rapidly with distance. However, in the majority of load cell designs, the strain gauges are close enough to the contact surfaces for changes in load distribution to significantly affect the load cell output. It is

this approximation of the integral of the axial stress over a cross-section by a sum of surface strains that is the fundamental reason for the sensitivity of load cells to their end-loading conditions.

1.4 Scope of this study

As already discussed there is a wide variety of load cell types in use in many different applications. All types are, to some extent, sensitive to their end-loading conditions. Analysis of the sensitivity of all the many different load cell designs would require more effort than was available for this study. It was decided to limit the scope of this study to column type compression cells, as these are the most important to NPL's force standards work. The object of the work described here was to develop numerical models of the influence of end-loading conditions on column load cells and to use these to evaluate existing designs and develop improved low-profile column load cell element geometries for use as force transfer standards.

1.5 Column load cells

From practical experience NPL and other force standards laboratories have found that if column load cells have a length to diameter ratio (or aspect ratio) greater than 3.5:1 and bridges with four axial and four circumferential gauges, their sensitivity to end-loading conditions is low-enough that they can be used in force standards work. However, there are some test conditions under which it would be an advantage to be able to use load cells of lower aspect ratio.

1.5.1 Requirement for low profile column load cells

Users may require a load cell of low-profile for several reasons. The first is where the working space of the machine to be calibrated is insufficient to accommodate an aspect ratio of 3.5:1. While most modern machines can accommodate such load cells, some older machines have compression spaces of only limited height. One type of machine where this problem is common are the machines used to test the compressive strength of concrete samples. Most were designed specifically for the purpose and have working volumes just sufficient to accommodate the cubic test pieces. A typical concrete-cube testing machine has a capacity of 3 MN with a working space height of 200 mm. In the past the traceability of the calibration of these machines received only little attention. However, recently there has been an increase in construction companies implementing quality systems and seeking NAMAS accreditation. This has highlighted the problem that, due to their limited working spaces, these machines cannot accommodate column load cells that comply with the

bearing pad test requirements of the EN standard. To replace all the existing machines with new machines with larger working spaces would be extremely expensive. This would be unnecessary if a load cell with a sufficiently low profile capable of complying with EN10002-3 could be developed.

Low aspect-ratios may also be desirable for reasons other than limitations of working space. For example in measuring dynamic or impact loads it is desirable that the lowest natural frequency of a load cell should be much greater than the frequencies being measured. It should therefore be as stiff as possible in all directions. As the stiffness of a column cell is inversely proportional to its height it is desirable that a column load cell for use in dynamic or impact tests should be of a low aspect ratio.

1.5.2 Multi-column designs

One approach to achieving a low-profile load cell of low end-loading sensitivity, is to use a multi-column design. Instead of using a single squat column, several (usually three or four) columns, each of high aspect ratio, are assembled on a common base. Usually a top pad is supported on the columns and the assembly is enclosed in a case, giving the assembly the external appearance of a very squat load cell. The output bridges of each individual column are connected in parallel to give a single output.

Unfortunately, such multi-column designs have the following disadvantages:

Each of the columns requires similar amounts of machining and gauging to a single column cell. Multi-column load cells are therefore more expensive to manufacture.

For the load cell output to be independent of the distribution of the force between the columns, the sensitivities of the columns must be adjusted to be equal to within a close tolerance. In practice this is difficult to achieve. As a result the load cell may be as sensitive to end-loading conditions as a single column cell.

The sum of the bending stiffnesses of the individual columns is much less than the bending stiffness of a single column. This may result in multi-column load cells being more sensitive to side forces, bending moments and torque.

In order to construct multi-column cells, screwed connections are usually included in the load path. These can cause large amounts of hysteresis.

As a result of these problems, multi-column load cell designs are usually expensive and have not proved to be very successful as low-profile force standards.

1.6 An overview of this thesis

This thesis is divided into nine chapters. The contents of each chapter is outlined below:

Chapter 1 - Introduction

This chapter. A general introduction to force measurement, load cells and end-loading sensitivity.

Chapter 2 - A review of previous work

A review of St Venant's principle and previous experimental and numerical work on load cell end-loading sensitivity.

Chapter 3 - Preliminary analysis of column load cells

An analytic study of the strain in plane cylinders subject to annular loadings. A relationship between the number of gauges in a load cell bridge and its sensitivity to non axisymmetric loading is also derived.

Chapter 4 - Experimental measurement of surface strains in cylinder

An experimental study of the strains in a cylinder loaded via contact pads of various profile.

Chapter 5 - Development of finite element analysis program

The development of a simple axisymmetric finite element program based on the NAG FE library. The results obtained from the program are compared with those from the analytic solution of chapter 3 and the experimental results of chapter 4.

Chapter 6 - Modelling contact

The extension of the finite element program to include infinite elements and frictional contact is described. The results from benchmark tests are compared with other published results. The results are also compared with the experimental results of chapter 4.

Chapter 7 - Automation of the modelling process

An algorithm developed to automatically mesh load cells of arbitrary shape is outlined. Two numerical measures of the insensitivity of load cells to end-loading conditions are also described.

Chapter 8 - Genetic shape optimisation

The implementation of a set of routines for adding genetic algorithm optimisation to the FE program is described. The performance of the routines is assessed on trial problems.

Chapter 9 - The Darwin load cell

The genetic algorithm/finite element program is used to optimise the geometry of a low-profile 3 MN load cell. A prototype of the resulting 'Darwin' design was manufactured and tested. The results from these tests are compared with the FE predictions. The performance of the new design is compared with that of a more traditional design.

Chapter 10 - Conclusions and proposals for further work

The work in this thesis is reviewed and conclusions drawn. In addition some proposals for further development of the work are made.

CHAPTER 2

A REVIEW OF PREVIOUS WORK

2.1 Introduction

Before starting the project a literature search of previous work was carried out using both computer and manual searches of abstracts. For the purposes of the following discussion, previous work has been divided into three categories by approach:- analytic, experimental or numerical, although some work overlaps more than one category.

2.2 Analytic studies

Workers at NPL and elsewhere became aware of the problem of end loading conditions during work with the first load cells during the 1950s. Since then much work has been carried out to investigate the problem. However, the mathematical study of the effect of contact stresses at distances removed from their point of application has a much longer history and as 'Saint-Venant's problem' is a classical problem in solid mechanics.

2.2.1 Saint-Venant's Principle

'Saint-Venant's Principle' was originally stated in 1855 by Barré de Saint-Venant [1855] in connection with the problem of a cylinder deformed by prescribed surface tractions on its plane ends. Boussinesq [1885] introduced a generalised statement of the principle applying to elastic bodies of arbitrary shape. The principle has been summarised as the 'elastic equivalence of equipollant systems of load' (Love. [1927, par. 89]). According to this principle, the strains produced in a body by the application, to a small part of its surface, of a system of forces statically equivalent to zero force and zero couple, are of negligible magnitude at distances that are large compared with the linear dimensions of the part.

A non too rigorous case can be made for the principle using an argument based on conservation of energy (Goodier [1937]). If p denotes the order of magnitude of the applied force per unit area, a a representative linear dimension of the loaded part, and E the material Young's modulus, the strain components are of the order p/E and the relative displacements are of the order pa/E . The work done in applying the force

is therefore of the order $p^2 a^3/E$. A stress of order p is associated with strain energies per unit volume of order p^2/E . The work done in applying the forces is therefore sufficient only to strain a volume of order a^3 . It is therefore to be expected that the effects of stresses applied over an area should be confined within volumes of the same linear order and should not extend into the 'far field'.

Saint-Venant was not able to prove his principle but offered it as a conjecture. In fact it has been proved that under certain exceptional conditions the theorem does not hold. However, the principle generally applies and in most engineering applications contact stresses can be replaced by their statically equivalent loads when analysing the strength components. Unfortunately in the case of load cell design, where differences of less than 0.1% in strain levels are significant, Saint-Venant's principle cannot be assumed to apply.

The studies of Saint-Venant and Boussinesq have been discussed above. Much work since then has been directed at formulating and proving more precise general theorems for 'Saint-Venant' problems. Notably Von Mises [1945] and Sternberg [1958] proved theorems for some related problems. Other workers have developed estimates for the rate of decay of strain energy within elastic bodies of general shape. Zanaboni [1937] and Goodier [1937] (see above) both utilised energy arguments. Recently, following papers by Toupin [1965] and Knowles [1966], there has been a revival of interest in these energy methods. Hogan and Knowles [1983] give a comprehensive review (updated by Hogan [1989]) of recent work based upon energy arguments. While this work has had some success in producing upper and lower bounds for the rate of decay of strain energy in general bodies these theories are not yet sufficiently advanced to be of use in predicting rates of decay of strain in bodies of arbitrary shape such as load cells.

2.2.2 Circular cylinders under axisymmetric loading

More pertinent to the present study is the work on the specific problem of circular cylinders. As the simplest form of a column load cell is a circular cylinder gauged around its mid-plane, a general analytic solution for a cylinder loaded on its plane ends would be highly relevant. It was this problem that was one of the subjects of Saint-Venant's original statement of his principle. While plane cylinders are geometrically simple, the analysis of their elastic behaviour has proved to be complex, and there has been little progress on the problem of cylinders subject to general loadings. Much more success has been achieved on the sub-problem of cylinders subject to axisymmetric loadings. The problem was first discussed by

Pochhammer [1876], Chree [1886, 1889] and Steklov [1892] using Fourier-Bessel series. Filon [1902] produced a large but incomplete set of solutions for the circular cylinder loaded on its side surface. Prokopov [1948, 1950] obtained a set of homogenous solutions satisfying the equilibrium conditions for an infinite solid cylinder. He went on to demonstrate that many loading conditions could be approximated by superposition of these homogenous solutions. The most complete analyses of the problem of a cylinder subject to axisymmetric loading over its plane ends have been by Little and Childs [1967], Klemm and Little [1970] and Power and Childs [1971]. Khadem and O'Connor [1969] derived a solution for a circular cylinder compressed between two elastic half spaces. This particular loading condition is very similar to real load cell end-loading conditions.

Other than for trivial load cases, none of the methods reviewed above completely satisfy all the boundary conditions on the side and end surfaces of either infinite or finite cylinders. However, the methods have been shown to be capable of approximating the state of stress in an axisymmetrically loaded cylinder. All the above works concentrate on analytical methods of solution and present only limited numerical results. It is unlikely that any of these methods can be extended to model geometries more complex than solid or hollow cylinders.

The only known analytical investigation of a load cell end-loading problem is by Kuipers [1953]. In this study thin walled cylindrical load cells subject to non-axisymmetric loading were analysed. It was assumed that in a thin walled shell, the stresses and strains are uniform through the wall thickness. Loadings around the rims of the cylinder were approximated as Fourier series in angle and their rates of decay with length calculated. Numerical results were presented for various loading harmonics and load cell length to diameter ratios. The results presented are valid only for thin walled elements and unfortunately are not likely to represent the behaviour of real load cells which are solid or thick walled.

2.3 Experimental studies

That load distribution has an effect on the output of load cells has been known since the 1950s and was acknowledged by the inclusion of the 'bearing pad test' in the 1964 edition of BS1610. The earliest published experimental works are believed to be those of Rohrbach [1970] and Feucht [1970].

2.3.1 The work of Rohrbach

Rohrbach suggests that the correct transfer of forces into the spring element is the biggest problem in force measurement. He states that the practical application of precision force transducers breaks down on the fact that strain gauges only determine surface strains, whereas the effective strain is distributed over the entire volume. An experiment is described in which the output of the individual gauges of two cylindrical load cells are compared. Each load cell is a 24 mm diameter cylinder of height 40 mm. Both have plane lower ends and are supported on a plane pad. The upper surface of one is plane while the other has a 30 mm radius spherical upper surface. Both are loaded by a laterally guided upper pad with a plane lower surface. The strain v load curves for the four individual strain gauges of the bridge, together with the bridge output, are given for the two geometries. Rohrbach's results are given in figure 2.1.

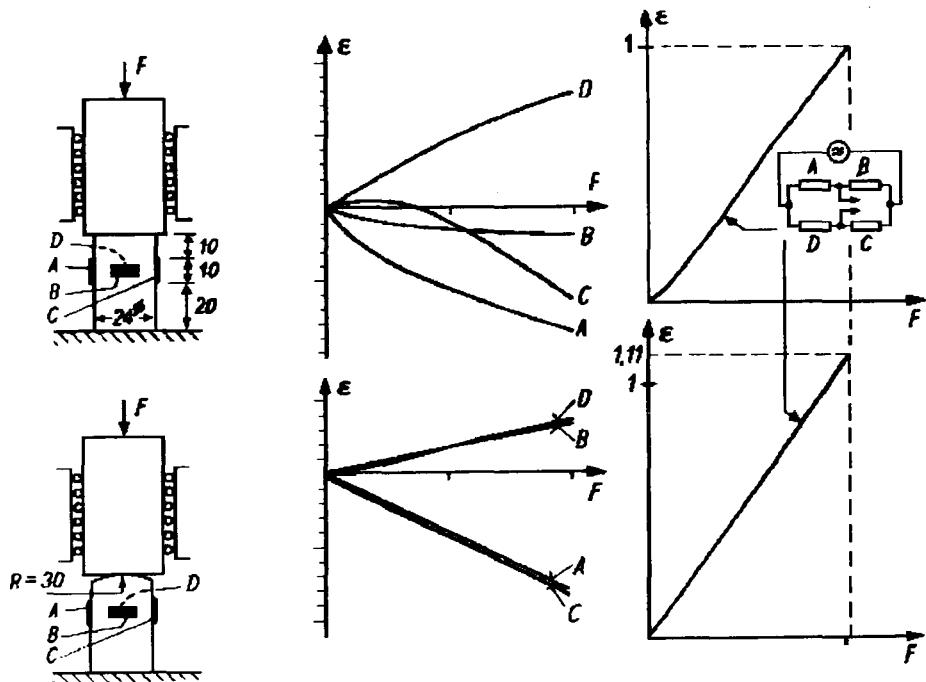


Figure 2.1: Transfer of force into a cylindrical load cell element
(from figure 4 of Rohrbach [1970])

The strains measured in the plane upper surface load cell were not linearly related to load. The strains in gauge B and D were even of opposite sign. Rohrbach suggests that this is due to the influence of unavoidable surface roughness and imperfect parallelism of the loading surfaces. He suggests that substantially better results are obtained when the spring element is provided with a spherical surface 'as the possible location of the place of application of the force is only slightly variable'.

In a further experiment Rohrbach manufactured a solid load cell with a waisted central section of length to diameter ratio 0.5. The output of the bridge was recorded and compared with the output of the load cell after the waisted section had been extended to length to diameter ratios of 1.0, 2.0, and 4.0. The results are shown in figure 2.2.

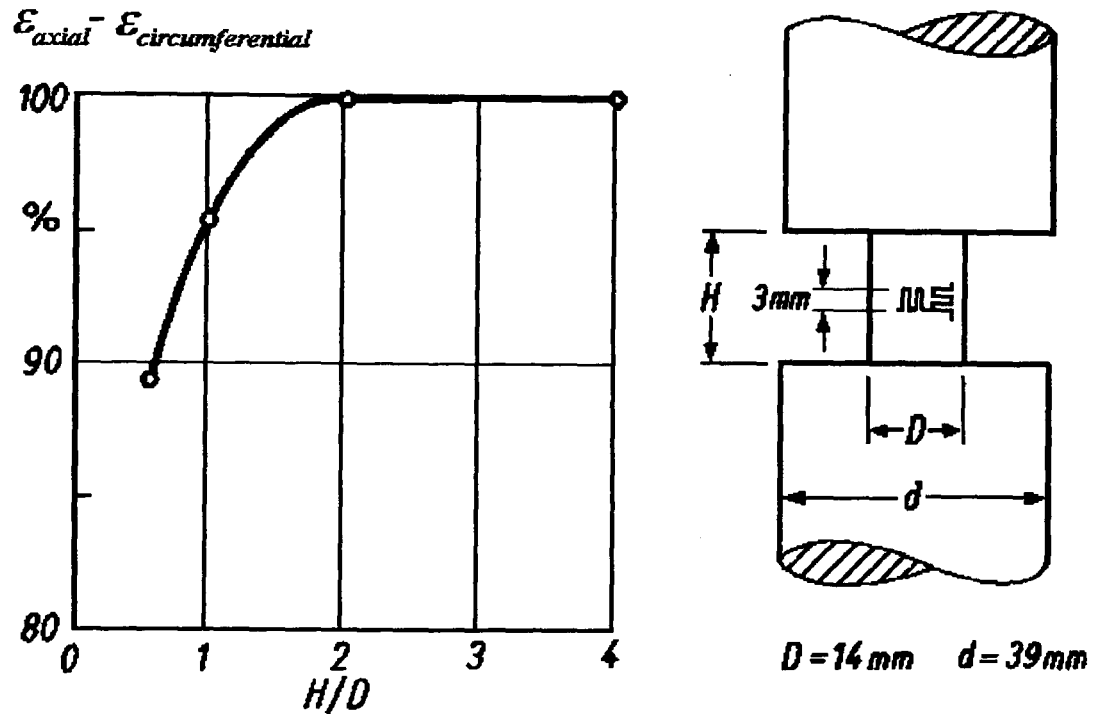


Figure 2.2: Errors due to radial restraint of cylindrical load cell
(from figure 5 of Rohrbach [1970])

Rohrbach interpreted the results as giving a comparison between the output of cylindrical load cells loaded in the presence and absence of radial slip at their contact surfaces. He concluded that, providing the cylinder has a height to diameter ratio greater than 2, the effect of slip at the contact surfaces would be negligible.

2.3.2 The work of Feucht

In a discussion of a paper by Hild [1970], Feucht presented results of some work on the development of low-profile load cells. He describes some tests on load cells fitted with 'equalising cushions' of yielding materials. In his discussion he refers to previous work by Johansson on annular cylinders. He briefly describes his own work on the use of a layer of yielding material as a means of equalising the distribution of stress over the ends of a load cell. He reports that he has experimented with cardboard, 'Klingerite', rubber, 'Dekaplast', lead and in addition rubber bags filled with glycerine. He also gives a brief summary of a test using rubber 'cushions'. He states that a full

account of this work is to be published later. Extensive literature searches have unfortunately failed to turn up reference to either this work or to the previous work of Johansson.

Freucht briefly describes a series of tests using a 100 kN cylindrical steel load cell 130 mm diameter and 140 mm high (aspect ratio 1.08). A thin layer of rubber was sandwiched between each end of the load cell and special end-caps. The end-caps incorporated seals to contain the pressure generated in the rubber 'cushion'. In order to maintain stability of the assembly, the top and bottom platens of the testing machine were linked by rigid lateral guides. Freucht assumed that this loading condition provided a uniform distribution of axial stress over the ends of the load cell. The output of the load cell bridge under this 'ideal' loading condition was used as a reference to compare the load cell output when loaded via three less ideal end-loading conditions. The first condition was the common one of loading between two large plane plates without any cushion. He found that the output in this case was 2% lower than the reference loading condition. When subject to annular loads applied at 43% and 78% of the load cell radius, the load cell showed, respectively, a 3.5% decrease and a 3% increases in output relative to the reference case. Feucht's results are shown in figure 2.3.

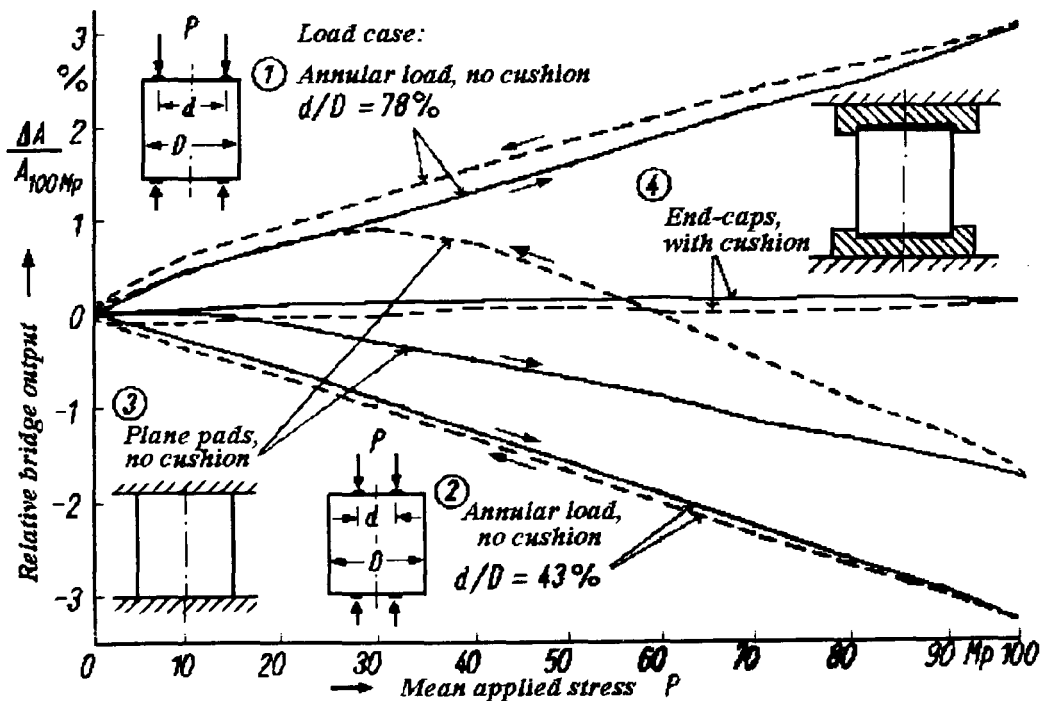


Figure 2.3: Effect of four different end-loading conditions on sensitivity, linearity, and hysteresis (from figure 2 of Feucht [1970])

Unfortunately although he states that he has carried out tests to determine the equalisation effect of the rubber cushions under six different annular loadings, he provided no results in the discussion. He also gave no details of the tests using materials other than rubber only making a general statement that the use of cushion materials caused problems of mechanical stability and that hard plastics and metals did not look promising at high loads. One important observation made by Feucht is that there is a relationship between sensitivity to end-loading conditions and hysteresis. Figure 2.3 shows that changing the end-loading conditions changes the load cell hysteresis as well as its sensitivity.

2.3.3 The work of Debnam & Jenkins

Debnam & Jenkins [1972] of NPL carried out an experimental study of the influence of end-loading conditions on load cells using four load cells chosen to be of different mechanical construction. The designs chosen were:

1. An NPL manufactured octagonal strain gauged billet without any protective case.
2. A commercially made four column load cell, each column having a square section.
3. A commercially made single column load cell, with a solid cylindrical billet, supported at its top end by a diaphragm which attached to its outer case.
4. A commercially made single column load cell, with an octagonal hollow billet.

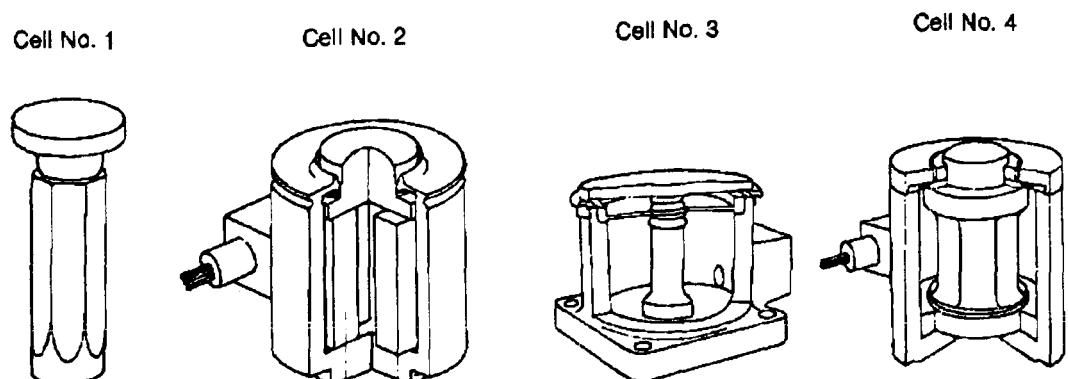


Figure 2.4: The four load cell designs tested by Debnam & Jenkins [1972]

The four load cells are illustrated in figure 2.4. The designs were representative of the range of compression load cells in use in 1972. The four designs were tested on conically raised and conically depressed pads as well as on flat pads of varying hardness.

Lower loading pad	Difference from average result for the flat pad, hardness 540 HV			
	Load cell No. 1	Load cell No. 2	Load cell No. 3	Load cell No. 4
Flat, hardness 270 HV	+0.002%	-0.011%	-0.025%	+0.005%
Conically depressed by 1:1000 hardness 540HV	+0.002%	+0.004%	-0.306%	+0.039%
Conically raised by 1:1000 hardness 540HV	+0.005%	+0.069%	+0.290%	-0.059%

Table 2.1: Debnam & Jenkins' results for four load cells of different design

It was found that variation of the profile of the contact surface of the loading pad had a much greater effect on load cell output than variation in the hardness of the material from which it was constructed. It was noted that the simple NPL octagonal billet (aspect ratio 3.7) performed significantly better than the commercial designs. Their results are presented in table 2.1. Further observations on the end-loading effect in load cells, including a discussion of the above results, are given in Jenkins [1979]

2.3.4 The work of Bray

Bray [1972] used photo-elastic and strain gauge techniques to investigate the effect of end-loading conditions on cylindrical load cells. In this study epoxy cylinders of various aspect ratios were loaded on pads made of various materials, profiles and surface finishes. The results in the study suffered from the problems of making strain gauge measurements on epoxy without introducing errors due to self-heating. Although pulsed voltage instrumentation was used, the results show poor repeatability. The author drew various conclusions concerning the effect of the various factors on the output, linearity and hysteresis of cylindrical load cells. The author concludes that for cylindrical elastic elements there exists a ratio of height to diameter (aspect ratio) for which the most satisfactory metrological characteristics are obtained. However, he does not give a value for this ratio. His results do however confirm that cylinders of low aspect ratio (<2.0) are much more sensitive to end-loading conditions than those of higher aspect ratio.

In addition to the studies summarised here, some experimental work has been carried out in order to verify the results from numerical models. Such work is summarised with the relevant numerical work in the next section.

2.4 Numerical studies

Numerical modelling of the performance of load cell billets has been based exclusively on the finite element (FE) method. No studies based on boundary element or other numerical methods were found.

Finite element analysis of load cells has been reported by many authors e.g. Barbato et al. [1980], Abdullah & Erdem [1978], Abdullah & Li [1983], Stefanescu [1988], Leinonen [1988, 1989]. Most of these studies have been to determine characteristics of load cells other than their end-loading sensitivity. The literature search revealed only three FE studies which address the end-loading problem for column load cells.

2.4.1 The work of Mitchell et al.

Mitchell et al. [1971] report an experimental and numerical study of a 3.6 MN (800,000 lbf) column load cell. The design was typical of many column cells, having a waisted central section and a domed loading cap (figure 2.5).

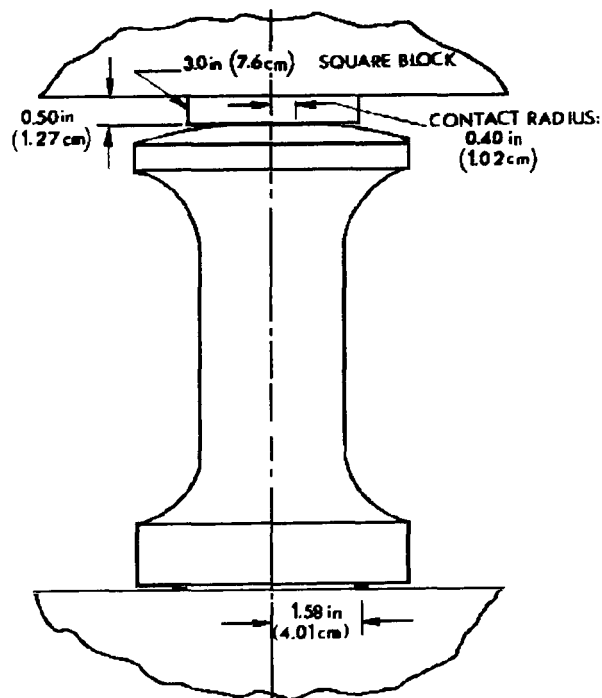


Figure 2.5: Load cell loading arrangement (from figure 6 of Mitchell et al. [1971])

A finite element model of the load cell element was constructed using three node triangular elements. The surface strains were evaluated using the FE programme for several loading conditions. In order to verify the FE results, a total of 54 strain gauges were applied to the load cell billet, aligned in both the axial and circumferential directions. The billet was loaded when supported via four rings of mean radius 17%, 33%, 67%, and 96% of the radius of the lower loading surface.

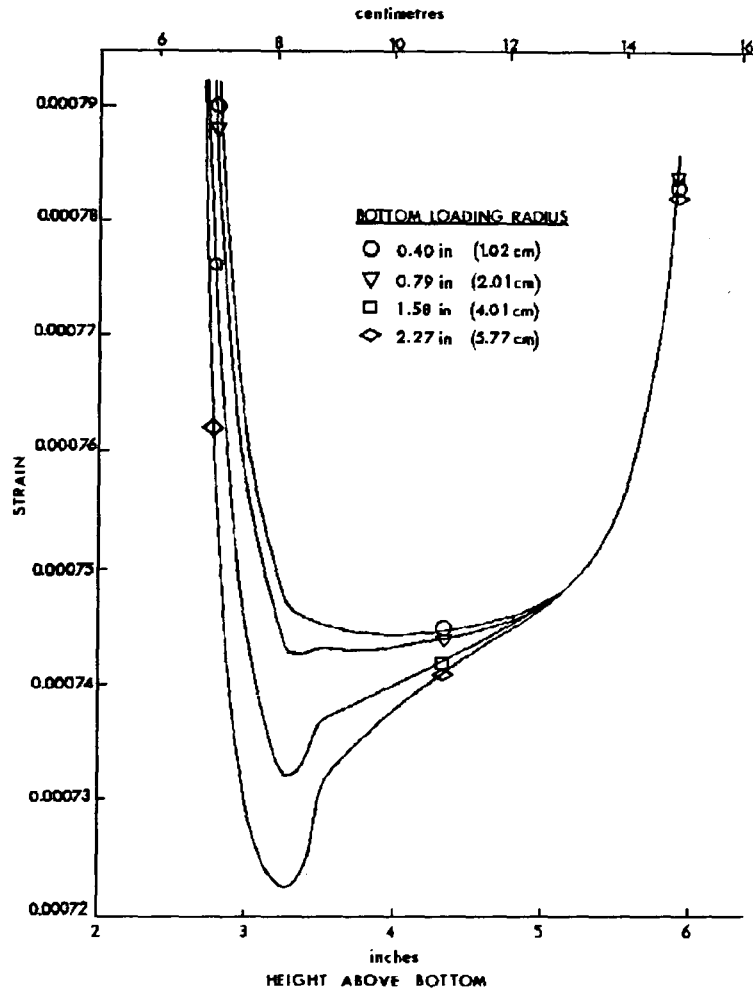


Figure 2.6: Axial surface strains over central section
(from figure 8 of Mitchell et al. [1971])

Figure 2.6 shows the axial strains measured by gauges over the central cylindrical section, together with the FE results. The experimental results (symbols) are shown to be in good agreement with the values calculated by the FE programme (lines). The authors point out, however, that the agreement at 4.3 inches from the bottom is imposed by the method used to determine the value of Young's modulus used in the FE analysis. It can be seen that the dependence of axial strain on loading radius decreases rapidly as the distance from the loaded end increases.

The degree of agreement shown between the two methods, even allowing for the imposed agreement at the centre, confirms the finite element method to be useful in analysing the behaviour of load cells under various end-loading conditions.

2.4.2 The work of Sundin & Jonsson

Sundin & Jonsson [1985] used FE methods to develop a low profile load cell for measuring impact forces. It was desired that the load cell should have a squat form in order to maximise its stiffness and consequently its lowest natural frequency. The transducer design was unusual in that it relied on measuring circumferential strain only. Four turns of resistance wire were wrapped around the steel element and formed the active arm of a $\frac{1}{4}$ Wheatstone bridge. The stepped cylinder design of the load cell elastic element is shown in figure 2.7.

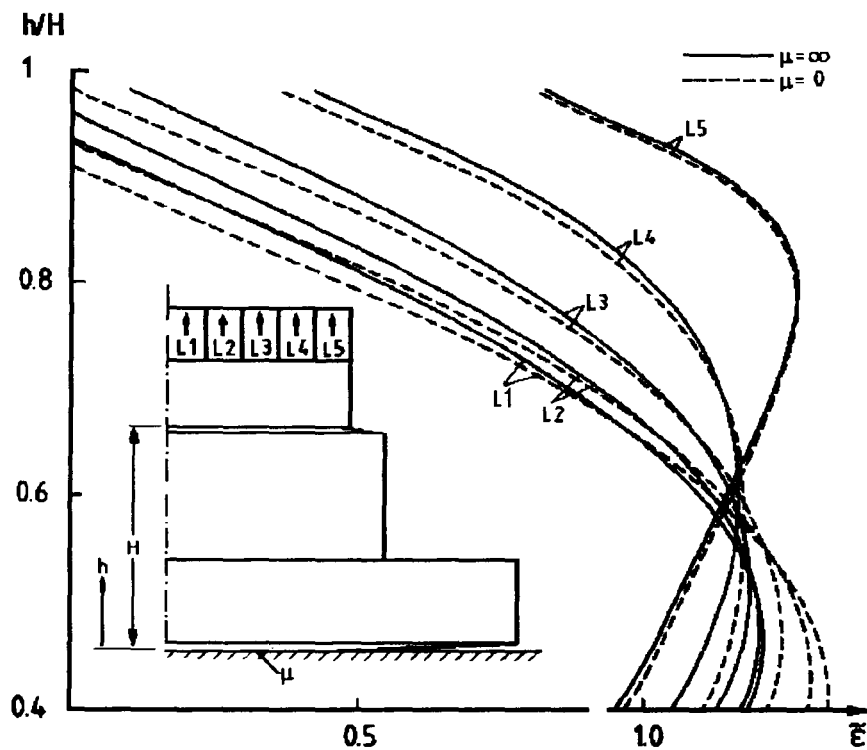


Figure 2.7: Variation of load cell sensitivity with step position
(from figure 3 of Sundin & Jonsson [1985])

Also shown in figure 2.7 are the results of FE analyses carried out to determine the influence of the position of the step change in radius on the end-loading sensitivity. The analysis determined the circumferential strain in the resistance wire for various annular load radii and step heights. The results show that there is a value ($h=0.585 H$) for which the load cell sensitivity is a minimum. The authors manufactured a transducer of this geometry and tested it under different radial load distributions. The

experimental results demonstrated that this high natural frequency transducer exhibited the predicted low sensitivity to end-loading variations. While other papers have described the use of FE methods in analysing the performance of existing designs, Sundin & Jonsson's work is the only example known to the author of an FE method being used to develop a force transducer with reduced end-loading sensitivity.

2.4.3 The work of Williams

Williams [1983] of NPL carried out a finite element analysis of a semi-infinite plane cylinder subject to annular loads at various radii. Each load case was a compressive annular load superimposed on an equal uniform tensile load (figure 2.8). The difference between the strains for an annular load and a uniform distributed load are therefore calculated directly.

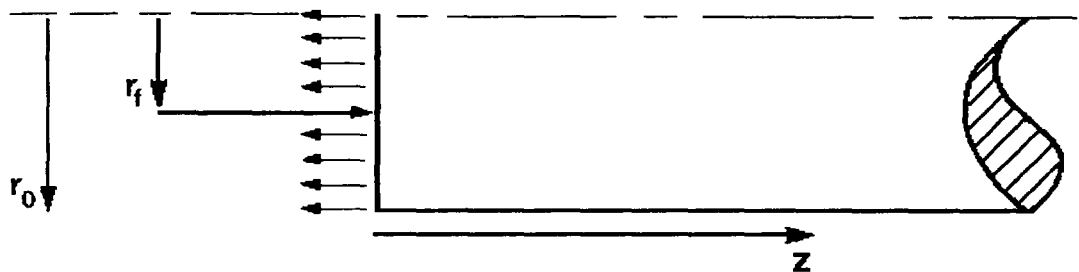


Figure 2.8: The problem analysed by Williams

The surface strains in the cylinder were plotted against distance from the loaded end. It was assumed that the results from a semi-infinite cylinder can be applied to finite cylinders with negligible error. (In chapter 3 this assumption will be shown to be correct.) Williams determined the axial and circumferential components of strain and used these results to predict the output of a full strain gauge bridge bonded at mid-height on cylinders of various aspect ratios. Bridge outputs were calculated for aspect ratios from 1.5 to 4.0. Williams' results are shown in figure 2.9.

The results confirm that, in general, end-loading sensitivity decreases rapidly with increase in aspect ratio. However a local reduction in the spread of strains is apparent for aspect ratios around 1.5. Extrapolations of Williams' curves to lower aspect ratios, suggest that lower aspect ratios may have even lower end-loading sensitivity.

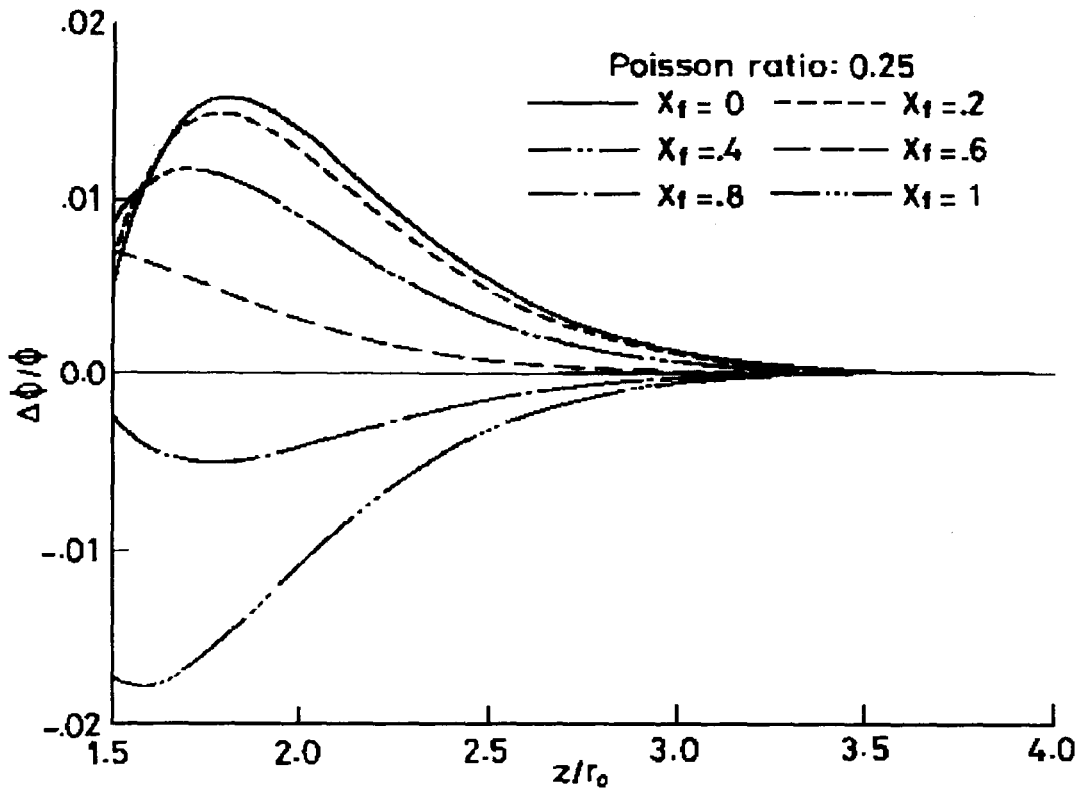


Figure 2.9: Fractional difference in bridge output with load radius
(from figure 3.3 of Williams)

2.5 Conclusions

The works described above have adopted three alternate approaches to the analysis of end-loading sensitivity. Much work has been carried out on analytic solutions of simple geometries. However there is little prospect of extending these analytic methods to give useful results for more complex geometries. Experimental work has demonstrated the influence of load cell shape on its end-loading sensitivity, and has highlighted the relationship between a column load cell's aspect ratio and its end-loading sensitivity and hysteresis. Numerical techniques have been shown to agree with experimental strain measurements and in one case FE analysis has been used to develop a load cell geometry with reduced sensitivity to end-loading conditions.

The works reviewed above confirm that, in general, end-loading sensitivity can be reduced by maximising the load cell aspect ratio. However, the works of both Sundin & Johnson and Williams have indicated that the dependence of end-loading sensitivity on aspect ratio is complex. There may therefore be potential to exploit the complexities of the relationship to design low aspect ratio load cells with low sensitivity to end-loading conditions.

PRELIMINARY ANALYSIS OF COLUMN LOAD CELLS

3.1 Introduction

The study by Williams has been described in the previous chapter. This FE study indicated that the behaviour of cylindrical load cells of aspect ratio below 1.5 may be more complex than previously assumed. The eventual aim of this study was to develop finite element models of load cells of general axisymmetric shape. For such a FE model to be useful, the accuracy of its results must be demonstrated. In this chapter, numerical results from an analytic solution of the problem of a cylinder loaded over an annulus will be presented. In later chapters, these results will be used to validate the finite element model. Before presenting the analytic results, consideration will be given to the response of axisymmetric load cells to general stress distributions.

3.2 Axisymmetric column load cells subject to general stress distributions

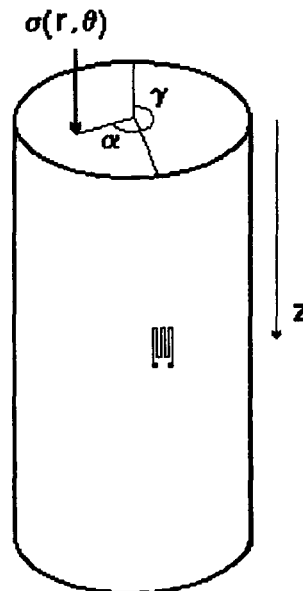


Figure 3.1: Column load cell subject to general stress distribution

Consider an axisymmetric column load cell with a bridge composed of a number of axial and circumferential strain gauges equispaced around its circumference. We may represent an arbitrary stress distribution over one of its ends as a combination of

normal, tangential and radial stress components applied at points on the end surface with polar co-ordinates r, θ (figure 3.2):

$$\sigma(r, \theta) = \sigma_n(r, \theta) + \sigma_t(r, \theta) + \sigma_r(r, \theta) \quad 3.1$$

Initially we will consider only the effect of the normal stress component, $\sigma_n(r, \theta)$, on the output of the strain gauges aligned along the axis of the load cell. The contribution to the bridge output from each of these gauges arising from the normal stresses may be represented by:

$$\phi_j = \Gamma \int_0^{r_0} \int_0^{2\pi} h_j(r, \alpha_j) \cdot \sigma_n(r, \theta) \cdot d\theta \cdot r \cdot dr \quad 3.2$$

where Γ is the gauge factor of the strain gauges and $h_j(r, \alpha_j)$ is a strain influence factor relating the strain at the gauge location to the applied normal stress. The value of this factor is dependent on the element geometry, and the location of the strain gauge. α_j is the angular position of the point r, θ relative to the angular position of the j th gauge. i.e. $\alpha_j = \theta - \gamma_j$ where γ_j is the angular position of the gauge. For convenience and without loss of generality we may define both θ and γ_j to be relative to the angular position of the first gauge.

$$\therefore \gamma_j = \frac{2\pi j}{g}, \quad j = 0 \rightarrow g-1 \quad 3.3$$

where g is the number of equispaced gauges.

The contribution to the bridge output due to the effect of the normal stress components on the axial gauges may be represented by:

$$\phi_n^a = \frac{\Gamma}{g} \sum_{j=0}^{g-1} \int_0^{r_0} \int_0^{2\pi} h_j(r, \alpha_j) \cdot \sigma_n\left(r, \alpha_j + \frac{2\pi j}{g}\right) d\alpha_j \cdot r \cdot dr \quad 3.4$$

If the load cell element is axisymmetric and the axial strain gauges are all of the same pattern and are mounted in similar positions, the strain influence factors $h_j(r, \alpha_j)$ are independent of j . We may therefore drop this subscript, and write the above:

$$\phi_n^a = \frac{\Gamma}{g} \int_0^{r_0} \int_0^{2\pi} h(r, \alpha) \sum_{i=0}^{g-1} \sigma_n \left(r, \alpha + \frac{2\pi j}{g} \right) d\alpha . r . dr \quad 3.5$$

We may represent any arbitrary normal stress distribution on the end face as a Fourier series in angle:

$$\sigma_n(r, \theta) = \sum_{k=0}^{\infty} [A_k(r) \cos(k\theta) + B_k(r) \sin(k\theta)] \quad 3.6$$

where $A_k(r)$ and $B_k(r)$ are functions of r only.

We may therefore represent the contribution to the output from the axial gauges due to an arbitrary normal stress distribution as:

$$\phi_n^a = \frac{\Gamma}{g} \int_0^{r_0} \int_0^{2\pi} h(r, \alpha) \sum_{k=0}^{\infty} [A_k(r) C_k(g, \alpha) + B_k(r) S_k(g, \alpha)] d\alpha . r . dr \quad 3.7$$

where
$$C_k(g, \alpha) = \sum_{j=0}^{g-1} \cos \left(k\alpha + \frac{2\pi jk}{g} \right) \quad 3.8$$

and
$$S_k(g, \alpha) = \sum_{j=0}^{g-1} \sin \left(k\alpha + \frac{2\pi jk}{g} \right) \quad 3.9$$

Equations 3.8 and 3.9 may be rewritten in the form:

$$C_k(g, \alpha) = \cos(k\alpha) \operatorname{Re}(E_k) - \sin(k\alpha) \operatorname{Im}(E_k) \quad 3.10$$

$$S_k(g, \alpha) = \sin(k\alpha) \operatorname{Re}(E_k) + \cos(k\alpha) \operatorname{Im}(E_k) \quad 3.11$$

where
$$E_k = \sum_{j=0}^{g-1} e^{\frac{2\pi jk}{g}} \quad 3.12$$

We may rewrite 3.12:
$$E_k = 1 + e^{\frac{2\pi ki}{g}} + \dots + e^{\frac{2\pi(g-1)ki}{g}} \quad 3.13$$

Summing this geometric series we obtain:

$$E_k = \frac{e^{2\pi ki} - 1}{\left(e^{\frac{2\pi ki}{g}} - 1 \right)} \quad 3.14$$

Evaluating 3.15:

if $k = mg$ (m any integer including $m = 0$) then

$$E_{mg} = g \text{ therefore } C_{mg} = g \cos(mg\alpha) \text{ and } S_{mg} = 0$$

if $k \neq mg$ then

$$E_k = 0 \text{ therefore } C_k = 0 \text{ and } S_k = 0$$

Therefore the contribution to the bridge output due to the effect of the normal stress components on the axial gauges is given by:

$$\phi_n^a = \Gamma \int_0^{r_o} \int_0^{2\pi} h(r, \alpha) \sum_{m=0}^{\infty} A_{mg}(r) \cos(mg\alpha) d\alpha \cdot r \cdot dr \quad 3.15$$

The combined output of the axial gauges is therefore only sensitive to normal stress components at angular frequencies which are integer multiples of the number of gauges. Similar results can be derived for the effects of the other two stress components on the combined output of the axial gauges, as well as the effect of all the stress components on the combined outputs of the circumferential gauges. We may therefore conclude that an axisymmetric load cell with a strain gauge bridge consisting of g equispaced axial gauges and g equispaced circumferential gauges, is only sensitive to components of the stress distributions that are integer multiples of g .

In order to assess the implications of this we should consider how such angular variations in contact stress are likely to arise and which of these are likely to be of significant in practical load cell applications. It is obvious that the 0th multiple (the 0th 'angular harmonic') corresponds to the axisymmetric component of the stress distribution. It is also clear that application of a bending moment to the load cell would result in a significant 1st harmonic component. Loading a load cell on a rectangular platen which exhibits greater bending stiffness about one horizontal axis might result

in a significant 2nd harmonic component. Beyond the 2nd harmonic, mechanical arrangements that might give rise to contact stress distributions having the requisite order of cyclic symmetry become harder to imagine. The author has no evidence to show that stress distributions of such high order do not arise in practice, however, it seems reasonable to hypothesise that, in the well controlled mechanical conditions of force standards machines, angular harmonics of contact stress above the 2nd are insignificant. Assuming this to be the case, we may conclude that load cells used in force standards work should have a minimum of three axial and three circumferential gauges. However, the requirement that the bridge be symmetric results in a practical minimum of four axial and four circumferential gauges.

Most column load cells used in standards work do, in fact, have bridges of four axial and four compression strain gauges. They are therefore sensitive only to the 0th, 4th, 8th, 12th harmonics of the normal stress distribution. If we make the assumption argued above, that under the conditions encountered in force standards work the harmonics of 3rd order and above are negligible, we can limit our consideration to the 0th, axisymmetric, harmonic of the contact stress distribution. Practical experience of tests with such load cells in force standards work confirms that the effects of axisymmetric loadings on column load cells are much greater than those arising from high order non axisymmetric loadings. In attempting to analyse and improve the performance of column load cells the scope of this study will therefore be restricted to axisymmetric loadings only.

3.3 Bridge strain

The output of a column load cell is proportional to the difference between the output of its axial and its circumferential gauges. If both the load cell geometry and the applied stress distribution are axisymmetric and all the gauge locations are at the same height, all the gauges will be subjected to the same strains. The load cell output will therefore be proportional to the difference between the axial and circumferential strains at this height. i.e. $\phi \propto (\varepsilon_a - \varepsilon_c)$. As an aid to future discussion the quantity $\varepsilon_a - \varepsilon_c$ will be given the name 'bridge strain' and the symbol ε_b . While this quantity is not strictly a strain, the use of the term will be retained as a reminder of its origin and non-dimensional nature. Minimising the variation of bridge strain with change in stress distribution minimises the load cell's end-loading sensitivity.

3.4 Homogenous Solution Study

3.4.1 Introduction

As an initial attempt to evaluate the influence of end-loading conditions on column load cells, an analysis of a semi-infinite solid cylinder subjected to annular loading was performed. In practice, few load cells are cylindrical and none are semi-infinite. However, an analytic solution is available for semi-infinite cylinders. In the next section it will be shown that the results from the analysis of semi-infinite cylinders can be applied to cylinders of finite length without significant error. Analysis of the behaviour of cylinders should give an insight into the behaviour of load cells of more typical shape. An analytic solution will also provide a useful comparison with results to be obtained later by other methods.

3.4.2 The modelling of finite cylinders as semi-infinite

The limitation that the solution applies only to semi-infinite cylinders, does not in fact limit the relevance of the results in calculating the strains at the mid-height of finite cylinders. If the stress distribution for a semi-infinite cylinder is taken to apply to a finite cylinder it is apparent that at the unloaded end stresses exist and therefore there is a mismatch in boundary conditions. However, the solutions will be shown to decay rapidly with distance from the loaded end. The mismatch of stress is therefore small compared with the stresses of interest at mid-height. These small spurious stresses could be corrected by superimposing equal and opposite stresses on the unloaded end of the finite cylinder. These 'corrective' stresses would in turn decay with distance and therefore their effect on the strains at mid-height would be diminished further. These corrective strains would themselves lead to mismatch between the stresses and applied loading at the loaded end. Corrective stresses could continue to be superimposed at alternate ends until the stresses at the loaded end were equal to the applied loading and there were no stresses at the unloaded end.

In practice we will assume that the values of strain and displacement at a distance z from the loaded end of a semi-infinite cylinder, radius r , apply at the mid-height of a cylinder of equal radius and height $2z$ (i.e. of aspect ratio $A = \frac{z}{r}$) loaded over one end only. We can obtain an estimate for the error associated with this assumption by considering the rate of decay of the solutions. Results given later show that the slowest decaying component of the solution, decays approximately as $e^{-2.7\zeta}$, where the normalised axial co-ordinate ζ is the ratio between the axial co-ordinate and the cylinder radius. We will assume this 'worst case' rate of decay to apply. At the equivalent of mid-height the component will have decayed to a value $e^{-2.74}$ of its value

at the loaded end. At the unloaded end its value will be reduced by $e^{-5.4A}$. This mismatch would be corrected by applying an equal and opposite stress distribution at the free end. These corrective stresses would also decay by a factor of $e^{-2.7A}$ at the mid-height. The error at the mid-height from omitting this correction would therefore be:

$$\frac{e^{-5.4A} \times e^{-2.7A}}{e^{-2.7A}} = e^{-5.4A} \quad 3.16$$

Consider, by way of example, the results at mid-height of a finite cylinder of aspect ratio 1.0, the error will be $e^{-5.4} = 4.52 \times 10^{-3}$. The error from the assumption that the values at $\zeta = 1.0$ for a semi-infinite cylinder apply to the mid-height of a cylinder of aspect ratio $A = 1.0$ will therefore be less than 0.5%.

As practical load cases will include other faster decaying components, the errors will be less than for this worst case scenario. We may therefore conclude that if solutions obtained for a semi-infinite cylinder are applied to finite cylinders loaded at one end, no significant error will be caused by the failure to satisfy the boundary conditions at the unloaded end.

3.4.3 Analysis method

The analysis method was based on that used by Little & Childs [1967] and Prokopov's analysis as summarised in chapter 7 of L'Ure [1964]. Multiples of the so-called 'homogenous' solutions are superimposed, such that the boundary conditions are approximated. These homogenous solutions are the axisymmetric solutions of the equations of elastic equilibrium for a semi-infinite cylinder which is free from loading on its side surface. Derivations of the homogenous solutions for a semi-infinite cylinder is given by L'Ure and Little & Childs. The discussion here will be limited to the approximation of the boundary conditions and the derivation of the strain components.

The displacement of a point in a circular cylinder, radius r_0 , under axially symmetric loading may be represented as an infinite sum of multiples of the homogenous solutions. The displacements are given by:

$$u = \sum_{s=1}^{\infty} L_s u(x, \beta) e^{i\beta_s \zeta} \text{ in the radial direction} \quad 3.17$$

and

$$w = \sum_{s=1}^{\infty} L_s w(x, \beta) e^{i\beta_s \zeta} \text{ in the axial direction} \quad 3.18$$

where $u(x, \beta_s) e^{i\beta_s \zeta}$ and $w(x, \beta_s) e^{i\beta_s \zeta}$ are the components of the displacements

associated with the homogenous solutions, L_s are complex coefficients, $x = \frac{r}{r_0}$ the

normalised radial co-ordinate, and $\zeta = \frac{z}{r_0}$ the normalised axial co-ordinate. β_s are the

roots of the transcendental equation (equation 7.4.11 of L'Ure) $\varphi(\beta) = 0$, where:

$$\varphi(\beta) = \beta^2 \sum_{s=0}^{\infty} \left[1 - \frac{(m-1)(2s+1)}{m(s+1)(s+2)} \right] \frac{(2s)!}{(s+1)!(s!)^3} \left(\frac{\beta}{2} \right)^{2s} \quad 3.19$$

where m is the reciprocal of the Poisson's ratio.

The real part of β_s determines the axial period of the component and the imaginary part the rate of decay.

The displacement functions $u(x, \beta_s)$ and $w(x, \beta_s)$ are given by:

$$u(x, \beta_s) = \frac{1}{I_1(\beta_s)} \left[-x I_0(\beta_s x) + \left(\frac{2(m-1)}{m\beta_s} + \lambda_s \right) I_1(\beta_s x) \right] \quad 3.20$$

$$w(x, \beta_s) = \frac{-i}{I_1(\beta_s)} \left[x I_1(\beta_s x) + \left(\frac{2(m-1)}{m\beta_s} - \lambda_s \right) I_0(\beta_s x) \right] \quad 3.21$$

in which $\lambda_s = I_0/I_1$, where I_0 and I_1 are the modified Bessel functions of the first kind of order 0 and 1. From the equations for strain in cylindrical co-ordinates:

$$\varepsilon_\theta = \frac{u}{r}, \quad \varepsilon_r = \frac{\partial u}{\partial r}, \quad \varepsilon_z = \frac{\partial w}{\partial z}$$

We can obtain the associated strains:

$$\varepsilon_{\theta} = \frac{1}{r} \sum_{s=1}^{\infty} L_s u(x, \beta_s) e^{i\beta_s \zeta} \quad 3.22$$

$$\varepsilon_r = \frac{\partial u}{\partial r} = \frac{\partial u}{\partial x} \cdot \frac{\partial x}{\partial r} = \frac{1}{r_0} \frac{\partial u}{\partial x} = \frac{1}{r_0} \sum_{s=1}^{\infty} L_s u'(x, \beta_s) e^{i\beta_s \zeta} \quad 3.23$$

where

$$u'(x, \beta_s) = \frac{1}{I_1(\beta_s)} \left[-I_0(\beta_s x) - x\beta_s I_1(\beta_s x) + \left(\frac{2(m-1)}{m\beta_s} + \lambda_s \right) \left(\beta I_0(\beta_s x) - \frac{I_1(\beta_s x)}{x} \right) \right] \quad 3.24$$

$$\varepsilon_z = \frac{\partial w}{\partial z} = \frac{\partial w}{\partial \zeta} \cdot \frac{\partial \zeta}{\partial z} = \frac{1}{r_0} \frac{\partial w}{\partial \zeta} = \frac{1}{r_0} \sum_{s=1}^{\infty} i\beta_s L_s w(x, \beta_s) e^{i\beta_s \zeta} \quad 3.25$$

The complex coefficients, L_s , depend on the stress distribution over the end $\zeta = 0$:

$$\sigma_z = \frac{2G}{r_0} \sum_{s=1}^{\infty} L_s \sigma_z(x, \beta_s), \quad \tau_{rz} = \frac{2G}{r_0} \sum_{s=1}^{\infty} L_s \tau_{rz}(x, \beta_s) \quad 3.26$$

where G is the material shear modulus and:

$$\sigma_z(x, \beta_s) = \frac{1}{I_1(\beta_s)} \left[(2 - \beta_s \lambda_s) I_0(\beta_s x) + x\beta_s I_1(\beta_s x) \right] \quad 3.27$$

$$\tau_{rz}(x, \beta_s) = -\frac{i\beta_s}{I_1(\beta_s)} \left[x I_0(\beta_s x) - \lambda_s I_1(\beta_s x) \right] \quad 3.28$$

With an infinite number of terms, values of the multiplying factor L_s can be calculated such that σ_z and τ_{rz} are equal to the applied loading $F(x)$ and $\Phi(x)$. However for a finite number of terms the applied loading can only be approximated. This approximation will be made so as to minimise the integral of the square of the errors over the end $z = 0$ given by:

$$\Psi = \int_0^1 \left\{ \left[F(x) - \sum_{s=1}^{\infty} (M_s \sigma_z^{(s,r)} - N_s \sigma_z^{(s,i)}) \right]^2 + \left[\Phi(x) + \sum_{s=1}^{\infty} (M_s \tau_{zr}^{(s,r)} - N_s \tau_{zr}^{(s,i)}) \right]^2 \right\} x dx \quad 3.29$$

Where the real and imaginary parts of the coefficients are given by $L_s = M_s + iN_s$, and the real and imaginary parts of the homogenous stresses are given by $\sigma_z(x, \beta_s) = \sigma_z^{(s,r)} + i\sigma_z^{(s,i)}$ and $\tau_{zr}(x, \beta_s) = \tau_{zr}^{(s,r)} + i\tau_{zr}^{(s,i)}$. To minimise Ψ we require that

$\frac{\partial \Psi}{\partial M_k} = 0$ and $\frac{\partial \Psi}{\partial N_k} = 0$ for $k = 1 \rightarrow n$ where n is the number of superimposed solutions.

Equating the real and imaginary parts of the partial derivatives we obtain:

$$\sum_{s=1}^n (A_{sk} M_s + B_{sk} N_s) = \phi_k \quad 3.30$$

$$\sum_{s=1}^n (B_{ks} M_s + C_{sk} N_s) = \psi_k \quad 3.31$$

A_{sk} , B_{sk} and C_{sk} are functions of β only. ϕ_k and ψ_k are functions of the loading on the face $\zeta = 0$, given by:

$$\phi_k + i\psi_k = \int_0^1 [F(x)\sigma_z(x, \beta_k) - \Phi(x)\tau_{zr}(x, \beta_k)] x dx \quad 3.32$$

Equating the real and imaginary parts of this equation gives $2n$ simultaneous equations. These can be solved for the first n values of the coefficients, $L_s = M_s + iN_s$, which best approximate the loading on the end face. From these the strains at any position within the semi-infinite cylinder can be calculated.

3.4.4 Approximation of an annular load

The stress distributions modelled were equivalent to a tensile annular loading superimposed on a compressive uniform load (the loading used by Williams, figure 2.8). The value of the stresses were defined such that there was no resultant axial force. The end surface was defined to be free of radial stress. The stresses over the ends are defined by:

$$\sigma_f(r) = \frac{F}{\pi r_o^2} \quad (r = 0 \rightarrow r_f, r = r_f + \delta r \rightarrow r_o) \quad 3.33$$

$$\sigma_f(r) = \frac{F}{\pi r_o^2} - \frac{F}{2\pi r_f \delta r} \quad (r = r_f \rightarrow r_f + \delta r) \quad 3.34$$

$$\tau_f(r) = 0 \quad 3.35$$

$F(x)$ and $\Phi(x)$ are given by:

$$F(x) = \frac{r_o}{2G} \sigma_f(x), \quad \Phi(x) = \frac{r_o}{2G} \tau_f(x) \quad 3.36$$

Writing $x_f = \frac{r_f}{r_o}$ equation 3.32 becomes

$$\phi_k - i\psi_k = \frac{Fr_o}{2\pi G} \left[\frac{1}{r_o^2} \int_0^1 \sigma_z(x, \beta_k) x dx - \frac{1}{2} \int_{x_f}^{x_f + \delta x} \frac{\sigma_z(x, \beta_k) x}{r_f \delta r} dx \right] \quad 3.37$$

$$\therefore \phi_k - i\psi_k = \frac{F}{2\pi r_o G} \left[\int_0^1 \sigma_z(x, \beta_k) x dx - \frac{1}{2} \sigma_z(x_f, \beta_k) \right] \quad 3.38$$

For any given value of F and r_f , the values of ϕ_k and ψ_k can be calculated from 3.38 to give the right hand sides of simultaneous equations, 3.30 & 3.31. The values of A_{sk} , B_{sk} , and C_{sk} calculated from the roots of the transcendental equation complete the $2n$ equations which can be solved for the real M_s and imaginary parts N_s of the

coefficients. The displacements and strains at any particular point in the body can then be calculated from equations 3.20 to 3.25.

3.5 The analysis program

3.5.1 Overview

The program 'CYSTRESS.FOR', used to carry out the above analysis, was developed and run on a VAX 6230 computer and is written in VAX FORTRAN. At the time development of the program was started, the SUN SPARCstation used for the work described later in this thesis had not yet been acquired. When the SPARCstation was later installed development was continued using the VAX. The SPARCstation was used for local display of the displacements, stresses and strains using the FEMVIEW finite element post-processing program.

3.5.3 Optimum parameter values

The accuracy and computation time of the solution are determined by the value of three parameters:

K - the number of homogenous solutions used to approximate the loading and give a solution

BESSTOL - the tolerance used in calculating the Bessel function values.

INTTOL - the tolerance used in integrating functions of the applied stresses.

The optimum values of these parameters were determined by a trial and error process. The values of all three were changed while the value of the bridge strain at the point $r = r_0$, $\zeta = 1$ were monitored with load, $F = \pi$, applied either at $x_f = 0.01$ and $x_f = 1.0$. This point was assumed to be reasonably representative of the region of interest. Various combinations of the three values of the parameters were tried until a combination was found for which no significant change in the bridge strain value at this point was observed when either *K* was incremented or when *BESSTOL* or *INTTOL* were reduced. The optimum values found using this method were $K=10$, $BESSTOL=0.0001$ and $INTTOL=0.01$. The bridge strain at the above point for these parameter values and for some other more computationally costly values are given in table 3.1.

	$XF=0.01$	$XF=1.0$
$K=10, BESSTOL=0.0001, INTTOL=0.01$	+ 0.1889	- 0.1171
$K=10, BESSTOL=0.000001, INTTOL=0.01$	+ 0.1885	- 0.1174
$K=10, BESSTOL=0.0001, INTTOL=0.0001$	+ 0.1889	- 0.1171
$K=15, BESSTOL=0.0001, INTTOL=0.01$	+ 0.1919	- 0.1180

Table 3.1: Effect of parameter values on bridge strain values ($m=4, E=1$)

It is evident that increasing K or reducing $BESSTOL$ or $INTTOL$ has little effect on the bridge strain values. The values $K=10, BESSTOL=0.0001, INTTOL=0.01$ therefore appeared to provide a reasonable compromise between accuracy and computation time and were used in all subsequent calculations.

3.6 Results from program CYSTRESS.FOR

It was shown in section 3.4.2 that the strains at a distance z from the loaded end of a semi-infinite cylinder can be equated with the strains at the mid-height of a finite cylinder of height $2z$ loaded at both ends. An insight into the behaviour of cylinders of finite length can therefore be gained by using the **CYSTRESS.FOR** programme to analyse the state of strain in a semi-infinite cylinder.

The strain values in the semi-infinite cylinder are functions of its radius, its elastic constants, and the applied load. In investigating the effect of axisymmetric stress distributions it is therefore necessary to choose representative combinations of these parameters. It was decided, that scaling of the results to other problems would be simplified if as many parameters as possible were 'normalised' to unity. The cylinder was therefore specified to be of 1 m radius and Young's modulus 1 Nm^{-2} . However, as the calculated strains do not scale linearly with the material's Poisson ratio, this parameter was not set to unity. Instead it was assigned the value 0.3 which is a typical value for steels.

Six load cases were analysed, each of which consisted of a 1 Nm^{-2} uniformly distributed tensile stress over the end face (total force $\pi \text{ N}$) superimposed upon a compressive force of equal magnitude (total force $\pi \text{ N}$) applied over an infinitely thin annulus. These equipollant annular stress distributions were therefore similar to those

used by Williams [1983] and depicted in figure 2.8. The stress value of 1 Nm^{-2} was again chosen so as to normalise the problem to facilitate scaling to other values. Modelling only equipollant annular stress distributions does not result in any serious loss of generality as any axisymmetric normal stress distribution can be created by the superposition of a number of such distributions combined with a uniform tensile or compressive stress.

Results were calculated for annular load radii of 0.01, 0.2, 0.4, 0.6, 0.8 and 1.0. The strains and displacements were evaluated at radial and axial intervals of 0.1. The results are illustrated in figures 3.2 to 3.17. In figures 3.2 to 3.7 the surface axial, circumferential and bridge strains are plotted against distance from the loaded end. It

was stated above that the strain at a distance $\zeta = \frac{z}{r_0}$ from the loaded end of a semi-

infinite cylinder can be equated with the strain at the mid-height of a finite cylinder of aspect ratio $A = \zeta$. The graphs can therefore be interpreted as showing strain versus cylinder aspect ratio. For each strain component graphs are presented covering the range $0.5 < \zeta < 2.0$ and the range $0.9 < \zeta < 1.8$. In addition figures 3.9 to 3.14 show contour plots of the bridge strain for each annular load radius.

3.6.1 Surface axial strain

Figures 3.2 and 3.3 show the variation in surface axial strain with distance from the loaded end. Figure 3.2 shows that in general the axial strain decays rapidly with distance. Figure 3.3 shows an expanded view of the mid section of figure 3.2. It can be seen from this figure that each curve crosses the axis between $\zeta = 1.3$ and $\zeta = 1.7$. The sign of the surface axial strain associated with a particular load radius is therefore a function of distance from the loaded end. For example an equipollant annular load applied at the periphery of the cylinder causes a decrease in surface axial strain at axial distances between $0.5r_0$ and $1.6r_0$ whereas at greater axial distances, the axial strain is increased.

3.6.2 Surface circumferential strain

Figures 3.4 and 3.5 show the variation of surface circumferential strain with distance from the loaded end for each load case. For $\zeta > 0.8$ the surface circumferential strain arising from all the load cases decays rapidly with distance in accordance with St Venant's principle. However it is apparent that the relationship between surface circumferential strain and distance from the loaded end is more complex in the region $0.5 < \zeta < 0.8$.

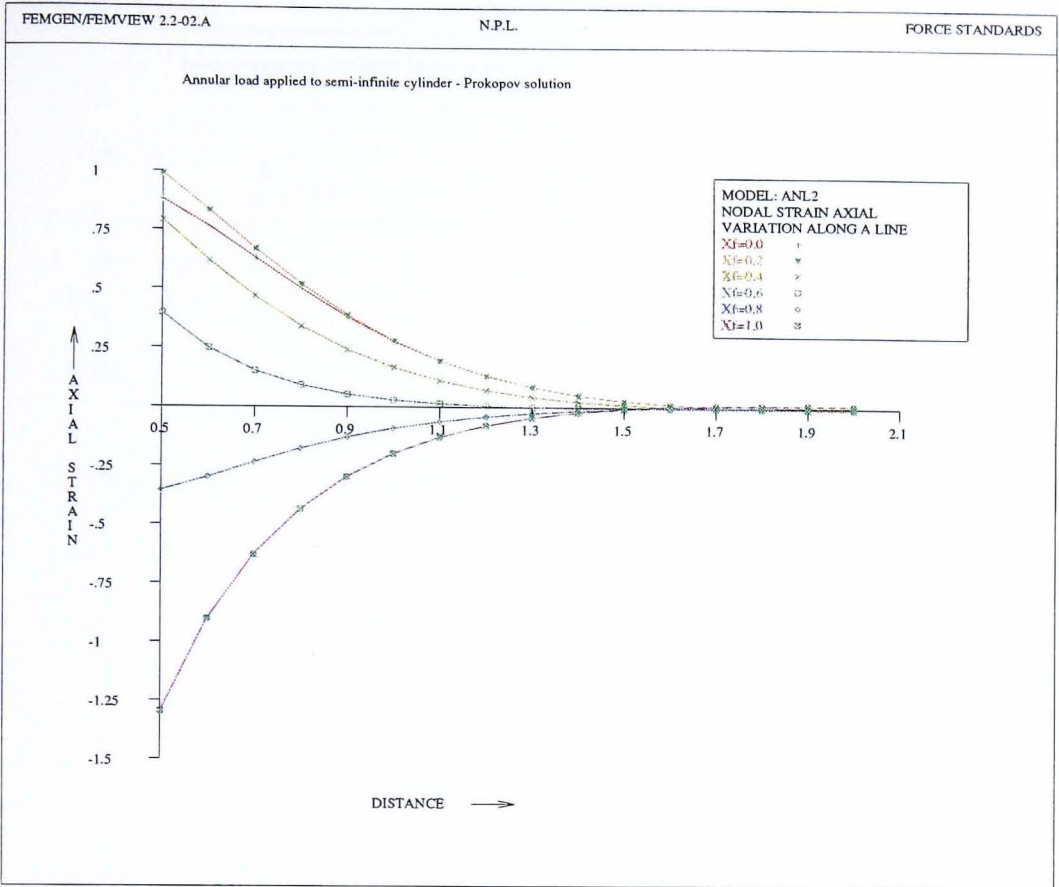


Figure 3.2: Surface axial strain v distance from loaded end: Prokopov solution: $z=0.5r$ to $2.0r$

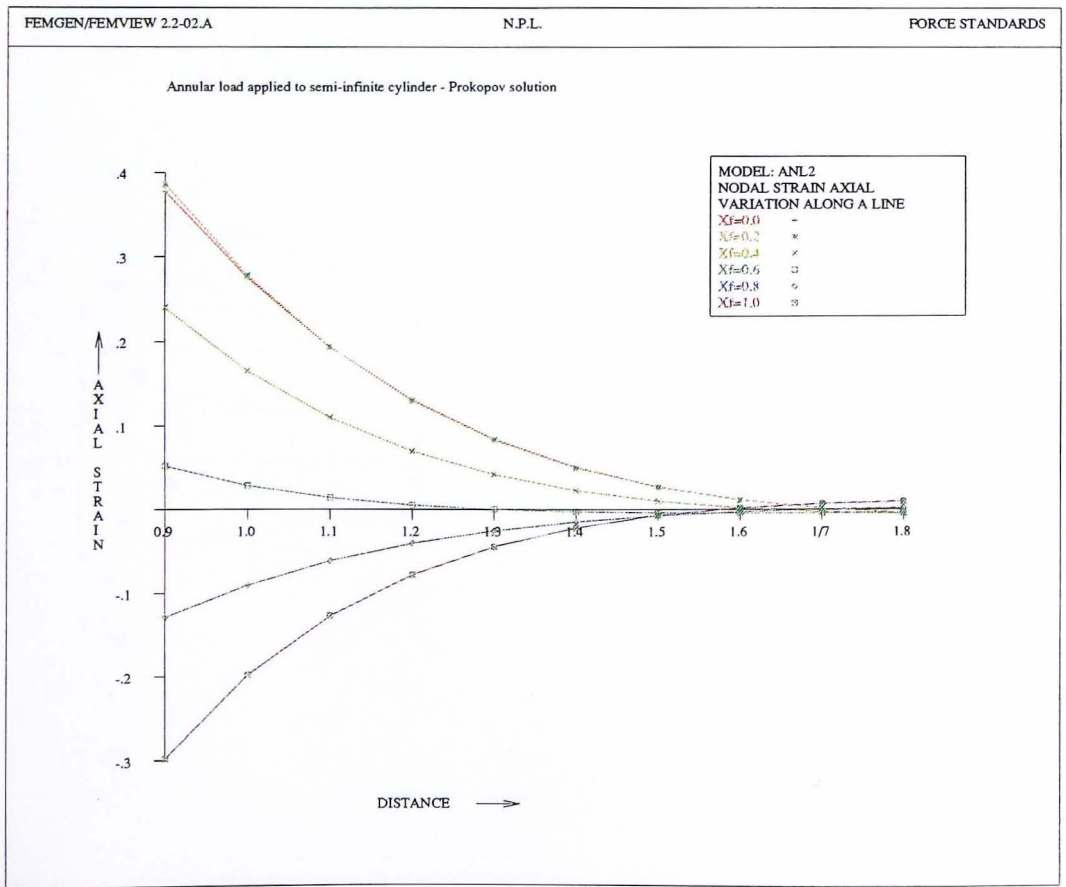


Figure 3.3: Surface axial strain v distance from loaded end: Prokopov solution: $z=0.9r$ to $1.8r$

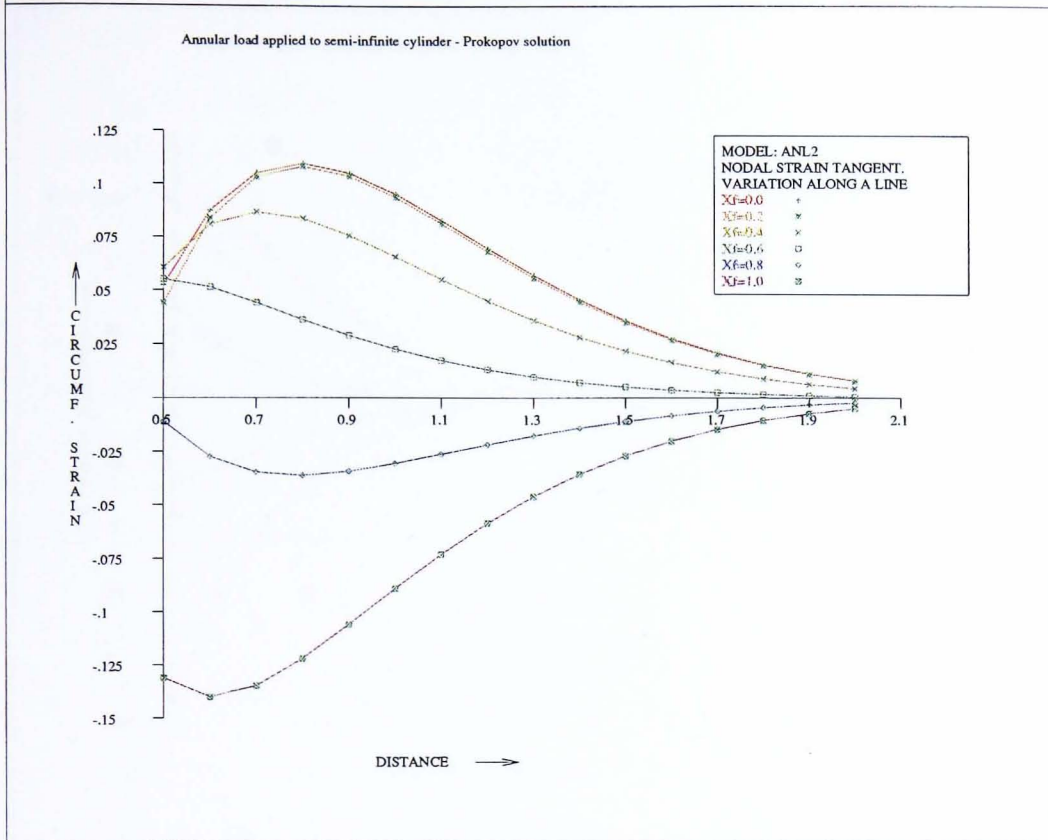


Figure 3.4: Surface circumferential strain v distance from loaded end: Prokopov solution: $z=0.5r$ to $2.0r$

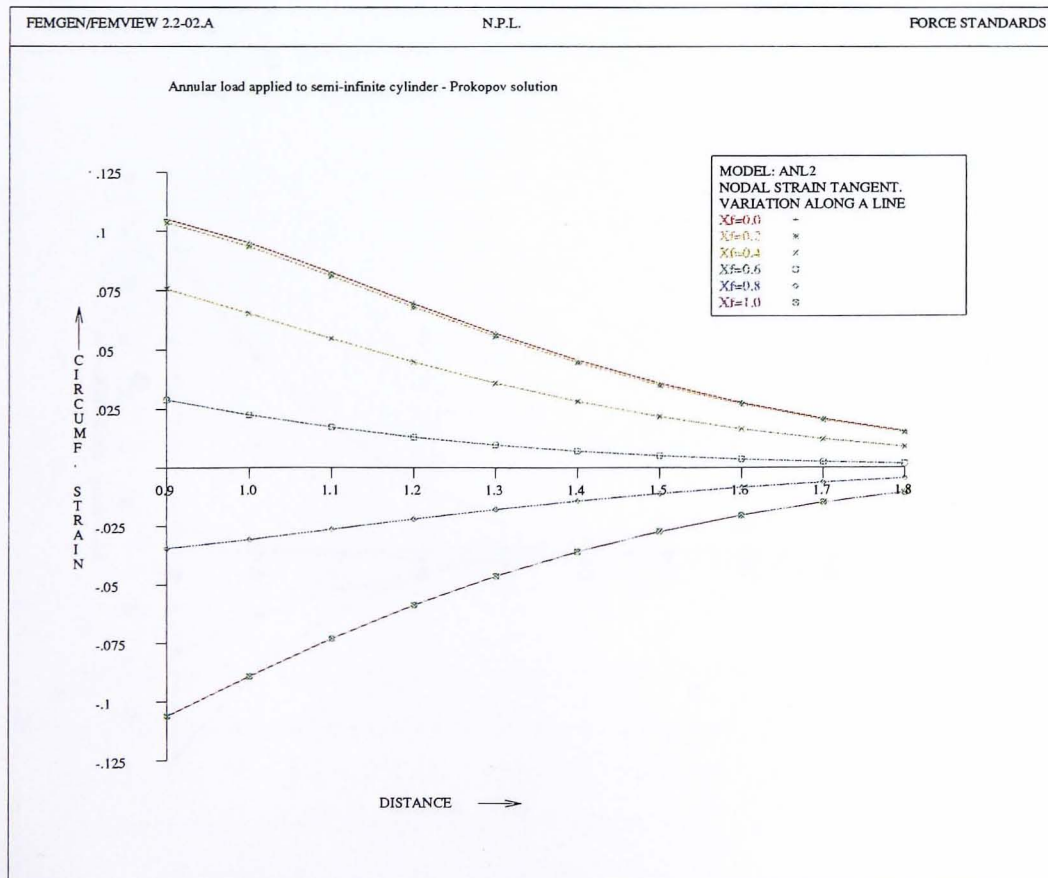


Figure 3.5: Surface circumferential strain v distance from loaded end: Prokopov solution: $z=0.9r$ to $1.8r$

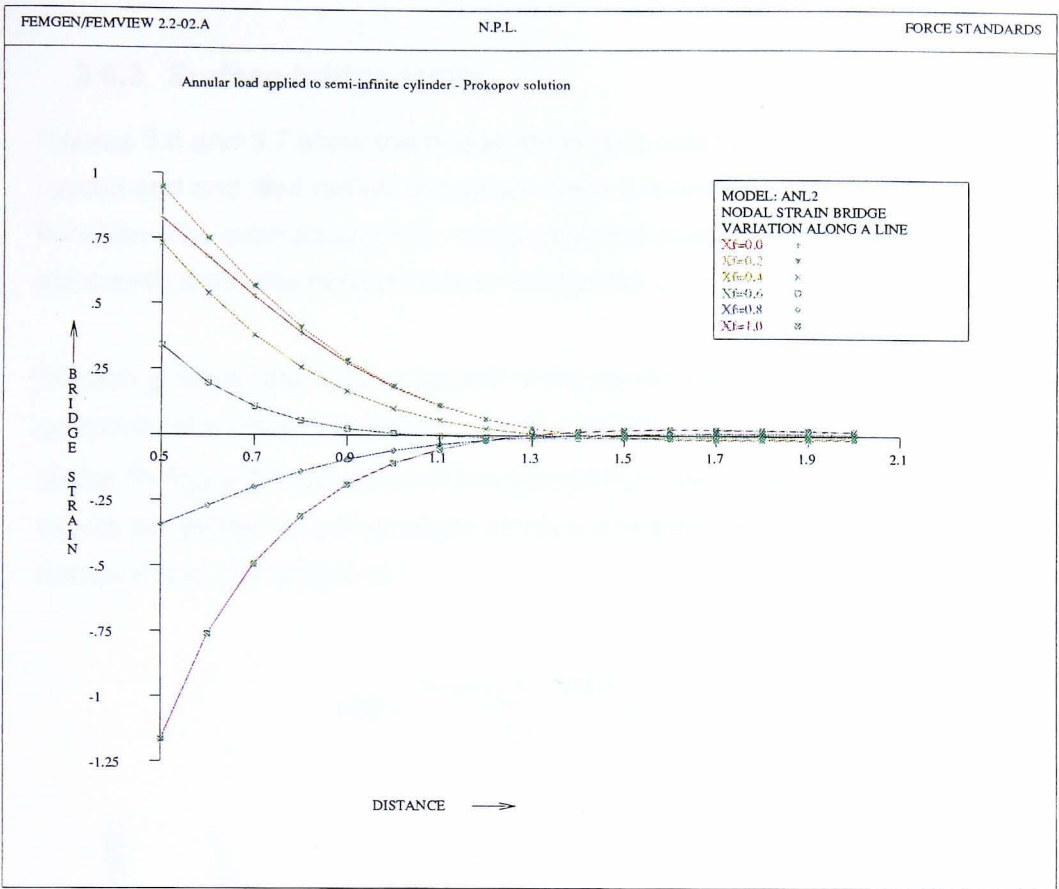


Figure 3.6: Surface bridge strain v distance from loaded end: Prokopov solution: $z=0.5r$ to $2.0r$

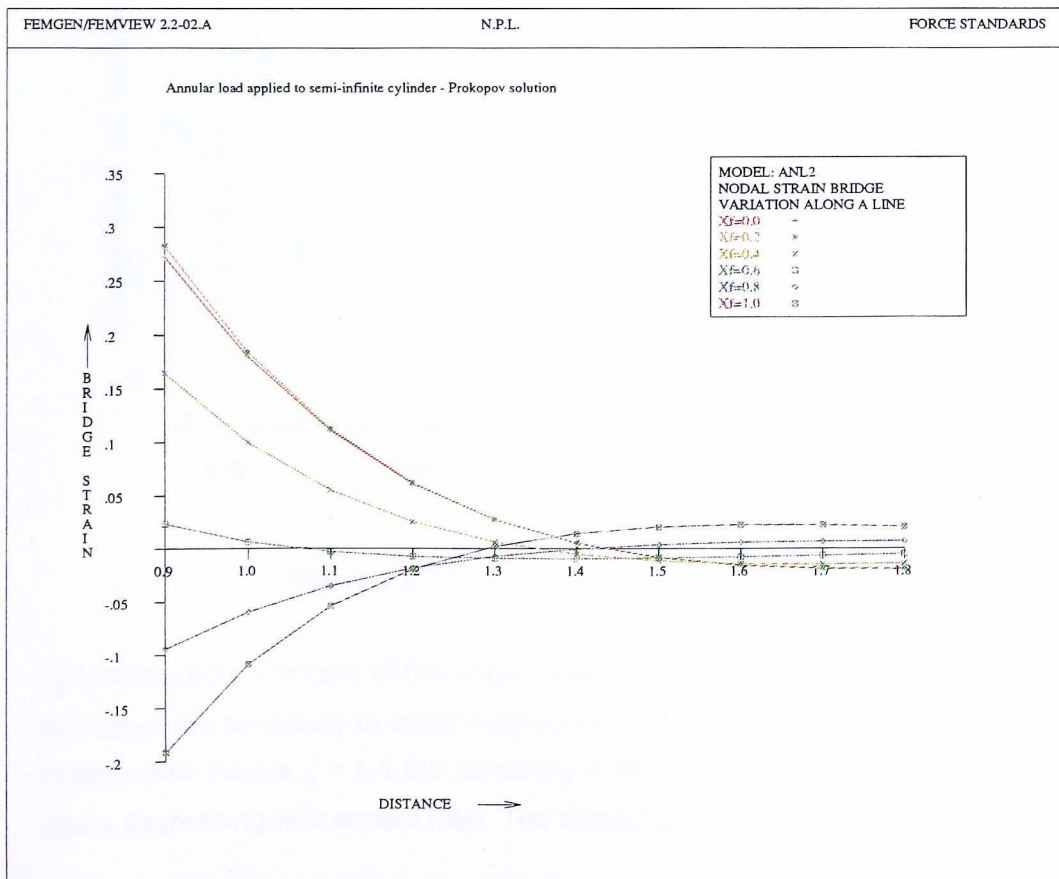


Figure 3.7: Surface bridge strain v distance from loaded end: Prokopov solution: $z=0.9r$ to $1.8r$

3.6.3 Surface bridge strain

Figures 3.6 and 3.7 show the bridge strain (see section 3.3) against distance from loaded end and load radius. In overall shape it is similar to the graph of axial strain variation. The subtraction of the circumferential strain however shifts the region where the curves cross the horizontal axis to between $\zeta = 1.1$ and $\zeta = 1.5$.

At each ζ value, the vertical spread of the curves provides an indication of the sensitivity of a cylindrical load cell, of aspect ratio ζ , to the radial distribution of normal stress. In figure 3.8 the value of this spread has been plotted against aspect ratio. The values are plotted as percentages of the surface bridge strain due to a 1 Nm^{-2} uniform tensile stress, calculated as:

$$100 \times \frac{\text{Max}(\varepsilon_b) - \text{Min}(\varepsilon_b)}{1 + \nu} \quad 3.40$$

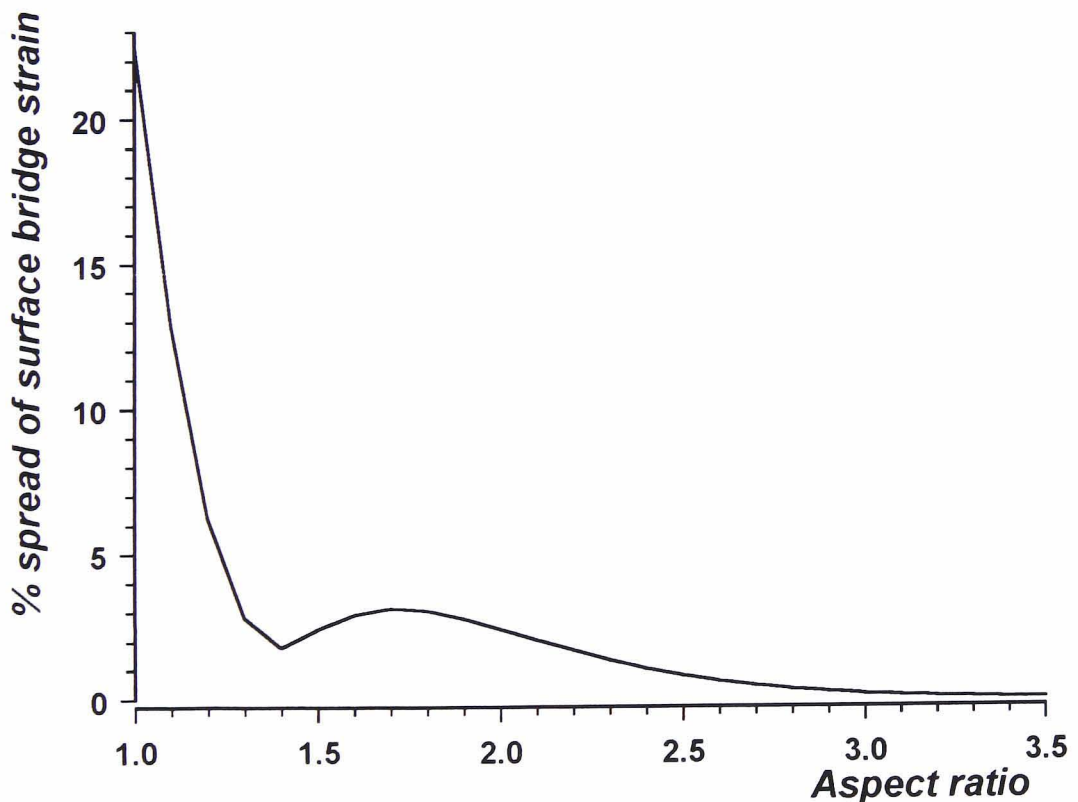


Figure 3.8: Spread of bridge strain v aspect ratio

The most striking feature of the graph is the dip in sensitivity around $\zeta = 1.4$. Below this value the sensitivity to radial load distribution increases rapidly with decrease in aspect ratio. Above $\zeta = 1.4$ the sensitivity rises to a maximum around $\zeta = 1.7$ before again decreasing with aspect ratio. The spread at $\zeta = 1.4$ is approximately equal to

that at $\zeta = 2.2$. These results indicate that, for cylindrical load cells with aspect ratios greater than 1.7, increasing the aspect ratio leads to a reduction in sensitivity to the radial distribution of normal stress. However, perhaps surprisingly, the output of a cylindrical load cell of aspect ratio 1.4 is predicted to be less dependent on the radial distribution of normal stress than load cells of any other aspect ratio between 0.5 and 2.2.

Figures 3.9 to 3.14 are contour plots showing the full field bridge strain between $\zeta = 0$ and $\zeta = 4$ for each equipollant annular load radius. Comparison of the six plots reveals the area of low variation in surface bridge strain around $\zeta = 1.4$ as a thin band which remains green in all the plots.

3.7 Conclusions

It has been shown that load cells with the gauge configurations normally used in transfer standards can be considered to have negligible sensitivity to commonly arising non-axisymmetric load distributions.

A program has been written to calculate the strains and displacements in a semi-infinite cylinder subject to an equipollant annular load using Prokopov's method of superposition of homogenous solutions. It has been shown that the results for a semi-infinite cylinder may be applied to a finite cylinder without significant error.

The calculations confirm the long accepted rule that in general the sensitivity of a cylindrical load cell to the radial distribution of normal stress decreases with aspect ratio. In particular it is shown that this sensitivity rises rapidly as aspect ratios are reduced below 1.4. Unexpectedly the results also predict a local minimum in this end-loading sensitivity around aspect ratios of 1.4.

In the next chapter, results from the analysis presented in this chapter will be compared with those obtained by experiment. In chapter 5, the results will also be compared with those obtained using the finite element method.

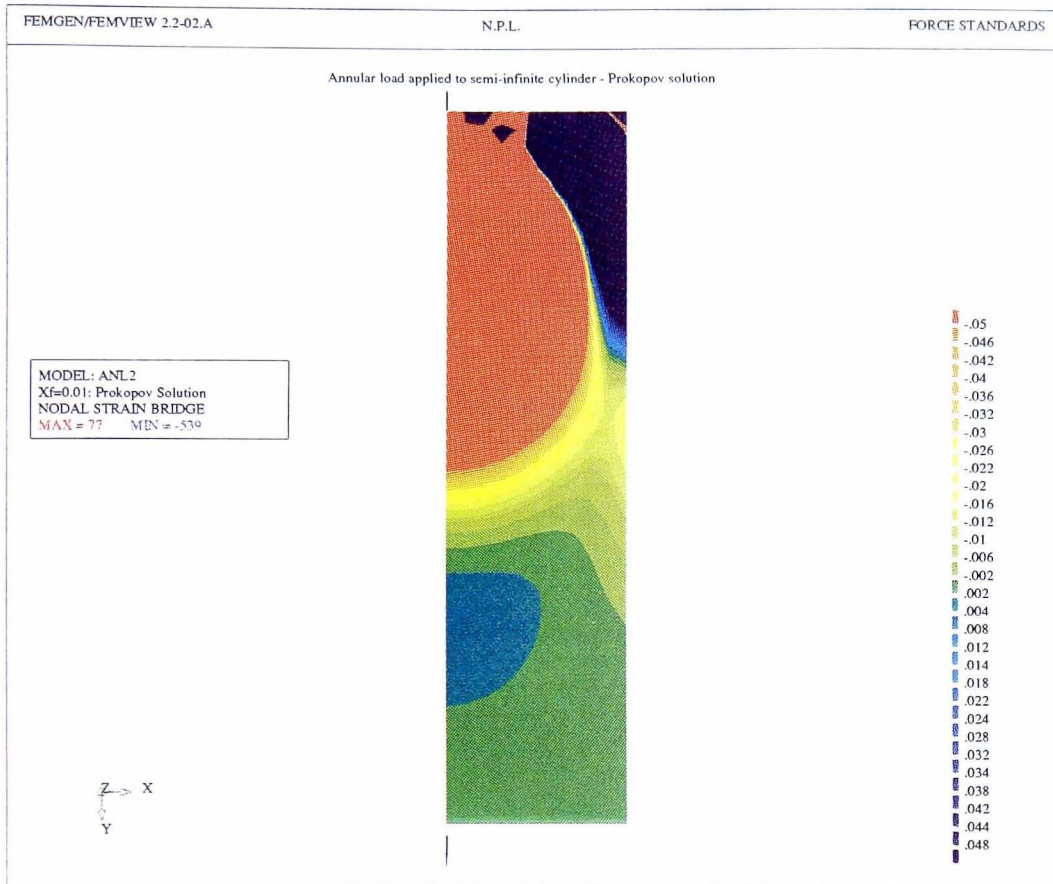


Figure 3.9: Contours of bridge strain due to equipollant annular load with $X_f=0.01$: Prokopov solution

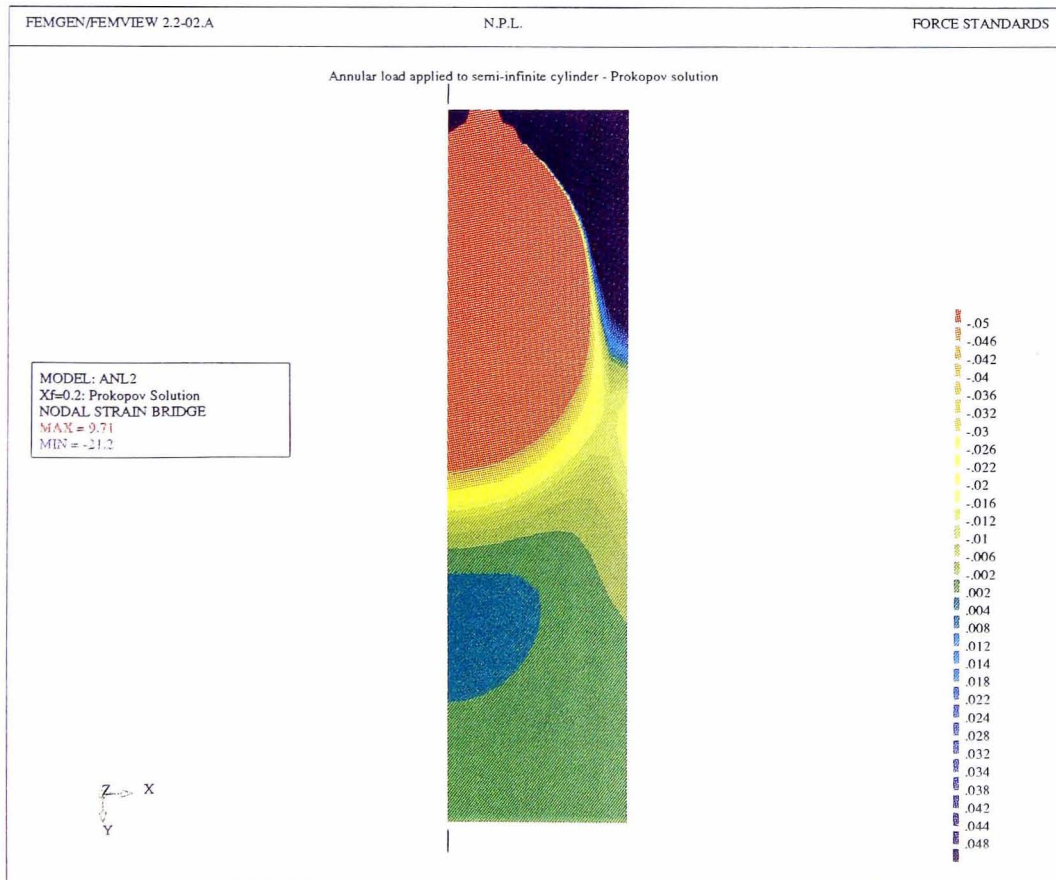


Figure 3.10: Contours of bridge strain due to equipollant annular load with $X_f=0.2$: Prokopov solution

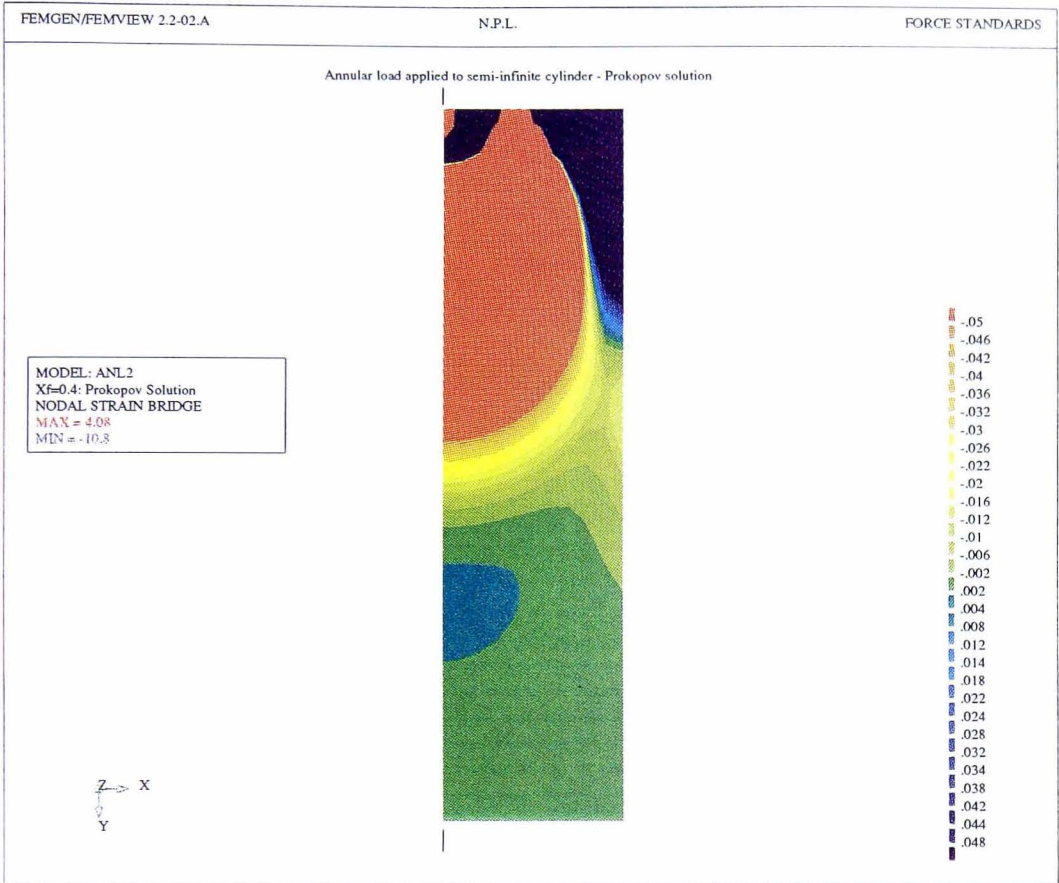


Figure 3.11: Contours of bridge strain due to equipollant annular load with Xf=0.4: Prokopov solution

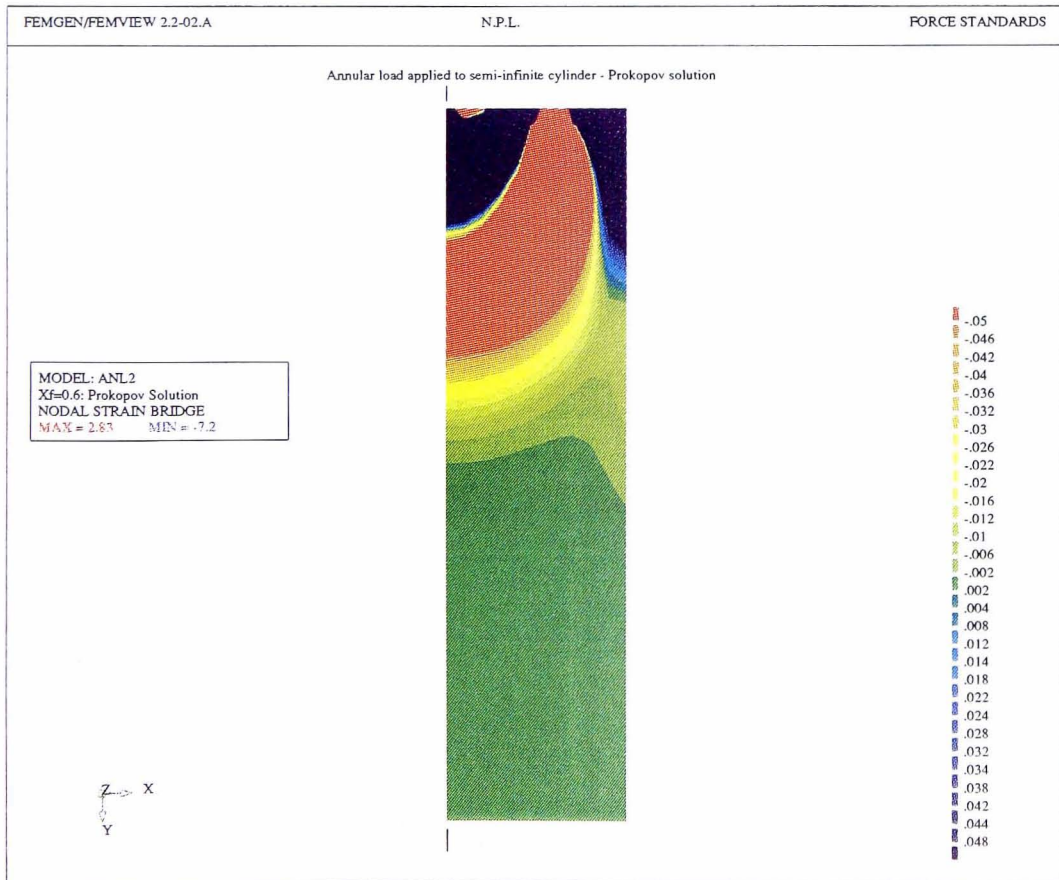


Figure 3.12: Contours bridge strain due to equipollant annular load with Xf=0.6: Prokopov solution

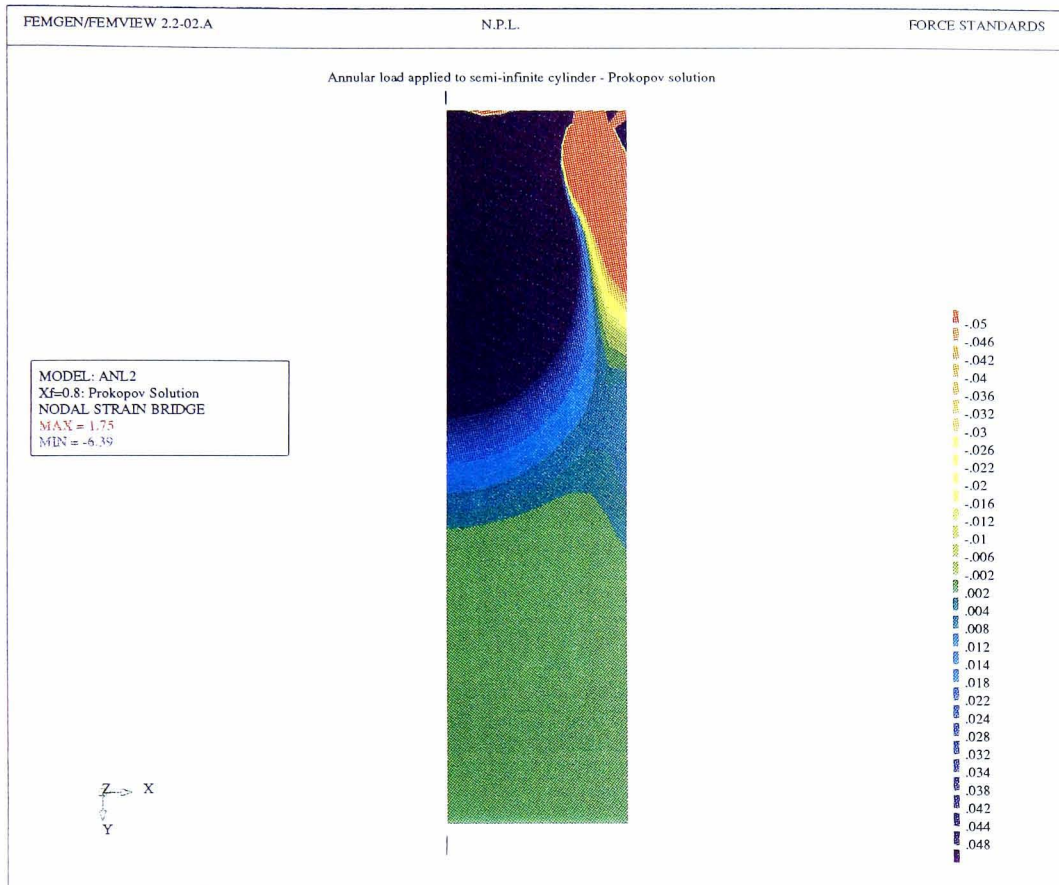


Figure 3.13: Contours of bridge strain due to equipollant annular load with Xf=0.8: Prokopov solution

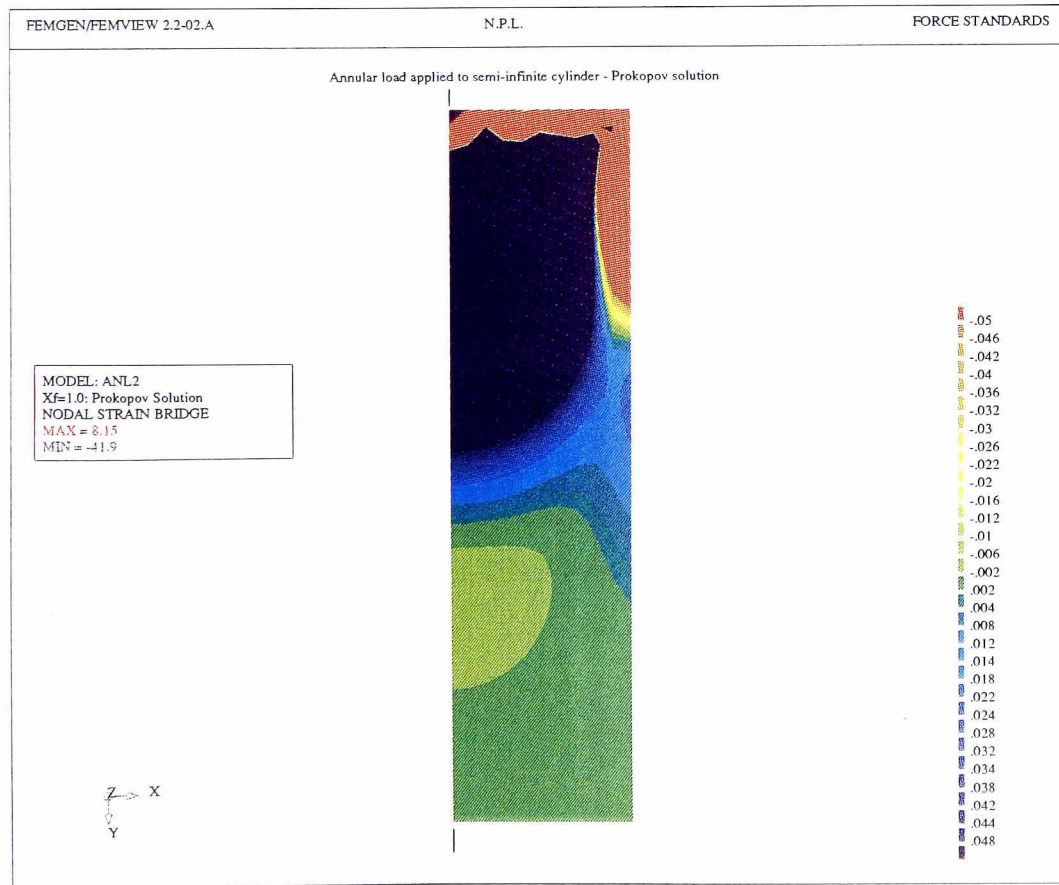


Figure 3.14: Contours of bridge strain due to equipollant annular load with Xf=1.0: Prokopov solution

MEASUREMENT OF SURFACE STRAINS IN A CYLINDER

4.1 INTRODUCTION

The results presented in the last chapter predict that cylindrical column load cells with length to diameter ratios of around 1.4 will exhibit low sensitivity to radial stress distribution. In the analysis some assumptions and approximations were made. In particular it was assumed that the loaded end surface is free from shear stress. In practice some radial shear stress will be present in most end-loading conditions. The applicability of the analytic results to such real loading conditions was therefore investigated by performing experiments both to verify the predictions of the analysis and to relate the results for annular loading to more general load conditions.

The aim of the experiments was to determine the surface strains in a long cylinder when loaded upon surfaces of different profile. A steel cylinder was located on pads of various profiles and loaded in a deadweight machine. The analytic study had indicated that the area of most interest was either side of $\zeta = 1.4$. Strain gauges were therefore used to measure the axial and circumferential strains in this region. Results showing the influence of the pad surface profile on the outputs of the gauges will be presented.

4.2 Strain gauged cylinder

A cylinder of aspect ratio 4 (40.1 mm diameter x 160 mm long) was manufactured from 835M30 steel, hardened and tempered to condition Z (plate 4.1). A pair of multi-element gauges was attached to each end of the cylinder. (Note that only one of each pair is visible in the photograph) The aspect ratio had been chosen to be such that loading conditions on one end of the cylinder would have a negligible effect on the gauges applied at the opposite end. This allowed the effect of the contact stresses at either end to be considered in isolation from the effect of the stresses at the other.

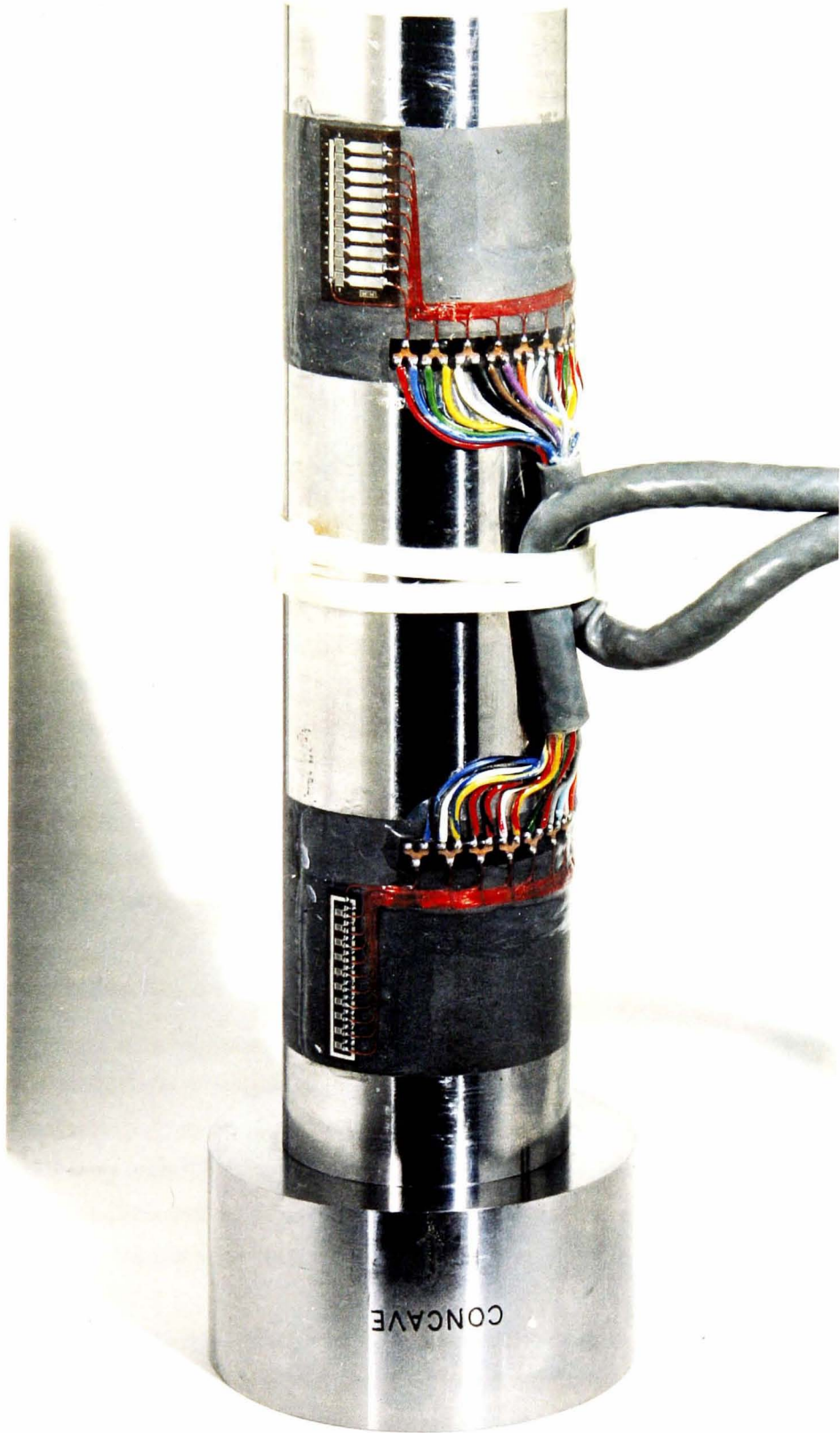


Plate 4.1: The strain gauged cylinder

4.2.1 Strain gauges

The strain gauges used were Micro-Measurements' strip gauges, a pair of type EA-06-031-ME-120 on one end and a pair of EA-06-031-MD-120 on the other. Each strip consisted of ten 120Ω strain gauge grids on a common backing. The gauge patterns are open faced constantan alloy, self temperature compensated to $10.8 \text{ ppm}/^\circ\text{C}$ ($6 \text{ ppm}/^\circ\text{F}$), to match the thermal expansion coefficient of steel. The backing material is a cast polyimide. The gauges were bonded to the cylinder with M-Bond 610 epoxy-phenolic adhesive and protected from mechanical and chemical damage by the application of a layer of M-Coat C silicone rubber. The MD pattern gauges were aligned parallel to the long axis of the strip, while the ME pattern gauges were aligned perpendicular to the strip axis.

On both strip types the strain gauge patterns are spaced at intervals of 2.03 mm ($=0.08''$) along the strip axis. The cylinder radius, r_o , was specified as 20.3 mm in order that the spacing of the gauges in the patterns would be equal to $0.1 r_o$. However, the actual radius of the cylinder following manufacture was measured to be 20.05 mm . Each strip was positioned so that the centre of the first gauge was 18.05 mm from the end of the cylinder. The centres of the ten gauges of each strip were therefore located at $0.1r_o$ intervals between $0.9r_o$ and $1.8r_o$.

In the experiments the cylinder was centralised upon the pad of interest and the outputs of the gauges at the lower end monitored. Depending upon which end of the cylinder was used, either the axial or circumferential surface strains were measured.

4.2.2 Instrumentation

The instrument used to measure the output of the strain gauges was the HBM DMP39-S6. The DMP39 is a high precision AC ratio bridge, the S6 version of which is capable of accepting up to 16 independent bridge inputs. AC instrumentation has the advantage of being insensitive to thermal EMFs. However, due to the sensitivity of AC systems to bridge capacitance and inductance, care had to be taken to avoid sources of high or variable capacitance and inductance.

The instrument provides a 5 volt 225 Hz excitation to the bridge and measures the ratio between the bridge output signal and the bridge excitation voltage measured by sense leads. Systems with such sense leads are known as six-wire systems and are less sensitive to variations in lead wire resistance (see for example BSSM [1979]).

The instrument is micro-processor controlled and self-calibrating. Either periodically or upon external command, a reference bridge can be switched into the system to allow the indicator's sensitivity to be measured and adjusted. This internal reference used is a high stability fixed inductive divider. The indicator has a display resolution of 1 ppm and experience in its use has shown that under ideal conditions its uncertainty can approach this 1 ppm resolution. When used with strain gauge bridges this indicator is therefore sufficiently accurate for its uncertainty to be insignificant compared with other sources of error.

4.2.3 Strain gauge bridge circuit

The circuit of the strain gauge bridges is shown in figure 4.1. Each pair of gauges (at the 0° and 180° positions) were connected in parallel minimising their sensitivity to bending moments. Each pair was connected as the active arm of a quarter Wheatstone bridge. The other, passive, arm of each half-bridge was formed by a $60\ \Omega$ resistor. In order to minimise the effect of variation of lead-wire resistance with temperature, the strain gauges were connected into the half bridges using the 3-wire configuration. All the individual half bridges shared a common $500\ \Omega + 500\ \Omega$ resistive divider which formed the other half of each full bridge. The bridge completion resistors were non-inductively wire-wound with a temperature coefficient of resistance of less than $3\ \text{ppm}/^\circ\text{C}$.

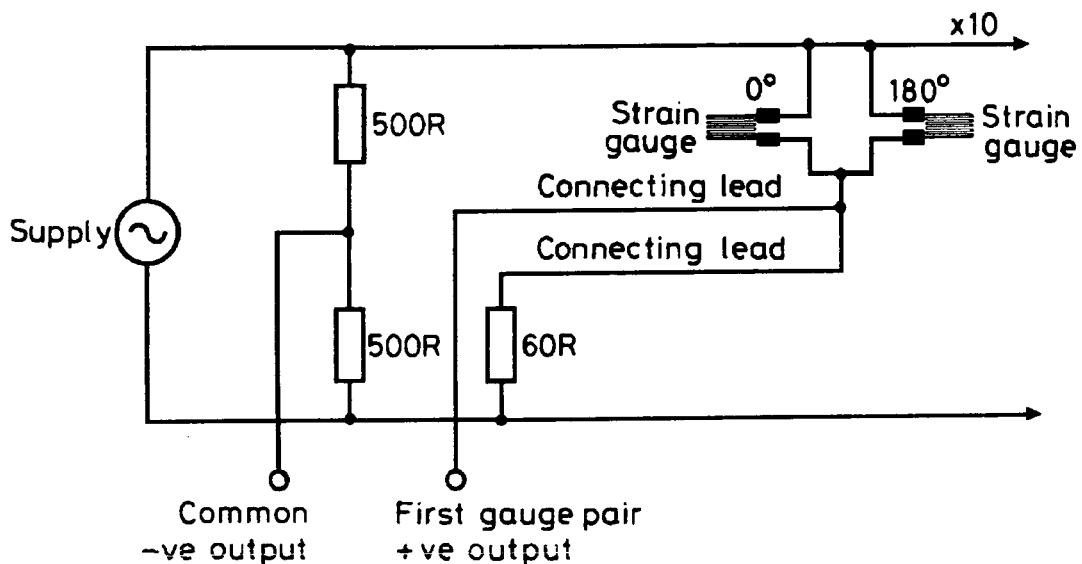


Figure 4.1: Circuit of strain gauged cylinder (only one gauge pair shown)

4.2.4 Thermal effects on bridge output

Although the gauges were self temperature compensated for steel, no provision was made to compensate for any departure of the cylinder's coefficient of linear expansion from the nominal value for steel. Nor was any attempt made to compensate the bridge outputs for changes in gauge factor or in the cylinder's Young's modulus. The bridge outputs were therefore temperature dependent.

In order to reduce the influence of temperature, a procedure was adopted by which the gauge outputs recorded on each test pad were referred to those recorded on a plane pad. Immediately prior to loading the cylinder upon each test pad, the gauges were 'calibrated' by recording their outputs when loaded upon a plane pad, equal in diameter to the cylinder. If the temperature of the cylinder remains reasonably constant during this procedure, the ratio between the gauge outputs on the two pads will be virtually independent of temperature. In order to promote temperature stability, the cylinder, reference plane pad, and test pad were kept in thermal contact for several hours before each test. The cylinder was also protected from draughts and heat by a metal foil jacket.

4.2.5 Creep of the strain gauge output

All strain gauge installations exhibit some creep. The gauges applied to the cylinder were no exception. In order to minimise the effect of this time dependent change in output, the timing of the application and removals of each load and of the recording of the readings was carefully controlled. After each change of load a 'dwell time' was allowed to elapse before the outputs from the gauges were recorded. By pausing for the dwell time, the initial period of rapid creep was avoided, ensuring the readings were taken on the flatter part of the creep curve where they are less affected by small errors in timing. It was found that a 20 second dwell time gave the best compromise between overall test duration, and therefore temperature variation, and creep response

4.2.6 Control and data logging

A HP87-XM computer controlled the test timings and automatically recorded the bridge outputs. Commands and data were exchanged between the HP87 and the DMP39 over the IEEE-488 bus. During each run the programme carried out a series of five load applications via the flat reference pad, followed by five load applications via the pad under test

The test results were transferred on floppy disc to the SUN SPARCstation. A FORTRAN programme translated the experimental data to a Femview neutral file, so as to mimic the results of a finite element analysis. This allowed the use of Femview's graph plotting facilities to present the data in the format used for the earlier analytic results and also used to present finite element results later in this thesis. In addition to axial and circumferential strains, the programme also calculated bridge strain values.

4.2.7 Loading pads

A set of twelve loading pads were manufactured for use during the tests. The pads were made from 817M40 steel, hardened and tempered to condition V. This heat treatment results in a yield stress of approximately $1,200 \text{ MNm}^{-2}$. Five of the pads were manufactured to be equal in diameter to the cylinder ($1.0r_o$), while a further seven were to be manufactured 50% larger in diameter ($1.5r_o$).

4.2.7.1 $1.0r_o$ radius pads

Five of the pads were of diameter 40.1 mm and height 80 mm. As the diameter of these pads was equal to that of the strain gauged cylinder, the loading conditions were approximately symmetric about the contact plane. Radial shear stresses at the contact surface between these pads and the cylinder should therefore have been small. The contact surface was defined by a raised disc or ring, 0.3 mm proud of the top surface of the pad. The contact profiles of the $1.0r_o$ radius pads were as follows:

Plane: Used as the reference during the tests on both the $1.0r_o$ and $1.5r_o$ pads.

Central disc: Outer radius of contact area $0.5r_o$. Mean radius of contact area $0.25r_o$.

Inner ring: Inner radius $0.375r_o$, outer radius $0.625r_o$. Mean radius of contact area $0.5r_o$

Outer ring: Inner radius $0.667r_o$, outer radius $0.833r_o$. Mean radius of contact area $0.75r_o$

Edge ring: Inner radius $0.866r_o$, outer radius r_o . Mean radius of contact area $0.933r_o$

The disc and ring pads were designed such that they each contacted over $\frac{1}{4}$ of the area of the end face of the cylinder. The profiles of the five $1.0r_0$ pads are shown in figure 4.2.

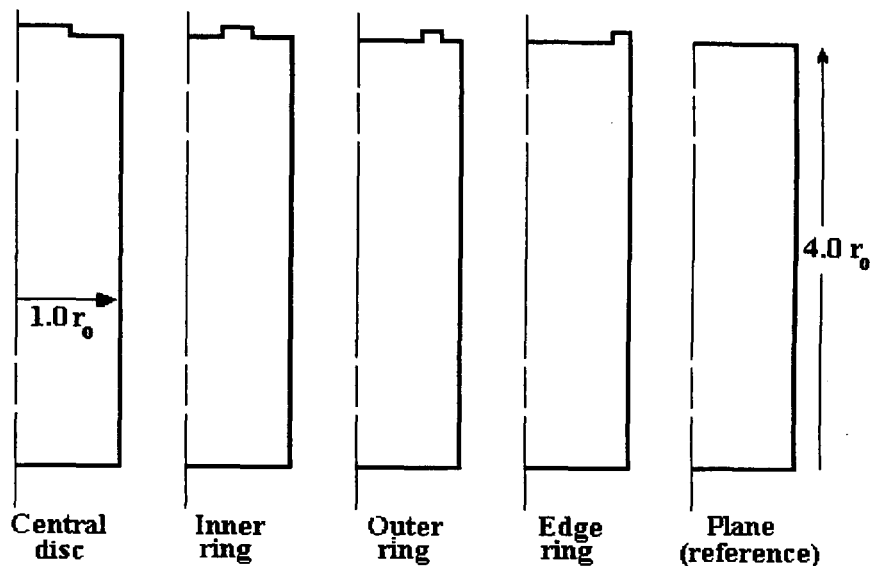


Figure 4.2: $1.0r_0$ loading pads (profiles exaggerated)

4.2.7.2 $1.5r_0$ radius pads

The dimensions of the $1.0r_0$ pads were chosen to minimise contact shear forces. However, their dimensions relative to the strain gauged cylinder are not typical of the loading conditions encountered in the use of load cells. A further seven pads were therefore manufactured with dimensions more representative of those used during the calibration and use of load cells.

Each pad was of height 30 mm and diameter 60 mm, 50% greater than the diameter of the strain gauged cylinder. Five of these $1.5r_0$ pads had the same inner radii, outer radii, and mean contact radii as the five $1.0r_0$ pads. In addition two pads were manufactured with the profiles specified in the EN10002-3 bearing pad test:

The seven $1.5r_0$ pads are illustrated in figure 4.3.

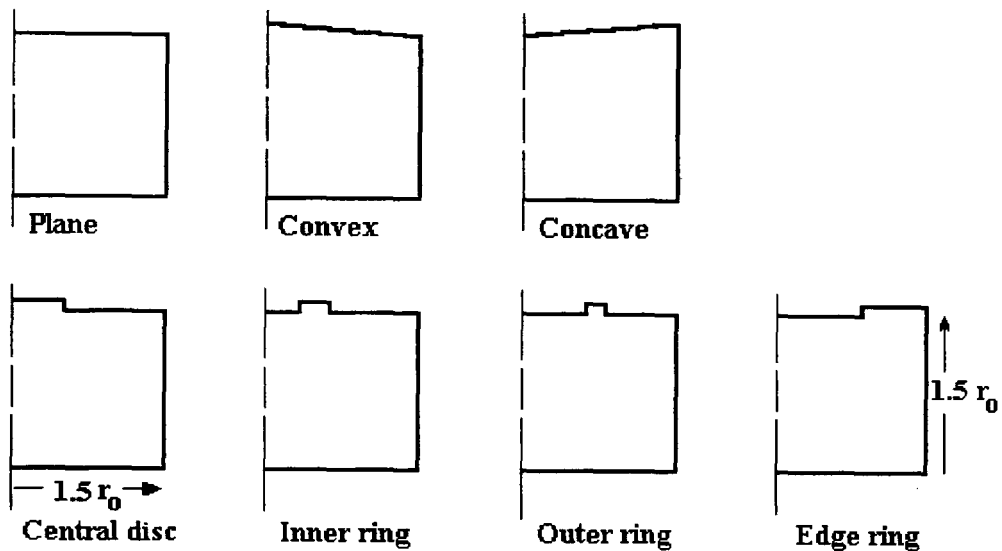


Figure 4.3: $1.5r_0$ loading pads (profiles exaggerated)

4.2.8 Test method

The tests were carried out using the NPL 1.2 MN deadweight force standard machine. The computer indicated when changes of load were required. However, the machine was controlled manually.

Each pad was placed centrally upon the compression platen of the deadweight machine. The strain gauge cylinder was then placed on the pad with the end to be monitored lowermost. A specially manufactured locating ring ensured that the cylinder was centred upon the pad to within 0.1 mm. In order to minimise the effect of bending moments, the load was introduced via a ball seat unit located on the top of the cylinder.

Prior to each test the end faces of the cylinder were checked against a ground reference surface using engineers' blue. The heat treatments of the steels had been specified so as to ensure that the contact faces of the loading pads would yield before those of the cylinder. Despite this, after loading on the disc and ring pads the end surfaces of the cylinder were found to be no longer flat. The deformation was not apparent to the naked eye, however, it could clearly be seen as a variation in the engineers' blue contact pattern. Before each test, this distortion was corrected by lightly hand-lapping the end faces against a surface which was known to be flat.

4.2.9 Calculation of results

The results were calculated using the following procedure:

Each set of five readings from each gauge pair were averaged.

For each pad the average at zero force was subtracted from the average at 300 kN to calculate output differences.

The ratio between the output of each gauge pair when loaded on the test pad and when loaded on the reference pad was calculated.

The output ratios were used to calculate results comparable with the results presented in the previous chapter. These analytic results were for a 'normalised' case of a unit radius, unit Young's modulus cylinder, subject to a uniform tensile stress of 1 Nm^{-2} superimposed upon equal compressive annular loads. Each measured output ratio was therefore converted into a 'normalised' strain value, as if the reference load case was for a cylinder of unit radius, unit Young's modulus, and 1 Nm^{-2} uniform applied stress. This normalised strain is given by: $\varepsilon = (\phi_p / \phi_{rp} - 1)\hat{\varepsilon}$, where ϕ_p is the output difference on the test pad, ϕ_{rp} is the output difference on the reference pad and for axial strain $\hat{\varepsilon} = 1$ and for circumferential strain $\hat{\varepsilon} = \nu$. The measured value of Poisson's ratio, 0.301, (see section 4.4) was used in these calculations. It is these normalised strain values which are presented in the graphs of results.

It should be borne in mind that this normalisation does not make the experimental and analytic results directly equivalent. Any comparison should therefore be made with care. In particular it should be noted that the contact stress distribution will be affected by local yielding and, in the case of the conical pads, closure of the gap. The normalised strains are therefore not necessarily the strains that would be obtained if the experiment were to be repeated with a cylinder and pads of the same geometry, unit Young's modulus and an axial force equivalent to an axial stress of 1 MNm^{-2} . However, scaling the experimental and analytic results so that both are relative to similar uniform strain fields does allow some comparison to be made.

4.3 Results

4.3.1 Tests on plane, central disc, and ring pads

Tests were carried out using the plane, central disc, and the three ring pads with an applied force of 300 kN. An additional loading condition was created by loading the cylinder via the $1.5r_c$ plane pad with a layer of grease applied to the contact surfaces. The 300 kN applied force is equivalent to a mean axial contact stress of 238 MNm^{-2} on the plane pads and 952 MNm^{-2} on the disc and ring type pads, which have a quarter of the contact area.

4.3.1.1 $1.0r_c$ pads

The results for the four $1.0r_c$ pads are the most directly comparable with the analytic results. In order to ensure that the analytic results were for conditions as close as possible to those of the experiment, a further run of **CYSTRESS.FOR** (see chapter 3) was carried out, to calculate results for annular load radii equal to the mean contact radii of the four $1.0r_c$ pads. These results are given in figures 4.4, 4.6, and 4.8 and may be compared with the experimental results of figures 4.5, 4.7, and 4.9. It is evident from the comparison that there is very good qualitative agreement between the analytic calculations and the experimental results. However, the quantitative agreement between the analytic and experimental results, is less good (note the difference in vertical scales). The measured strain differences were consistently smaller than those predicted by the analytic results. This lack of quantitative agreement between the two sets of results may result from:

There may be significant error in the strain measurements due to the limitations of the experimental method.

The assumption was made in the analytic solution that the contact stress distribution can be represented by an annular load at the pad's mean contact radius. The actual distribution of stress within the contact area during the experiment is unknown.

It is to be expected that there will be areas of local stress concentration, in particular at the outer and inner peripheries of the contact areas. These stresses may be high enough to cause local yielding of the strain gauged cylinder. The deformation observed following loading on the ring and disc pads indicates that such local yielding did occur. As the analytic solution takes no account of yield, some difference between the experimental and analytic results is therefore to be expected.

In the author's opinion, given the above limitations, the level of agreement between the two sets of results is very good.

4.3.1.2 $1.5r_o$ pads

The results of the tests on the $1.5r_o$ plane, disc and ring pads are shown in figures 4.10 to 4.12. Unlike the loading condition on the $1.0r_o$ pads, there is no similarity about the contact plane. It is therefore to be expected that radial shear stresses will be present at the interface, resulting in a difference between the $1.5r_o$ pad results and those for the equivalent $1.0r_o$ pads. These differences are evident if figures 4.10 to 4.12 are compared with the $1.0r_o$ pad results in figures 4.5, 4.7, and 4.9.

In particular, the strains when loaded upon a flat $1.5r_o$ pad are significantly different from those on the $1.0r_o$ flat reference pad. This difference can be understood by considering the stiffness of each pad in the vicinity of the edge of the cylinder. The $1.5r_o$ pad has additional material beyond $r = 1.0r_o$, which results in its stiffness in this vicinity being greater than that of either the cylinder or the $1.0r_o$ reference pad. The extra axial stiffness will concentrate the axial stress towards the cylinder periphery, while the extra radial stiffness will result in the generation of radial shear stresses. From comparison between the curves for the plane and greased pads in figures 4.10 to 4.12, it is apparent that these shear stresses have a significant effect on the bridge output. It is not possible to know the change in coefficient of friction caused by the introduction of the grease, however it was sufficient to cause a significant change in the bridge strain.

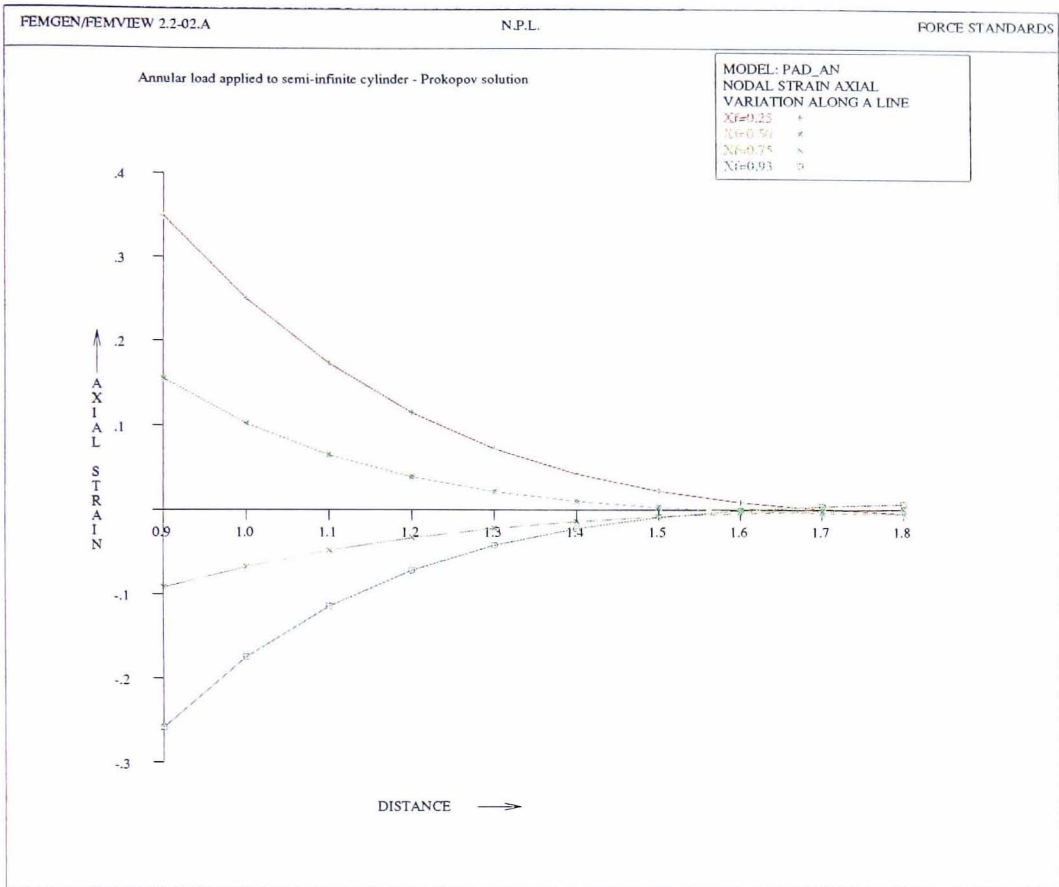


Figure 4.4: Surface axial strain v distance from loaded end: Prokopov solution: mean pad contact radii

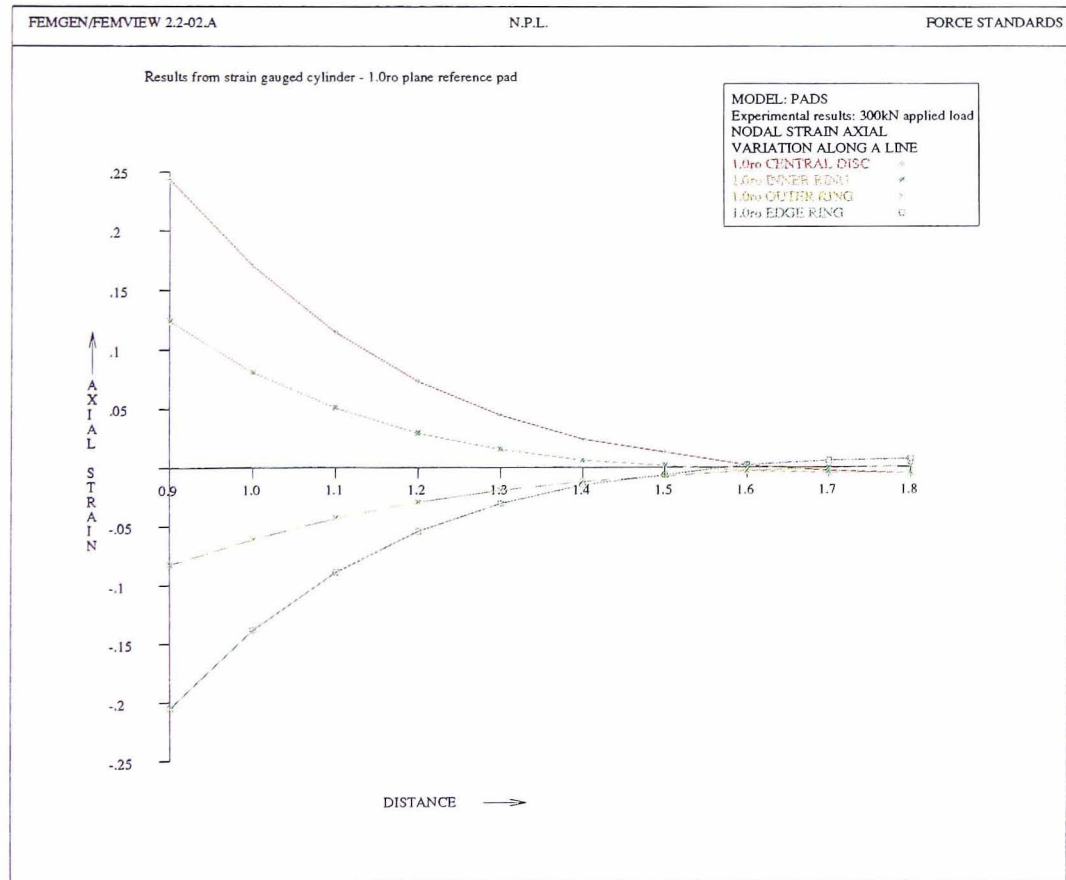


Figure 4.5: Surface axial strain v distance from loaded end: experimental results: 1.0ro pads

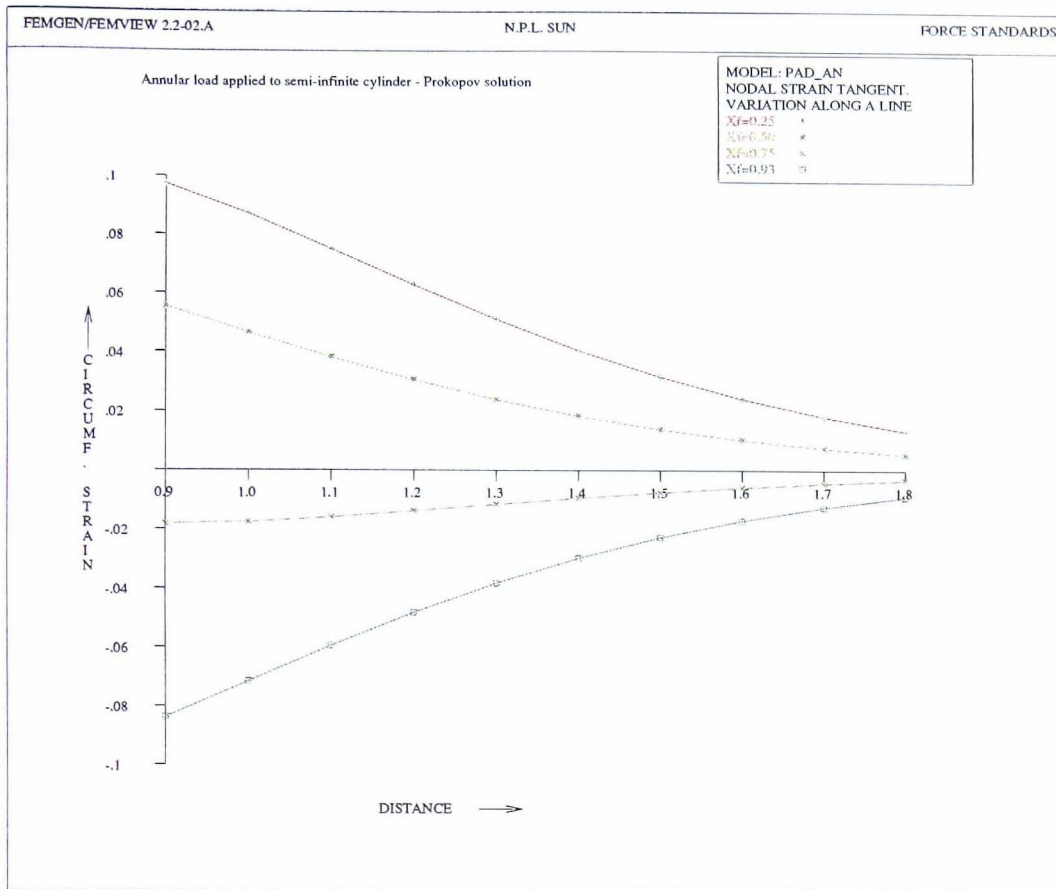


Figure 4.6: Surface circumferential strain v distance from loaded end: Prokopov solution: mean pad contact radii

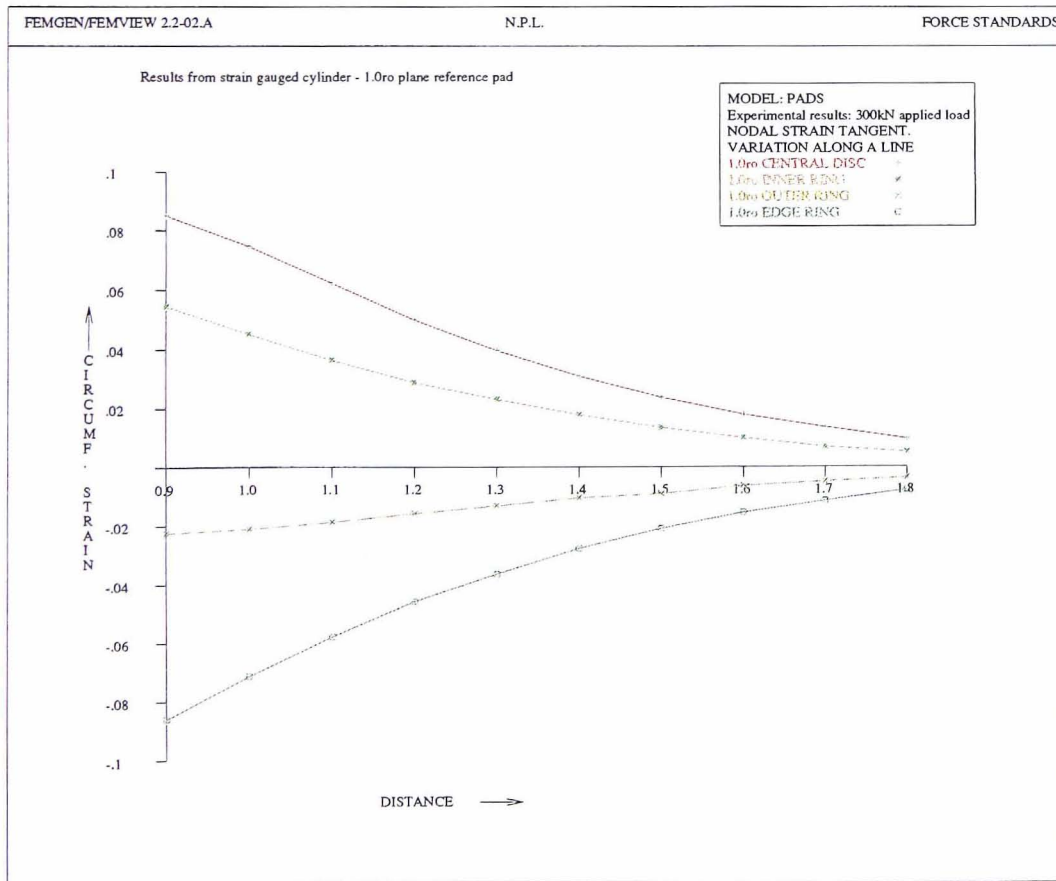


Figure 4.7: Surface circumferential strain v distance from loaded end: experimental results: 1.0ro pads

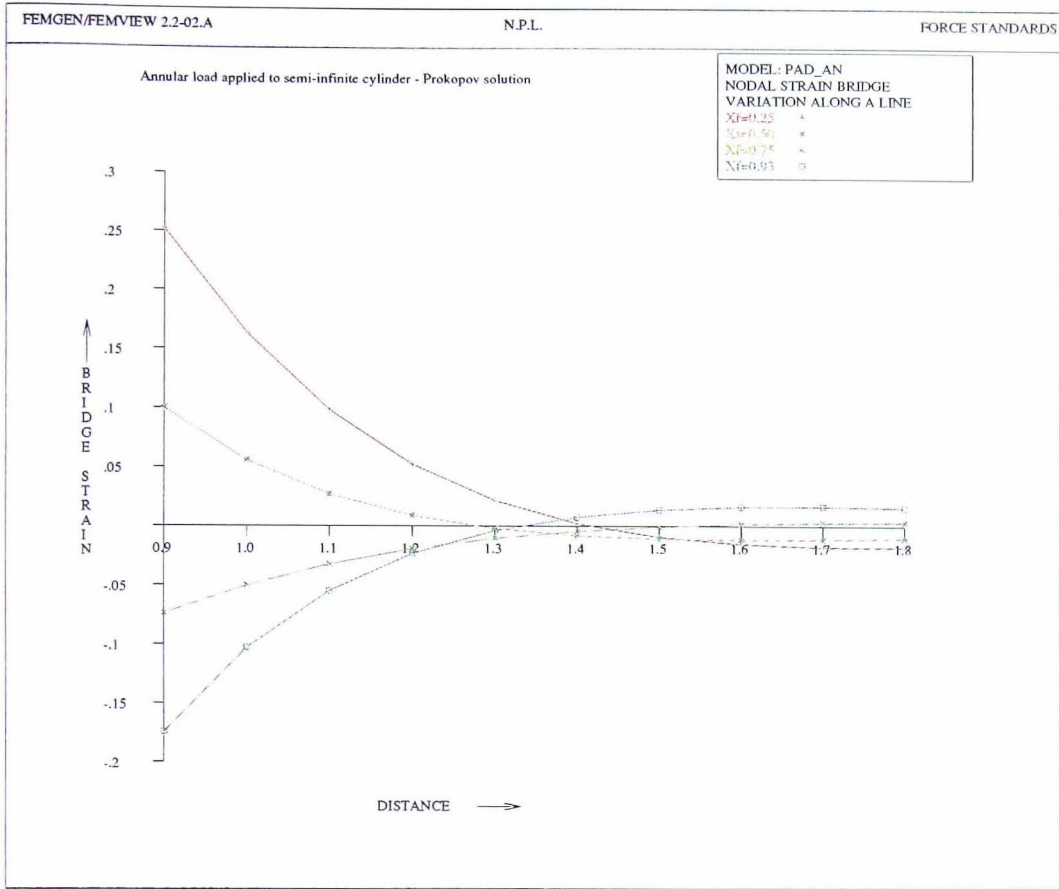


Figure 4.8: Surface bridge strain v distance from loaded end: Prokopov solution: mean pad contact radii

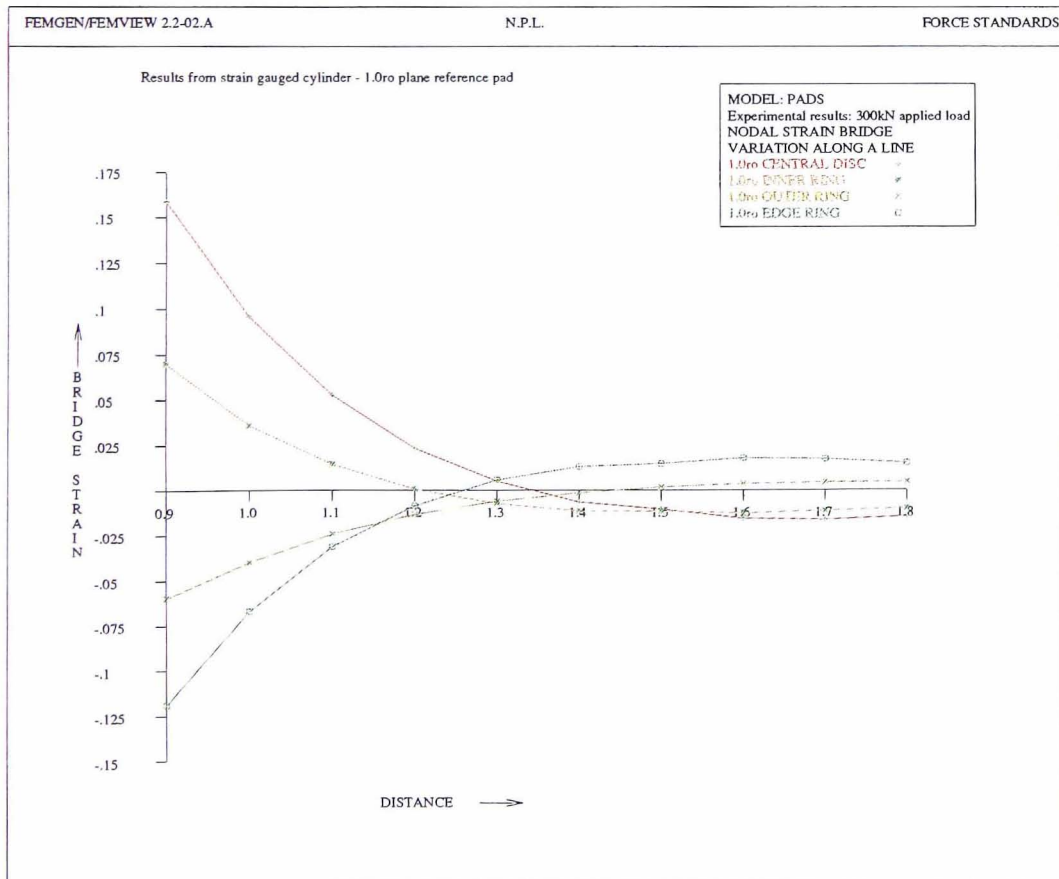


Figure 4.9: Surface bridge strain v distance from loaded end: experimental results: 1.0ro pads

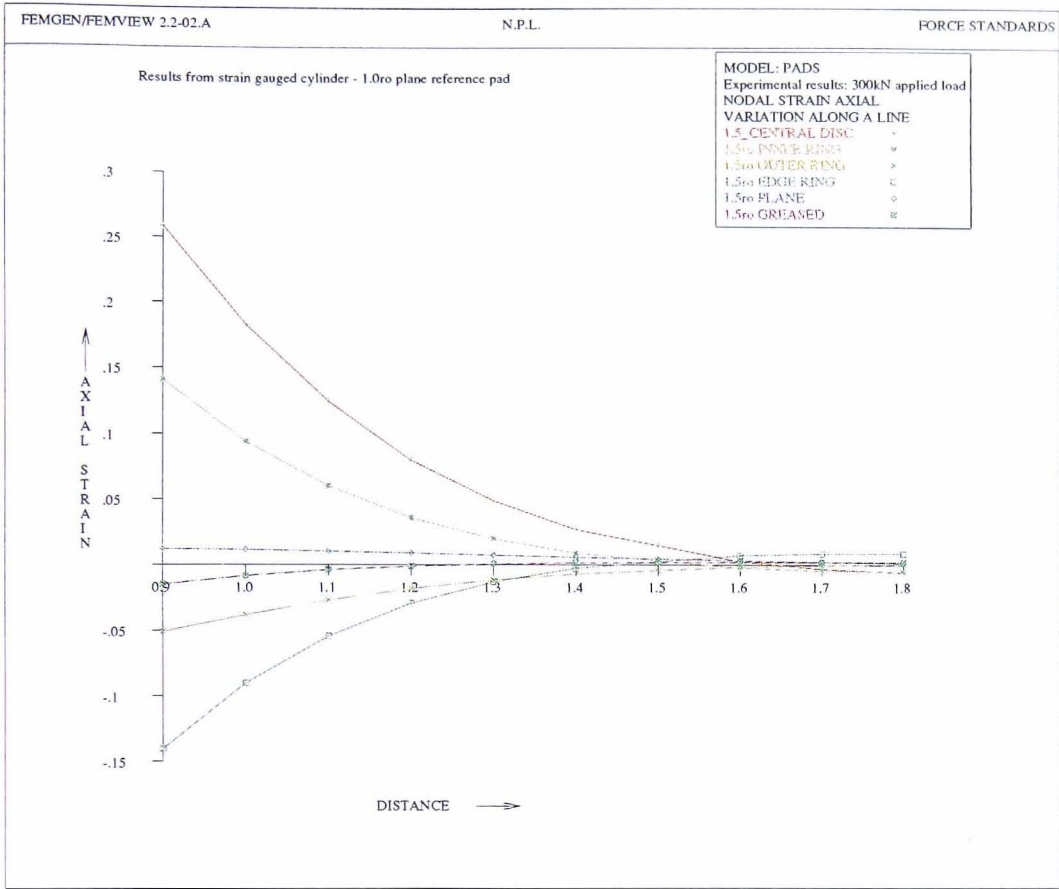


Figure 4.10: Surface axial strain v distance from loaded end: experimental results: 1.5ro pads

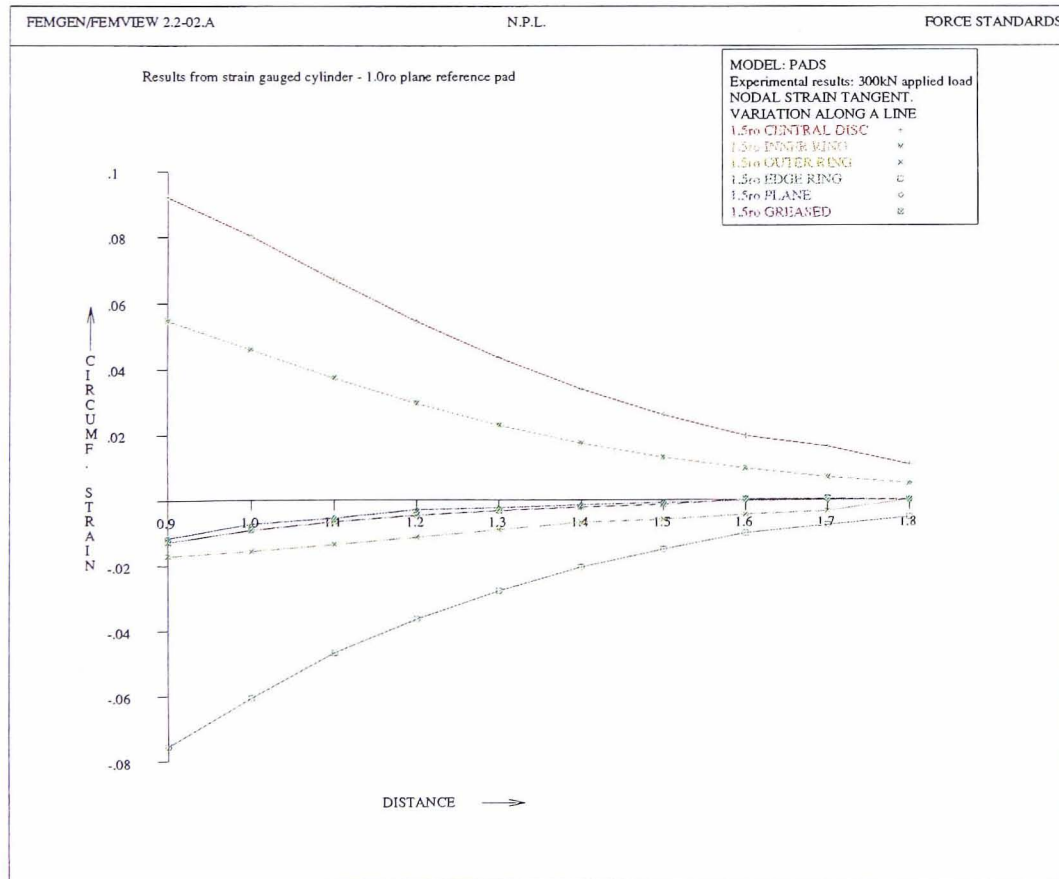


Figure 4.11: Surface circumferential strain v distance from loaded end: experimental results: 1.5ro pads

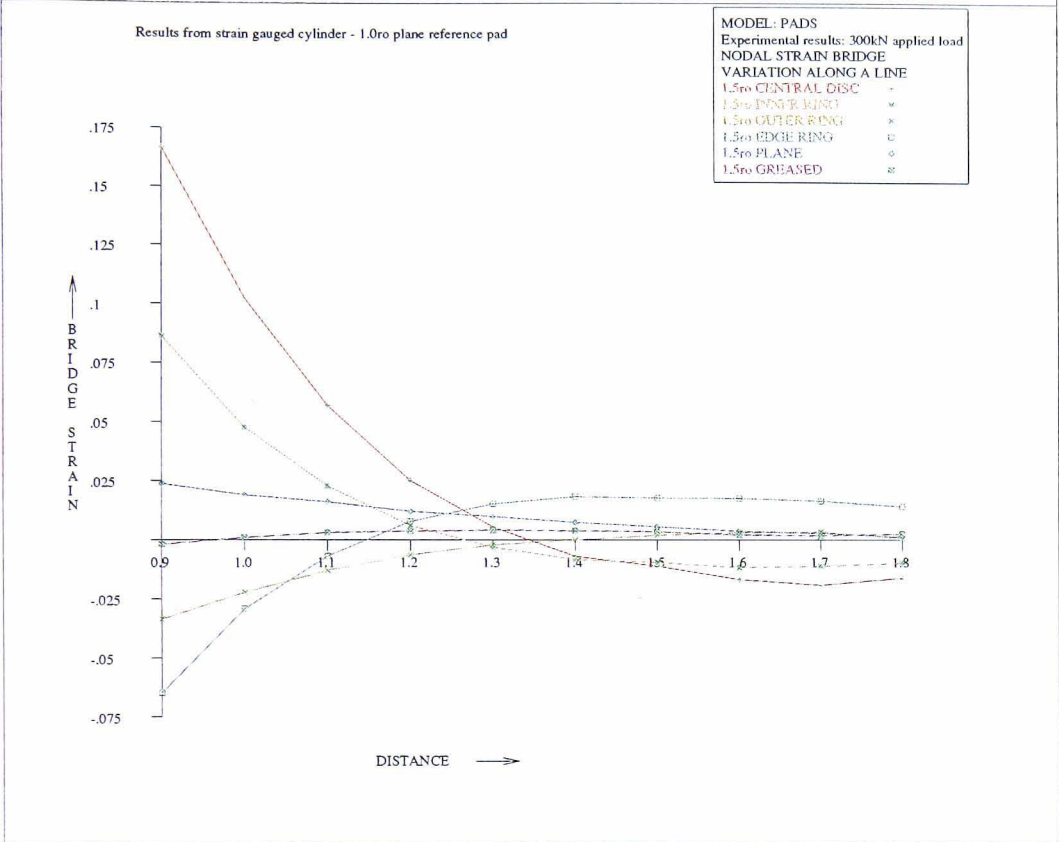


Figure 4.12: Surface bridge strain v distance from loaded end: experimental results: 1.5ro pads

4.3.2 Tests on the concave and convex pads

It was expected that the contact stress distributions of the convex and concave pads would depend on the magnitude of the applied load. To determine the influence of this, tests on the concave and convex pads were carried out at 30, 50, 100, 150, 200, 250 and 300 kN. The results are presented in figures 4.13 to 4.15. It should be noted in comparing the results at different loads that each has been normalised to the output on the plane $1.0r_p$ reference pad at the same load. The normalisation factors therefore differ between loads by up to a factor of ten.

It can be seen that the departure of the strain values from those associated with uniform stress is proportionally much greater for the smaller applied loads. That this is to be expected can be understood by considering the contact conditions as a load is gradually applied to a convex pad. Initially contact will be at a central point only. As the load is increased, the contact area will be spread outwards until contact is made over the entire cylinder end face and the initial gap has closed. In this condition the stress will be greatest at the centre, decreasing with radius to zero at the periphery. This initial loading therefore results in a highly non-uniform stress distribution. Further increasing the load will not necessarily result in a uniform increase in stress over the contact area. However, stress is likely to increase more uniformly than during the initial stage while the gap was closing. It is therefore to be expected that the stress distribution will become more uniform as the load is increased. A similar argument applies to loading on the concave pad.

No deformation was apparent during the flatness checks following loading on the concave, plane and convex pads. It is therefore probable that, unlike the disc and ring pads, local yielding did not occur. The results from the concave and convex pads will therefore be especially useful in verifying the finite element models presented later in this work, which also do not model yield.

In figure 4.16 the concave, convex and plane pad loading conditions which are equivalent to those of the EN10002-3 bearing pad test are presented separately. Figure 4.17 presents the results for all twelve of the loading conditions at 300 kN. In chapter 6 both of these graphs will be compared with results from a finite element model.

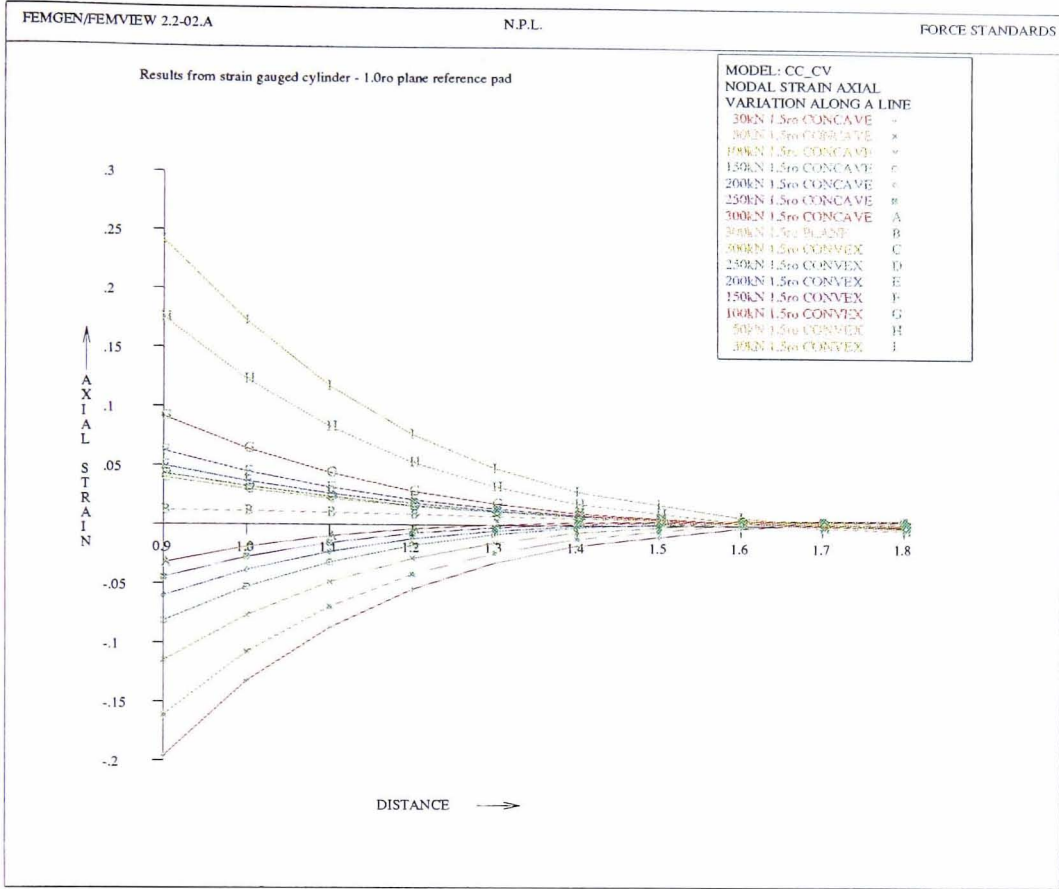


Figure 4.13: Surface axial strain v distance from loaded end: experimental results: concave/convex pads

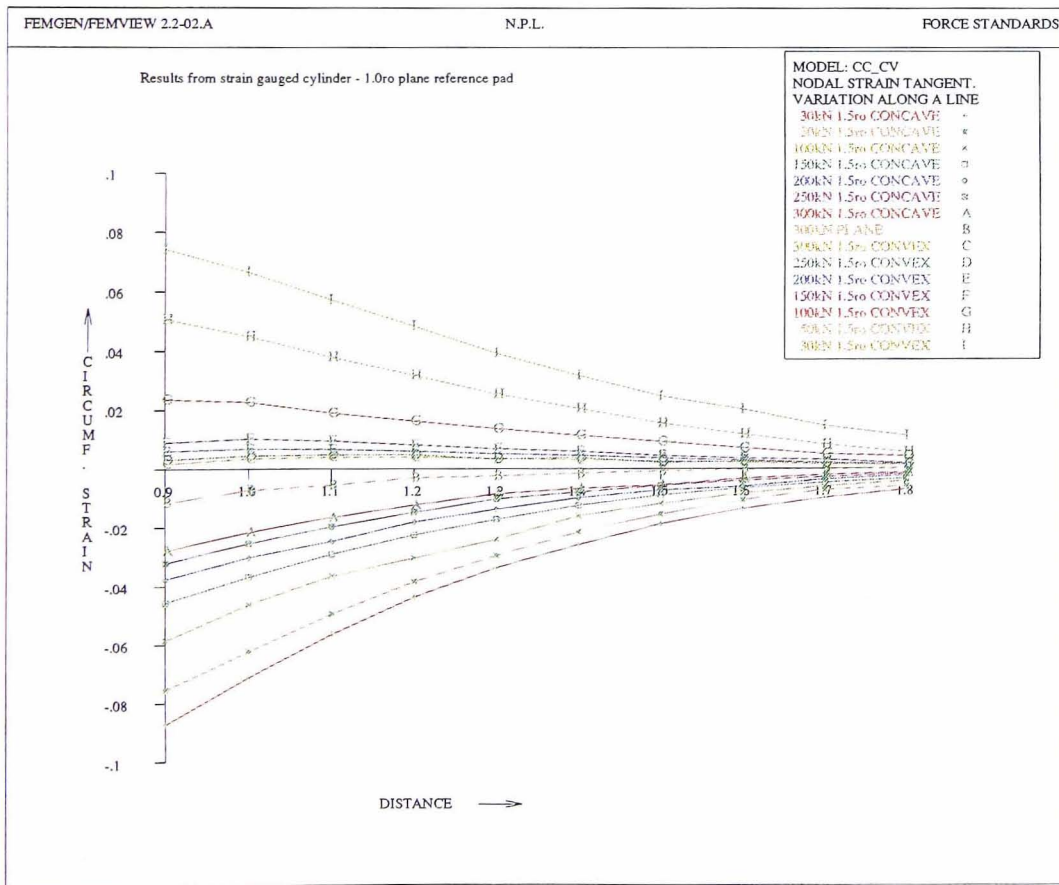


Figure 4.14: Surface circumferential strain v distance from loaded end: experimental results: concave/convex pads

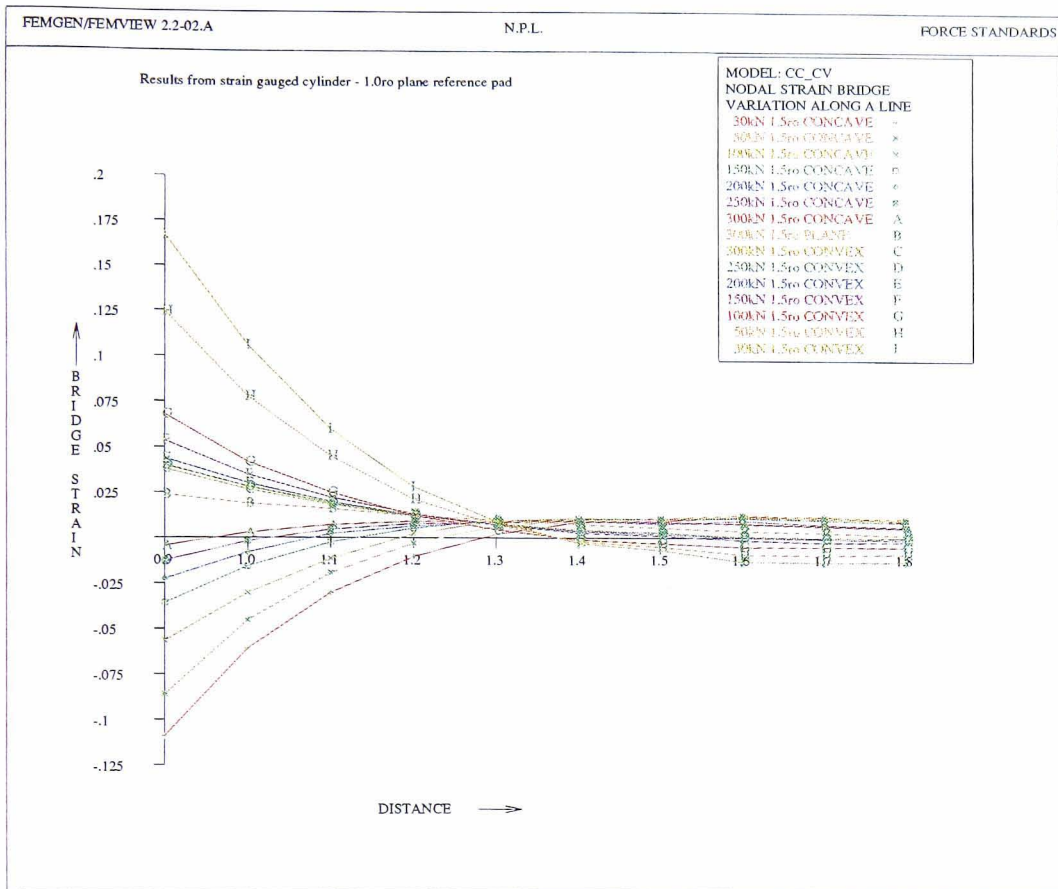


Figure 4.15: Surface bridge strain v distance from loaded end: experimental results: concave/convex pads

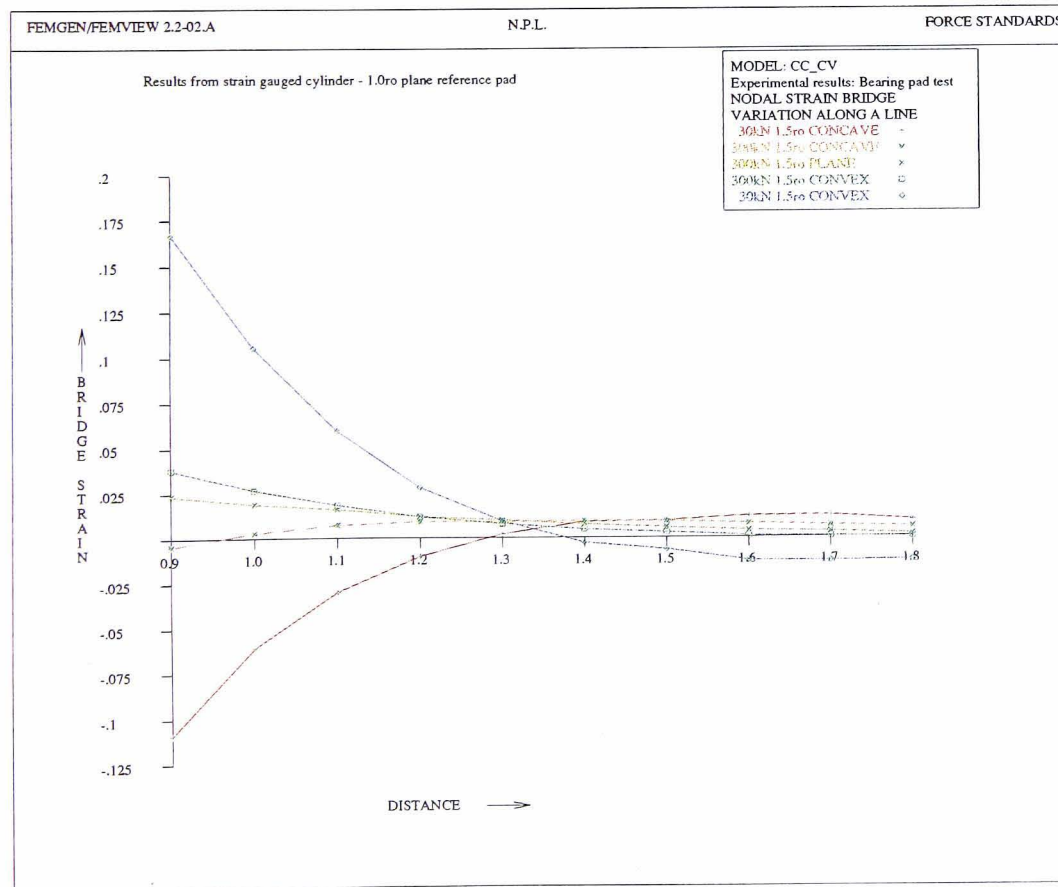


Figure 4.16: Surface bridge strain v distance from loaded end: experimental results: bearing pad test

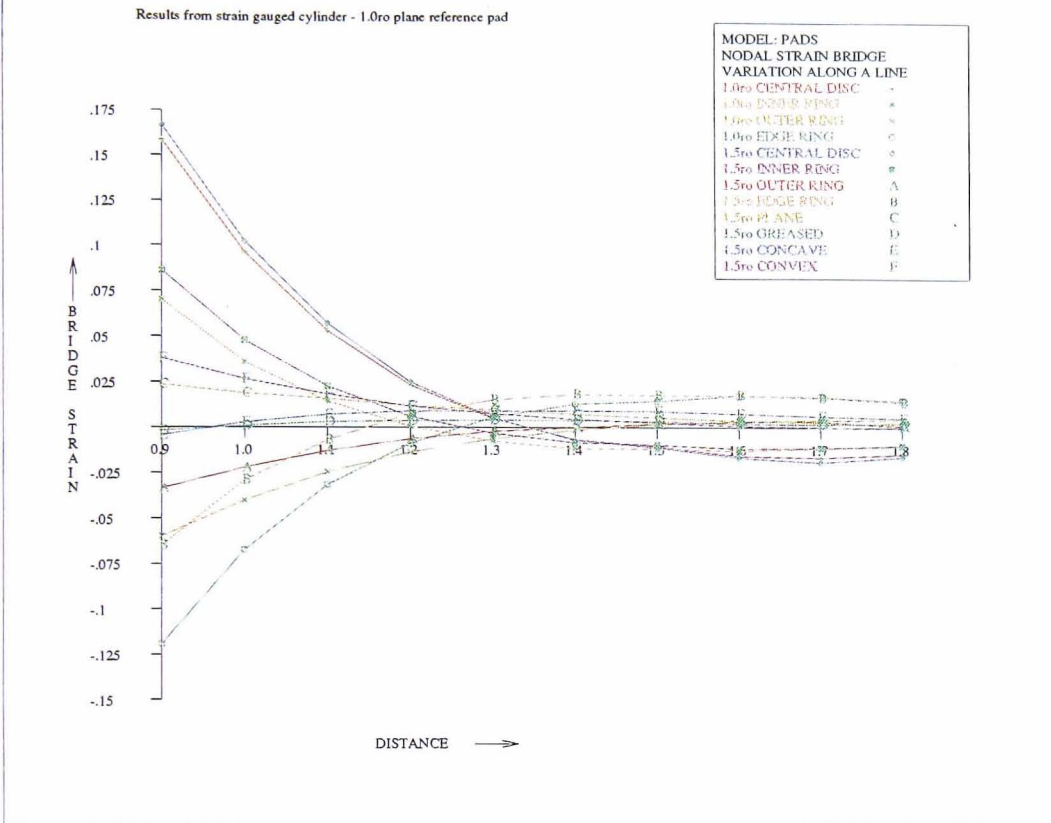


Figure 4.17: Surface bridge strain v distance from loaded end: experimental results: all pads

4.4 Measurement of Young's modulus and Poisson's ratio

4.4.1 Strain gauge configuration

The earlier calculations of the bridge strains required use of Poisson's ratio. It was therefore important to accurately determine the value of this parameter. For comparison with later finite element analysis results, determination of the Young's modulus of the cylinder was also required.

In order to measure these parameters strain gauges were applied on the cylinder's mid-plane, where they would be reasonably isolated from the influence of end-loading conditions at either end. Two Micro-Measurements CEA-06-25OUT-350 strain gauge patterns were used, each of which has two 350 Ω constantan grids encapsulated in a common polyimide matrix. The two gauge grids are orientated at right angles to each other and are self temperature compensated for steel at 10.8 ppm/ $^{\circ}$ C (6 ppm/ $^{\circ}$ F). The gauges were bonded, 180 $^{\circ}$ apart using M-Bond 200 cyanoacrylate based adhesive, their grids accurately orientated along the cylinder's axial and circumferential directions. The installation was protected with a thin coat of M-Coat A polyurethane based coating. Note that the gauges are absent from photo 4.1.

Each pair of gauges was connected as the active arm of a quarter Wheatstone bridge using the three-wire technique. To ensure the maximum accuracy of measurement of Poisson's ratio, the same bridge completion circuit was used for the measurement of both axial and circumferential strain.

The cylinder was placed between two flat pads, each equal in radius to the cylinder, and height 80 mm. A ball seat unit was placed upon the upper pad and a force of 300 kN applied in the 1.2 MN dead-weight machine. For each gauge pair, the output from the strain gauge bridge was recorded during seven load applications.

Load application	Axial bridge output mV/V	Circ. bridge output mV/V
1	-0.6022	0.1802
2	-0.6026	0.1790
3	-0.6020	0.1798
4	-0.6025	0.1792
5	-0.6024	0.1788
6	-0.6028	0.1794
7	-0.6028	0.1800
Mean	-0.6025	0.1795

Table 4.1: Output from gauges at mid plane

4.4.2 Results

The results recorded during the tests are given in table 4.1.

The output, ϕ , of a symmetric $\frac{1}{4}$ Wheatstone bridge is given by:

$$\phi = \frac{\Gamma}{4}(\varepsilon_l + \alpha\varepsilon_t) \quad 4.1$$

where Γ is the gauge factor, ε_l and ε_t are the longitudinal and transverse strain components and α is the transverse sensitivity of the gauge.

$$\therefore \varepsilon_c = \frac{4\phi_c}{\Gamma_c} - \alpha\varepsilon_a = \frac{1}{\alpha} \left(\frac{4\phi_a}{\Gamma_a} - \varepsilon_a \right) \quad 4.2$$

The axial strain is therefore given by:

$$\varepsilon_a = \frac{4(\phi_a\Gamma_c - \alpha\phi_c\Gamma_a)}{\Gamma_a\Gamma_c(1-\alpha^2)} \quad 4.3$$

similarly for circumferential strain:

$$\varepsilon_c = \frac{4(\phi_c\Gamma_a - \alpha\phi_a\Gamma_c)}{\Gamma_a\Gamma_c(1-\alpha^2)} \quad 4.4$$

The calibration data sheet provided with the strain gauges gave the gauge factors of the patterns as 2.085 in the axial direction and 2.095 in the circumferential direction, with a transverse sensitivity of 0.5%.

The strain values calculated from equations 4.3 and 4.4 are:

Axial strain:	-1158 μ strain
Circumferential strain:	349 μ strain

Giving a Poisson's ratio for the cylinder:

$$\text{Poisson's ratio} = 0.301$$

The axial stress σ_a applied to the cylinder is given by $\sigma_a = \frac{F}{\pi r_o^2}$. The axial force F was 300 kN while the radius r_o was measured to be 20.05 mm. The axial stress was therefore calculated to be $\sigma_a = 237.5 \text{ MNm}^{-2}$. Dividing this value by the measured axial strain gives a value for the cylinder's Young's modulus.

Young's modulus=205.2 GNm⁻²

These measured values agree exceptionally well with the 'book' values for this steel, given as 205 GNm⁻² and 0.3.

4.5 Conclusions

The surface strains near the ends of a plane cylinder have been measured while the cylinder was loaded upon pads of various profile. When loaded upon pads of equal diameter, the strains recorded from the cylinder show reasonable agreement with those calculated from Prokopov's solution. This agreement over the strain gauged portion is encouraging and gives some confidence in the predictions of the analytic results. Radial shear forces, present in some of the experimental loadings, but absent from the analytical model, have been shown to have a significant effect on the surface strains. As such radial stresses are present in most real load cases, their effect will have to be modelled if accurate predictions of end-loading sensitivity are to be made.

CHAPTER 5

DEVELOPMENT OF A SIMPLE FINITE ELEMENT ANALYSIS PROGRAM

5.1 Introduction

The analytic work described earlier has shown reasonable agreement with results measured experimentally. However the analytic solution is only valid for the case of a circular cylinder in the absence of radial shear forces. In addition the radial distribution of stress must be known for a solution to be obtained.

If an analysis method is to be useful in developing improved load cell designs, it must be free of these limitations. Such a method should be capable of:

Modelling axisymmetric objects of arbitrary profile.

Modelling any axi-symmetric combination of axial and radial shear contact stresses.

Modelling contact problems where the profiles and friction coefficients of the contact surfaces are known but where the contact stresses are not known a priori.

The above combination of capabilities would allow the modelling of load cells of arbitrary shape, loaded on the plane, concave and convex pads associated with the EN10002-3 bearing pad test.

Two analysis methods with the above capabilities are presently in general use. These are the finite element and boundary element methods. As City University and NPL staff had some familiarity with the finite element method this method was chosen to continue the work of this study.

5.2 The finite element method

The finite element method is a method for approximating the set of partial differential equations governing the behaviour of a physical system within some domain by a set

of algebraic equations which can be solved using numerical methods. The theory of the finite element method is described in many books, for example Zienkiewicz [1977], NAFEMS [1986], and will not be repeated here.

5.3 Choice of finite element software

There are many commercial packages implementing the finite element method. Most of these accept a text file defining a problem and output the solution displacements, stresses and strains to a text file. Many packages also feature a pre- and post-processor which allows the problem to be defined interactively using a PC or graphics terminal. The results can be viewed as contour plots, graphs, vectors etc. Third party pre- and post-processors are also available for all the major FE packages.

These commercial packages are very capable, can solve a wide variety of problems and are fairly easy to use. An example of such a package, PAFEC FE, was available on the NPL VAX mini-computer. Most such packages would be capable of meeting the criteria outlined in section 5.1. However, their ease of use is bought at the expense of flexibility. While most packages allow some program control of the solution by the user, this is usually very limited. It was anticipated that development of improved load cell designs would eventually require some form of iterative method. The standard FE packages would not provide the flexibility of program control required to implement such a system.

An alternative to using a commercial finite element package is to write custom analysis programs using a library of finite element routines. This requires a greater understanding of the theory and practice of the finite element method but has the advantage of giving the user complete control over the solution algorithm. It was decided that the increase in flexibility would be worth the extra development effort of this approach.

City University had used the NAG finite element library extensively in such programs in the past and the staff were experienced in its use. It was therefore decided to base the analysis program on the NAG finite element library. Originally known as the SERC finite element library, the library is a collection of FORTRAN routines which implement all the algorithms necessary to perform the common types of finite element analysis. The user provides a main program which calls the routines in the correct order to carry out the analysis.

As well as performing the FE solution to the problem, a means of defining the problem to be solved and of displaying the solution are also required. Staff at City University were familiar with the Femview pre- and post-processor, having used it on several projects. It was therefore decided that the analysis program should interface to this software package.

5.4 The axisymmetric finite element program, `axi.f`

Supplied with the NAG library are a suite of example programs which illustrate the use of the routines. The supplied examples include static and dynamic analysis of solids and various potential problem analyses. The supplied static analysis example performs a 2-D linear elastic solution. Also included in the library are the strain displacement routines appropriate to an axisymmetric analysis. It would therefore have been reasonably straightforward to modify the example program to carry out axisymmetric analyses.

However, it was foreseen that, although initially a reasonably simple analysis was required, a more complex program would eventually be called for. It was judged that the linear style of the example program would prove too inflexible during later development stages. The decision was therefore taken to write the axisymmetric program from scratch using a modular program structure. Splitting the program down into callable modules would hopefully allow later development of more complex program structures without rewriting of the basic modules.

The modular axisymmetric FE program was named '`axi.f`'. The program reads the geometry and loadings from an input file written by the Femview pre-processor, performs a linear static axisymmetric analysis and writes an output file in a format that can be read by the Femview post-processor.

5.5 Tests on the simple finite element program

Although the NAG FE library is a mature product and therefore should be reasonably bug free, `axi.f` contains a large amount of untested code. In addition some of the methods and algorithms used are different to those given in the NAG example programs. Examples include the methods used for numerical integration of triangular elements and the extrapolation of Gauss point strains to the nodes. It was therefore essential to verify the performance of the program against test problems for which results have been derived using other methods. A set of such 'benchmark' tests are published by the National Agency for Finite Element Methods and Standards

(NAFEMS [1989]). Unfortunately while most types of analysis are well covered by these tests, the only axisymmetric benchmark applies to thin shells only. In the absence of such recommended tests, the following problems were used to test the axi.f program.

5.5.1 Infinite thick cylinder under internal pressure

The infinite thick hollow cylinder under internal pressure is a classical problem in solid mechanics with a analytic solution due to Lamé. The test problem was a cylinder of internal radius 1 m, external radius 2 m, subject to an internal pressure of 1 Pascal. The material constants were defined as:- Young's modulus: 1.0 Nm⁻² and Poisson's ratio: 0.3.

5.5.1.1 Lamé's analytic solution

The analytic solution to the problem is given (Timoshenko & Goodier 1982) as:

$$\sigma_r = \frac{r_i^2 p}{r_o^2 - r_i^2} \left(1 - \frac{r_o^2}{r^2} \right) \quad 5.1$$

5.5.1.2 Comparison of results with different mesh geometries

To evaluate the axi.f finite element program with different element types and mesh densities, The Lamé problem described above was analysed by modelling a radial section of the cylinder using the following mesh configurations:

Four 8-node quadrilateral elements, each 0.25 m square.

Eight 8-node quadrilateral elements, each 0.125 m square.

Eight 6-node triangular elements, each a right angled isosceles triangle with shorter sides 0.25 m.

Sixteen 6-node triangular elements, each a right angled isosceles triangle with shorter sides 0.125 m.

The above mesh configurations are illustrated in figure 5.1. In each case the nodes along the lower plane, $z = 0$, were restrained in the axial direction. In the application which is the subject of this work the primary consideration is the accuracy of the calculation of the strain values. In table 5.1 the percentage differences between the

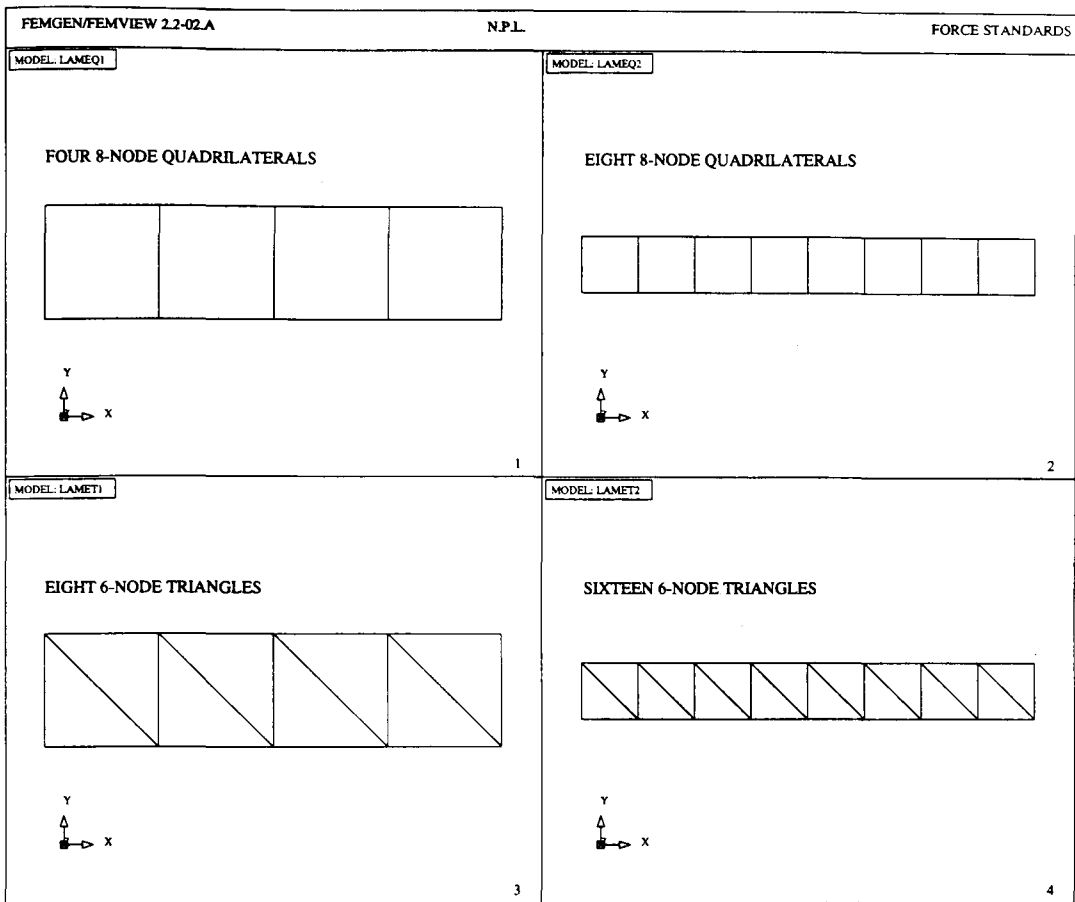


Figure 5.1: Mesh configurations used to analyse Lamé's problem

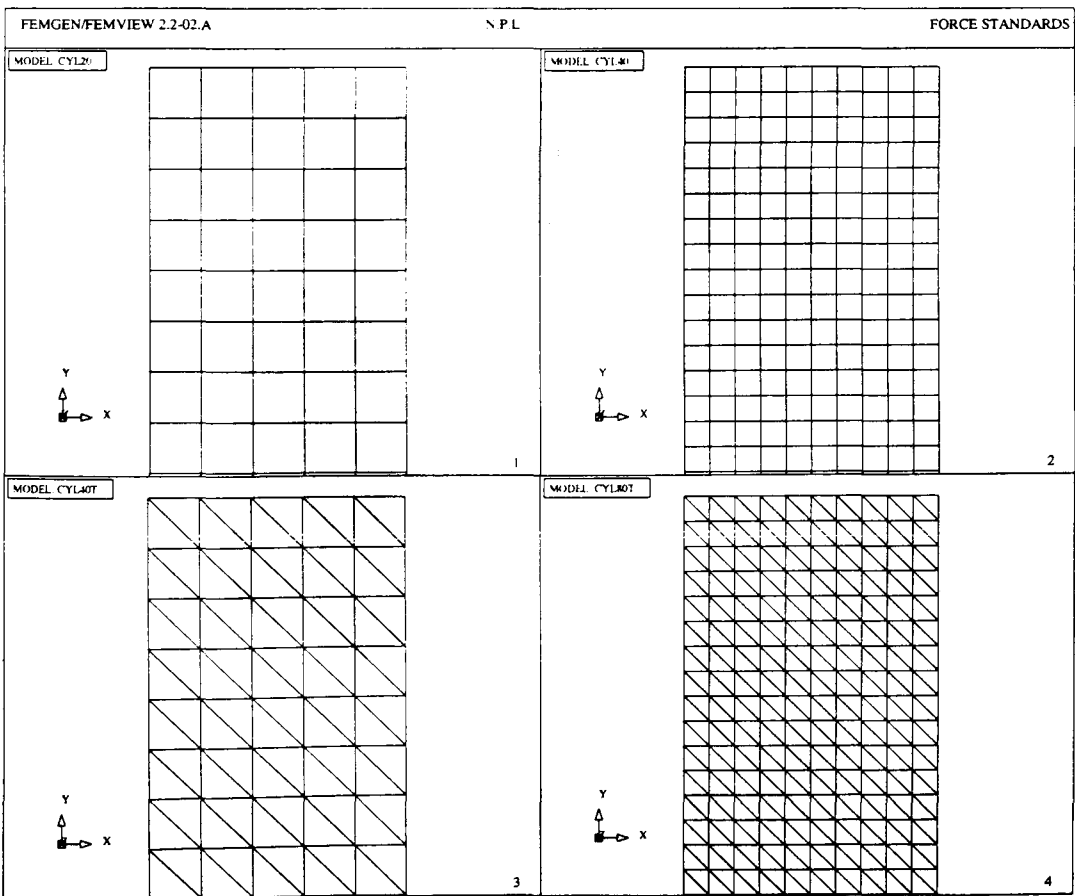


Figure 5.2: Mesh configurations used to analyse cylinder of aspect ratio 4.0

finite element strain results along the plane $z = 0$ together with the Lamé solution, have been tabulated.

4 x 8-node quadrilaterals			8 x 8-node quadrilaterals			8 x 6-node triangles			16x 6-node triangles		
ε_r	ε_θ	ε_z	ε_r	ε_θ	ε_z	ε_r	ε_θ	ε_z	ε_r	ε_θ	ε_z
-2.6	-2.0	0.0	-0.8	-0.6	0.0	-1.5	-1.5	-0.2	-0.4	-0.4	0.0
-2.7	-1.8	0.0	-0.6	-0.4	0.0	-3.1	-2.4	-0.3	-0.7	-0.5	0.0
-2.1	-1.1	0.0	-0.5	-0.3	0.0	-2.4	-1.4	-0.1	-0.5	-0.3	0.0
-1.8	-0.8	0.0	-0.5	-0.2	0.0	-2.0	-1.0	0.0	-0.5	-0.2	0.0
-2.1	-0.6	0.0	-0.5	-0.1	0.0	-2.6	-0.8	0.0	-0.6	-0.2	0.0

Table 5.1: Percentage error of strains from finite element solution, with various mesh configurations

It is apparent for that for all four mesh geometries the axial strain is predicted with little error. This is to be expected as the axial strain has a constant value and is therefore capable of being represented exactly by the 2nd order shape functions (as also could a strain distribution which varied linearly across the element). The strains in the other two directions decrease as the inverse square of the radius. These strains cannot therefore be represented exactly by the piece wise linear approximation of the finite element method. Errors between the finite element and exact solutions are therefore to be expected. Both the quadrilateral and triangular coarse meshes show errors of around 1-3% in calculating these strain components. It can be seen that in both cases refining the mesh (by a factor of two in each dimension) results in a significant reduction in error to values of less than 1%. For both the quadrilateral and triangular elements the solution therefore appears to converge on the correct solution.

The magnitude of the errors for these Lamé 'benchmark' tests were judged to be acceptable and were taken to indicate that the two element types had been correctly implemented.

5.5.1.3 Discussion of FE model of thick cylinder under internal pressure

The above results from `axi.f` show satisfactory agreement with Lamé's solution using reasonable densities of quadrilateral or triangular elements. This provided some confidence that the finite element algorithm had been correctly implemented in the program `axi.f`.

Like all benchmark tests, the results of the above tests do not indicate that a particular combination of element type and mesh density is suitable for analysing axisymmetric problems in general. In order to obtain a good understanding of the accuracy of a particular element/density combination when applied to a problem of interest, it is desirable that a test be carried out which is as similar as possible to the target problem. Lamé's problem has the advantage of having an explicit solution which can be evaluated without error. However, the problem is not very similar to that of the column load cells under axisymmetric loading, the subject of this study. A second test was therefore carried out, in which the results from the earlier analytic study of a semi-infinite cylinder under annular loading were compared with the results from the FE program for a long cylinder subject to annular load. This further test had the disadvantage of lacking a solution that is known to be correct, but was representative of the type of problem to be analysed later.

5.5.2 Analysis of long cylinder subject to annular load

The second test model was a cylinder of 1m radius and height 4m. It has been shown in section 3.4.2 that the results from a semi-infinite cylinder can be applied to a finite cylinder of this aspect ratio without significant error. The earlier analytic results for a semi-infinite cylinder can therefore be compared with results calculated using the finite element analysis to give a check on the accuracy of the program when modelling a problem similar to those to be modelled later.

5.5.2.1 Results with various finite element mesh geometries

The cylinder was modelled using four mesh geometries. The upper portion of each mesh is shown in figure 5.2.

The four FE models were:

CYL20x5Q - An 8-node quadrilateral mesh each element being a square of side 0.2 m.

CYL40x10Q - An 8-node quadrilateral mesh each element being a square of side 0.1 m.

CYL40x10T - An 6-node triangular mesh each element being a right angled isosceles triangle with shorter sides of 0.2 m.

CYL80x20T - An 6-node triangular mesh each element being a right angled isosceles triangle with shorter sides of 0.1 m.

Each model was subjected to a compressive annular load of magnitude π superimposed on an uniformly distributed tensile load of equal value. Values of 1.0 Nm⁻² and 0.3 were used for the Young's modulus and Poisson's ratio, respectively. The parameter which will be of greatest interest in later analyses is the 'bridge strain' and therefore values of bridge strain were calculated using each of the above meshes. For each mesh the surface bridge strains between 0.9 m and 1.8 m from the loaded end are shown in figures 5.3 to 5.6. For the CYL40x10Q mesh contour plots of the bridge strain values are also shown in figures 5.7 to 5.12.

5.5.2.2 Discussion of results

The first comparison to be made is between the results for the CYL20x5Q quadrilateral mesh and the denser CYL40x10Q quadrilateral mesh. It is apparent from the similarity of the two plots of bridge strain that the FE solution has converged at the CYL20x5Q mesh density. Comparison of the two plots from the CYL40x10T triangular mesh and the denser CYL80x20T triangular mesh reveals small differences. However, the results can again be said to have converged at the coarser mesh density. These results give some indication of the order of mesh density required in analysing annular loaded cylinders. The results indicate that for both quadrilateral or triangular elements, acceptable accuracies should be obtained with element sides of the order of 1/10th of the cylinder radius.

Comparison can also be made between the FE results and those obtained earlier using the Prokopov solution. The bridge strain contour plots of figures 5.7 to 5.12, calculated using the FE mesh CYL40x10Q, can be compared with the contour plots calculated using the Prokopov solution given in figures 3.9 to 3.14. Minor differences between the two sets of plots are apparent in the region close to the loaded annulus. However, away from this region the bridge strain values calculated using the FE and homogenous solution methods are in extremely good agreement. Although not presented here, the axial and circumferential strain results displayed similar levels of agreement.

5.5.3 Conclusions from the 'benchmark' tests

The tests on a thick cylinder under internal pressure have shown the program `axi.f` to give results in close agreement with Lamé's exact analytic solution. This gives some

confidence that the FE algorithm is correctly implemented. The second set of tests on the annular loaded cylinder are for a problem similar to the analyses required later in this project. The FE results from `axi.f` agree closely with those calculated by superposition of homogenous solutions. It is highly improbable that these two totally different calculation methods would give such similar results unless both sets of results are substantially correct. This agreement therefore gives a high level of confidence in the basic FE program in analysing cylinders under axisymmetric loading.

5.6 Conclusions

A simple axisymmetric finite element program has been developed around the routines of the NAG finite element library. Tests on the program have shown it to accurately model Lamé's problem. The results from the program have also been shown to be in excellent agreement with the results of the analysis presented in chapter 3. Comparison of the results from meshes of different density have indicated the approximate size of element required to analyse axisymmetric problems with acceptable accuracy.

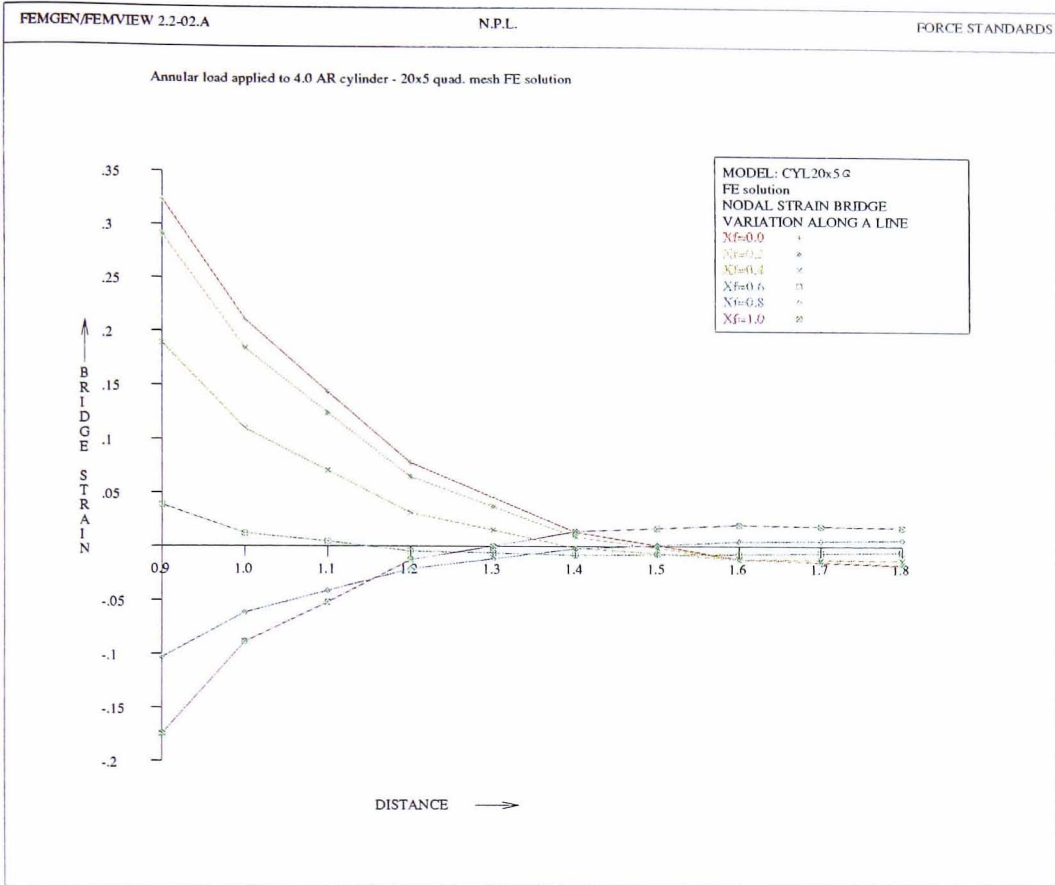


Figure 5.3: Surface bridge strain v distance from loaded end: 20x5 quad. mesh

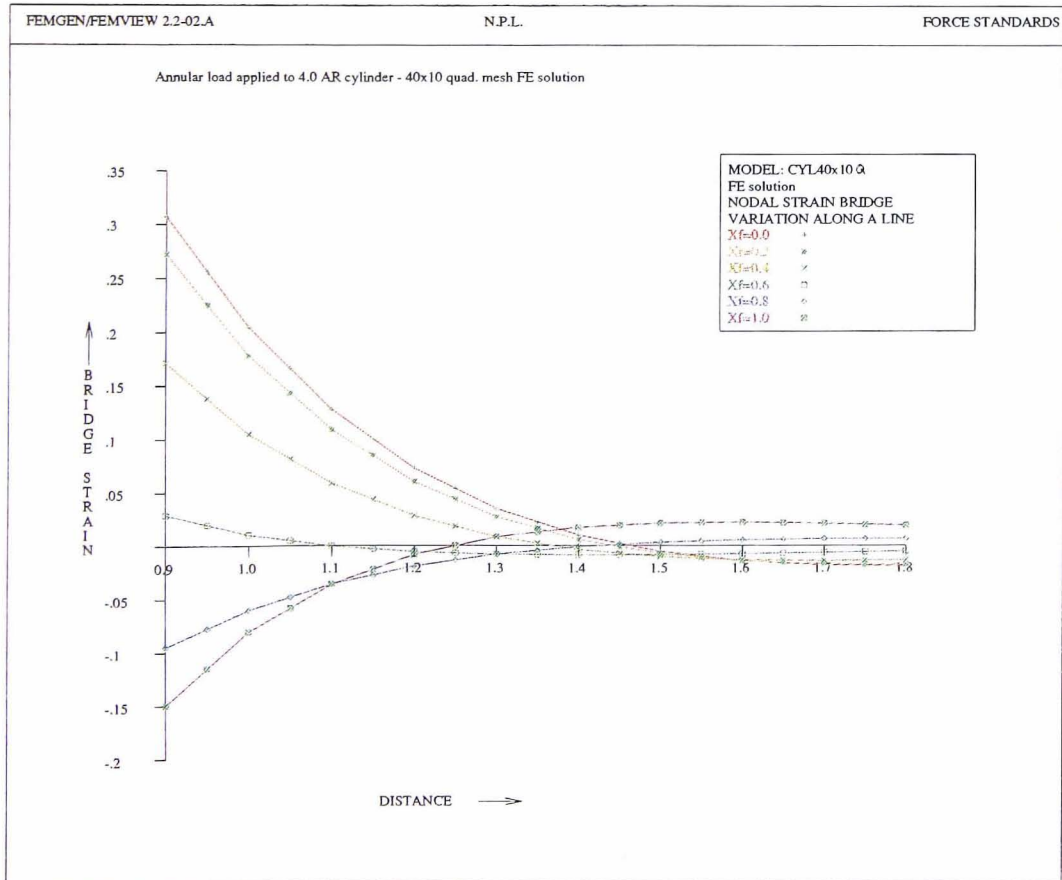


Figure 5.4: Surface bridge strain v distance from loaded end: 40x10 quad. mesh

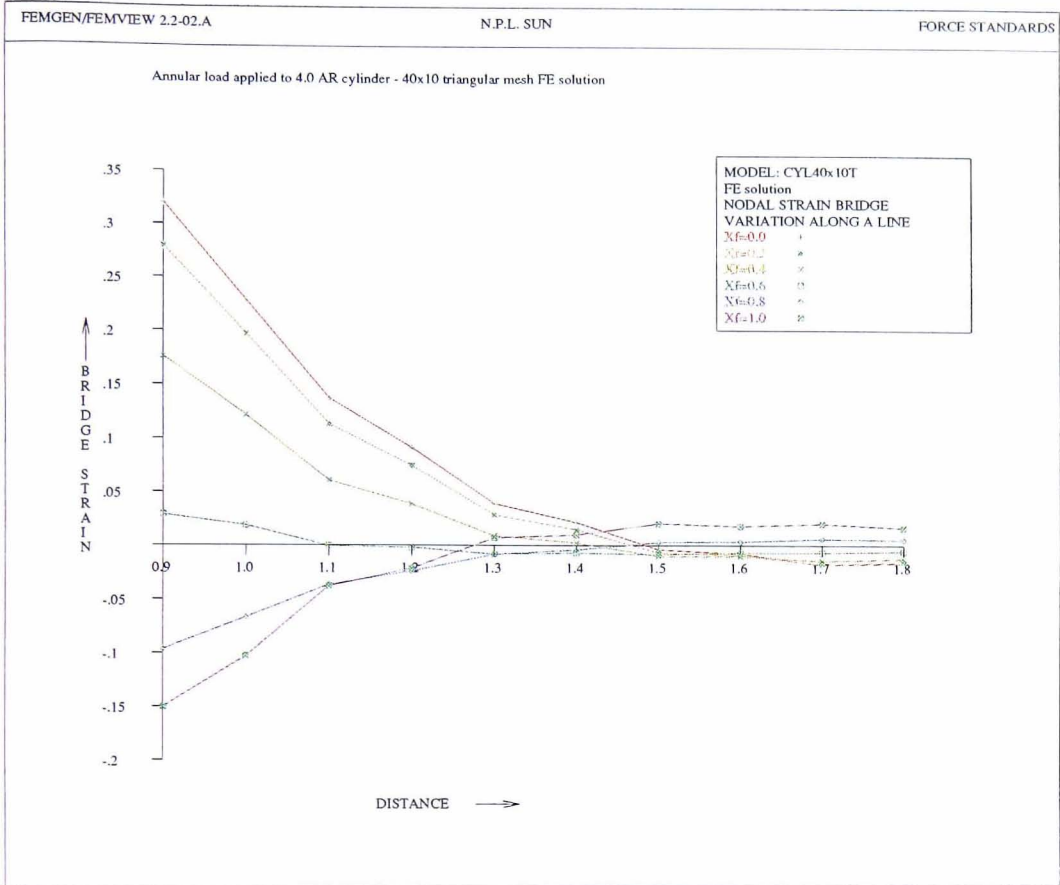


Figure 5.5: Surface bridge strain v distance from loaded end: 40x10 triangular mesh

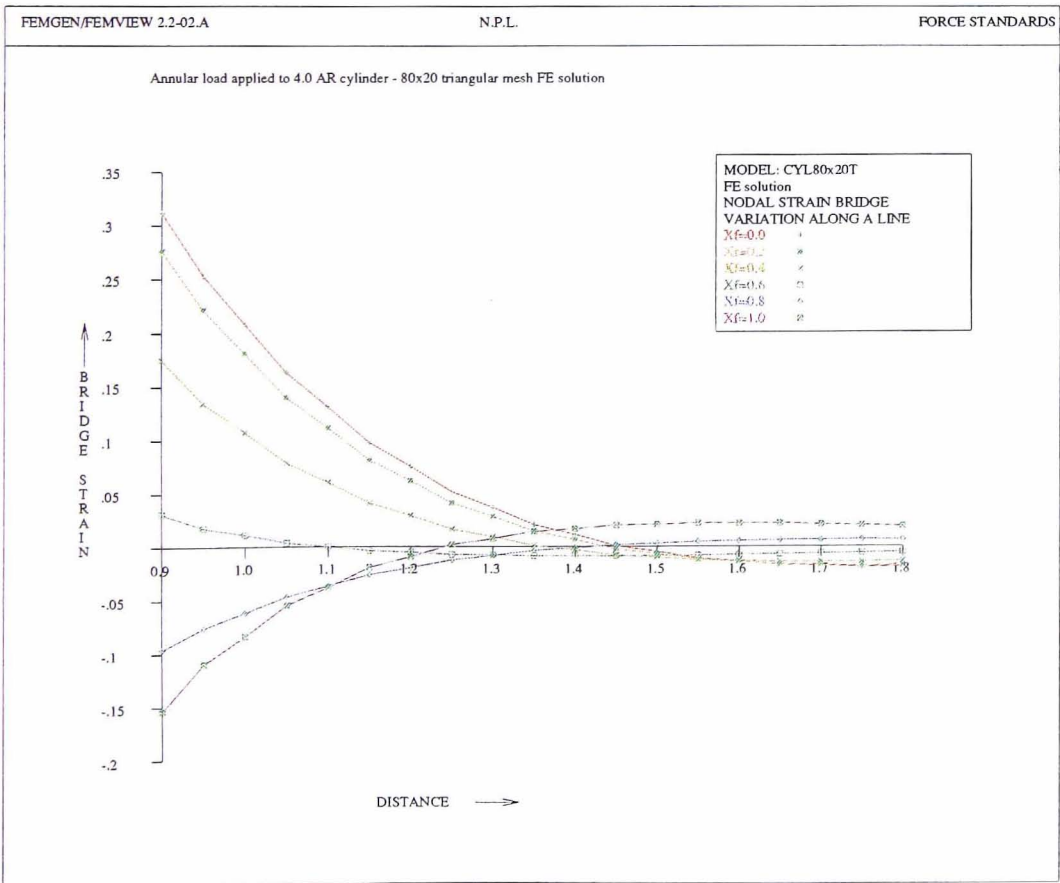


Figure 5.6: Surface bridge strain v distance from loaded end: 80x20 triangular mesh

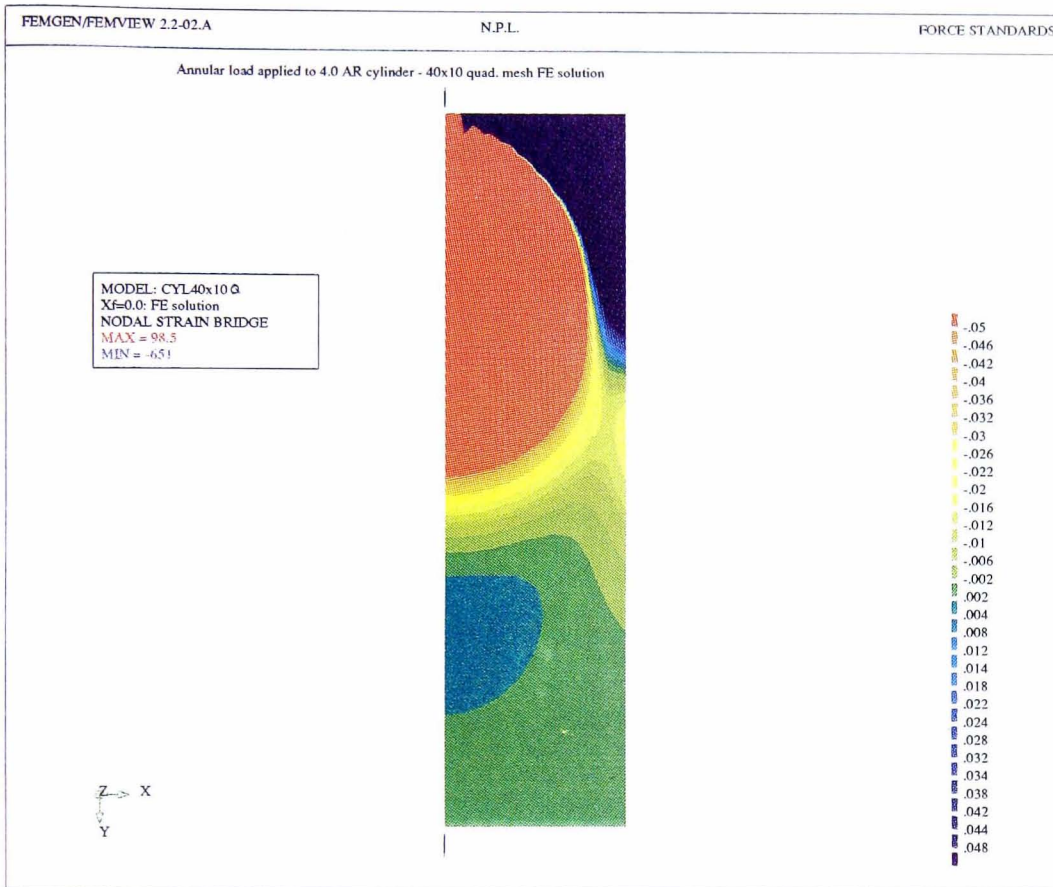


Figure 5.7: Contours of bridge strain due to equipollant annular load with $X_f=0.0$: 40x10 quad. mesh FE solution

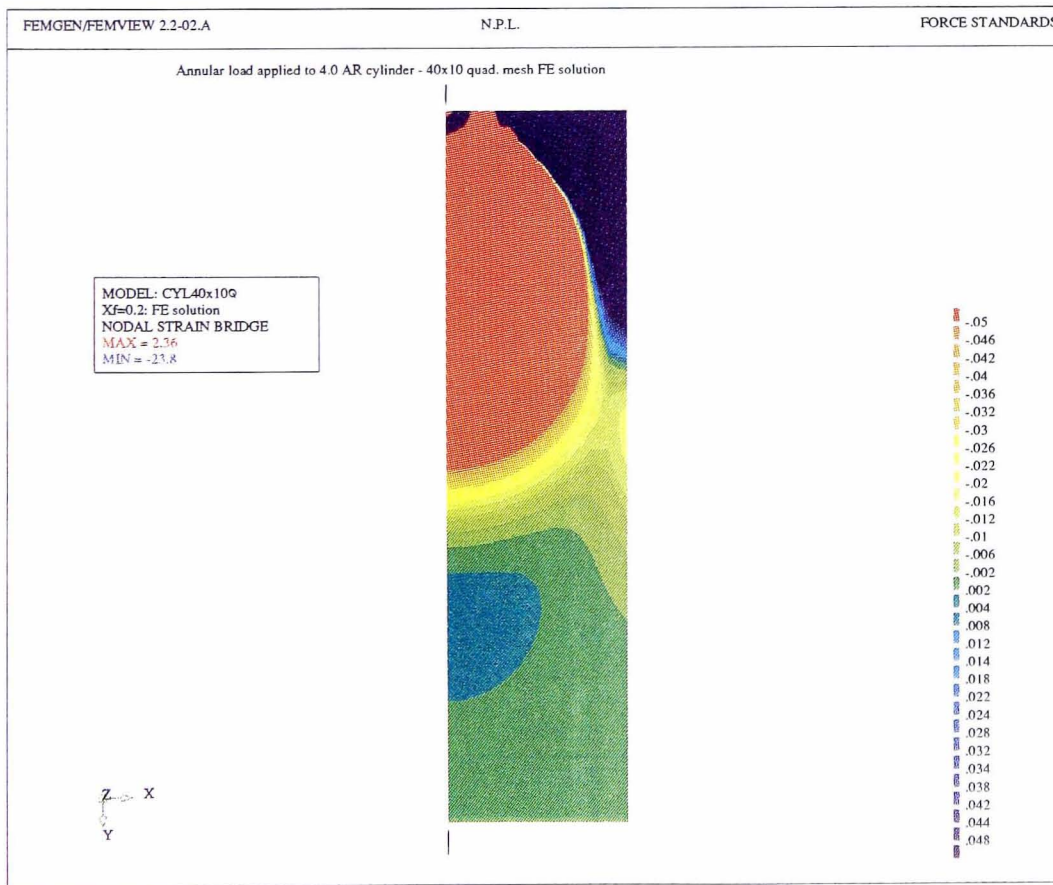


Figure 5.8: Contours of bridge strain due to equipollant annular load with $X_f=0.2$: 40x10 quad. mesh FE solution

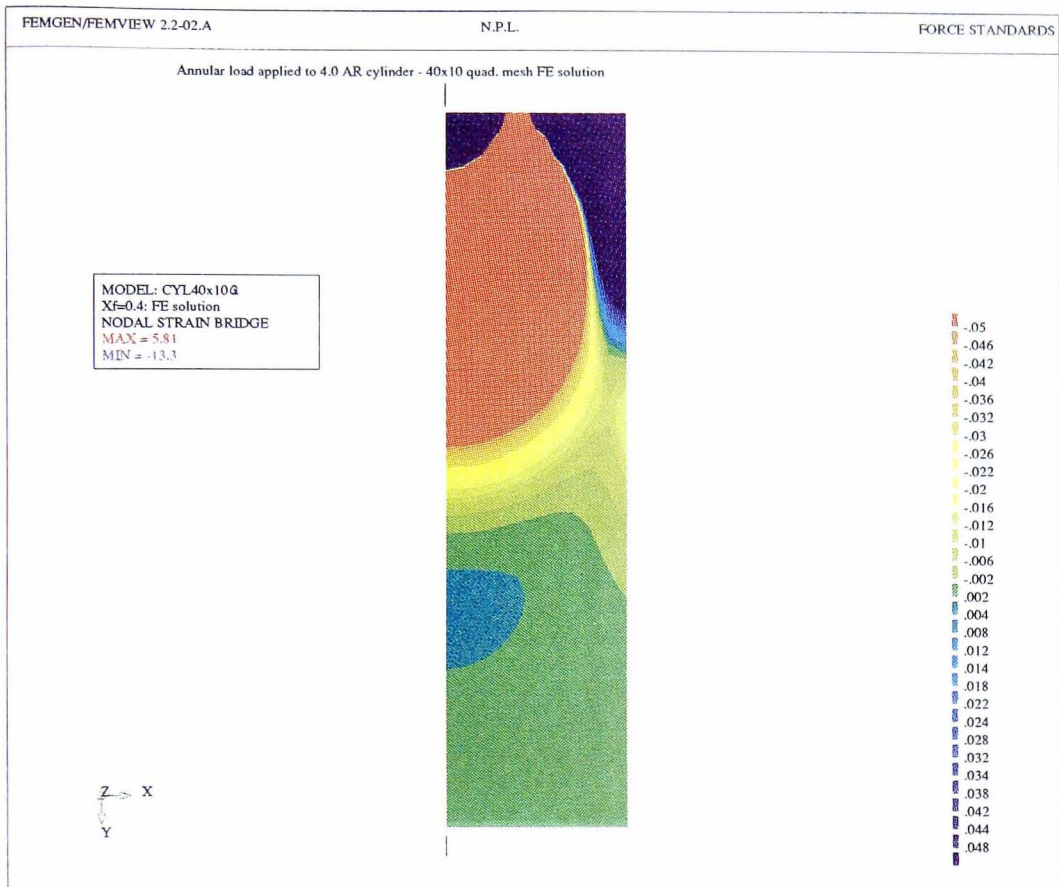


Figure 5.9: Contours of bridge strain due to equipollant annular load with Xf=0.4: 40x10 quad. mesh FE solution

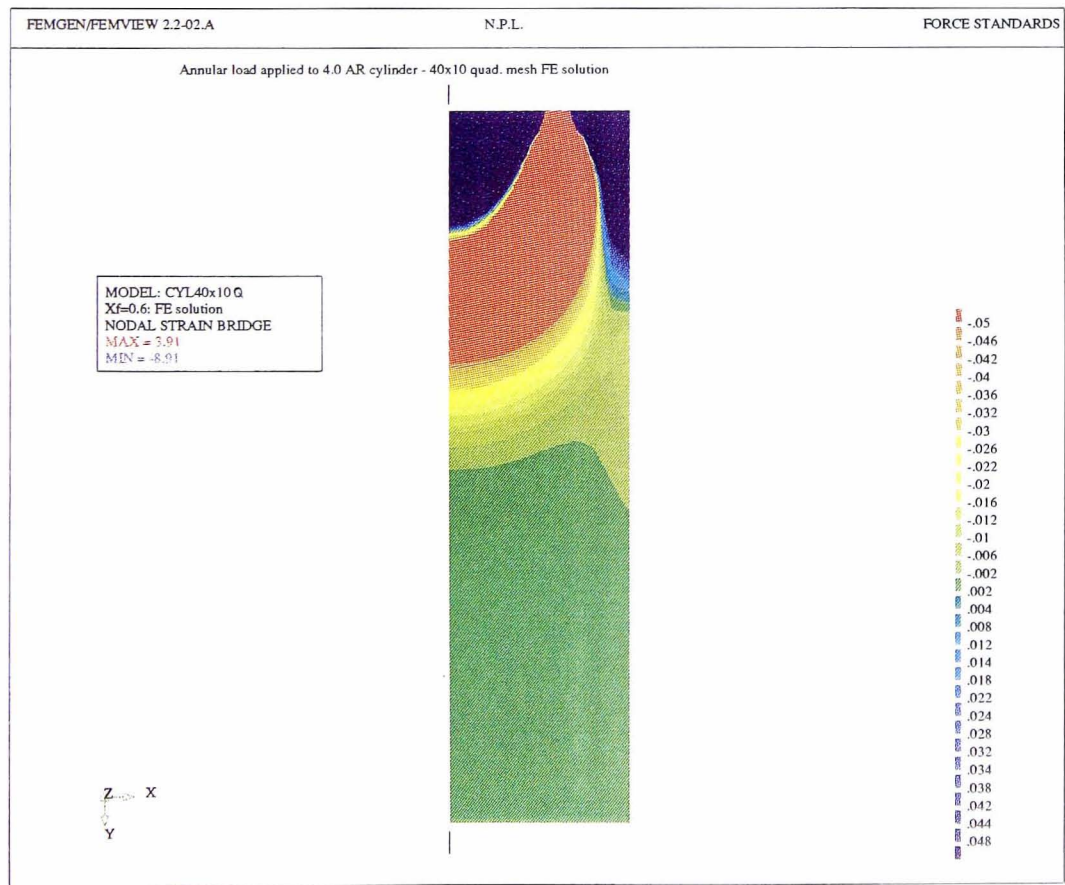


Figure 5.10: Contours of bridge strain due to equipollant annular load with Xf=0.6: 40x10 quad. mesh FE solution

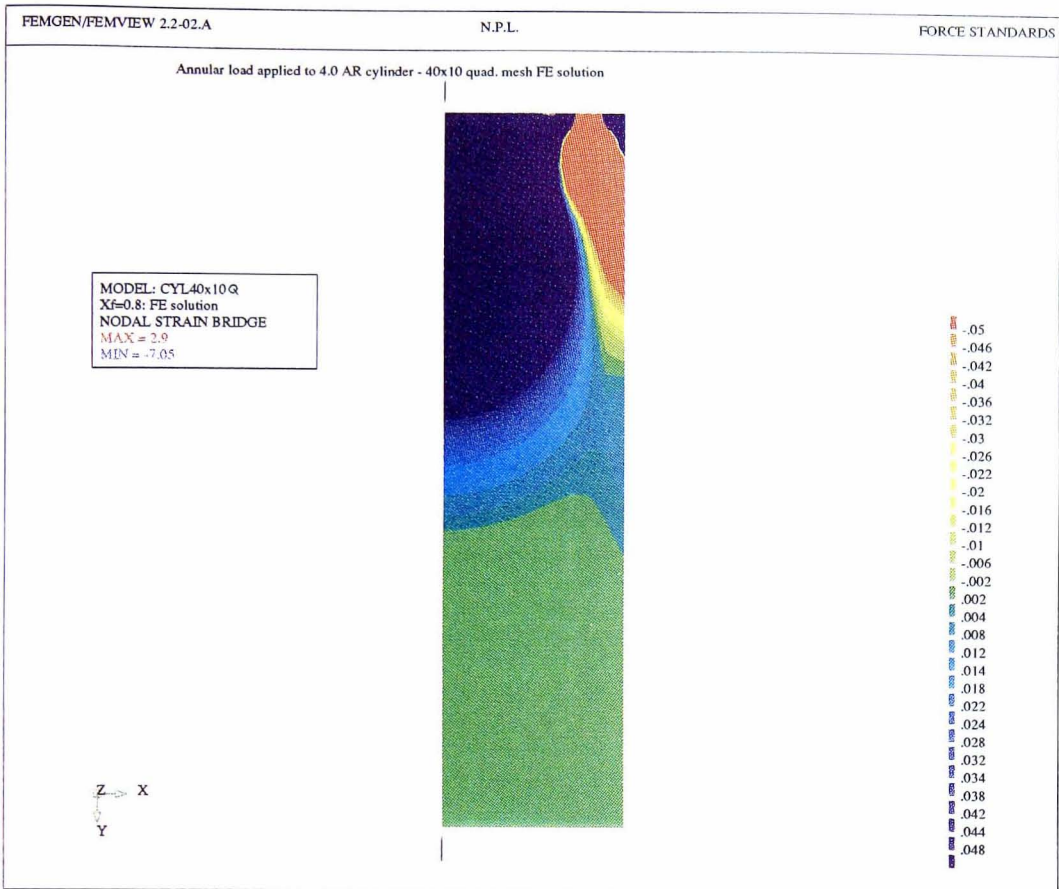


Figure 5.11: Contours of bridge strain due to equipollant annular load with Xf=0.8: 40x10 quad. mesh FE solution

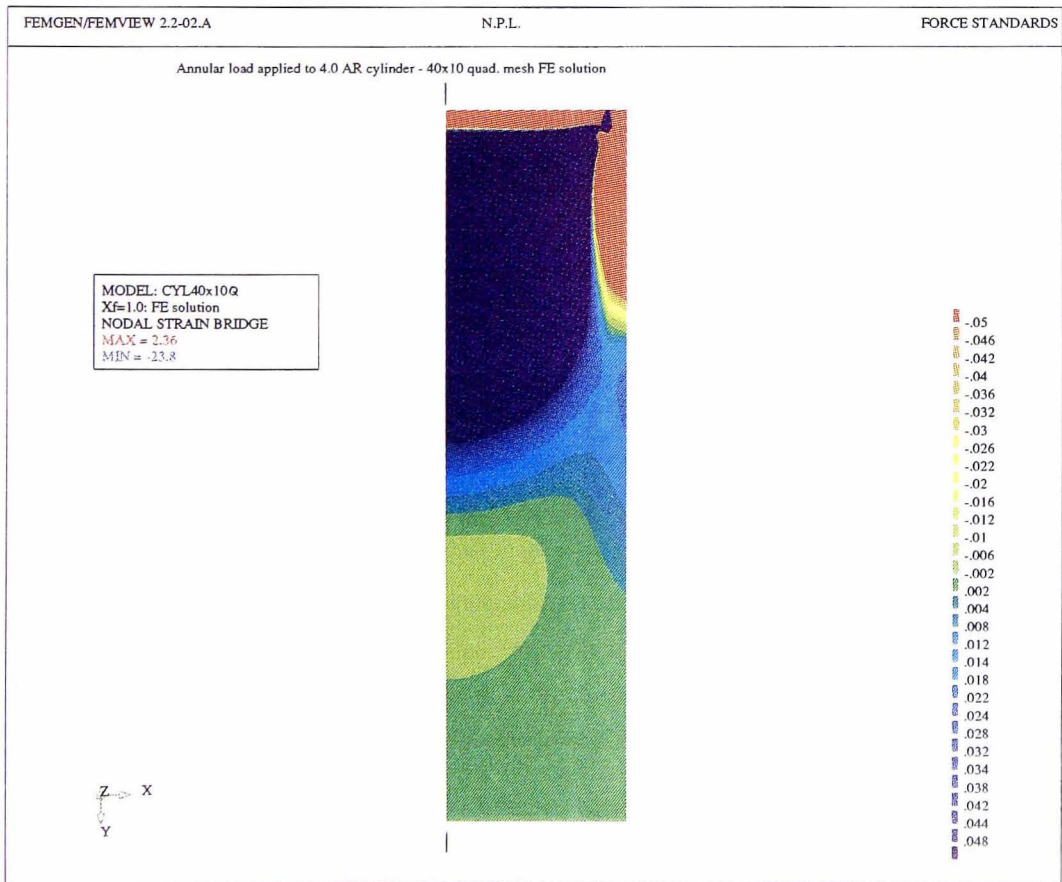


Figure 5.12: Contours of bridge strain due to equipollant annular load with Xf=1.0: 40x10 quad. mesh FE solution

MODELLING CONTACT

6.1 Introduction

In the last chapter it was shown that the program `axi.f` successfully analyses plain cylinders under annular loading in the absence of shear. However, in general load cells are subject to radial shear stresses at the contact interface. These contact stresses depend on the contact coefficient of friction and the relative stiffnesses of the load cell and the pads it contacts. For the finite element program to model these contact problems, the following additional functionality therefore was required:

Modelling of the stiffness of contact pads.

Modelling of the contact process between the pads and a load cell.

The program `axi.f` was modified in order to add the above capabilities.

6.2 Finite element analysis using infinite elements

Most contact pads have a large radius relative to that of the load cell and are therefore effectively infinite in the axial direction. It would be possible to model such pads with large but finite dimensions. However, in doing so, large meshes with many degrees of freedom and having large bandwidths would be created. The modelling of pads using such meshes would be computationally costly, the extra computation possibly exceeding the computation required in modelling the load cell itself. If only one analysis was to be undertaken the extra time taken would not be significant. However, it was realised that in order to develop an improved load cell design, a shape optimisation scheme would be required. As this would almost certainly be iterative in nature, the extra computation associated with modelling the pad would be significant. One possible method of reducing the bandwidth and total degrees of freedom would be to reduce the mesh density with distance from the contact surface. This is commonly achieved by making the node spacing a logarithmic function of distance from the region of interest. However a superior technique for modelling such problems, using so-called infinite elements, can be used. Infinite elements allow the modelling of areas that are effectively infinite without requiring excessive numbers of

degrees of freedom and with reasonable stiffness matrix bandwidths. A capability to model infinite elements was therefore to the axisymmetric finite element program.

6.2.1 Introduction to infinite elements

Infinite elements are finite elements whose shape functions are defined between finite values and infinity. Their use allows the finite element method to be used to model problems with domains that are effectively unbounded. A comprehensive review of the development and use of infinite elements in static problems is given by Bettess and Bettess [1984]. Two main approaches have been followed in the use of infinite elements. These two approaches are classified as either decay function or mapped elements.

6.2.1.1 Decay function infinite elements

Decay function elements use the usual shape functions multiplied by a factor which decays to zero at infinity. Anderson and Ungless [1977] and Bettess [1977] independently described the use of a $1/r$ factor (r being the global coordinate in the infinite direction), while elements using factors of the form $1/r^n$ have been described by Lynn and Hadid [1979]. Chow and Smith [1980] have also described the use of decay function elements with an exponential decay factor. For best results the decay function should match the rate of decay in the problem to be analysed. The decay function is therefore chosen to match the rate of decay, if known, of the far-field solution of the problem to be solved. It should be noted that, although not known as 'mapped' elements, these elements require a mapping between the finite local element co-ordinates and the infinite global coordinates of the problem.

6.2.1.2 Mapped infinite elements

Mapped infinite elements use two mappings. One is used to map the element geometry between the finite local and the infinite global coordinates while a second transforms the normal polynomial shape function from the local to the global co-ordinate system. Usually a mapping function is chosen which transforms the normal polynomial shape function in the finite domain to a polynomial in inverse powers of r . The order of this polynomial can be increased by increasing the order of the corresponding shape function.

Zienkiewicz et al [1983] have reported mapped finite elements in which the same mapping function is used for both mappings. These Zienkiewicz mapped infinite elements have the advantage that the Gauss integration points used to integrate the

mapped function are those used with the normal finite shape function from which it is mapped. This minimises the changes required in adding provision for Zienkiewicz mapped infinite elements to existing finite element programs. Modification is limited to the addition of a new shape function routine incorporating the mapping, together with a routine to evaluate the shape function's Jacobian matrix.

6.2.2 Two dimensional Zienkiewicz mapped infinite elements

The program `axi.f` was modified to add a capability of modelling infinite domains. Because of its relative ease of implementation, the Zienkiewicz mapped infinite element was selected for this.

Both Zienkiewicz et al [1983] and Bettess & Bettess [1984] present one dimensional infinite elements and outline the extension of the method to two dimensions. The application to two-dimensional elements will be presented here.

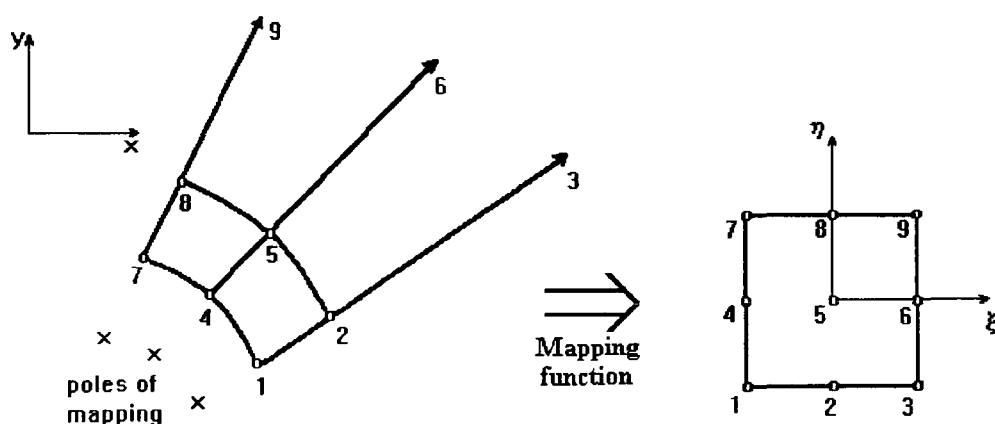


Figure 6.1: Mapping of infinite elements

The 2-D infinite element as reported by Zienkiewicz is shown in figure 6.1. It has six finite and three infinite nodes. The unknown function is represented as a normal quadratic shape function in terms of the local element coordinates ξ and η which are mapped to global coordinates x and y . The node positions used in the mapping are coincident with those associated with the quadratic function. The element is therefore iso-parametric.

The mapping is based on Lagrangian shape functions N_1, N_2, N_3 in the finite η direction and infinite mapping functions \tilde{N}_0 and \tilde{N}_2 in the infinite ξ direction.

The two dimensional mapping is given by:

$$\begin{aligned}
 x = & N_1(\eta) \left[(2x_1 - x_2) \tilde{N}_0(\xi) + x_2 \tilde{N}_2(\xi) \right] \\
 & + N_2(\eta) \left[(2x_4 - x_5) \tilde{N}_0(\xi) + x_5 \tilde{N}_2(\xi) \right] \\
 & + N_1(\eta) \left[(2x_7 - x_8) \tilde{N}_0(\xi) + x_8 \tilde{N}_2(\xi) \right]
 \end{aligned} \tag{6.1}$$

with a similar expression for y .

In the non infinite direction the mapping is similar to a normal shape function with Lagrangian shape functions given by

$$N_1(\eta) = \frac{\eta(\eta-1)}{2} \tag{6.2}$$

$$N_2(\eta) = 1 - \eta^2 \tag{6.3}$$

$$N_3(\eta) = \frac{\eta(\eta+1)}{2} \tag{6.4}$$

The mapping of co-ordinates in the infinite direction (along a line of constant η), can be written:

$$\alpha = \tilde{N}_0(\xi) \alpha_0 + \tilde{N}_2(\xi) \alpha_2 \tag{6.5}$$

where $\tilde{N}_0(\xi) = \frac{-\xi}{1-\xi}$ and $\tilde{N}_2(\xi) = 1 + \frac{\xi}{1-\xi}$. α_1 and α_2 are the coordinates of the finite nodes in the infinite direction and α_0 is defined such that α_1 lies mid-way between α_0 and α_2 .

The above mapping therefore satisfies the requirement that

$$\text{when } \xi = -1, \alpha = (\alpha_0 + \alpha_2)/2 = \alpha_1, \tag{6.6}$$

$$\text{when } \xi = 0, \alpha = \alpha_2, \quad 6.7$$

$$\text{and when } \xi = 1, \alpha = \frac{\xi}{(1-\xi)}(\alpha_2 - \alpha_o) + \alpha_2 = \infty. \quad 6.8$$

The mapping also satisfies $\tilde{N}_0(\xi) + \tilde{N}_2(\xi) = 1$, a necessary condition for the mapping to be independent of the origin of the coordinate system.

$$\text{Inverting the mapping gives } \xi = 1 - \frac{2(\alpha_1 - \alpha_o)}{\alpha - \alpha_o} \quad 6.9$$

The shape function on which the infinite element is based can be represented in the infinite direction as a polynomial:

$$P = a_0 + a_1\xi + a_2\xi^2 + \dots \quad 6.10$$

Substituting the inverse mapping to transform the polynomial into the α domain gives

$$P = b_0 + \frac{b_1}{r} + \frac{b_2}{r^2} + \dots \quad 6.11$$

a polynomial in inverse powers of r , where $r = \alpha - \alpha_o$. It can be seen that the expression has a pole at α_o . In theory the coordinates of the nodes should be arranged such that this pole coincides with any singularity associated with the problem. It has been shown however (see Appendix 1 of Zienkiewicz [1983]) that small differences between the positions of the pole and the problem singularity do not give rise to significant error. In the case of the problems under consideration here, the singularity is well defined, being at the point or plane of contact and there is therefore no difficulty in ensuring that the pole of the polynomial and the problem's singularity are coincident.

The boundary conditions at infinity can be imposed in one of two ways. If the displacements are known to decay to zero at infinity, the shape functions associated with these nodes can be eliminated. Alternatively, if the full shape function is retained, the displacements of the nodes at infinity can be restrained in the normal way.

6.2.3 Implementation of infinite elements

Whereas Zienkiewicz based the infinite element on a 9-node shape function, the infinite elements implemented in `axi.f` were based on 8-node quadratic shape functions. This was in order to retain compatibility with the Femview pre/post-processor which is unable to create, or display the results from, 9-node elements. The mapping function used in calculating the Jacobian matrix is, however, the same 9-node mapping function used by Zienkiewicz. This hybrid 8/9-node function is therefore not iso-parametric.

6.2.4 Test problems using infinite elements

6.2.4.1 Boussinesq's problem

As an example of the use of infinite elements, Zienkiewicz presents the results of an analysis of Boussinesq's problem of a point load applied to an elastic half-space. A unit load is applied at the origin to an elastic half-space, with unit Young's modulus and Poisson's ratio 0.1. Two sets of results are given, one using the truncated mesh of linear elements shown in figure 6.2 and the other the mesh of quadratic finite and infinite elements shown in figure 6.3. In order to verify the implementation of infinite elements in the program two similar analyses were carried out using `axi.f`.

The first used the truncated mesh of 16 elements of figure 6.2 with quadratic elements in place of the linear elements used by Zienkiewicz. The nodes at the mesh perimeter were restrained in the axial direction only.

The second analysis used the mesh of 12 quadratic and 4 infinite quadratic elements of figure 6.3. The mid-side nodes of the infinite elements were positioned such that the poles of the polynomial coincided with the singularity at the origin due to the applied point load. The shape functions associated with the nodes at infinity were restrained in the axial direction only.

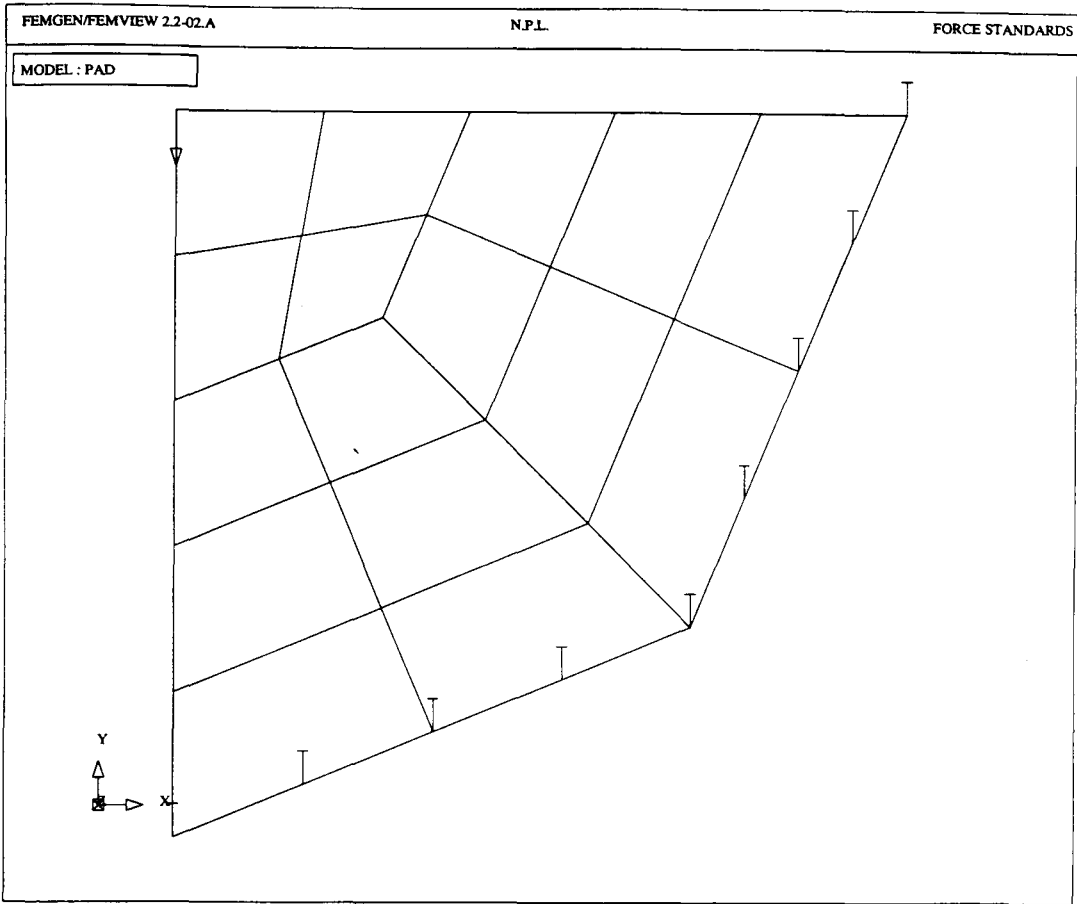


Figure 6.2: Mesh used to analyse Boussinesq's problem: 16 finite elements

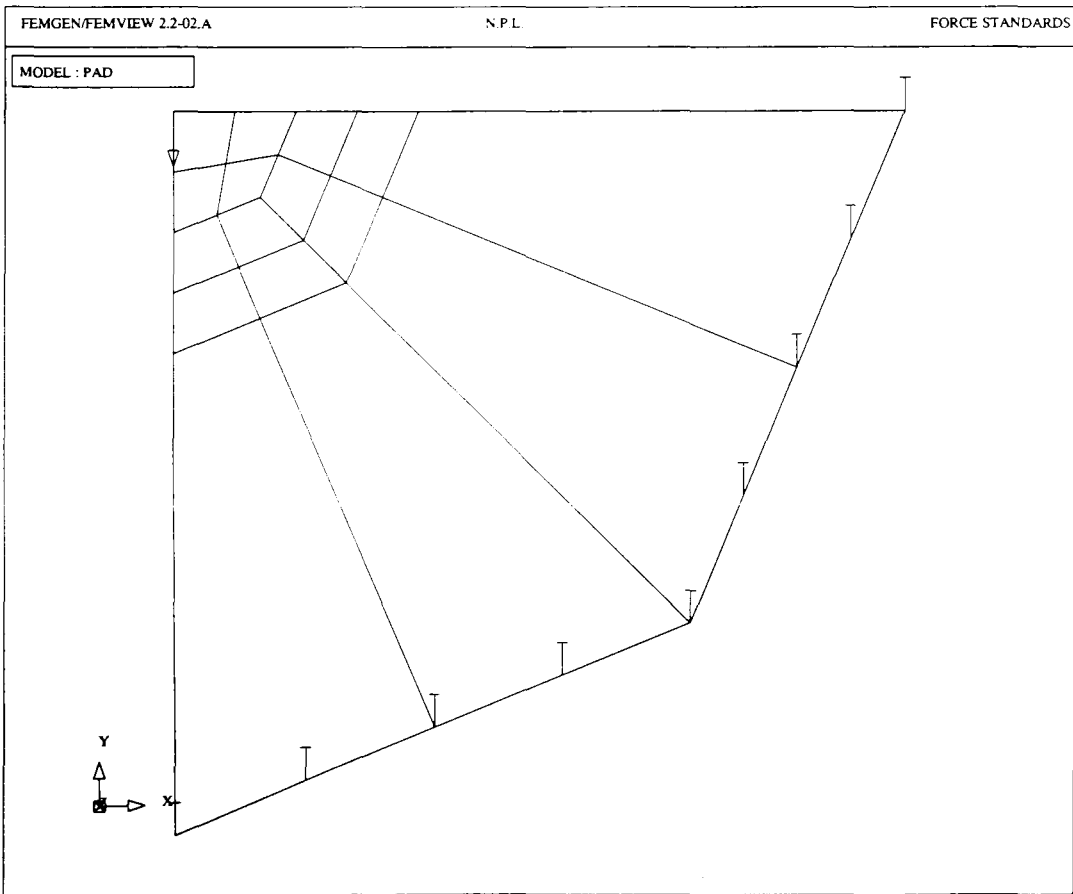


Figure 6.3: Mesh used to analyse Boussinesq's problem: 12 finite + 4 infinite elements

The results of the two analyses are presented in table 6.1 together with the results given by Zienkiewicz and Boussinesq's exact solution.

z	Exact solution (Boussinesq)	16 linear elements (Zienkiewicz)	16 quadratic elements (axi.f)	12 quad. & 4 inf. quad. (Zienkiewicz)	12 quad. & 4 inf. quad. (axi.f)
1.0	0.4902	0.3720	0.3698	0.5272	0.5292
2.0	0.2451	0.1337	0.1793	0.2468	0.2500
3.0	0.1634	0.0658	0.0593	0.1634	0.1642
4.0	0.1225	0.0243	0.0215	0.1225	0.1183
8.0	0.0613	-	-	0.0612	0.0678

Table 6.1: Comparison of analyses of Boussinesq's problem

From the results it can be seen that for the truncated meshes, the quadratic elements of *axi.f* give no noticeable improvement over the linear elements used by Zienkiewicz. In both cases, replacing the outer 4 elements by infinite elements results in a significant improvement in accuracy. Zienkiewicz's results with infinite elements can be seen to be in very good agreement with the exact solution. The agreement between the equivalent results from *axi.f* and the exact solution is slightly poorer. However, the differences between the results of *axi.f* and those obtained by Zienkiewicz are small and are probably due to the representation of the unknown function by 8-node quadrilaterals in place of the 9-node quadrilaterals used by Zienkiewicz.

6.2.4.2 Axisymmetric cylindrical punch on a foundation

- frictionless contact

To further test the implementation of infinite elements a comparison was made with a benchmark problem. Olukoko et al. [1993] proposed three 'benchmark' examples for the comparison of finite element contact routines. One of these examples, described as an axisymmetric punch on a foundation, is similar to a cylindrical load cell on a semi-infinite pad. The problem is defined as a 1 m radius cylinder, 2 m high loaded on a cylindrical foundation of height and radius 4 m. Both the cylinder and the foundation have a Young's modulus of 1 Nm^{-2} and a Poisson's ratio of 0.3. A uniform axial stress of 1 Nm^{-2} is applied to the top face of the smaller cylinder. The calculated contact stresses and displacements are presented for both frictionless contact and contact with a coefficient of friction of 0.2.

Results from two different analyses are presented in the paper. One analysis used the finite element method while the other is from a boundary element solution. The results from the two methods are shown to be in good agreement. The assumption is

therefore made that the results are correct and can be used as a benchmark. In this section, the frictionless benchmark results will be compared with an analysis using `axi.f`. Later in this chapter, after discussion of the implementation of a contact algorithm, the benchmark problem with friction will also be analysed.

An analysis was carried out using `axi.f` and two different mesh configurations. The 'graded' mesh was designed to be as similar as possible to that used by Olukoko. The uniform mesh uses infinite elements to model the foundation as semi-infinite. In both cases uniform pressure was applied to the free end of the cylinder and frictionless contact was imposed by coupling the axial freedoms of the pairs of nodes along the contact surface.

The graded mesh is illustrated in figure 6.4. Because of limitations of the method of specifying graded mesh densities in Femview, the graded mesh has a ratio between adjacent element sides in the radial direction of 1.166 rather than the 1.15 ratio used by Olukoko. In the axial direction, ratios of 1.091 for the cylinder and 1.189 for the foundation were used. Olukoko does not state the axial ratios used so these values were based on estimates from Olukoko's figure 2.

The uniform mesh model illustrated in figure 6.5 models the cylinder as twenty rows of ten 8-node quadrilateral elements. The foundation, modelled by Olukoko as a large cylinder, was modelled as a semi-infinite half-space using a combination of finite and infinite elements. As the dimensions of the foundation cylinder in Olukoko's analysis were large compared with those of the punch, its contact stiffnesses were assumed to be equivalent to those of an elastic half-space. The mesh comprised two layers of 'non-infinite' elements, extended to infinity using infinite elements. The nodes of the foundation at infinity were restrained in the axial direction.

Tables 6.2 and 6.3 show the results from `axi.f` for both meshes together with the finite element results of Olukoko. The results from the graded mesh and those from Olukoko's paper are interpolated from the nodal values.

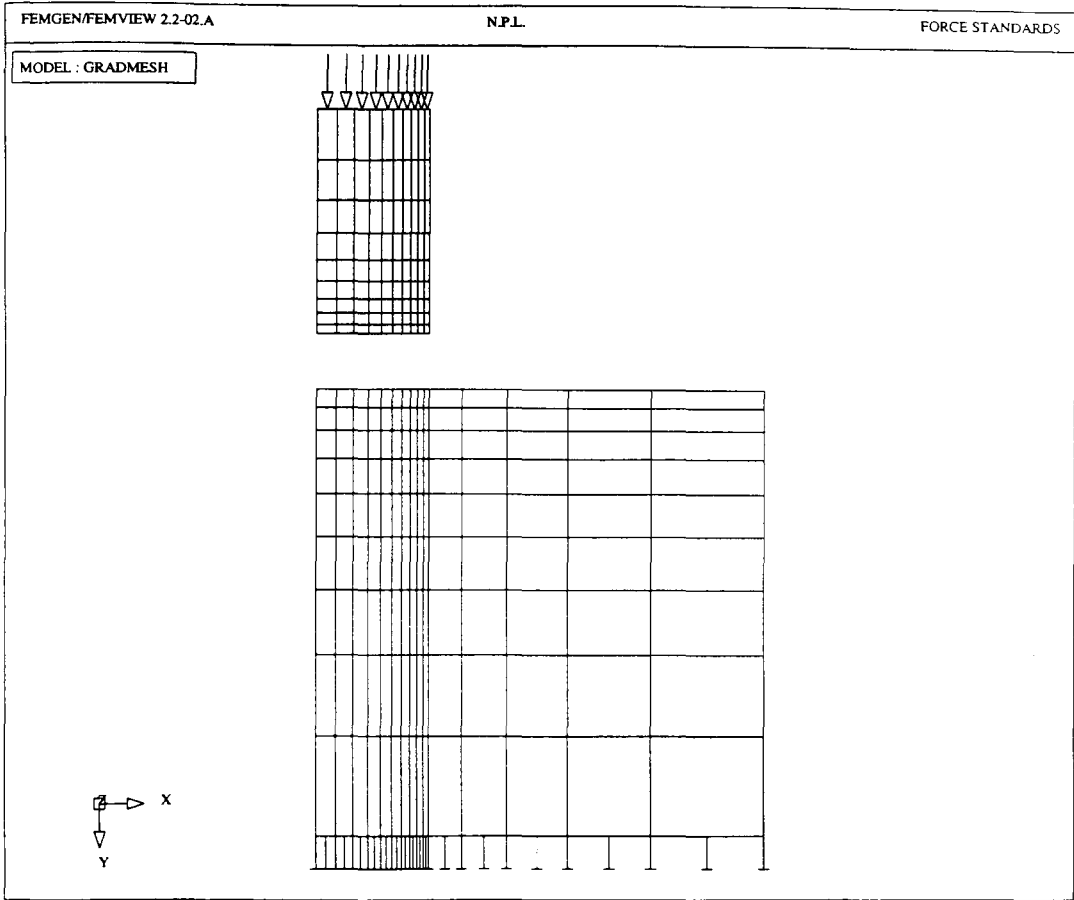


Figure 6.4: Graded mesh used for Olukoko benchmark tests

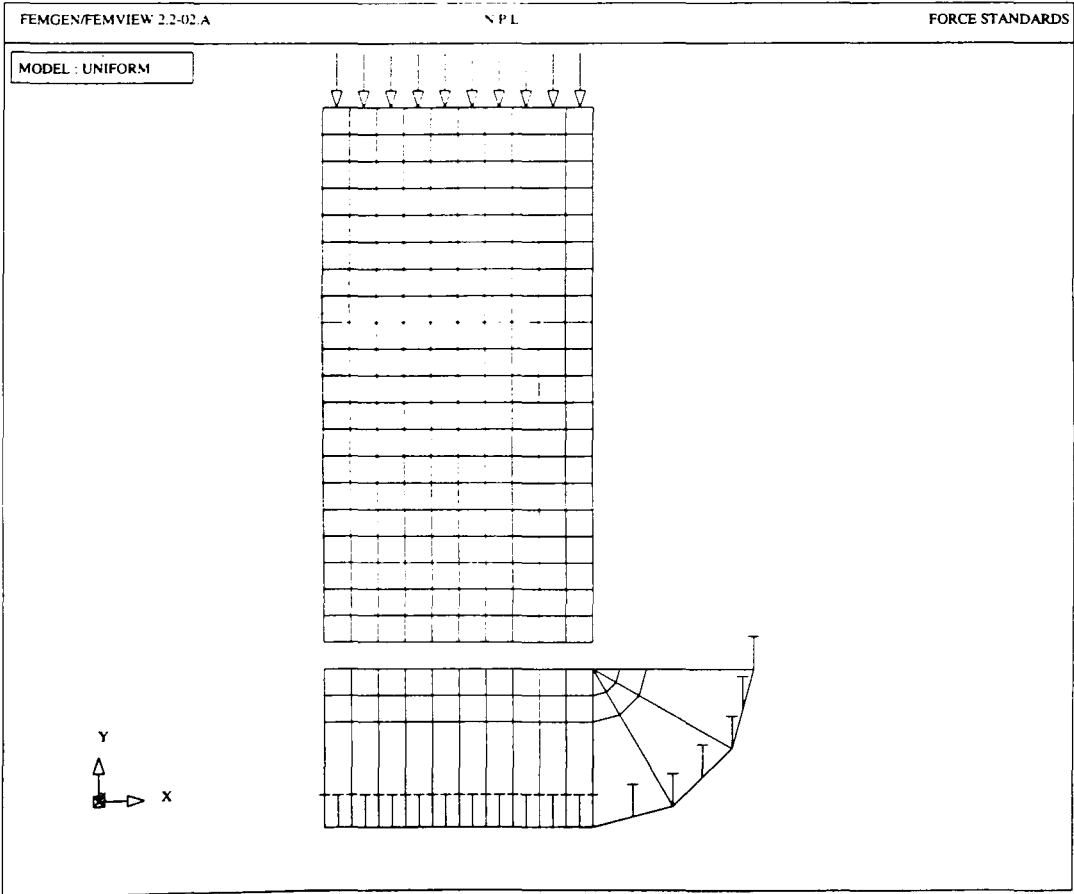


Figure 6.5: Uniform mesh used for Olukoko benchmark tests

radius	Axial stress			
	graded mesh	uniform mesh	Olukoko et al.	Khadem & O'Connor
0.0	0.785	0.793	0.790	0.8
0.1	0.788	0.787	0.788	0.8
0.2	0.792	0.794	0.794	0.8
0.3	0.801	0.803	0.801	0.8
0.4	0.814	0.817	0.814	0.8
0.5	0.833	0.834	0.833	0.8
0.6	0.860	0.857	0.863	0.825
0.7	0.902	0.885	0.905	0.85
0.8	0.967	0.960	0.974	0.925
0.9	1.124	0.929	1.131	1.2
1.0	2.560	2.140	2.954	1.7

Table 6.2: Axial stress for frictionless contact of cylinder on elastic foundation

radius	Radial slip		
	graded mesh	uniform mesh	Olukoko et al.
0.0	0.000	0.000	0.000
0.1	0.059	0.062	0.059
0.2	0.117	0.123	0.117
0.3	0.177	0.185	0.177
0.4	0.237	0.247	0.237
0.5	0.298	0.310	0.298
0.6	0.361	0.376	0.361
0.7	0.428	0.446	0.428
0.8	0.500	0.525	0.500
0.9	0.582	0.608	0.583
1.0	0.702	0.735	0.699

Table 6.3: Radial slip for frictionless contact of cylinder on elastic foundation

Also shown in table 6.2 are values of contact stress for frictionless contact between a finite cylinder and an elastic half-space taken from figure 1 of the paper by Khadem and O'Connor [1969]. Their approach was to derive expressions for displacement in both bodies from the axisymmetric equations of elasticity and the relevant boundary conditions. By approximating the contact stresses as Chebyshev polynomials and equating the axial displacements at the boundary, they were then able to obtain a set of simultaneous integral equations from which the contact stresses were calculated.

Apart from the axial stress values close to the periphery of the contact zone, there is very good agreement between the benchmark results and those obtained using the

graded mesh. As the true axial stress at unit radius is infinite, the lack of agreement at this point is not of great concern.

The *axi.f* results from the uniform mesh show reasonable agreement with the benchmark results for radii less than 0.7. The level of agreement gradually deteriorates as the radii approach 1.0. When comparing these results, the presence of the singularity at the periphery should again be borne in mind.

A further comparison can be made with the results of Ohte [1973] who solved the same problem as Olukoko et al. using a different mesh. The results for normal stress and radial slip do not differ significantly from those in tables 6.2 and 6.3. However, in addition the paper gives the axial displacements of the contact surface relative to the central point. Equivalent results are not given in the papers of Olukoko et al. or Khadem & O'Connor. The axial displacements taken from figure 7 of Ohte's paper together with the results of *axi.f* are given in table 6.4. Both the graded and uniform meshes give values of displacement which are in good agreement with those calculated by Ohte.

radius	Axial displacement		
	graded mesh	uniform mesh	Ohte
0.0	0.00	0.00	0.00
0.1	0.00	0.00	0.00
0.2	0.01	0.01	0.01
0.3	0.02	0.02	0.02
0.4	0.04	0.04	0.03
0.5	0.06	0.06	0.05
0.6	0.10	0.10	0.08
0.7	0.14	0.14	0.12
0.8	0.19	0.19	0.16
0.9	0.27	0.27	0.23
1.0	0.43	0.44	0.38

Table 6.4: Axial displacements for frictionless contact of cylinder on elastic foundation

The graded mesh therefore gives results which are very close to the benchmark values. The agreement between the contact stresses and displacements calculated from the uniform and the benchmark results is not quite as good. However, the aim of this study is the prediction of strain values. At 1 m above the contact surface, the graded mesh gave a value of 1.3129 for the surface bridge strains in the small cylinder while the uniform mesh gave a value of 1.3136. The small difference of less than 0.05% indicates that, although the two models predict different contact stress

values near the periphery of the contact area, the effect on strain values away from the immediate vicinity of the end is small.

Later in this chapter, further tests are reported using infinite elements in the analysis of contact problems with friction. The results from these later tests and the tests described above, lead the author to believe that the implementation of the infinite element routines was correct.

Although the above analysis was of two bodies in contact, the method of imposing frictionless contact by coupling axial freedoms is extremely limited. It can not be extended to cases involving contact friction or non-conformal contact surfaces. To model these types of problem a true contact algorithm was required.

6.3 Finite element analysis of contact problems

6.3.1 Introduction

Various methods have been developed for the solution of contact problems using the FE method. A comprehensive review of these is given by Pascoe et al. [1989]. FE algorithms for the solution of elastic contact problems usually have two solution stages. The first involves the calculation of the area over which contact takes place and the determination of the zones of frictional sticking and slipping within this area. In the second stage these contact conditions are imposed on the finite element model. In some algorithms these two stages may be combined. In general the contact conditions are a function of the applied loads, rendering the problems inherently non-linear. The problem is usually linearised either by applying the load incrementally, by using some form of iterative solution method or by a combination of the two.

The methods used to determine the area of contact, and the zones of stick and slip are generally similar for all the algorithms. Sticking contact is initially assumed to take place over the maximum possible contact area. Then, within either an iterative loop or an incremental loading procedure, the normal and tangential forces at the contact nodes are evaluated. It is assumed that negative normal force at a node indicates loss of contact, while a tangential force greater than the normal force multiplied by the friction coefficient indicates slippage. The equations governing contact at these nodes are modified to impose these conditions and the next increment or iteration is executed. The assumption that negative forces imply loss of contact is not always valid for high order elements, especially 3-D brick elements. In these cases the contact condition can be determined more accurately by evaluating either the loads at

the Gauss points or the uniform stresses equivalent to the nodal loads on each element.

There are several methods for imposing the contact conditions upon the FE solution. These include penalty, flexibility, Lagrange multiplier and transformation matrix methods. Pascoe [1989] should be referred to for a full description of these methods. Only the first two of these methods will be discussed here.

6.3.1.1 Penalty methods

Penalty methods are one of the most common ways of imposing contact conditions. These methods make use of special gap elements joining the meshes of the two bodies together over the area of potential contact. For 2-D problems the gap elements are line elements joining pairs of nodes. The stiffness of these elements in each direction is set to values which are either very small or very large relative to the stiffnesses of the rest of the mesh. The elements can therefore be made to appear as either a solid connection between the two nodes, a rigid axial connection allowing relative radial movement or a very flexible connection which effectively imposes no connection between the nodes. Gap elements can be incorporated into existing finite element systems without much modification to the main FE algorithm. For this reason this method is popular in commercial FE packages. A disadvantage of this approach is that the accuracy of the results is dependent on a good choice of values used for the 'rigid' and 'free' stiffnesses. In addition for each iteration, a full solution of the FE equations is required. This method may therefore be computationally costly.

6.3.1.2 Flexibility methods

In flexibility methods, a matrix of flexibility coefficients corresponding to each of the degrees of freedom of the contact nodes is calculated for each body. The equations of contact in terms of these coefficients together with the rigid body equilibrium equations are then solved to calculate the contact forces. The equations of contact may be modified and the solution repeated as part of an iterative method. The calculation of the flexibility matrices of both bodies takes a time comparable to a single iteration of a penalty method. However, once the flexibility matrices have been calculated there is little computational overhead for each subsequent iteration. The flexibility matrices are also independent of the contact conditions and therefore do not require to be recalculated in order to solve the contact problem with a different initial contact gap or friction coefficient. When large number of iterations are required or where more than one contact condition is to be applied between the same pair of bodies, this method is much quicker than the use of gap elements.

6.3.1.3 Choice of contact algorithm

The choice of algorithm for modelling contact in the program `axi.f` was made between the above two algorithms. Penalty methods using gap elements have been widely reported and are used in many commercial packages. They therefore had the advantage of being well understood and would allow the implementation in `axi.f` to be compared directly with results from a similar algorithm implemented in a commercial package such as PAFEC FE. However, the ultimate aim of the project was the development of an optimised load cell shape, and this would require a large number of iterations. Speed of solution was therefore a more important consideration. In the problems to be analysed in this project, contact between the same two bodies, would be modelled with varying contact conditions, i.e. different pad profiles and coefficients of friction. The flexibility method of solution promised to be significantly faster in analysing these problems than methods using gap elements. It was therefore decided to use a flexibility method. The method chosen was based on that described by Sachdeva and Ramakrishnan [1981].

6.3.2 The contact algorithm

6.3.2.1 Method of analysis

Francavilla and Zienkiewicz [1975] described a relatively simple technique for modelling contact between two elastic bodies in the absence of friction. Sachdeva and Ramakrishnan [1981] reported a modification to the algorithm to handle situations involving friction. The method adopted here is an adapted from their technique. The method reported in Sachdeva and Ramakrishnan's paper restrains one body while applying body forces to the other. In the method described here both bodies are axially restrained and the sum of the contact forces equated to the applied body forces. It was assumed that the contact surface can be considered to be normal to the axis of symmetry without significant error. In the case of the EN10002-3 pads the slopes are $\tan^{-1}1:1000$. This assumption is therefore valid.

Each body is restrained in the axial direction (figure 6.6). Usually the restrained nodes will be at infinity or on an axis of mirror symmetry. The restrained nodes are prevented from axial displacement relative to other restrained nodes on the same body. Axial displacement of one body's restrained nodes relative to those of the other body, Δ , is however allowed.

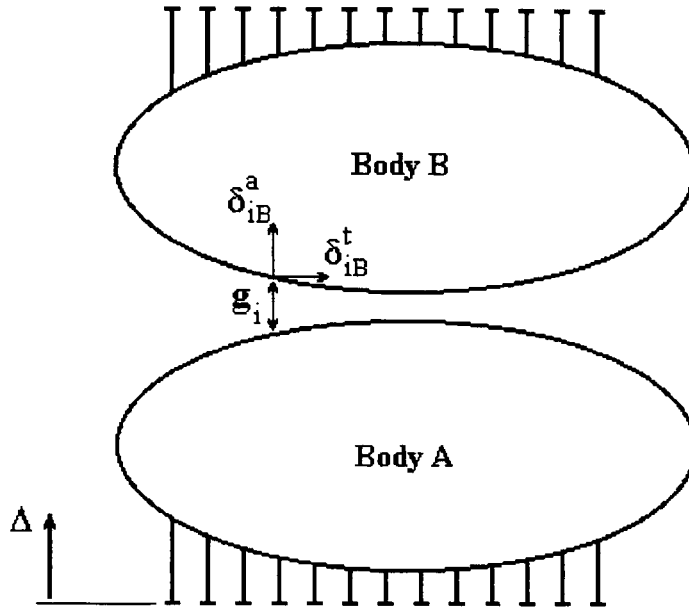


Figure 6.6: Contact between two bodies

An initial gap profile is specified in terms of the gaps at each pair of nodes, g_i . For each load increment, compatibility between the axial and tangential displacements, δ^a and δ^t , of the pairs of nodes in contact is represented by the set of compatibility equations:

$$\delta_{iB}^a - \delta_{iA}^a = \Delta - g_i \text{ in the axial direction} \quad 6.12$$

and if no slip takes place

$$\delta_{iA}^t - d_{iA}^t = \delta_{iB}^t - d_{iB}^t \text{ in the tangential direction} \quad 6.13$$

where d_{iA}^t and d_{iB}^t are the displacements of the nodes before application of the load increment.

The relation between the displacements and the force components, p^a and p^t at the contact nodes is given by:

$$\delta_{iA}^a = \sum_{j=1}^n C_{ij}^A p_j \text{ and } \delta_{iB}^a = -\sum_{j=1}^n C_{ij}^B p_j \quad 6.14$$

where C_{ij}^A and C_{ij}^B are the elements of the matrices obtained when the full flexibility matrices of the two bodies are reduced so as to include only those elements corresponding to the n contact degrees of freedom (see section 6.3.2.2). The compatibility equations can therefore be re-written:

$$\Delta + \sum_{j=1}^n (C_{ij}^A + C_{ij}^B) p_j^a = g_i \text{ in the axial direction} \quad 6.15$$

and at node pairs where no slip takes place

$$\sum_{j=1}^n (C_{ij}^A + C_{ij}^B) p_j^t = \Phi_i \text{ in the tangential direction} \quad 6.16$$

where $\Phi_i = d_{iA}^t - d_{iB}^t$ is the relative slip between the contact node pair prior to application of the current increment.

If slip does take place at a pair of nodes Coulomb's law of friction is assumed to apply and the latter equations are replaced by the equations relating the force components, p^a and p^t at the node pair:

$$p_i^t = \mu p_i^a \quad 6.17$$

If a pair of nodes loses contact, the axial and tangential forces are set to zero by replacing the displacement compatibility equations by:

$$p_i^a = 0 \text{ and } p_i^t = 0 \quad 6.18$$

One final equation equates the contact forces to the axial force applied to the bodies and makes the number of equations equal to the number of unknowns and therefore determinate:

$$\sum_{i=1}^n p_i^a = F \quad 6.19$$

Following solution of the equations the value of the relative slip at the slipping nodes Φ_i can be calculated from equation 6.16.

The algorithm based on the above method is therefore:

1. The stiffness matrices for both bodies are calculated as normal.
2. The full stiffness matrices are reduced to include only the degrees of freedom associated with the contact nodes.
3. The reduced matrices are inverted to transform them into flexibility matrices.
4. Initially all nodes are assumed to be in contact and sticking. The relative slip at each node pair is set to zero
5. The applied load is set to the first increment.
6. The simultaneous equations are solved for the contact forces.
7. If any of the axial forces are negative, contact is assumed to be broken at the node pair. The displacement compatibility equations at this node pair are therefore replaced by the equations setting all forces at these nodes to zero.
8. If the ratio between the tangential and axial loads at a node pair is greater than the coefficient of friction, the nodes are assumed to slip. The tangential displacement compatibility equation at the node pair is replaced by the equation imposing Coulomb friction at this node. The relative displacement due to slip at each slipping node pair is updated.
9. Steps 5-7 are repeated until all axial forces are positive and the ratio of tangential to axial forces is less than the coefficient of friction at all nodes in contact.
10. If the applied load is less than the final load, its value is incremented and steps 6-9 repeated.

6.3.2.2 Reduction of the stiffness matrix

Step 2 above requires that the full stiffness matrix is reduced to a form which includes only the degrees of freedom associated with the nodes in the contact region.

Figures 6.7 to 6.9 show the reduction process. Multiples of the rows and columns are subtracted in order to set all elements along a front to zero. The front starts at the first degree of freedom as shown in figure 6.7.

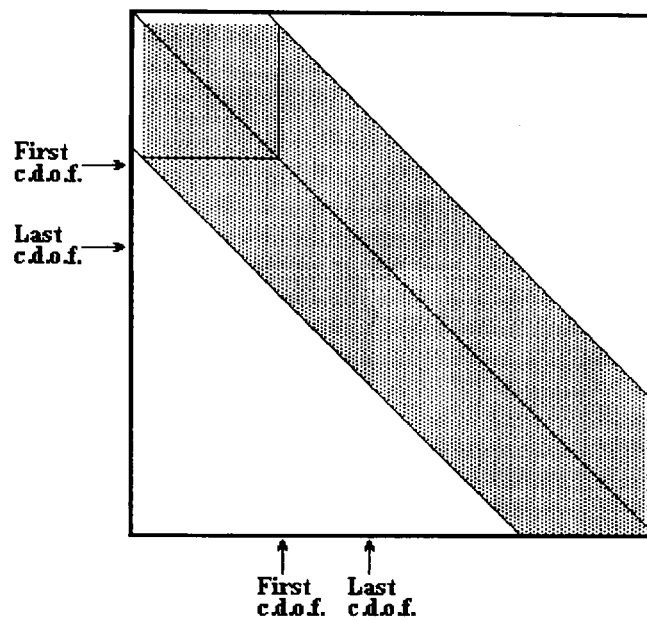


Figure 6.7: Matrix reduction: start of first elimination pass

The front is moved down the diagonal, leaving behind a region of zero elements. The front stops when all elements below the first contact degree of freedom (c.d.o.f.) have been set to zero as shown in figure 6.8.

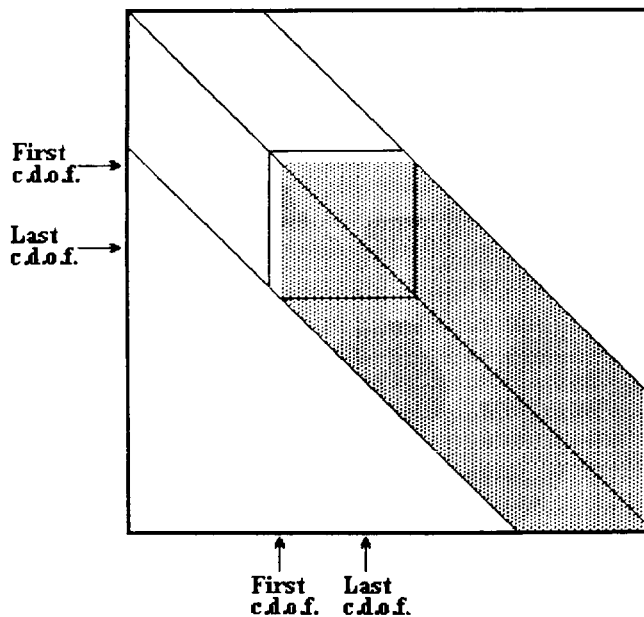


Figure 6.8: Matrix reduction: end of first elimination pass

The algorithm can be written in psuedo-code as:

Do $k = 1, first_contact_dof - 1$

Do $j = k + 1, total_dof$

Do $i = j, total_dof$

$$K_{ij} = K_{ij} - \frac{K_{kj} \times K_{ki}}{K_{kk}}$$

Continue

Continue

Continue

Note that the above sets the elements K_{ij} of the stiffness matrix to zero if either $i = k$ or $j = k$, thereby zeroing the elements along the front.

Once the high order elements have been eliminated a similar process can be used to eliminate the elements in the range $last_contact_dof$ to $total_dof$ to zero as illustrated in figure 6.9. The result is a stiffness matrix relating only forces and displacements at the contact nodes.

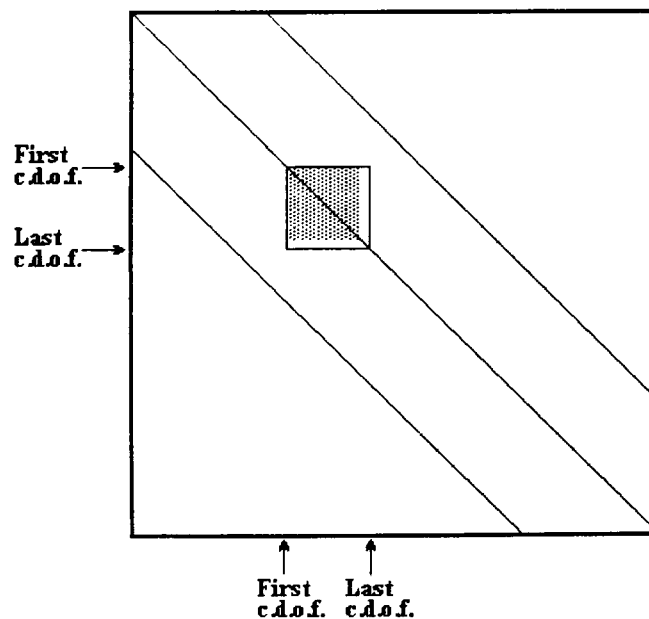


Figure 6.9: Matrix reduction: end of second elimination pass

6.3.3 Tests on contact algorithm

6.3.3.1 Axisymmetric cylindrical punch on a foundation - contact with friction

In order to verify the contact algorithm, the axisymmetric problem suggested as a benchmark by Olukoko and described in section 6.2.4.2 was again analysed. The same pair of meshes were used, however, this time the contact conditions were imposed using the contact routine. It should be noted that the contact routine imposes uniform axial displacement at the loaded end rather than uniform pressure. This change should have a negligible effect on the contact forces. In each case as contact is flat to flat, only one load iteration was used.

The first analysis was with a zero coefficient of friction. This was therefore similar to the frictionless analysis carried out earlier. The results of the analysis using the contact algorithm were virtually identical to those obtained from the earlier analysis, indicating that the contact algorithm works correctly in the absence of friction.

The second analysis was with a coefficient of friction of 0.2. The results from both meshes are given, together with the results of Olukoko et al. in tables 6.5 and 6.6.

radius	Axial stress			Shear stress		
	graded mesh	uniform mesh	Olukoko et al	graded mesh	uniform mesh	Olukoko et al
0.0	0.744	0.738	0.747	0.004	-0.001	0.000
0.1	0.748	0.739	0.747	0.026	0.026	0.026
0.2	0.752	0.746	0.750	0.049	0.055	0.047
0.3	0.758	0.755	0.757	0.103	0.090	0.077
0.4	0.775	0.771	0.770	0.127	0.141	0.128
0.5	0.786	0.785	0.788	0.156	0.155	0.157
0.6	0.814	0.810	0.814	0.162	0.160	0.163
0.7	0.857	0.837	0.858	0.171	0.169	0.172
0.8	0.929	0.944	0.934	0.185	0.174	0.187
0.9	1.133	0.867	1.105	0.211	0.158	0.221
1.0	3.28	2.55	4.383	0.710	0.574	0.877

Table 6.5: Contact stresses for cylinder on elastic foundation, $\mu = 0.2$

radius	Radial slip		
	graded mesh	uniform mesh	Olukoko et al.
0.0	0.000	-0.001	0.000
0.1	0.000	0.000	0.000
0.2	0.000	0.000	0.000
0.3	0.000	0.000	0.000
0.4	0.000	0.001	0.009
0.5	0.013	0.020	0.014
0.6	0.040	0.050	0.041
0.7	0.076	0.089	0.076
0.8	0.120	0.141	0.121
0.9	0.179	0.199	0.180
1.0	0.308	0.327	0.305

Table 6.6 Radial slip for contact of cylinder on elastic foundation, $\mu = 0.2$

There is good agreement between the results from the contact algorithm and the benchmark results. In particular the graded mesh results are very close to those of Olukoko et al. As was the case in the absence of friction, the uniform mesh results showed slightly poorer agreement. However, comparison of bridge strains away from the immediate vicinity of the contact surface showed good agreement between the results of the two meshes. For example, 1 m from the contact surface, the surface bridge strain in the smaller cylinder was calculated for the graded mesh to be 1.2779. The value calculated for the uniform mesh was 1.2783 a difference of less than 0.03%. As it is these bridge strain values which are of interest in this study, this level of agreement was encouraging.

6.3.4 Conclusions from benchmark tests

The analyses of the Olukoko benchmark problem, both with and without friction, indicated that the contact algorithm had been correctly implemented. Although the graded mesh gave results in better agreement with the benchmark, the results demonstrated that the combination of a uniformly spaced mesh and a contact pad modelled using infinite elements could be used to calculate the bridge strains with acceptable accuracy. It was assumed that this conclusion could be applied to the problem of more general shapes in contact with half-spaces.

This is important in the context of this study because:

A uniformly spaced mesh would be much easier to generate automatically than a mesh graded according to the expected distribution of stress at the interface.

Modelling the contact pads using a combination of finite and infinite elements results in many fewer degrees of freedom and a smaller bandwidth than the graded mesh equivalent. The solution would therefore be much quicker.

6.4 Comparison between finite element model and experimental results

The above 'benchmark' tests have given a comparison between the contact algorithm of `axi.f` and results obtained from other algorithms. An alternative evaluation of the algorithm was available by comparison with the experimental results described in Chapter 4. The results of contact analyses using `axi.f` will be presented and compared with these experimental results in the following sections.

6.4.1 1.0 r_0 pads

Contact between the strain gauged cylinder and the 1.0 r_0 pads was analysed using the program `axi.f`. The 4.0 aspect ratio cylinder was modelled with a mesh of 10 (radial) by 40 (axial) 8-node quadrilateral elements. The pad was meshed with two rows of ten quadrilateral elements extended axially to infinity by ten infinite elements. A contact coefficient of friction of 0.3 was used in the calculations.

The results for the 1.0 r_0 pads are presented in figures 6.10 to 6.12. Comparison of these figures with figures 4.5, 4.7 and 4.9 show the finite element results to be in excellent agreement with the earlier experimental results.

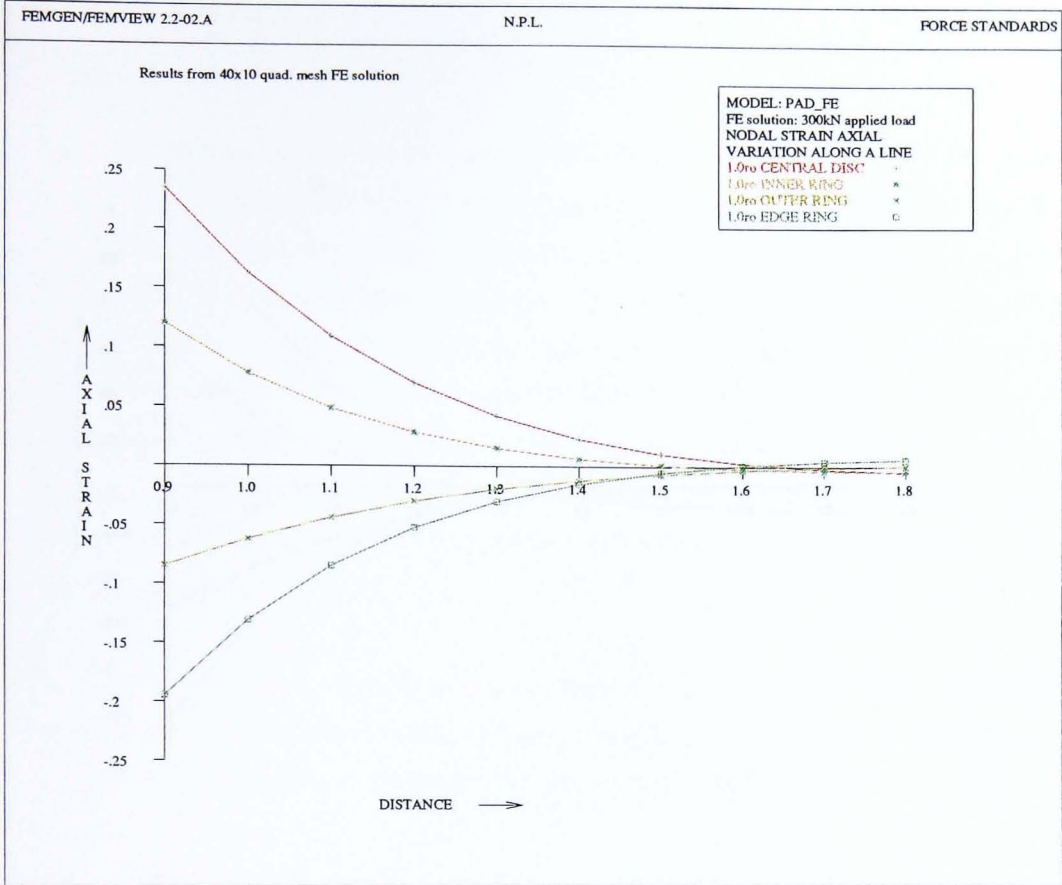


Figure 6.10: Surface axial strain v distance from loaded end: FE contact analysis: 1.0ro pads

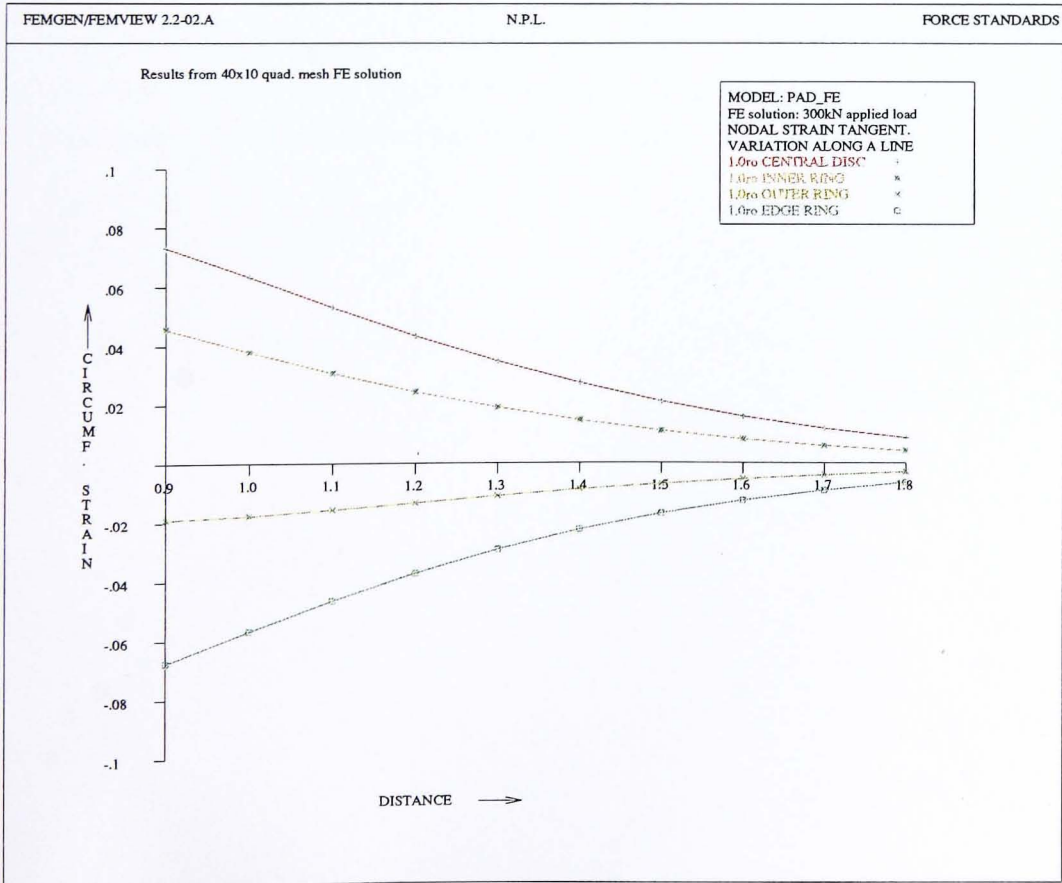


Figure 6.11: Surface circumferential strain v distance from loaded end: FE contact analysis: 1.0ro pads

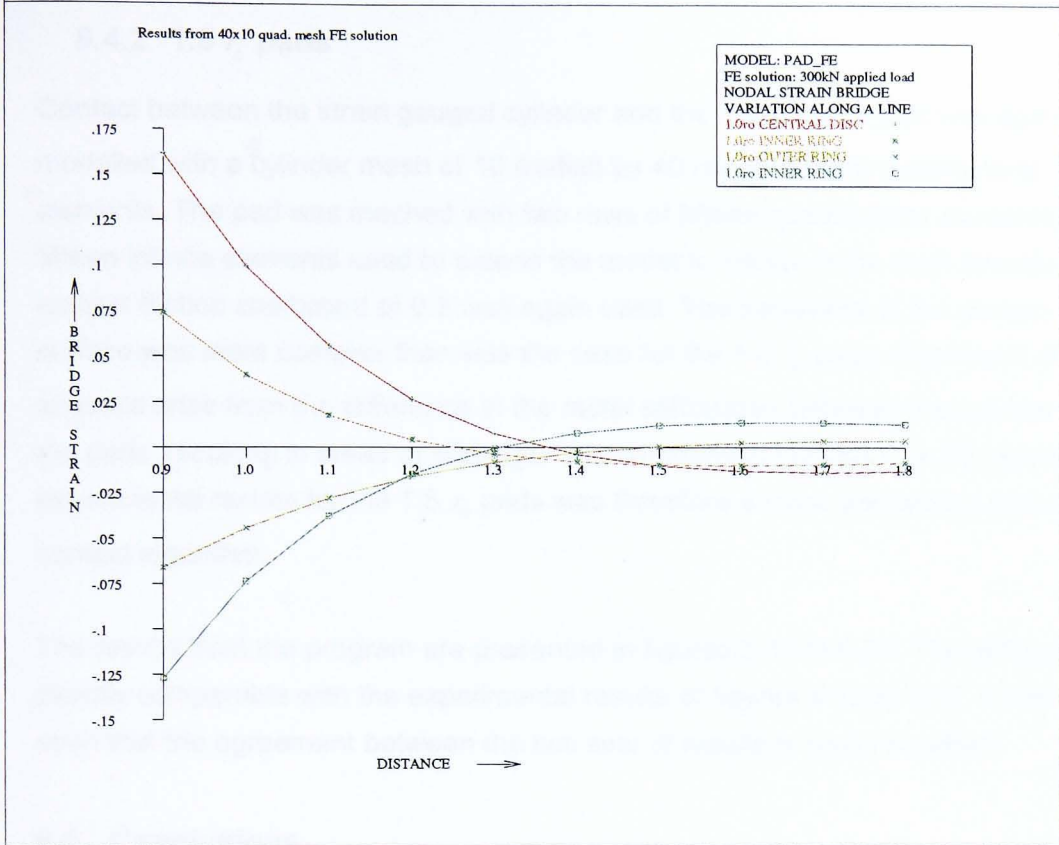


Figure 6.12: Surface bridge strain v distance from loaded end: FE contact analysis: 1.0ro pads

6.4.2 1.5 r_0 pads

Contact between the strain gauged cylinder and the 1.5 r_0 plane pad was again modelled with a cylinder mesh of 10 (radial) by 40 (axial) 8-node quadrilateral elements. The pad was meshed with two rows of fifteen quadrilateral elements with fifteen infinite elements used to extend the model to infinity in the axial direction. A contact friction coefficient of 0.3 was again used. The behaviour at the contact surface was more complex than was the case for the 1.0 r_0 pads. Significant shear stresses arise from the difference in the radial stiffnesses between the cylinder and the pads, resulting in areas of slippage. The comparison between the FE results and experimental results for the 1.5 r_0 pads was therefore a more demanding test of the contact algorithm.

The results from the program are presented in figures 6.13 to 6.20. These figures are directly comparable with the experimental results of figures 4.10 to 4.17. It can be seen that the agreement between the two sets of results is again excellent.

6.5 Conclusions

In this chapter the development and implementation of routines to model infinite elements and contact between two bodies have been described. The addition of these two capabilities allow the efficient modelling of contact between load cells and pads which are effectively semi-infinite. The infinite element and contact routines have been verified against 'benchmark' problems. More significantly, analyses using both infinite elements and the contact routines have been shown to be in excellent agreement with the experimental results of chapter 4.

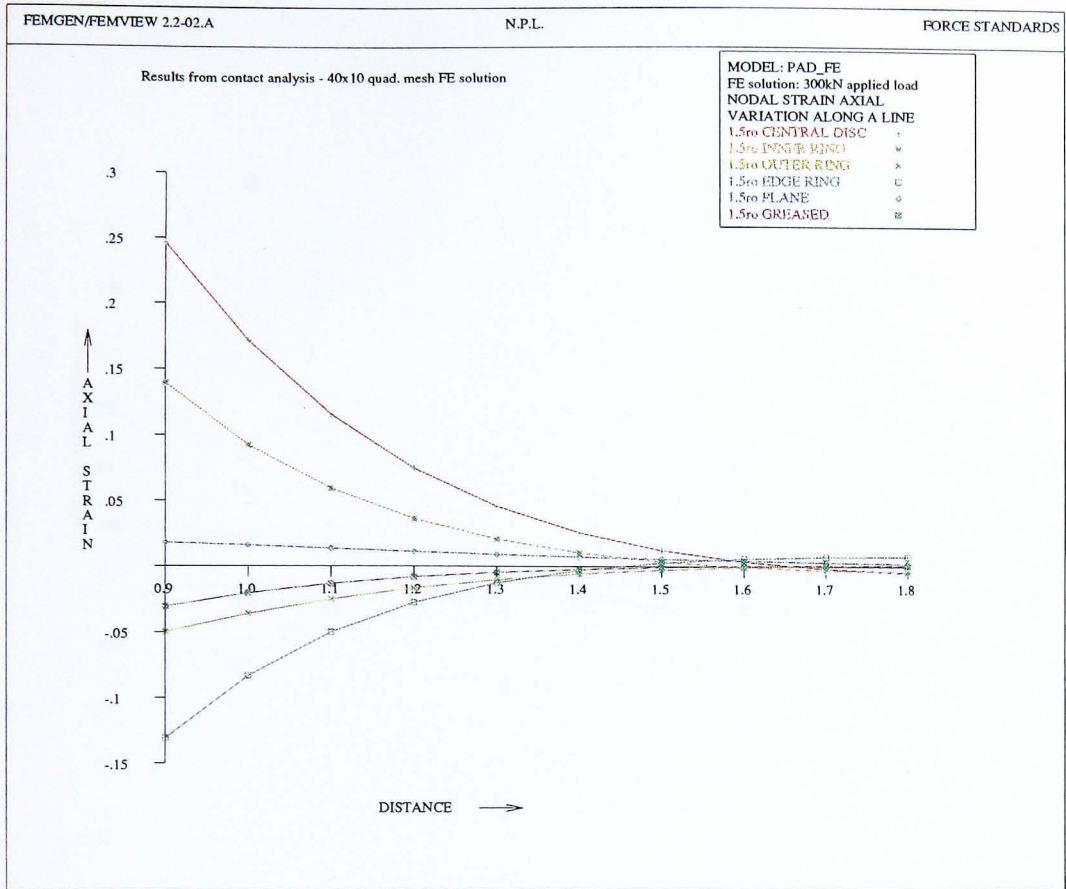


Figure 6.13: Surface axial strain v distance from loaded end: FE contact analysis: 1.5ro pads

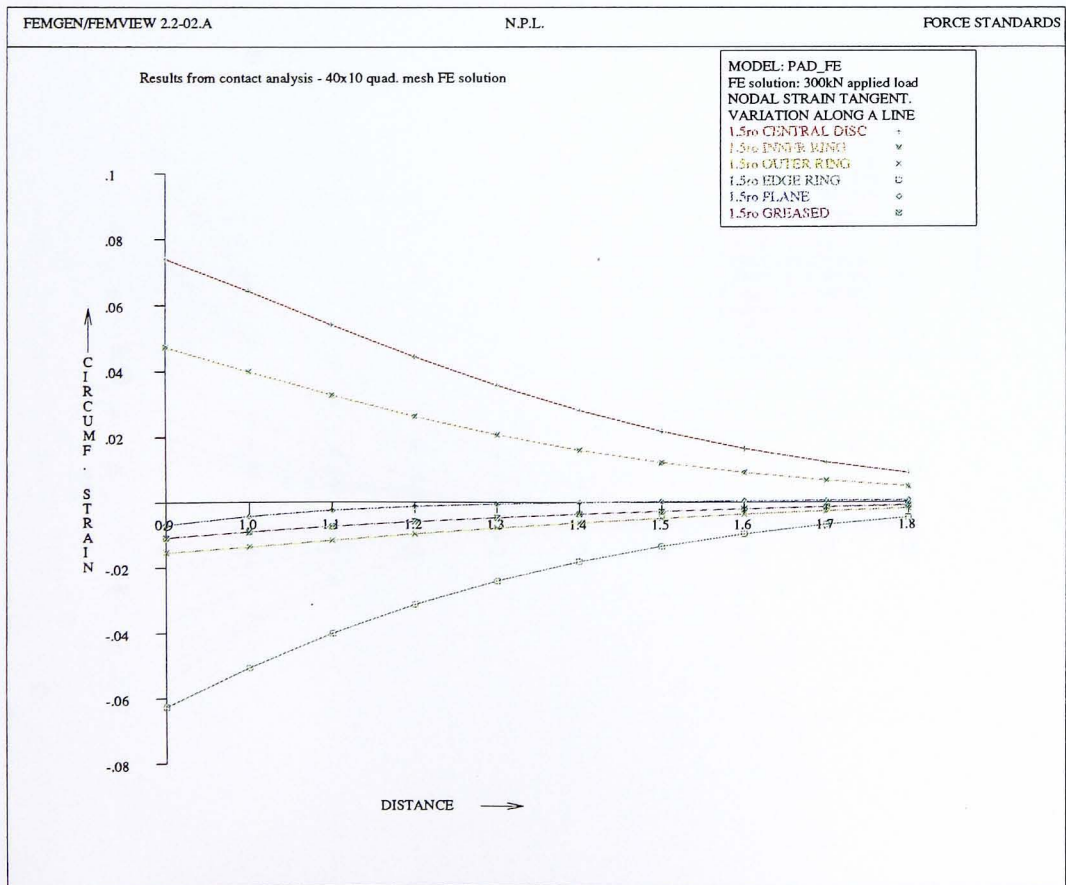


Figure 6.14: Surface circumferential strain v distance from loaded end: FE contact analysis: 1.5ro pads

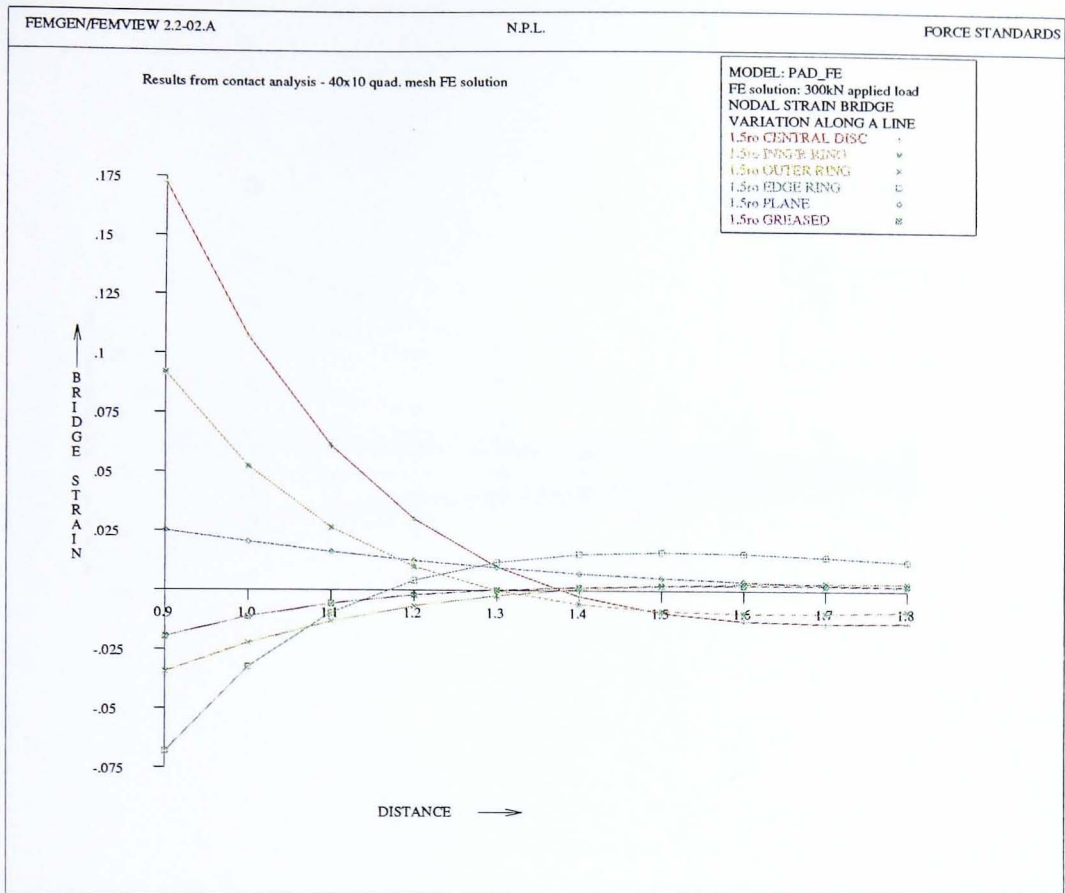


Figure 6.15: Surface bridge strain v distance from loaded end: FE contact analysis: 1.5ro pads

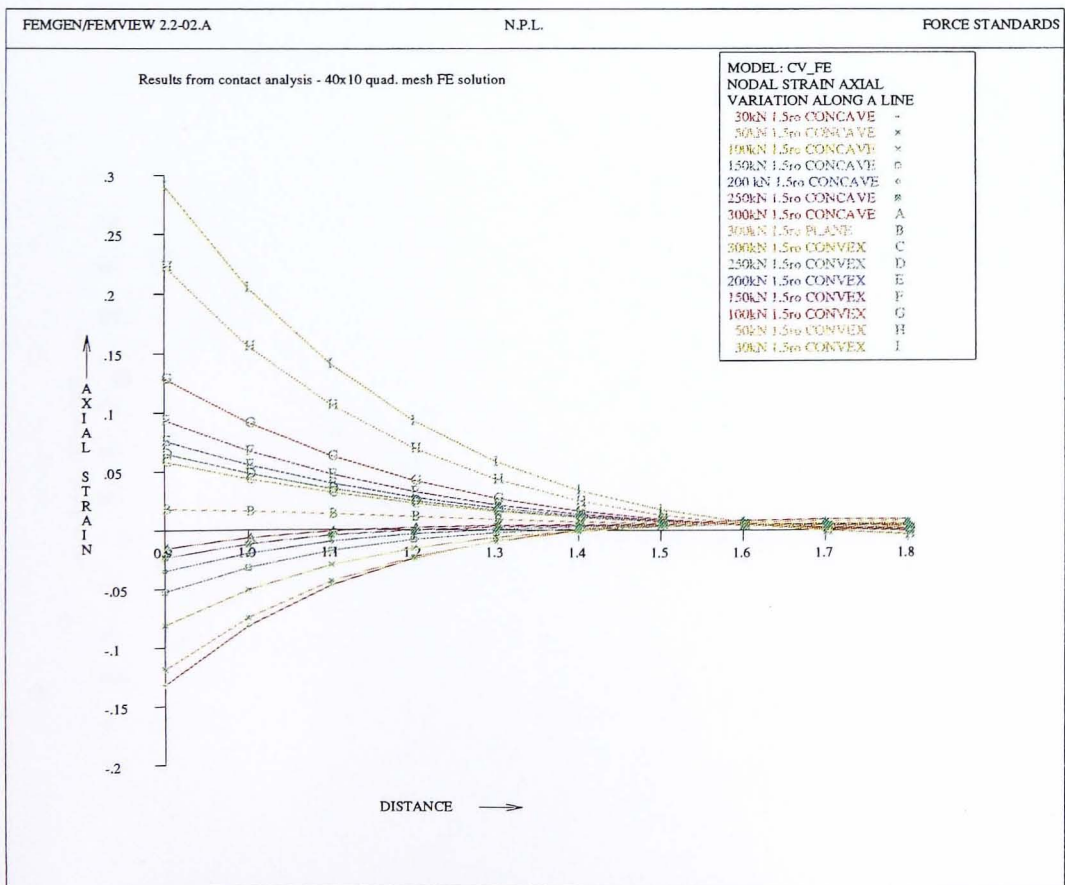


Figure 6.16: Surface axial strain v distance from loaded end: FE contact analysis: concave/convex pads

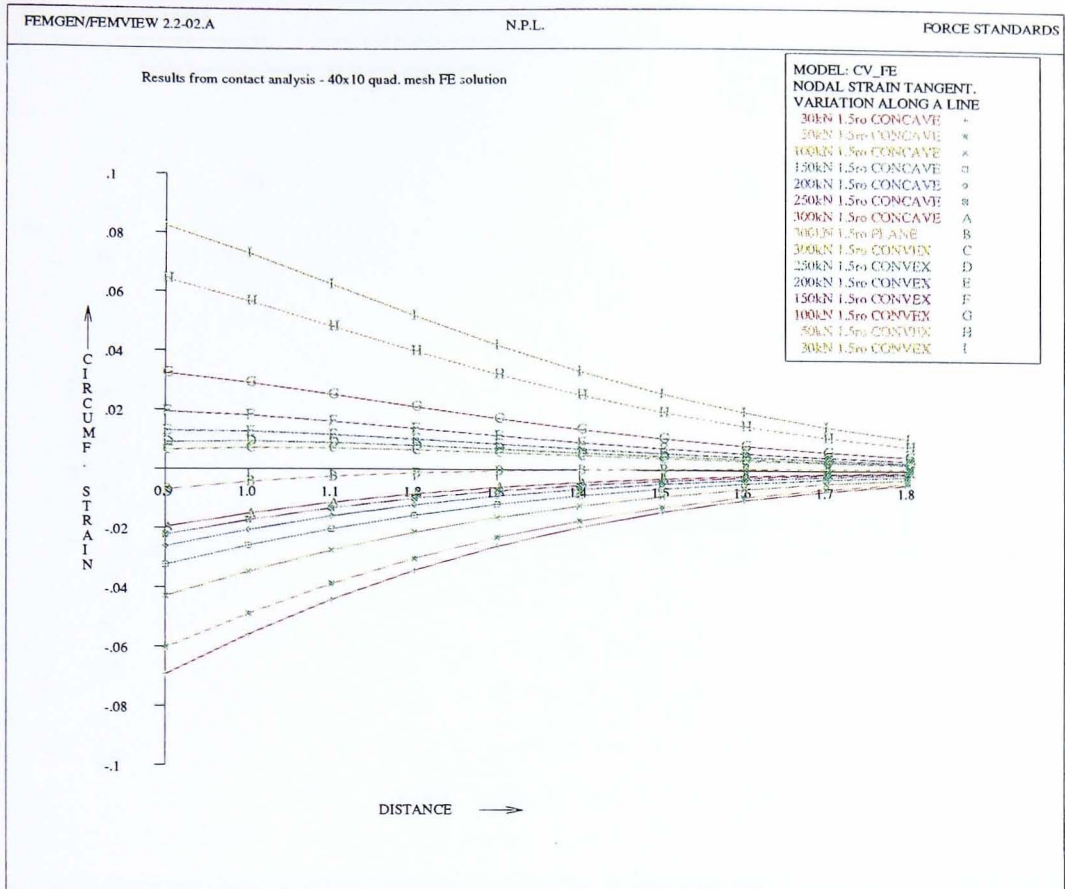


Figure 6.17: Surface circumferential strain v distance from loaded end: FE contact analysis: concave/convex pads

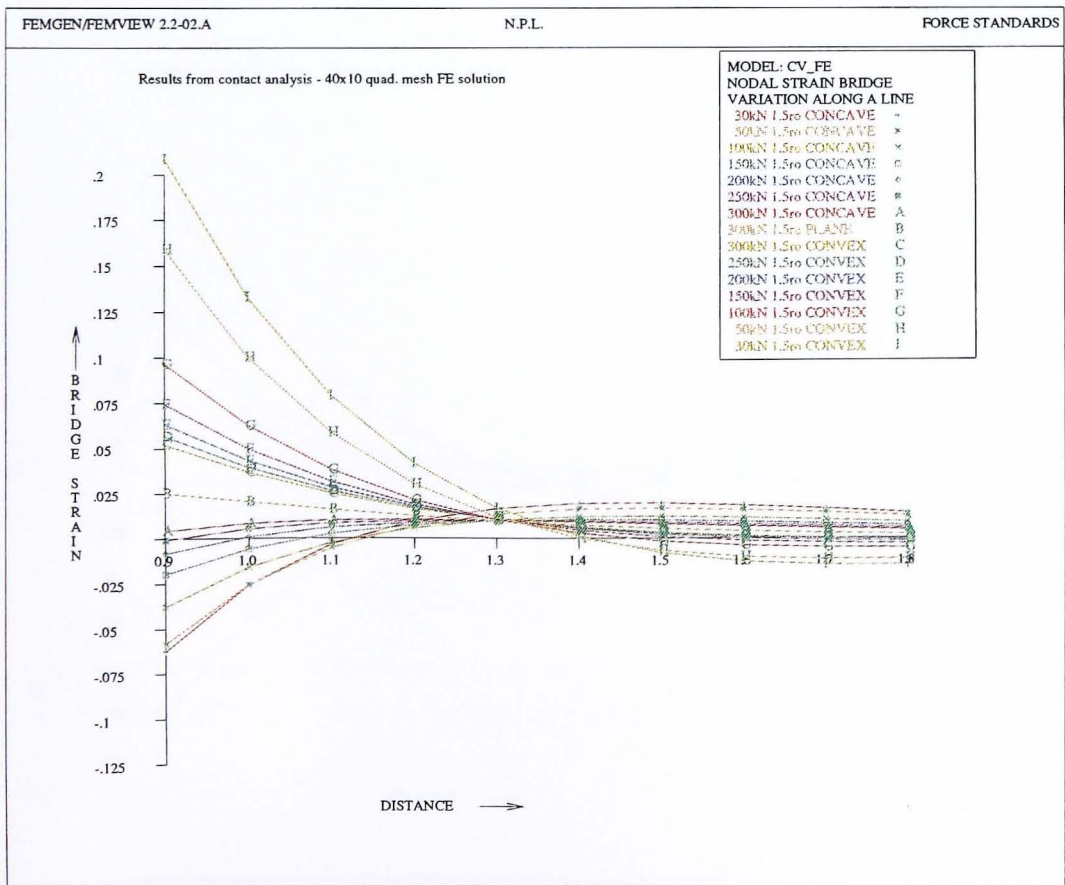


Figure 6.18: Surface bridge strain v distance from loaded end: FE contact analysis: concave/convex pads

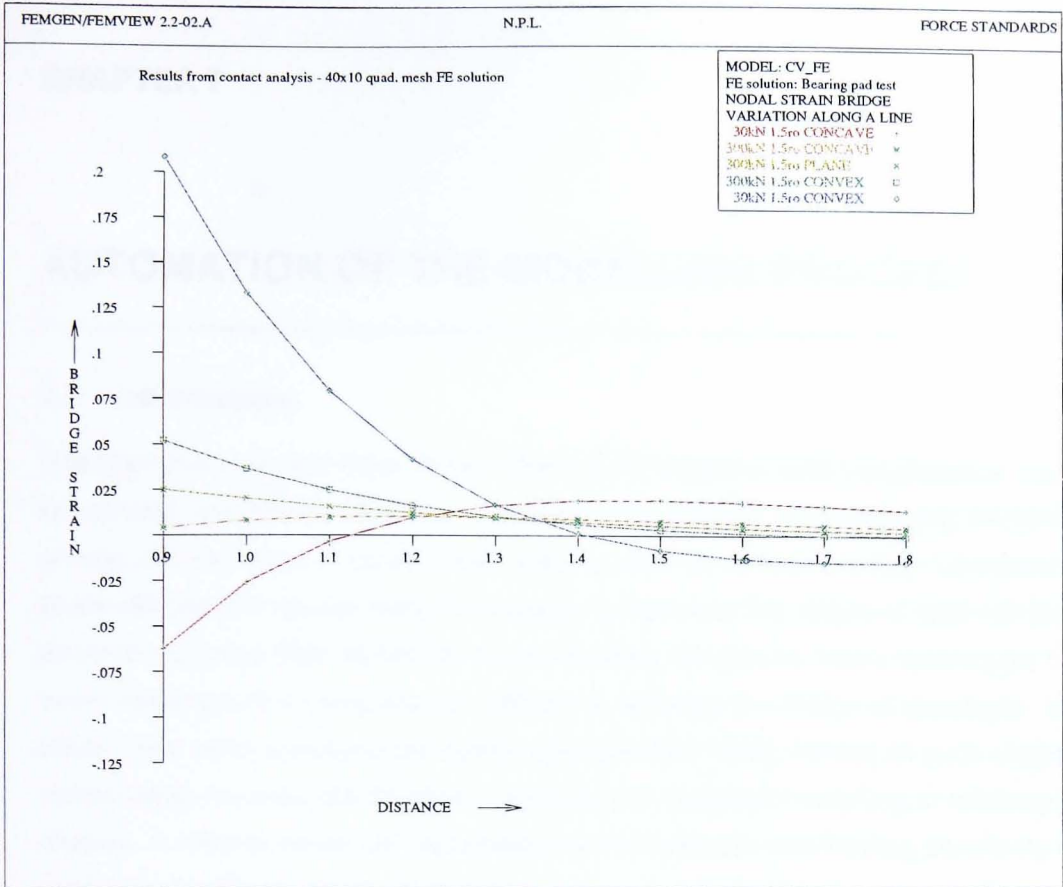


Figure 6.19: Surface bridge strain v distance from loaded end: FE contact analysis: bearing pad test

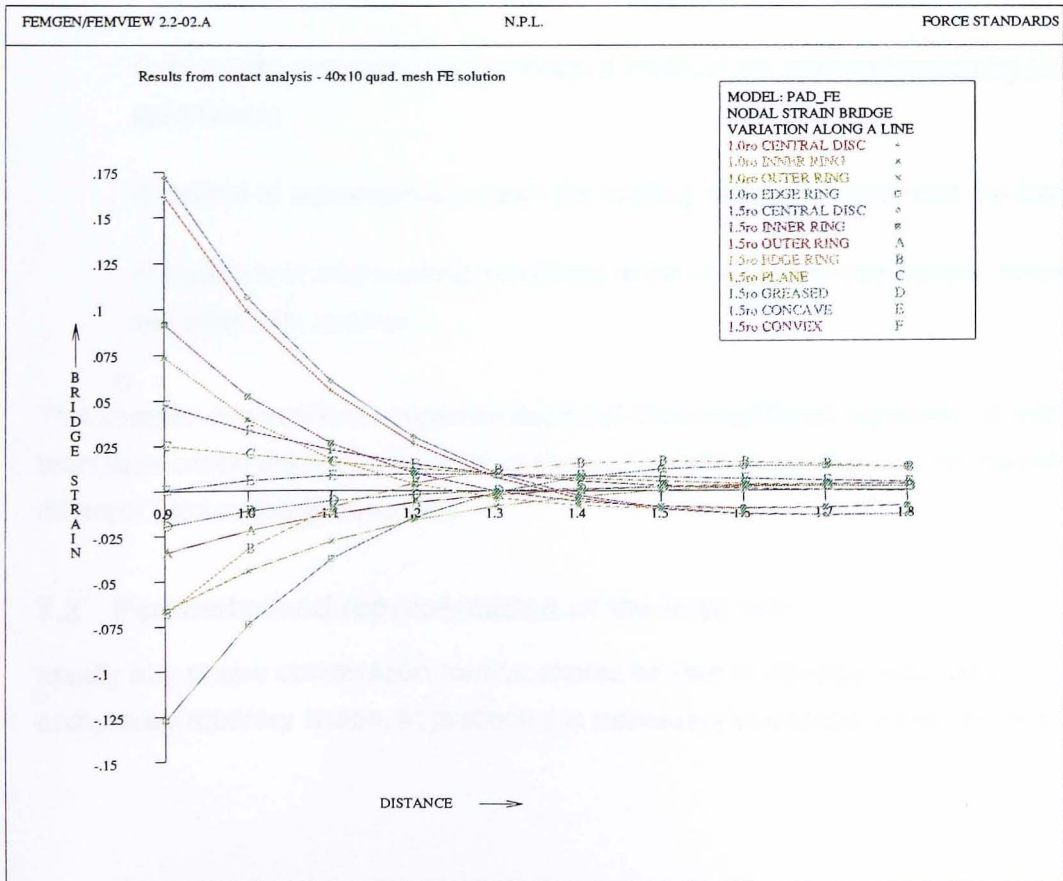


Figure 6.20: Surface bridge strain v distance from loaded end: FE contact analysis: all pads

AUTOMATION OF THE MODELLING PROCESS

7.1 Introduction

The previous chapters have shown that the FE program `axi.f` incorporating routines for contact and infinite elements is capable of modelling and predicting the behaviour of load cell elements in contact with loading pads of various profiles. Ultimately this study will use the results from FE analysis to optimise the shape of load cell elements so as to minimise their sensitivity to end-loading conditions. Many techniques have been developed for using the FE method to optimise the shape of structures. Many of these have been surveyed by Haftka and Granfhi [1986]. Almost all such shape optimisation routines are iterative, requiring the repeated modelling of arbitrary shapes. A routine which can automatically evaluate the end-loading sensitivity of a load cell of arbitrary shape is therefore a prerequisite to developing a shape optimisation program. In addition to the basic FE contact analysis program already described, such a routine requires the following additional components:

A representation of the load cell geometry as a set of parameters

A routine to automatically generate a mesh of the load cell geometry from it's parameters.

A routine to automatically mesh the loading pads in contact with the load cell.

A measure of end-loading sensitivity to be used in the comparison of one load cell billet with another.

This chapter describes the implementation of these additional elements. In addition a technique which dramatically reduced the computation time required for modelling the different load cases is described.

7.2 Parameterised representation of the load cell

Ideally any shape optimisation routine should be free to develop load cells of completely arbitrary shape. In practice it is necessary to impose some practical limits

on the range of permissible shapes. These limits arise from the following considerations:

The load cell element must interface with the loading surfaces of the machines in which it will be loaded. Generally this will require the upper and lower contact surfaces to be plane. The load cell must also fit within the available loading space, imposing limits on its overall height and diameter.

The geometry must be capable of being accurately modelled. Geometries which would require the use of special elements or which would be difficult to automatically mesh will be avoided. Geometries which result in high stress concentrations, which therefore might lead to local yielding are also unsuitable for analysis unless plastic behaviour can be modelled.

The geometry must be able to be represented by a number of design variables or parameters. The optimisation process is the determination of values of these variables which minimise the objective function.

The geometries under consideration must be reasonably simple to manufacture. Load cells with complex shapes such as re-entrant surfaces and holes of varying diameter would be prohibitively expensive to manufacture. A suitable cylindrical area must also be provided for the installation of strain gauges.

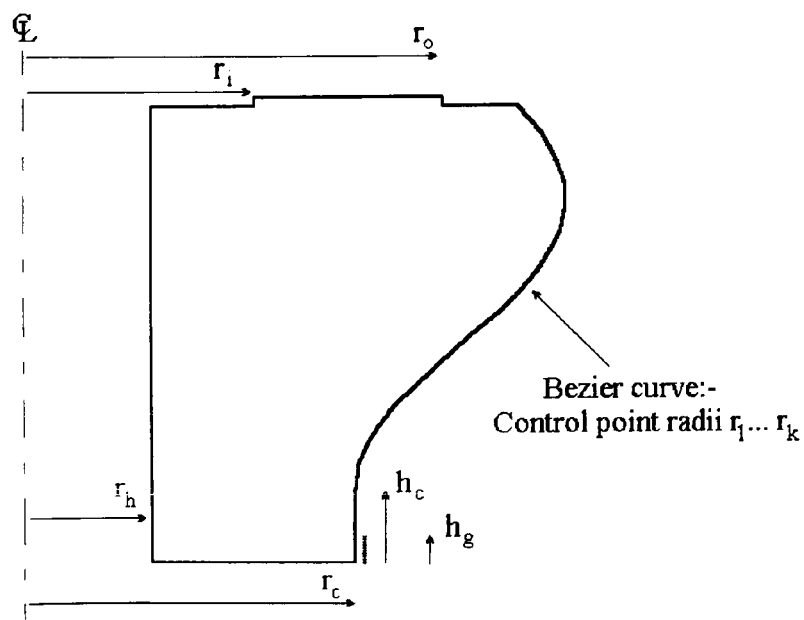


Figure 7.1: Parameterised load cell geometry

Imposing these constraints while allowing as much variation as possible in the shape of the load cell is a matter of judgement. In the case of this study, the parameterised representation of the load cell which was chosen with these constraints in mind is shown in figure 7.1.

The load cell shape is defined by the following:

The load cell is axisymmetric and has mirror symmetry about its mid-plane.

Its upper and lower surfaces are plane and normal to the axis of symmetry.

A slightly raised area is machined on both the upper and lower surfaces. These areas limit the area of contact between the load cell and its loading pads. The inner and outer radii of these surface are denoted by r_i and r_o respectively. The possibility that $r_i = 0$ and that r_o is equal to the radius of the end faces, allowing contact over the entire surface, is not excluded.

A plane hole of radius r_h is bored down the centre of the load cell. The possibility of this radius being zero, the element therefore being solid, is not excluded.

The lateral surface of the load cell is a smooth curve, blending into a central cylindrical section where the strain gauges are applied. This central section is of height h_c and radius r_c .

7.2.1 Representation of the lateral surface

The parameterisation of the lateral surface could be achieved in several ways. Perhaps the most straightforward, considering that the finite element method is to be used, is to use the co-ordinates of nodes on the boundary as the design variables. However, it has been shown that this approach has several disadvantages (Kikuchi et al. [1986]). A large number of variables is required to define the boundary as a set of nodal points and this results in an overly complex optimisation problem. More importantly as element shape has a direct effect on the analysis, a small but significant coupling takes place between the nodal positions and the analysis results. This coupling is separate from the physical effect of variations in the boundary shape and does not represent real behaviour but is an artefact of the FE technique. As a result optimisations using nodal co-ordinates as variables frequently converge on mesh geometries containing badly distorted elements. Methods which rely on infrequent re-meshing of the structure during the optimisation are especially prone to

this, although methods such as the one to be used here where the geometry is re-meshed frequently can still suffer from this effect.

In order to de-couple the geometry description from the nodal co-ordinates an alternative specification for the lateral boundary is required. One approach used by early workers in shape optimisation was to represent the boundary as a simple polynomial, the coefficients being used as the design variables. However it has been found that high order polynomials can result in oscillatory boundary shapes during optimisation. As alternatives to simple polynomials, Braibant and Fleury [1983] and Shyy and Fleury [1988] suggested the use of Bézier and B-spline functions to represent the boundary. Both are widely used for representing curved surfaces in CAD and drawing software. Both of these mathematical curve representations share many useful properties including the following:

Each is defined by a set of control points which when joined together form a defining polygon. Each curve lies within the convex hull of this polygon.

The curves are independent of the axes or units used to define the location of the control points.

The ends of the curve are coincident with and tangential to the ends of the defining polygon.

The curves are capable of representing virtually any function.

B-splines represent a curve as a set of polynomial sections each of which pass through a number of control points and are joined at other control points known as knots. B-splines therefore have a variable which defines the order of the polynomial sections and the number of derivatives which are continuous at the knots. B-splines of order one are straight lines joining the control points, all derivatives being discontinuous at the knots. A second order B-spline representation of a curve consists of a series of quadratic curves, joined at every second control point, such that the first derivative is continuous. As the order is increased, higher order derivatives of the curve become continuous. The order of the B-splines governs the extent to which the effect of the control point positions are localised. Varying the order of the B-spline, also varies the smoothness of the boundary. Bézier curves are B-splines with order equal to the number of control points. The position of each control point of a Bézier curve has a global effect on the whole curve.

The order of B-spline which provides the best representation depends on the particular application. One possibility considered was to make the order of the B-spline used to represent the lateral surface itself a design variable to be optimised. However, it was thought that this extra flexibility was unnecessary and that a fixed order of curve could be used. It was decided to represent the lateral surface as a Bézier curve. This high order B-spline would ensure that the surface was smooth, minimising stress concentrations. It was also felt that the global influence of the control point co-ordinates of Bézier curves would serve to further de-couple these variables from the effect of local variations in element geometry. The stability problems encountered by workers who have used low order polynomial boundary representations with FE optimisation programs should therefore be avoided.

The number of control points used by the program was variable, but twelve were typically used. The control points were equispaced in height between the top of the load cell and the top of the central cylindrical portion. The design variables were the radial co-ordinates of each of the control points. In order to ensure that the Bézier curve blended smoothly with the central cylindrical section, the radii of the lower two control points were set to be equal to the radius of the cylindrical section, imposing a vertical tangent at the join.

The shape to be optimised was therefore characterised by the following variables:

h_g the height of the gauged area = half-height of gauge pattern.

h_c and r_c , the height and radius of the central cylindrical section.

A , the cell aspect ratio, the ratio of its overall height to the diameter of the central section.

r_i and r_o , the inner and outer radii of the raised contact area.

r_h , the radius of the central hole.

$r_1 \dots r_k$, the radii of the k control points of the Bézier curve defining the lateral surface.

h_c , r_c and the bottom two control point radii r_{k-1} and r_k (equal to r_c) were specific to the problem to be solved and held constant during the optimisation. The aim of the

optimisation was to set the remaining variables to their optimum values. With a lateral surface defined by twelve control points there were 14 variables to be optimised.

7.3 Automatic mesh generation

7.3.1 Requirements

In order that an optimisation algorithm could be implemented, the finite element analysis had to be fully automated. A meshing algorithm, capable of automatically meshing load cells of arbitrary shape, was therefore required. Several such automatic meshing algorithms have been developed. Some commercial FE packages include an automatic meshing facility, although these usually require some input by the operator rather than being truly automatic. An algorithm to mesh the parameterised load cell described above has less demanding requirements than these more general algorithms. While a general algorithm must cope with objects of arbitrary shape, the axial, top, and bottom boundaries of the parameterised load cell shape are defined by straight lines, only the Bézier lateral surface requiring special treatment. General routines are also often required to provide local refinement of the mesh in areas of high strain gradient. High strain gradients should not arise in column load cells, other than at the contact surfaces. A uniform mesh density could therefore be used, adaptive mesh refinement being unnecessary.

The requirements of the meshing algorithm for this algorithm were therefore reasonably limited. The main consideration however was simplicity and ease of implementation. Several previously reported meshing algorithms were examined, however none appeared to offer the desired level of simplicity. A new meshing algorithm was therefore developed to take advantage of the simplification offered by having only one non-straight boundary.

7.3.2 The automatic meshing routine

The automatic meshing algorithm starts with a rectangular grid of points covering the region within which the object lies. These points eventually become the corner nodes of the elements and are therefore named vertices. Each vertex is examined to determine whether it is close enough to the object boundary to be captured. Captured vertices are moved so as to lie on the boundary. Non-captured vertices lying outside the boundary are discarded. The retained vertices are joined to form the corner nodes of the quadrilateral and triangular elements of the mesh. Thus far the method is similar to that reported by Kela, Saxena and Perucchio [1987], however, the method

differs in the criteria used both for capturing the vertices and the algorithm for creating the elements joining the vertices.

7.3.2.1 The boundary capture criteria

The boundary capture algorithm is applied to the curved lateral boundary only. Judicious choice of the grid spacing in the vertical and horizontal directions is sufficient to ensure that grid vertices lie along the three straight boundaries. The implementation of the capture algorithm is as follows:

Each row of vertices on the grid is considered separately. Working outwards from the inner boundary a crude estimate of the minimum distance from the grid vertex to the lateral boundary is made by approximating the boundary as a series of straight lines joining the values of the Bézier curve at the height of each row. The smaller of the perpendicular distances from the grid vertex to the line segments above and below the row is used as the estimate (P_1 in figure 7.2). Grid vertices for which this distance is greater than the mean grid spacing are not considered for capture by the boundary. However, the radial distance from these vertices to the boundary is also calculated and used to eliminate those grid vertices which are external to the boundary.

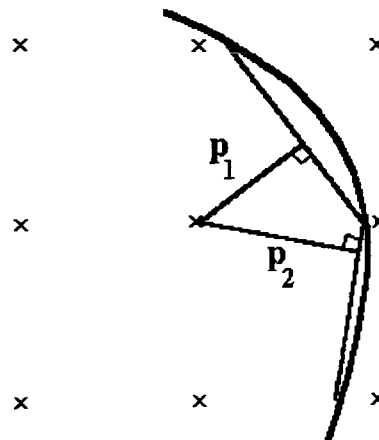


Figure 7.2: Crude estimate of distance from boundary

If the crude estimate of the distance is less than the mean spacing of the grid the vertex is considered for capture by the boundary. A more accurate (and computationally more costly) calculation of the distance to the boundary is made for these vertices. Defining x as the radial co-ordinate and y as the vertical co-ordinate,

the distance P from the grid vertex x_g, y_g to a point x_b, y_b on the boundary is given by:

$$P^2 = (x_b - x_g)^2 + (y_b - y_g)^2 = (\beta(y) - x_g)^2 + (y_b - y_g)^2 \quad 7.1$$

Where the Bézier curve representing the boundary has been represented by $x = \beta(y)$. The point on the boundary closest to the grid vertex is at the value of y_b for

which $\frac{\partial P^2}{\partial y_b} = 0$. Differentiating the equation for P^2 with respect to y_b results in the closest point on the boundary being given by:

$$\beta'(y_b)(\beta(y_b) - x_g) + (y_b - y_g) = 0 \quad 7.2$$

The program solves this equation for y_b using the Newton-Rapheson method. The solution requires calculation of both the first and second derivatives of $\beta(y)$.

7.3.2.2 Setting the capture interval

Whether the grid vertex is captured by, and moved to, the boundary is determined by the variables *in-range* and *out-range* which define a capture interval. The choice of values for these variables determines the quality of the mesh. If the capture interval is set too wide, grid vertices a long way from the boundary are captured. When joined such vertices form elements which are highly distorted relative to their basic shape, resulting in poor accuracy (figure 7.3).

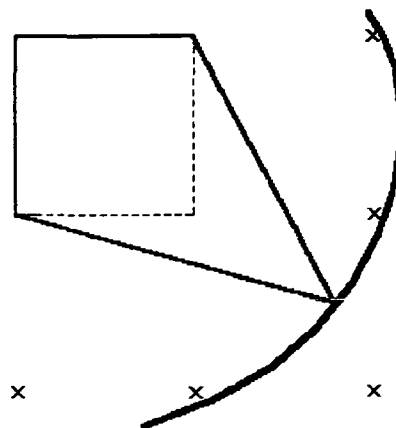


Figure 7.3: Capture interval too wide resulting in very distorted elements.

It is also possible with too wide a capture band that two vertices would be captured and moved to points on the boundary very close to one another (figure 7.4).

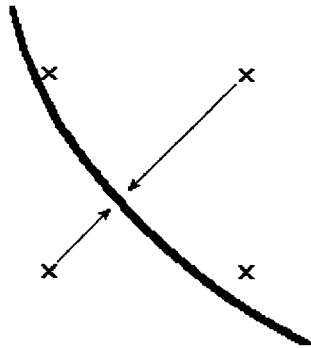


Figure 7.4: Capture interval too wide resulting in near coincident vertices

Similarly too narrow a capture band may result in long segments of the boundary being devoid of vertices. The values of *in-range* and *out-range* must be carefully chosen so as to avoid these problems. The values were set according to the following rather loose argument based on the production of quadrilateral elements with reasonable distortions from the basic square shape for two typical cases.

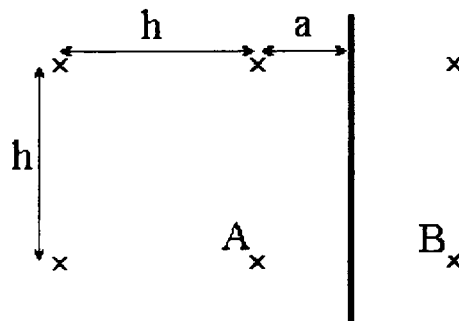


Figure 7.5: Grid of vertices with vertical boundary

Figure 7.5 shows the grid of vertices with the boundary approximated as a straight line in this case parallel to the vertical grid axis. In this situation the options are to capture either vertex A (figure 7.6), vertex B (figure 7.7) or both.

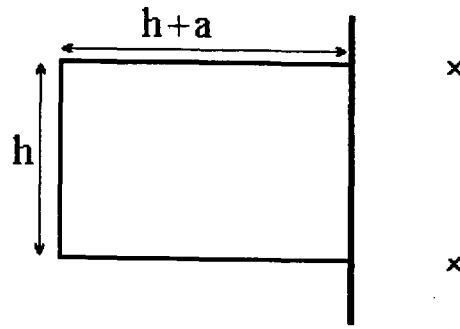


Figure 7.6: Element formed by capture of vertex A

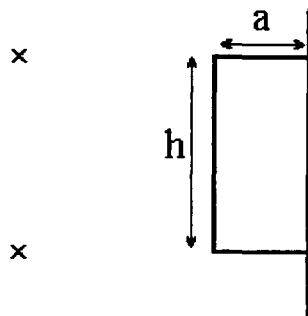


Figure 7.7: Element formed by capture of vertex B

Capturing both A and B is to be avoided as this results in two co-located boundary vertices and therefore a highly distorted mesh. To ensure that only one vertex is captured a threshold must be set at which the vertex capture switches from A to B. Ideally the ratio of the lengths of the quadrilateral elements formed should be as close as possible to unity. The ratio between the longest and shortest sides of the

quadrilaterals formed by the capture of A is $\frac{h+a}{h}$ and by the capture of B is $\frac{h}{a}$. In

order to minimise element distortion the strategy should switch at the value of a at which the two ratios are equal. This occurs when $a = 0.618h$. A strategy which captures the inner grid vertex if its distance to the boundary is less than $0.618h$ and captures the outer grid vertex if its distance to the boundary is less than $0.382h$ results in quadrilateral elements with a maximum ratio between the sides of 1.618.

This works for vertical and therefore also for horizontal straight boundaries. In practice the inner capture distance was set to $0.617h$ rather than $0.618h$ to insert a 'dead-band', to prevent rounding error leading to capture of both vertices.

While the above capture limits are satisfactory for horizontal and vertical boundaries, this is not necessarily the case for other boundary angles. In order to gauge the effect

of other boundary angles a straight boundary inclined at 45° to the grid axes was considered (figure 7.8).

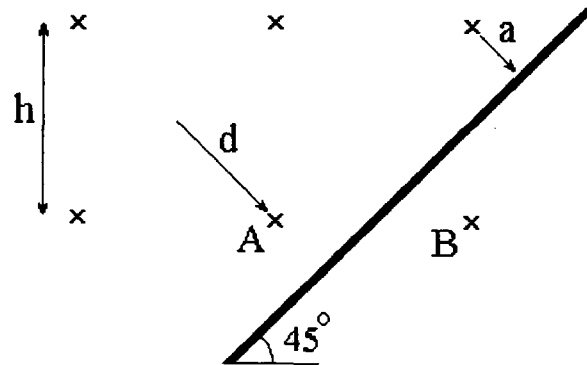


Figure 7.8: Grid of vertices with boundary inclined at 45° to the horizontal

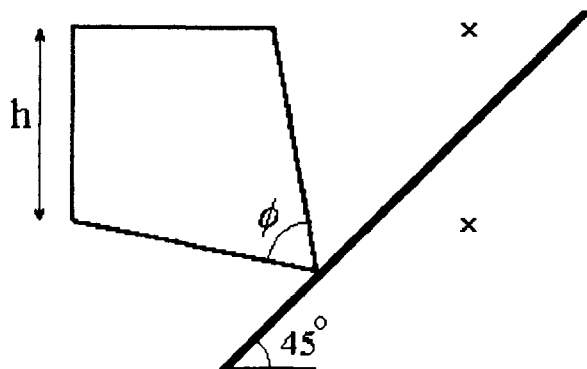


Figure 7.9: Element formed by capture of vertex A

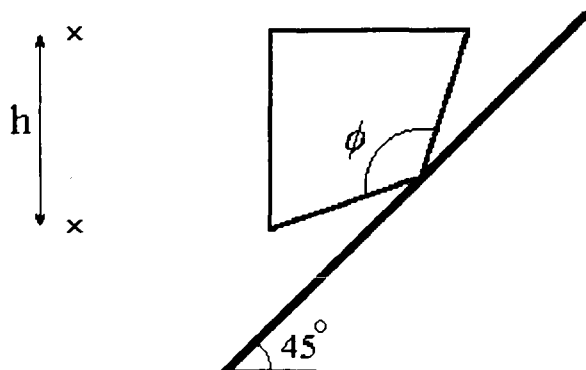


Figure 7.10: Element formed by capture of vertex B

The same 0.617/0.382 capture rule was used with the diagonal spacing of the grid, d , substituted for h . The two worst case scenarios in this case are shown in figures 7.9 and 7.10.

Element distortion may also be measured by the internal angle of the element sides meeting at the vertex on the boundary. A guideline for the range of acceptable distortion of quadrilateral elements are that the internal angles should lie in the range 60° to 120° . The internal angle of the quadrilateral can be calculated for each of the two limiting cases. If an internal node is captured when $a = 0.617d$, the internal angle, ϕ , is given by $2 \cdot \tan^{-1}(1.0/(1.0 + 0.617)) = 63^\circ$. If an external node is captured when $a = 0.382g$, the internal angle is given by: $2 * \tan^{-1}(1.0/(1.0 - 0.382)) = 117^\circ$. The included angles of the quadrilateral elements using the capture rule therefore lie between 63° and 117° and the distortions are therefore reasonable.

The above vertical/horizontal and 45° straight line boundary examples are special cases of the general problem. That a capture rule produces reasonable mesh distortions for these two special cases does not necessarily indicate that the rule will ensure that distortions are reasonable in all cases. However, in the absence of a rigorous proof of the applicability of the capture criteria to the general case, it was decided to implement the criteria and assess its performance when meshing general shapes.

The capture criteria can be summarised:- The vertex is captured if it is:

internal and less than $0.617 \times \textit{grid-spacing}$ from the boundary

or

external and less than $0.382 \times \textit{grid-spacing}$ from the boundary

where *grid-spacing* is given by $\max(|h \sin(\alpha)| + |v \cos(\alpha)|)$ where h and v are the horizontal and vertical mesh spacings and α is the angle of the boundary to the horizontal.

When implemented this boundary capture criteria was found to generate acceptable meshes for all shapes, however general.

Those grid vertices considered for capture, but outside the capture interval are either retained at their original co-ordinates or, if external to the boundary, eliminated. If the

end of the row is reached and no grid vertex in that row has been captured by the boundary, the internal vertex in the row having the largest radial co-ordinate is moved radially to the boundary. This ensures that at least one vertex in each row lies on the boundary.

7.3.2.3 Element generation

The mesh is constructed from a combination of 8-node quadrilateral and 6-node triangular elements. A procedure is therefore required to connect the vertices generated using the above algorithm, so as to form elements. Away from the boundary, where the vertices are retained in their original grid, the mesh is easily formed from quadrilateral elements. Close to the boundary, where vertices have been either eliminated or captured by the boundary, triangular elements must be combined with the quadrilateral elements in order to generate an acceptable mesh. The following procedure was found to generate acceptable element geometries for all the load cell shapes modelled.

The algorithm is illustrated in figures 7.11 to 7.13. During the vertex capture and elimination, two variables record the indices of the vertices captured by the boundary. For each row of vertices an entry in the array *top_vertices* records the upper-most boundary vertex, while the lower-most boundary vertex is recorded in the array *bottom_vertices*. The type and number of elements created between each row of vertices depend on the values of the entries in the arrays for the rows above and below.

Meshing between the rows of vertices is controlled by two indices. These are the value of the entry in *bottom_vertices* associated with the row above and the value of the entry in *top_vertices* associated with the row below. In the following description these values will be denoted by *BV_U* and *TV_L* respectively. The procedure is as follows:

Quadrilateral elements are used to mesh from the inner boundary out to either *BV_U* or *TV_L* depending on which of these is the inner-most. If *BV_U* equals *TV_L* the meshing of the row is complete.

If *BV_U* is greater than *TV_L*, triangular elements are created out from the last quadrilateral element. Each has its base along the top row and share *TV_L* as their lower vertices.

If TV_L is greater than BV_U , triangular elements are again created, this time with their bases along the lower row and common upper vertices.

This procedure is repeated until all the spaces between the rows of vertices have been meshed.

While the above procedure has not been rigorously proved to generate good quality meshes for arbitrary boundaries, it has been tested on many load cell shapes. It was found that, provided that the local radius of curvature of the boundary was larger than the spacing of the initial vertex grid, the generated mesh did not contain badly distorted elements. The algorithm was found to work well for the limited range of problems for which it was intended.

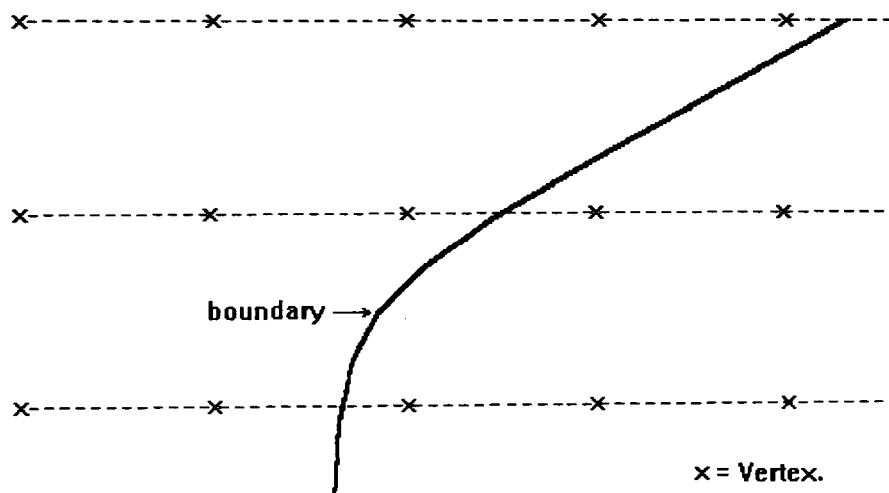


Figure 7.11: Initial rows of vertices and shape boundary

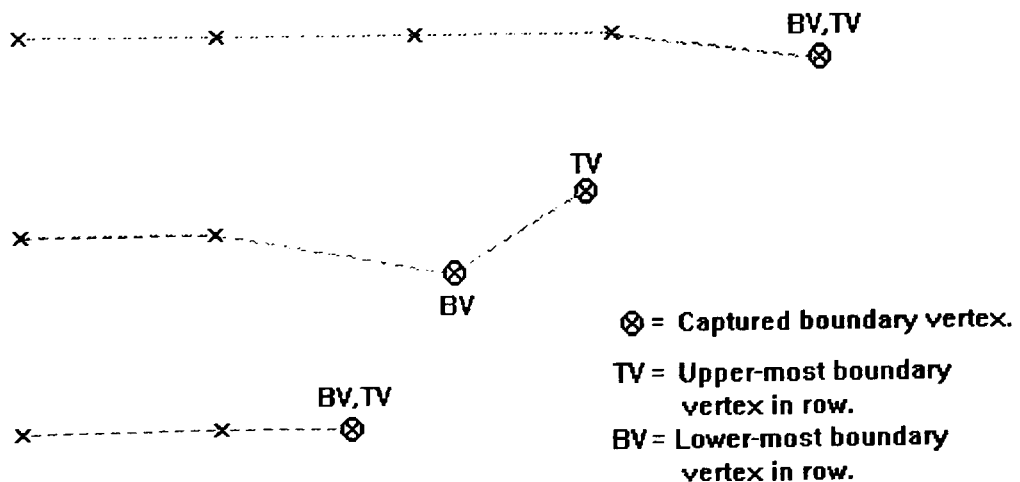


Figure 7.12: After capture by boundary and elimination of external vertices

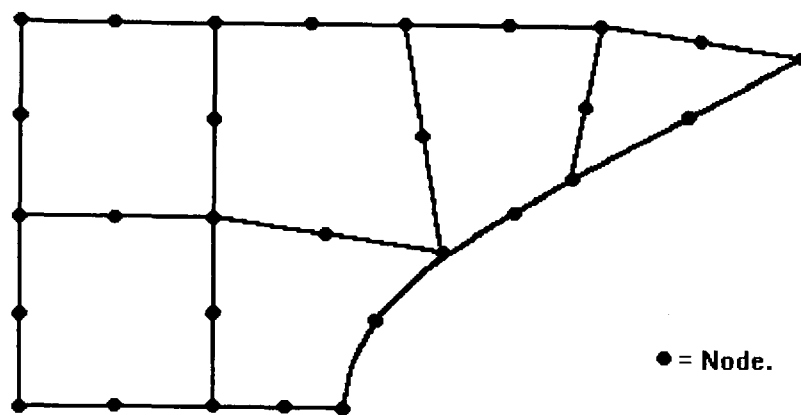


Figure 7.13: Mesh generated from vertices

7.3.2.4 Node generation

Following generation of the element topologies, the nodal co-ordinates and node numbers are calculated. The corner nodes of the elements are coincident with the element vertices. The co-ordinates of the mid-side nodes which are internal to the shape are calculated from the mean co-ordinates of the corner nodes on the same side. The co-ordinates of mid-side nodes lying on the boundary are calculated from the Bézier curve, the y co-ordinate being the mean value of the y co-ordinates of the corner nodes on the same side.

The nodes are initially numbered consecutively in the order of their creation, one node being created for each nodal position on each element. Before a stiffness matrix can be generated the nodes must be renumbered to reduce the matrix bandwidth and coincident nodes eliminated. The nodes are renumbered using the Shell-Mezgar algorithm. A search is then made to find and condense coincident nodes. The element topology matrices are modified to reflect the changes made in the node numbers.

Finally a search is made to identify nodes lying on the axis of mirror symmetry. An entry is made in the restraints vector to restrain these nodes in the y direction. The nodal freedom array is then constructed.

7.4 Meshing of the contact pads

Meshing of the contact pads is much easier than meshing the load cell. The pads have a plane upper surface while the lower boundary is modelled as extending to infinity. The pad mesh consists of two rows of quadrilateral elements extended axially to infinity by a row of infinite elements. The mesh may also to be extended radially to infinity using infinite elements. The mesh is therefore similar to that used in the

benchmark tests in chapter 6. Once the elements have been generated, the nodes are created, re-numbered and redundant nodes eliminated in a similar fashion to that followed for the creation of the load cell mesh.

7.5 Measures of end-loading sensitivity

The range of possible end-loading conditions to which a load cell may be subjected in service is virtually infinite. It was necessary to select a limited set of loading conditions which are representative of the variety of conditions to which they may be subjected. A measure which represents the variation in load cell output over these loading conditions as a single figure can then be constructed. In the next chapter a shape optimisation method will be outlined. For reasons which will become apparent in the next chapter, these measures will be defined so as to be able to formulate the optimisation as a maximisation rather than a minimisation. The term 'immunity', being the inverse of sensitivity, will be used for the two measures constructed for use during the optimisation.

7.5.1 EN-Immunity

The EN10002-3 bearing pad test is a widely accepted method for assessing end-loading sensitivity. It would appear reasonable to use this test as a basis for a measure. The measure based on the bearing pad test was named 'EN-immunity'. The bearing pad test specifies the six test conditions in table 7.1.

Applied load	Pad profile
Maximum	Plane
Maximum	1:1000 Convex
Maximum	1:1000 Concave
Minimum	Plane
Minimum	1:1000 Convex
Minimum	1:1000 Concave

Table 7.1: EN10002-3 bearing pad test load conditions

The friction conditions at the contact interface are not specified in the calibration standard. However, it is generally interpreted that the tests are to be carried out with the contact surfaces of both the load cell and pads clean and de-greased. Most sources give a value for the coefficient of friction for clean high tensile steel to high tensile steel contact of 0.3.

In practice it has been found that if a load cell passes the bearing pad test at its minimum load, it will also pass the bearing pad test at its maximum load. In

constructing a measure of the end-loading sensitivity it was therefore decided to only consider the sensitivity at minimum load.

The EN-immunity is calculated from the variation in bridge output when the minimum load is applied to the load cell under the following end-loading conditions.

1. Both ends loaded via an axially infinite $1.5 r_o$ plane pad, coefficient of friction: 0.3.
2. Both ends loaded via an axially infinite $1.5 r_o$ convex pad, slope 1:1000, coefficient of friction: 0.3.
3. Both ends loaded via an axially infinite $1.5 r_o$ concave pad, slope 1:1000, coefficient of friction: 0.3.

The above three load cases are double ended versions of those specified in EN10002-3. The EN-immunity was defined as:

$$\text{EN-immunity} = \frac{2 \varepsilon_{b1}}{\max((\varepsilon_{b2} - \varepsilon_{b1}), (\varepsilon_{b3} - \varepsilon_{b1}))} \quad 7.3$$

where ε_{b1} , ε_{b2} , and ε_{b3} are the mean bridge strain over the gauged area for load cases 1, 2, and 3. Note that the factor of 2 in the above definition, which is based on double-ended load cases (i.e. convex pad top and bottom), is to ensure comparability with the EN 10002-3 limits, which are based on single-ended load cases (i.e. plane pad on top, convex pad beneath).

It has been assumed this far that the bridge output is proportional to the bridge strain values at a single point. In practice strain gauges have a finite length and width and their output is a function of the strain values integrated over the gauge area. It was therefore necessary in evaluating the function to reflect these finite dimensions.

It was assumed that the bridge strain varies linearly over the gauge length. It was also assumed that the axial and circumferential gauges are of the same pattern with a square active area such that both have the same effective axial dimension. The bridge strain values used in calculating the immunity were the average of the bridge strain values at each end of the gauged area.

EN10002-3 class	Max. departure from plane pad at minimum load	EN-Immunity
Class 00	0.1%	1000
Class 0.5	0.2%	500
Class 1	0.4%	250
Class 2	0.8%	125

Table 7.2: EN-immunity values of EN 10002-3 classes

The main advantage of using the EN-immunity measure is that its value can be directly related to the limits of the EN10002-3 classes. The equivalent class limits at minimum load and equivalent EN-immunity values are given in table 7.2.

7.5.2 PCCU-immunity

Although the EN-immunity measure is directly comparable with the bearing pad test, it has some limitations. An ideal measure would be based on performance over tests representative of every possible loading condition. The EN10002-3 tests are carried out with clean, degreased contact surfaces. However, in industrial use load cells often experience contact conditions which are less controlled. The contact surfaces are sometimes, either intentionally or as a result of contamination, covered by a layer of grease or oil. The coefficient of friction in this case is much lower than 0.3. It is therefore important that a load cell should be insensitive to variations in the coefficient of friction. The EN-immunity measure defined in the previous section does not include any variation in contact friction. A more appropriate measure of end-loading sensitivity should include loading conditions with both high and low friction coefficients. A suitable measure, more representative than EN-immunity of the range of possible loading conditions, was constructed and is defined below. This measure was named PCCU-immunity (Predicted from Concave, Convex and Uniform load cases).

The measure was based on the variation in bridge output when the minimum load is applied to the load cell under the following five end-loading conditions.

1. Uniform pressure applied over both contact surfaces.
2. Both ends in frictionless contact with an elastic half-space with a convex surface, slope 1:1000.
3. Both ends in frictionless contact with an elastic half-space with a concave surface, slope 1:1000.

4. Both ends in contact with an elastic half-space with a convex surface, slope 1:1000, coefficient of friction: 0.3.
5. Both ends in contact with an elastic half-space with a concave surface, slope 1:1000, coefficient of friction: 0.3.

The above load cases are intended to be representative of the range of loading conditions likely to be encountered by a load cell in service. The PCCU-immunity measure was defined as:

$$\text{PCCU-immunity} = \frac{2\varepsilon_{b1}}{\max(\varepsilon_{bi}) - \min(\varepsilon_{bi})} \quad 7.4$$

where ε_{bi} is the bridge output in the i th load case. Again a factor of 2 was included to factor the results so as to be equivalent to those for single ended loading.

As before it was necessary in evaluating the function to take account of the finite length of the gauges. The value used was the minimum of two values calculated according to the above definition. One was calculated using the values at the centre of the gauge pattern. This point lies on the axis of mirror symmetry of the load cell. The other value was calculated from the bridge strain values at the ends of the gauge patterns.

7.6 Reducing computation time

In an iterative optimisation it is important that the time required to compute the immunity values is minimised. Evaluating either of the above immunity values conventionally requires the following procedure:

1. The load cell shape is meshed and its stiffness matrix constructed
2. The vector of nodal loads corresponding to uniform pressure is calculated.
3. The matrix equation is solved for the vector of displacements.
4. The bridge strain at the strain gauge locations is calculated from the nodal displacements.
5. The semi-infinite contact pad is meshed and its stiffness matrix constructed.

6. Both the load cell and pad stiffness matrices are condensed to include only the degrees of freedom at the contact surface.

7. For each of the contact pads:

The contact forces are calculated from the condensed stiffness matrices, the total applied force, the pad profile and the coefficient of friction.

The matrix equation is solved for the vector of displacements.

The bridge strain at the strain gauge locations is calculated from the nodal displacements.

8. The immunity value is calculated from the bridge strains.

The most computationally intensive part of the above procedure is the solution of the matrix equations for the displacement vectors. The computational efficiency of the above procedure could be improved by combining the separate matrix equations into one equation with multiple left and right hand sides. A call to a solution algorithm simultaneously solving this equation for all the nodal displacements would be faster than the separate calls to an algorithm solving for one right hand side a time. However a greater reduction in computation can be obtained by taking advantage of the fact that full-field calculations of the displacements and strains are not required. While it would be possible to limit the strain recovery to the element containing the two relevant nodes, the above procedure makes a full-field calculation of displacement for each of the five load cases. As the strain values are required at only two nodal positions this is computationally wasteful.

Computational efficiency can be improved by the application of Maxwell's reciprocal theorem to calculate contact surface influence factors for each of the two nodes of interest. For the element containing these nodes, displacement fields corresponding to unit bridge strain ($\varepsilon_a = -1$, $\varepsilon_c = \nu$) at each of the two nodes are calculated. Loads, equal and opposite to these nodal displacements, are then applied to each node of the element and the matrix equation solved for the displacements. According to the reciprocal theorem, the nodal displacements of the contact surface are equal to the corresponding influence factors. These influence factors give the values of bridge strain resulting from the application of unit loads at the corresponding contact nodes. The bridge strain at the two nodal points can therefore be found for any contact load

distribution by multiplying the vector of loads by the relevant vector of influence factors.

The modified procedure is therefore as follows:

1. The load cell shape is meshed and its stiffness matrix constructed
2. For each of the two nodes:

The element displacement field corresponding to unit bridge strain is calculated and equal and opposite loads applied.

The matrix equation is solved for the vector of displacements and copied to form the vector of influence factors.

3. The load cell stiffness matrix is condensed to include only the contact degrees of freedom
4. For each load case:

The contact pad is meshed and its stiffness matrix constructed and condensed to include only the contact degrees of freedom.

The contact forces are calculated from the condensed stiffness matrices, the total applied force, the pad profile and the coefficient of friction. For the uniform pressure load case, the contact loads are calculated directly.

The bridge strain at the strain gauge locations is calculated from the scalar product of the nodal loads vector and the vector of influence factors.

5. The immunity value is calculated from the calculated strains.

The above procedure requires the full matrix equation to be solved only once as opposed to the three or five solutions required by the original procedure. Tests showed that in calculating PCCU-immunity this procedure based on influence factors takes approximately half the time of the original procedure.

The routines for calculating the immunity values were tested on the SUN SPARCstation. It was found that a typical load cell shape could be meshed with approximately 150 elements, the bridge strain associated with the each loading condition calculated, and the immunity value evaluated, in 10 to 15 seconds.

7.7 Conclusions

A parameterised representation of load cell elastic elements of reasonably arbitrary shape has been developed together with a routine for automatically generating a FE mesh.

Two 'Immunity' measures of the end-loading sensitivity of load cells have been defined. One, the EN-Immunity measure is closely related to the EN10002-3 bearing pad test. The other measure, known as PCCU-immunity, is based on loading conditions both with and without contact friction. A computationally efficient procedure capable of evaluating the 'immunity' value has also been developed. The aim of the shape optimisation will be the maximisation of one or other of these measures.

GENETIC ALGORITHM SHAPE OPTIMISATION

8.1 Introduction

Many researchers have developed techniques for the automatic optimisation of structures using finite element techniques. Initial work concentrated on optimisation of so-called 'sizing' design variables. These variables such as plate thicknesses or beam cross-sections can be varied without requiring modification of the finite element mesh. However, for most problems modification of the boundary shape is more effective in achieving the optimum design (see Hatka & Grandhi [1986] for a review). The load cell optimisation problem considered here is an example of such a shape optimisation problem.

A shape optimisation program requires the following components:

An automatic meshing routine. Often such a routine also adaptively refines the mesh.

A routine for evaluating the objective function, the measure of the optimality of a combination of design variables.

An optimisation algorithm.

The development of an automatic meshing routine has been described in the last chapter. Adaptive mesh refinement is usually required where the area of interest is in a region of large stress and strain gradients. Such is the case when optimising the shape of a hole in a plate so as to minimise the stress concentration in the vicinity of the hole. In the case considered here, the maximum stress gradients occur in the vicinity of the contact surfaces. The area under the strain gauges, where the highest accuracy is required, is not subject to large strain gradients. Provided that a reasonable mesh density is initially provided in this region, there should be no need for adaptive mesh refinement. Earlier comparisons with experiment, outlined in chapter 4, have shown that acceptable accuracy can be achieved in this case without local refinement.

Appropriate objective functions and methods for their evaluation for load cell elements, represented as a set of variables, were described in the last chapter.

8.2 Optimisation algorithms

The purpose of an optimisation algorithm is to search the multi-dimensional variable space to find the maximum of the objective function. A good algorithm should be both efficient and reliable. In this context reliability refers to the algorithm's ability to find the global maxima for different objective functions and constraints. An efficient algorithm achieves this with the minimum computational effort. Depending on the methods they employ, optimisation algorithms can be classified as either gradient and gradientless.

8.2.1 Gradient methods

Gradient methods require the evaluation of the first derivatives of the objective function (e.g. Zienkiewicz et al. [1975]). The simplest are of the 'hill-climbing' variety. These iteratively vary the variables so as to follow the line of local maximum slope in order to progress towards a maximum. Some gradient algorithms also make use of higher order derivatives of the objective function in order to improve the search strategy. One problem with simple gradient optimisation algorithms is their tendency to converge on local rather than global maxima. Various modifications have been used to ensure that the algorithms iteratively converge on the global rather than a local maximum.

The main disadvantage of gradient methods is the requirement for the direct evaluation of partial derivatives of the objective function. The calculation of even the first partial differentials of an objective function based on the results of finite element analysis is very complicated. Methods which differentiate the FE equations have been successfully used. However where the objective function is a complicated function of the FE results, direct calculation of the derivatives may not be possible. Even where expressions for the derivatives can be derived, numerical inaccuracy in their evaluation may result in large errors in the calculated search direction.

An alternative to differentiating the discrete FE system of equations is to evaluate the partial derivatives by differentiating the continuum equations. Several authors have reported the use of such methods. While these methods are reported to be more efficient and avoid errors due to mesh distortion, other sources of numerical error may still reduce the reliability of the algorithm.

8.2.2 Gradientless methods

Gradientless methods (reviewed in Schnack & Iancu [1991]) avoid the mathematical and numerical difficulties associated with the evaluation of derivatives of the objective function. These methods can be sub-divided into two groups according to whether or not they include a significant random component in the search strategy.

The non-random methods alter the boundary shape in small increments according to some measure of the stress or strain in the body. For example in minimising the weight of a structure, the boundary may be moved inwards in areas of low stress and outwards in highly stressed areas. One implementation of this type of algorithm (Mattheck & Burkhardt [1990] and Baumgartner et al. [1991]) has been shown to mimic the growth of biological structures, such as trees and bones, when subjected to applied stress. The method of feasible direction (Schnack [1979]) is similar in that the variables defining the boundary are adjusted in the direction of a search vector which is specified separately.

The second group of methods are based on directed random or stochastic approaches. At first consideration, search strategies with high random components might be expected to be less efficient than those which use gradient information. However, the best of these algorithms have been found to be of comparable efficiency to the gradient methods. These methods are reasonably new and have rapidly gained popularity in solving a wide variety of optimisation problems. The adoption of these methods in FE optimisation problems has however been less rapid. The two most popular random gradientless methods are simulated annealing and genetic algorithms.

8.2.2.1 Simulated annealing

Simulated annealing is so called because it mimics the mechanism that takes place when a solid is slowly cooled from the molten state. If such cooling is very rapid the material may adopt a glassy state. Slower cooling will result in the material adopting one of its crystalline states. Such a crystal structure contains much less internal energy than the amorphous state. The probability of adopting a particular geometry depends on the rate of cooling and the internal energies of the different crystal geometries. However, below a certain rate of cooling, the crystal geometry with the lowest energy is invariably adopted. Annealing by slow cooling therefore locates the minimum of a multi-dimensional energy surface very reliably.

The simulated annealing algorithm (Kirkpatrick et al. [1983]) mimics the statistical mechanics of the physical process. The random component of the search arises from the effect of temperature. Initially the temperature is set such that the thermal energy is large in comparison with the internal energy surface. The temperature is then progressively reduced, thereby gradually reducing the random component of the search. The rate of cooling is set by the user and is a matter of judgement and experience. Providing the cooling is slow enough, the true minimum of the energy surface is reliably found.

Surprisingly, considering the reliability and ease of implementation of the algorithm, there appear to be no reports of the use of simulated annealing in conjunction with FE methods in the optimisation of structures.

8.2.2.2 Genetic algorithms

Like simulated annealing, genetic algorithms (GAs) mimic a natural process, in this case biological rather than metallurgical. Genetic algorithms were pioneered by Holland [1975] and apply simplified versions of the evolutionary processes of mutation, reproduction and selection to populations of 'individuals'. In biological evolution (coined 'survival of the fittest') each succeeding generation of the population becomes, on average, better adapted to its environment. The incredible success of this optimisation method can be seen in the variety of life on earth. Applying this method to the computational optimisation of non-biological problems might be expected to result in equal success. However, biological optimisation takes place over geological time-scales. It therefore might also be expected that the evolutionary procedure might not be particularly fast. In fact, simple implementations of GAs have demonstrated efficiencies that are comparable with the best directed search algorithms. So far there have been relatively few reports of the use of GA techniques in structural optimisation. Hajela & Lin [1992] and Dhingra & Lee [1993] both used GAs to optimise lattice structures. The report by Kasper [1991] is the only instance known to the author of GA optimisation being combined with the FE method. Kasper optimised the geometry of multiple conductors using a genetic algorithm with electromagnetic FE analysis.

8.2.3 Choice of algorithm

The ideal algorithm should be reliable, efficient and easy to implement. However, no one algorithm is superior to the others in all these respects. In deciding on the choice of algorithm, some attempt must be made to rank the importance of these characteristics. In the application considered here, the optimisation process will be

carried out reasonably infrequently. Having a fast efficient algorithm is therefore less important than in the case in a real-time application or where the optimisation would be required to be repeated many times. Ease of implementation and reliability are both of greater priority. Gradientless methods are generally easier to implement and with such a complicated objective function this is particularly likely to be so in this case. In general the random gradientless methods are also more reliable than the gradient methods. The choice of method in this case was therefore between the two random gradientless methods, simulated annealing and genetic algorithms. The judgement of the author was that the implementation of both these algorithms would be of similar complexity. The author had no evidence to suggest whether one of these algorithms was more reliable or efficient than the other. The choice between the two algorithms was therefore to a large degree arbitrary as it was felt that either would be equally suitable. The deciding factor between the two was the author's long standing interest in evolution, fostered by the popular books of Richard Dawkins and Stephen Jay Gould. The use of genetic algorithms therefore had more appeal and the decision was made in their favour.

8.3 The simple genetic algorithm

8.3.1 Introduction

The idea of a genetic algorithm is to harness the remarkable power of evolution by computationally emulating its processes. The biological version of evolution is in fact far from simple and it is therefore not practicable to incorporate all of its subtleties. However, several ways of implementing the basic mechanisms of evolution have been developed. The techniques adopted here are those pioneered by Holland. Overviews of the GA technique have been given by Holland [1992] and Forrest [1993]. A full account of the theory and practice of genetic algorithms can be found in Goldberg [1989]. However, a brief account of the basic principles and theory of what is known as the simple genetic algorithm will be given here.

8.3.2 String representation

Genetic algorithms involve the representation of a combination of design variable values as a string. Each of these 'individuals' represents a possible solution to the optimisation problem. In the problem considered here each individual string represents a possible load cell geometry. The string in the GA is analogous to the chromosome in genetics. However, unlike the biological implementation, most GAs use only a single string to encode each individual's characteristics. The simplest format for encoding the variable values is as a string of binary bits. Each bit by

biological analogy is named an allele. The position of each allele in the string determines its value and which variable it represents. For example the following string represents three variables, each encoded as eight bit values:

'100110111101011000010111'

For clarity this string will be written as:

AaaAAaAABBBbBbBBbcccCcCCC

where a upper-case letter represents binary 1 and a lower-case letter binary 0. The variables A, B and C therefore have decimal values 155, 214 and 23 respectively. Representations with higher cardinality are found in nature and have been used in some GA implementations. However the binary system is the simplest and the most general.

The universe of all possible strings defines the variable space in which the optimisation is to be carried out. A population of individuals can be represented by a set of such strings. Once an initial population of these strings has been created, the simulated processes of evolution can be applied to the population. In nature these processes are continual. However, in the simple genetic algorithm the evolutionary process is carried out generation by generation, with no survival of individuals from one generation to the next. Each new generation has the same number of individuals as its predecessor, each being created by a process of reproduction.

8.3.2.1 Selection of breeding pairs

In the simple genetic algorithm all individuals are asexual and are therefore able to mate with any other individual. In nature whether an individual reaches breeding age depends on a combination of random factors and on what has come to be referred to as the individual's fitness. The selection of mating pairs is determined by a combination of happenstance and attraction of one individual by another. This attraction is itself usually an expression of the individual's fitness. If the GA breeding process is to accurately mimic the biological process, the pairing of individuals should also combine random and fitness components. The selection process used could be described as 'breeding of the fittest'. Pairs of individuals to be mated are drawn from the population, with the selection process adjusted such that the probability of an individual's selection is approximately proportional to its fitness. It has been shown that the inclusion of a random component is essential to the correct functioning of

GAs. and that such a selection process out performs algorithms in which selection is based on fitness in a deterministic way.

The first few generations of population usually contain a few extraordinary individuals. Setting the selection probability proportional to an individual's fitness results in these high fitness individuals quickly dominating subsequent generations. This rapid convergence is undesirable as the global optimum may be missed. In this case it is therefore desirable that the range of selection probabilities be reduced. Conversely after many generations the maximum fitness is likely to be close to the mean fitness. If pressure for evolutionary improvement is to be maintained, the difference between the mean and maximum selection probability must be exaggerated. The necessary adjustments to the selection mechanism are made by applying a linear scaling to the fitness values.

8.3.2.2 Crossover

Each pair produces two offspring. In order that the new generation are not all simply copies of their parents, a method for combining the strings of the parents is required. The simple genetic algorithm employs a method named crossover that is analogous to the exchange of genetic material which takes place during fertilisation. In the biological case, some genetic exchange always take place. However, in the case of the simple genetic algorithm a random variable is tested to decide whether crossover takes place. If no crossover occurs the offspring are clones of their parents.

In the crossover process a point along the string is selected at random. Both strings are cut at this crossover point, the right hand portions exchanged, and rejoined to the left hand portions to create two new strings. For example using our previous notation:

Parent1 = AaaAAaAABbBbB|BbcccCcCCC

Parent2 = AaAAAaAaBbbBBB|bBcCCcccC

If crossover takes place at the position indicated by the bar, the following children will be produced:

Child1 = AaaAAAaAABbBbBbBcCCcccC

Child2 = AaAAAaAaBbbBBBBbcccCcCCC

8.3.2.3 Mutation

The final process implemented in the simple genetic algorithm is mutation. In this a small number of randomly selected bits from the strings of the new population are flipped to their opposite state. For example the previous child strings might be mutated to:

Child1 = AaaAaaAAB**Bb**BbBbBCC**C**cccC

Child2 = AaAAAaAabbbBBBBbcccc**C**CC

where the underlined characters represent those that have been subjected to mutation. It might be thought that such random mutation would be both unnecessary and disruptive to the evolutionary process. In fact it has been shown that a small rate of mutation is essential to maintain diversity in the populations and to allow the introduction of characteristics which are absent from the original string population.

8.4 Theory of the simple genetic algorithm

The simple genetic algorithm outlined above can be thought of as a search of the variable space with each individual representing a point in that space. It seems reasonable that breeding from the best individuals in successive populations will result in individuals which have higher and higher fitness. However, it is an essential part of the method that the search has a large stochastic element. It is not immediately obvious why adding a large degree of randomness improves rather than degrades the method. In all but trivial problems the number of points evaluated will be only a small fraction of the total points in the search space. It is therefore also not immediately evident that the method is likely to find and converge on the global rather than a local optimum.

8.4.1 Schemas

In order to understand the mechanism of the GA search, the concept of the schema must be introduced. A schema is a template describing patterns of bits in a string. A schema is represented by combinations of the symbols 0,1 and *, where * represents a 'don't care' bit. For example the 3-bit string '100' expresses the following seven schemas: '1**', '*0*', '**0', '10*', '1*0', '*00', and '100' (as well as the global '***'). The first three of these represent planes, the next three lines, and the last a point in the 3-dimensional search space of this example. In the higher dimensional space of the more general problem each of the schemas represent a hyper-plane. If each string has k bits each individual expresses 2^k schemas. The number of schemas is

therefore very much greater than the number of individuals. While it is unlikely that two individuals within a population will share identical strings, many schemas will be shared by several individuals. In evaluating the fitness of an individual, the fitness of all the schemas it expresses are also evaluated. The selection and reproduction process serves to preserve and replicate those schemas that give high fitness while selecting against those that reduce fitness. The genetic algorithm therefore really implements 'survival of the fittest schemas'. The number of schemas is much greater than the number of individuals evaluated. As most schemas cover a large number of points in the search space, the search method is highly parallel.

8.4.2 Crossover

Crossover is one of the means by which new strings and therefore new schemas are created. The generation of new schemas ensures that new areas of the variable space are searched. This advantage is however offset by the risk that the crossover process will break up existing high fitness schemas. Under the simple genetic algorithm, although crossover is a random process, some schemas are more susceptible to being broken up than others. The probability that a schema will be broken up is proportional to its defining length. A schema's defining length is the distance between the leftmost and rightmost non '*' bits in the schema. For example '*1001*' has a defining length of 3, whereas '*1*0*1*' has a defining length of 6. The defining length is equal to the number of sites within the schema at which crossover would lead to its break up. The second schema is therefore twice as likely to be broken up by the crossover process as the first schema.

Whether this bias against long schema affects the effectiveness of the algorithm depends on the mapping of the problem to the string. This can be illustrated by the biological example of optimising the body form of an animal for browsing the leaves of tall trees. Several alternatives could be used to map the body form to a string. If the area encoding length of legs is located a large distance from the area encoding length of neck, the schema for the combination of long legs and long neck will have a long defining length and therefore poor prospect of survival. However, encoding leg length and neck length in adjacent areas of the string would result in a short defining length and a good prospect for the evolution of a giraffe type animal. Care must therefore be taken in mapping the problem to the string to ensure that those characteristics which are likely to be complementary are mapped to neighbouring areas. However it is not always possible to predict which characteristics are likely to interact in this co-operative manner. In these situations, the bias against schemas with long defining

length can be overcome by replacing simple crossover by an algorithm incorporating reordering.

8.4.3 Reordering

In the simple genetic algorithm described above, the function of each allele is defined by its position in the string. In nature this direct correspondence is absent. Instead the function of a particular allele is independent of the position in which it appears. In the genetic algorithm a similar position-independence can be achieved by storing an index array alongside the string of alleles. The function of each allele is then defined by the corresponding entry in the index array rather than its position in the string. Under this system the following index string pairs would all represent the same gene values:

Index: '12345678'

String: '01100101'

Index: '87654321'

String: '10100110'

Index: '63715248'

String: '11000101'

As they all represent the same gene values, all the 40,320 possible representations have the same fitness. It might therefore be expected that there would be no advantage in varying the string order. However, consider the schema for allele '1', '5' and '7' all being 0. This schema is present in all the above strings. We can express the schema using the same index representations as above:

Index: '12345678'

Schema: '0***0*0*'

Index: '87654321'

Schema: '*0*0***0'

Index: '63715248'

Schema: '**000***'

The first two of these representations have defining lengths of 6. The last representation has a defining length of 2 and is therefore three times less likely to be destroyed during crossover. In a population containing all the above representations of the same string, the last representation of the above schema is likely to survive and multiply at the expense of the others. The survival prospect of a schema can therefore be improved by reordering its index. It is unlikely that each schema present in the initial population will be in its optimum order. However, if it can be arranged that allele order be inherited in the reproduction process, a mechanism will be created by which the optimum order can evolve in parallel with the evolution of optimum allele values.

Several methods for implementing inheritance of index order have been proposed. One method is known as 'partially matched crossover' and is abbreviated PMX. Its mechanism is best indicated by example. Consider two parent strings and indices:

```

Parent 1:   Index: '12|754|683'
            String: '11|000|101'

Parent 2:   Index: '46|823|571'
            String: '00|111|001'

```

Two crossover locations are chosen at random, in this case before the third and sixth alleles. The two string sections between these points are exchanged and then used to map the indices and alleles from one string to the other. In our example, the sections '754' and '823' are first exchanged. In the remaining portions of the each string 7 is exchanged with 8, 5 with 2, and 4 with 3. The corresponding alleles also undergo the same exchanges between strings. In our example the resulting strings are:

```

Child 1:    Index: '15|823|674'
            String: '10|111|100'

Child 2:    Index: '36|754|281'
            String: '10|000|101'

```

In this way each child inherits some of the storage order characteristics of each parent together with allele value information. This reordering allows high fitness schema of small defining length to evolve, regardless of the initial choice of mapping between allele function and string position.

8.4.4 Mutation

Without mutation, the population converges very rapidly on a solution. However the rapid loss of schema this involves can result in the premature loss of some high fitness schema which are under represented in the initial population. The solution found may then represent a local rather than global optimum. Raising the mutation rate slows the convergence of the population but reduces the mean fitness of the converged population. In practice a compromise is often applied. In this a high mutation rate is applied initially and the mean fitness of the population is monitored during the run. Once the population appears to have converged and no further improvement in mean fitness is observed, the mutation rate is reduced and the run continued. This process may be repeated, the mutation rate being reduced each time. The initial high mutation rate ensures that all areas of the variable hyper-space are searched, while the eventual low mutation rate ensures the population converges on the global optimum.

8.5 Choice of GA parameters

A set of genetic algorithm routines were written implementing the simple genetic algorithm using either simple crossover or partially matched crossover. The algorithm is governed by the parameters shown in table 8.1.

GA parameter	Value adopted
No of genes	as required
Gene length (in bits)	as required
Population size	100
Truncation factor	2
Survival factor	2
Crossover probability	0.6
Mutation probability	0.0333/0.0033

Table 8.1: Parameters governing GA optimisation algorithm

The first two of the parameters are determined by the number of design variables and the accuracy required. The values of the remaining five have a large effect on the efficiency and effectiveness of the optimisation. It is not possible to choose values for these parameters which optimise the performance of the GA routine for all problems. Choosing appropriate values is a matter of judgement and experiment. However, guidance can be obtained from the results of experiments carried out on the performance of GAs applied to a variety of test problems. In particular a study by De Jong [1975] studied the performance of GAs applied to a suite of test problems. The recommendations of this study, together with experience gained through use of

the above GA implementation on test problems, lead to the adoption of the values given in the second column of table 8.1. Unlike the other parameters, the value of mutation probability was usually modified during a run. Initially it was set to 0.0333 but was usually decreased to 0.0033 later in the run to improve convergence of the population on the solution.

8.6 Performance of GA routines on trial problems

In order to verify the functioning of the GA routines a simple optimisation program `ga_test.F` was written. The program was tested on trial optimisation problems with known solutions. The results from two of these optimisations will be presented here.

The first trial problem is the maximisation of the following function:

$$\phi(x, y) = 5f(x - 5) + 5f(y + 1) \quad 8.1$$

where the function $f(z)$ was defined by:

$$f(z) = \cos\left(\frac{z\pi}{2}\right) \text{ for } -1 < z < 1 \quad 8.2$$

$$\text{and } f(z) = 0 \text{ for all other values of } z \quad 8.3$$

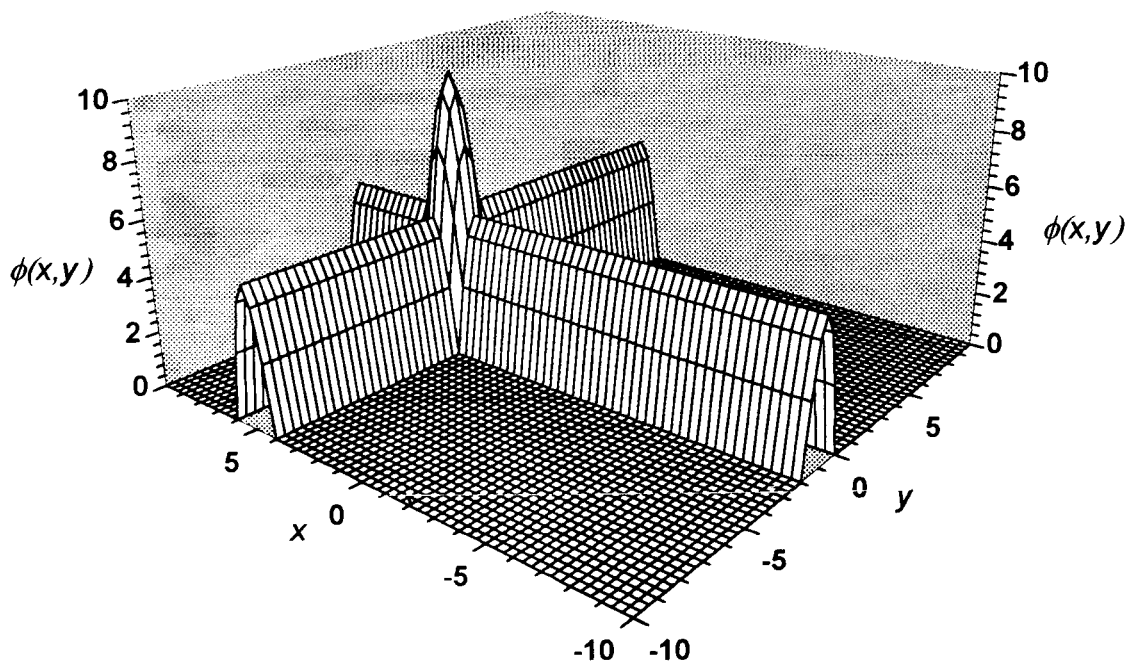


Figure 8.1: Function used in first trial GA optimisation

The surface defined by this function is illustrated in figure 8.1. The maximum value of the function is 10 and the optimum values of the parameters are $x = 5$ and $y = -1$. For the trial optimisations two 14 bit genes were used to represent x and y over the interval -10 to 10.

Figure 8.2 shows the mean fitness of each population of strings plotted against generation number for three runs using simple crossover. It can be seen that despite the different, randomly chosen, starting populations, the three runs display similar rates of convergence and finish with similar mean fitness values. In each case convergence was achieved within 20 generations.

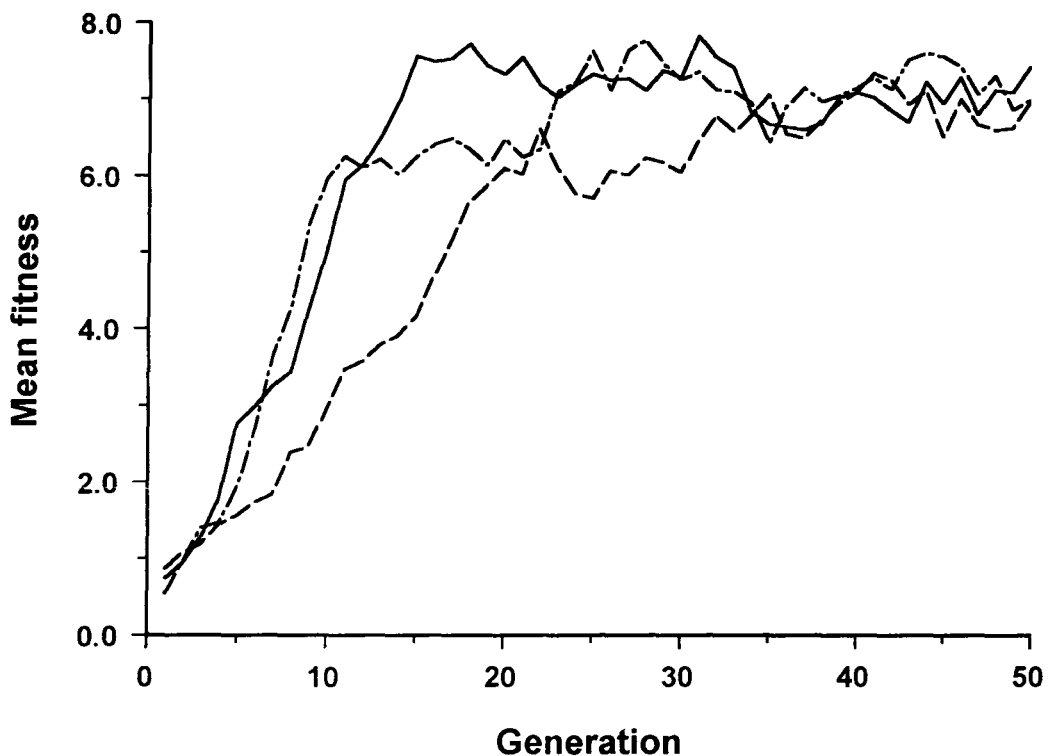


Figure 8.2: Three runs on first trial problem - without reordering

Figure 8.3 shows the mean fitness values together with the mean values of x and y during one of the runs. It can be seen that both variables converge on their optimum values very quickly.

Maximisations of this function were also carried out using partially matched crossover. The performance of the GA routines with PMX was very similar to that with simple crossover. That the addition of this reordering operator did not lead to any

improvement in performance is not surprising as the optimum values of x and y are in this case independent.

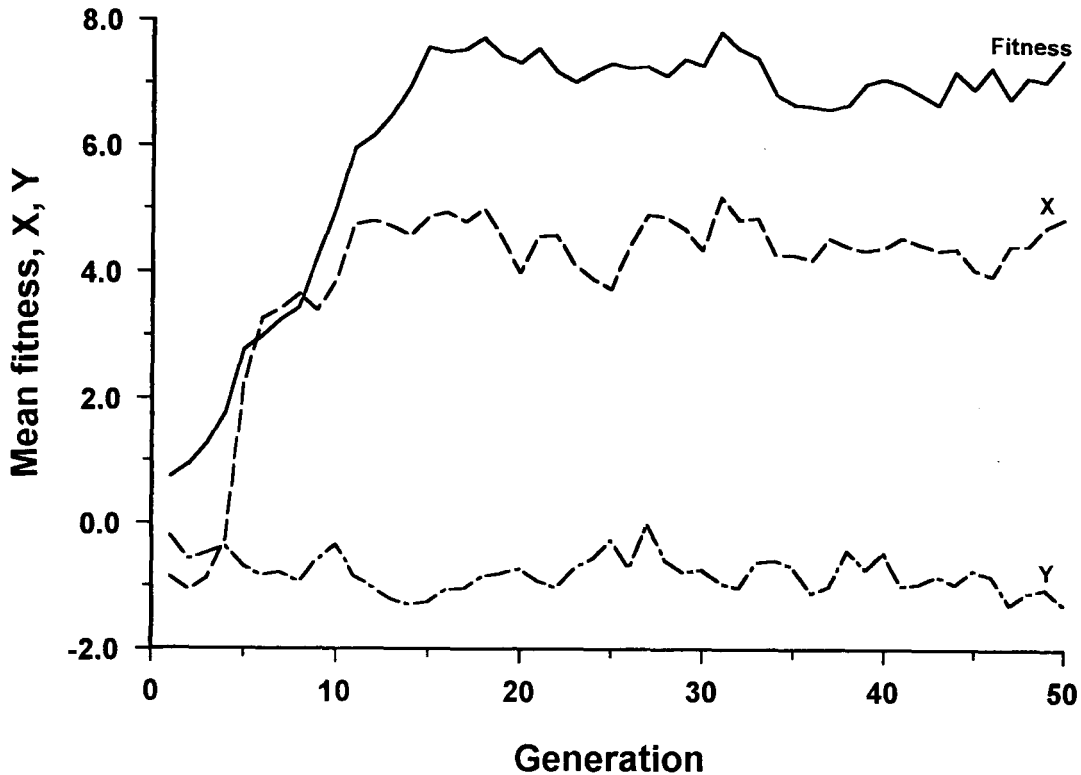


Figure 8.3: Mean fitness, X, and Y for run on first trial problem - without reordering

In order to test the implementation of partially matched crossover, a second problem was constructed in which the optimum values of the variables are dependent on each other. The second trial problem was the maximisation of the function

$$\phi(x, y) = 5 \times \max(f(x - 10), f(y - 10)) + 10f(r) \quad 8.4$$

$$\text{where } r = \sqrt{x^2 + y^2}$$

This function, plotted in figure 8.4, has a global optimum at $r = 0$. However unlike the previous function the optimum values of x and y are related. For the trial optimisation x and y are represented by 10 bit genes over the interval -10 to 10. Although there are only two variables, twenty such genes were used. x was assigned *gene_value*(1) and y assigned *gene_value*(20). The 18 genes between x and y played no part other than to separate the two active genes and increase the defining length of the initial schemas.

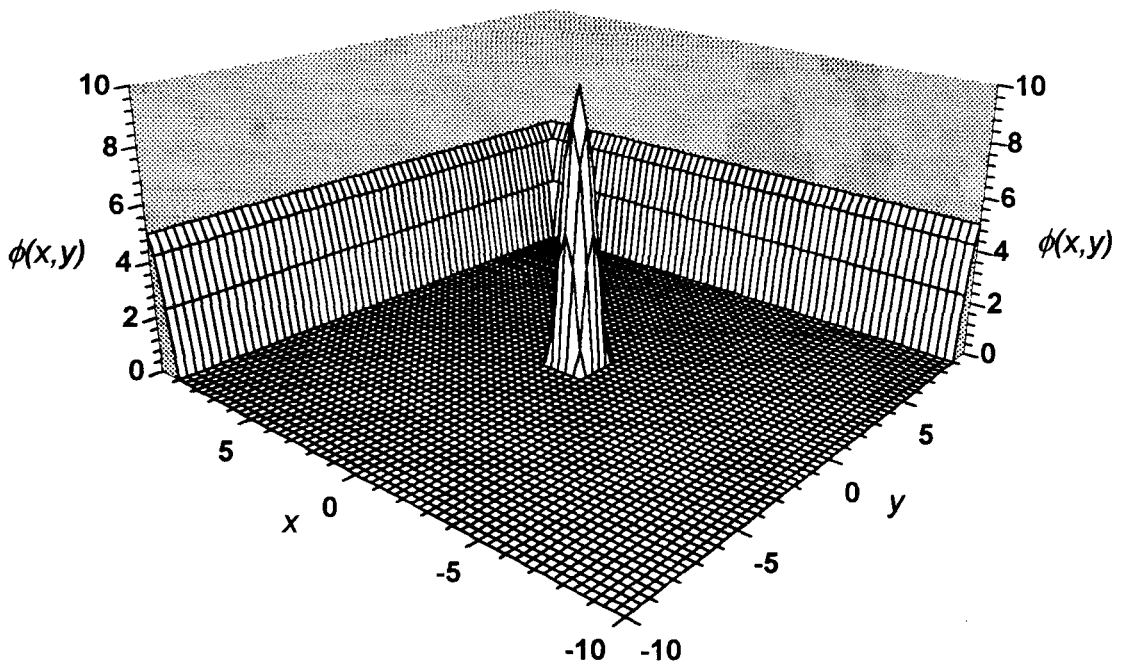


Figure 8.4: Function used in second trial GA optimisation

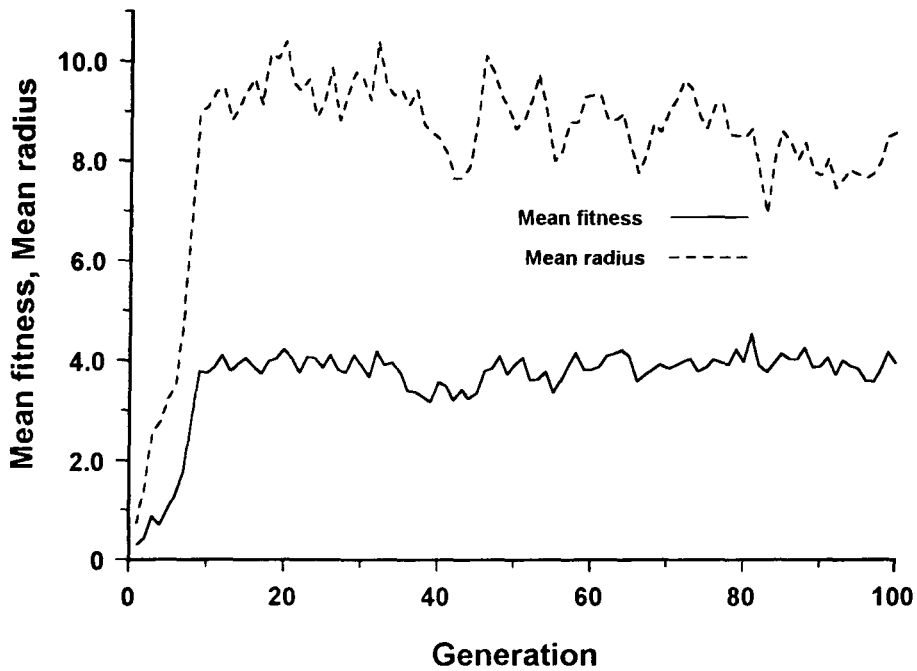


Figure 8.5: Mean fitness and radius for run on second trial problem - without reordering

Figure 8.5 shows the mean fitness levels of the population during a run with simple crossover. Also plotted is the mean value of r in each generation. It can be seen that the population has converged but not on the global optimum. Approximately two thirds

of the runs with the simple crossover algorithm exhibited this behaviour. The remaining one third of the runs converged on the global $r = 0$ optimum.

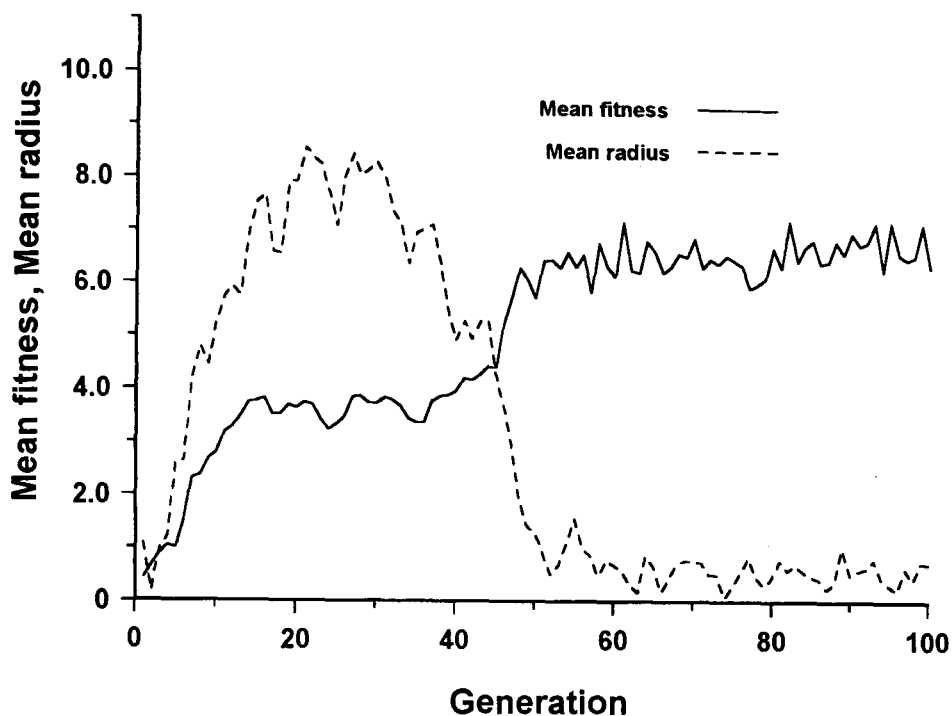


Figure 8.6: Mean fitness and radius for run on second trial problem - with reordering

Approximately one third of the runs maximising the same function using partially matched crossover also converged directly to the global optimum. Figure 8.6 shows the behaviour of a run typical of the remaining two thirds. Initially the behaviour was similar to that of the simple crossover routine. However after apparently converging on a local minimum for a period, the algorithm converged on the global optimum. This trial problem illustrates the advantage of the PMX routine. With simple crossover the genetic algorithm routine failed to find the global optimum for two thirds of the initial starting populations. With the PMX routine the algorithm eventually converged on the global optimum for all of the twenty starting populations tested.

8.7 Conclusions

A set of routines for implementing the simple genetic algorithm, both with and without reordering have been written. Tests have verified the operation of the routines on simple trial problems. The application of these routines to the optimisation of load cell geometry will be described in the next chapter.

THE 'DARWIN' LOAD CELL

9.1 Introduction

In previous chapters:

An accurate finite element model of axisymmetric load cells subject to various contact conditions has been developed and verified.

A parameterised representation of load cell geometries has been developed.

A simple method for automatically generating a 2-D finite element mesh of a parameterised load cell geometry has been developed.

Two numerical measures of the insensitivity of load cells have been defined.

A set of genetic algorithm function optimisation routines have been developed and tested.

This chapter describes a program which brings together these components. The program is used to optimise the shape of a low-profile 3 MN load cell.

9.1.2 The POGLE program

Routines implementing the above components have been described in previous chapters. A program which calls these subroutines so as to carry out a GA optimisation of load cell geometry was developed from the programs described in previous chapters. This program was named POGLE (Program for Optimising the Geometry of Load cell Elements). The program starts with a random population of strings. A call to a subroutine decodes each string to give the values of the geometric parameters. These parameters are the central hole radius, aspect ratio, inner radius of contact area, outer radius of contact area, and the control points of the Bézier curve. A call is then made to a subroutine to evaluate either EN-immunity or PCCU-immunity depending on which measure of fitness is to be maximised. Once the fitness of each of the strings has been evaluated, a call is made to a subroutine which 'breeds' and returns a new population of child strings. The process of evaluation and

breeding is repeated for each new generation. This iterative process is repeated until the program is interrupted.

9.2 Optimisation of 3 MN low-profile column load cell

In order to test the program a trial optimisation problem was required. Rather than choose an arbitrary problem it was decided to attempt to meet a requirement which conventional load cell development methods had failed to satisfy. The problem chosen was the design of a low profile 3 MN load cell for the calibration of concrete-cube testing machines.

9.2.1 Calibration of concrete-cube testing machines

In order to ensure that concrete used in construction is of the required strength, test samples are taken from each batch. The samples are poured into a cube-shaped mould and cured under controlled conditions. Once fully cured each cube of concrete is loaded to destruction in a specially designed test machine. The machines used in the tests have capacities of either 2 MN or 3 MN and are required to be calibrated to EN10002-3 class 1. The working spaces of these machines are designed to accommodate the moulded cubes of concrete, and have very little additional 'daylight' in which to accommodate a calibration device. At present these machines are calibrated using either dial gauge load columns or multi-column load cells. Dial gauge load columns are difficult to use, easily damaged, and do not lend themselves to modern calibration techniques. Multi-column load cells do not suffer from these disadvantages, but their complex construction and gauging makes them very expensive.

A single-column load cell would be cheaper to manufacture than multi-column load cells and be more robust and easier to use than the dial gauge columns. However, conventional design methods have failed to develop single-column load cells which both fit within the limited working volume and pass the bearing pad test for class 1. The POGLE program was used to develop a load cell for this application.

9.2.2 Problem specification

The problem is specified by the values of its fixed parameters. Some of these values, such as the maximum height, are explicitly defined by the problem. However, most parameters, like the maximum mean contact stress, have a range of acceptable values. Some degree of judgement is therefore required in assigning values to these parameters. The chosen values of the problem parameters are shown in table 9.1:

Parameter	Value	Notes
Maximum load	3 MN	
Minimum load	300 kN	
Maximum height	200 mm	Maximum height which can be accommodated in all concrete-cube machines.
Nominal strain gauge bridge output	2 mV/V	20 mV output for 10V excitation at maximum load
Gauge factor	2.05	Mean value for constantan gauges
Active gauge area	6.35 mm x 6.35 mm	¼" square gauges
Maximum mean contact stress	400 MNm ⁻²	Compatible with the very hard platens of concrete-cube machines.
Young's modulus	211 GNm ⁻²	Average value for high tensile steel
Poisson's ratio	0.3	Average value for high tensile steel
Maximum friction at contact surface	0.3	Median reported value for clean steel-steel contact

Table 9.1: Parameters specifying problem for 3 MN load cell

In addition to the variables which define the problem, there are other parameters which control its modelling and representation. The values chosen for these variables are given in table 9.2.

Parameter	Value	Notes
Minimum height	140 mm	
Maximum radii of Bézier control points	110 mm	
Number of load increments	20	Sets no. of increments used by contact routine
Gene length	10 bits	1 LSB approx. equivalent to 0.1 mm on radius or 0.06 mm on height
Population size	100	
Cross probability	0.6	
Mutation rate	0.033/0.003	Reduced after 30 generations
Truncation factor	2.0	
Survival factor	2.0	
Reordering	On	

Table 9.2: Parameters specifying modelling of 3 MN load cell

9.3 Results from the GA optimisation

Two separate series of runs of the program were carried out. In the first series the program used EN-immunity as the fitness measure. In the second the fitness measure was PCCU-immunity. In both cases, each run was started with a mutation rate of 0.033. During execution the mean fitness of each generation was monitored and assessed for convergence. It was judged that each population had converged after 30

generations. In order to encourage further improvement in the population the rate of mutation was then reduced to 0.003 and the program restarted. After a further 20 generations the program was stopped. Figure 9.1 plots the mean fitness against generation number, for one of the runs to optimise PCCU-immunity. The individuals in the final generation had a mean fitness of 158.9. Similar values were recorded for the other three runs.

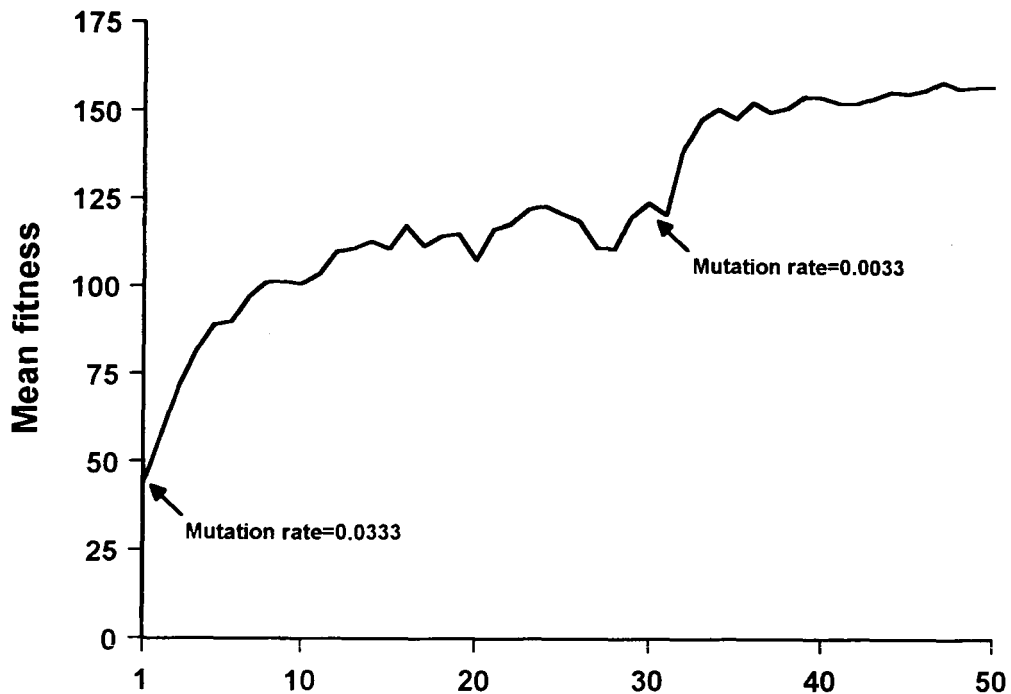


Figure 9.1: Mean fitness v generation for PCCU-immunity optimisation

For each of the two immunity measures the program was run four times. Examination of the individuals in each of the final populations showed that with the exception of a few 'lethals' the individuals within each population were very similar to each other and to the individual with maximum fitness. In addition, for each of the objective functions, there was found to be little difference, run to run, between either the fittest individuals or the final generations

9.3.1 Optimisation of EN-immunity.

The FE mesh of the individual with the overall maximum EN-immunity is shown in figure 9.2. This design has an overall height of 163.4 mm, a central hole of 7.3 mm and a maximum radius of 82.2 mm. A raised contact surface extends from 31.6 mm radius to 58.1 mm.

The EN-immunity of this design was calculated to be 284,932. This compares with the Class 00 EN-immunity limit of 500. A plain solid cylinder of equal height is calculated to have an EN-immunity value of 98. As measured by EN-immunity the performance of the evolved design is therefore very impressive. However, the PCCU-immunity of the design is calculated to be 96, a much smaller improvement over the 23 PCCU-immunity value calculated for the plain cylinder of equal height. The change in the relative merits of the two designs is dramatic and indicates the strong influence of the contact coefficient of friction on this design.

9.3.2 Optimisation of PCCU immunity

The automatically generated FE mesh of the individual with highest PCCU-immunity is shown in figure 9.3. This design has a mid-height radius of 55 mm, a maximum radius of 86 mm, and height of 185 mm. Unlike the design optimised for EN-immunity it has no central hole and contact takes place over the entire surface of the plane ends..

The design was calculated to have a PCCU-immunity of 173. This compares with the calculated PCCU-immunity of a plain solid cylinder of equal height of 22. By this measure the evolved design is therefore a significant improvement over this simple geometry. The EN-immunity of the design was calculated to be 2,349. This is a significant improvement over the figure of 81 calculated for a plain cylinder of equal height, but inferior to the EN-immunity design's value of 284,932. The fitnesses of the two optimised geometries and solid cylinders of equal height are summarised in table 9.3.

	Height	EN-immunity	PCCU-immunity
Shape optimised for EN-immunity	163.4 mm	284,932	96
Solid cylinder equal in height to above	163.4 mm	98	23
Shape optimised for PCCU-immunity	185 mm	2,349	173
Solid cylinder equal in height to above	185 mm	81	22

Table 9.3: Comparison of designs optimised for EN-immunity and PCCU-immunity

When judged against both the performance measures, the design optimised for PCCU-immunity was judged to offer better all-round performance than the design optimised for EN-immunity. In addition the absence of a central hole and the plane ends would simplify its manufacture. It was therefore decided to further investigate

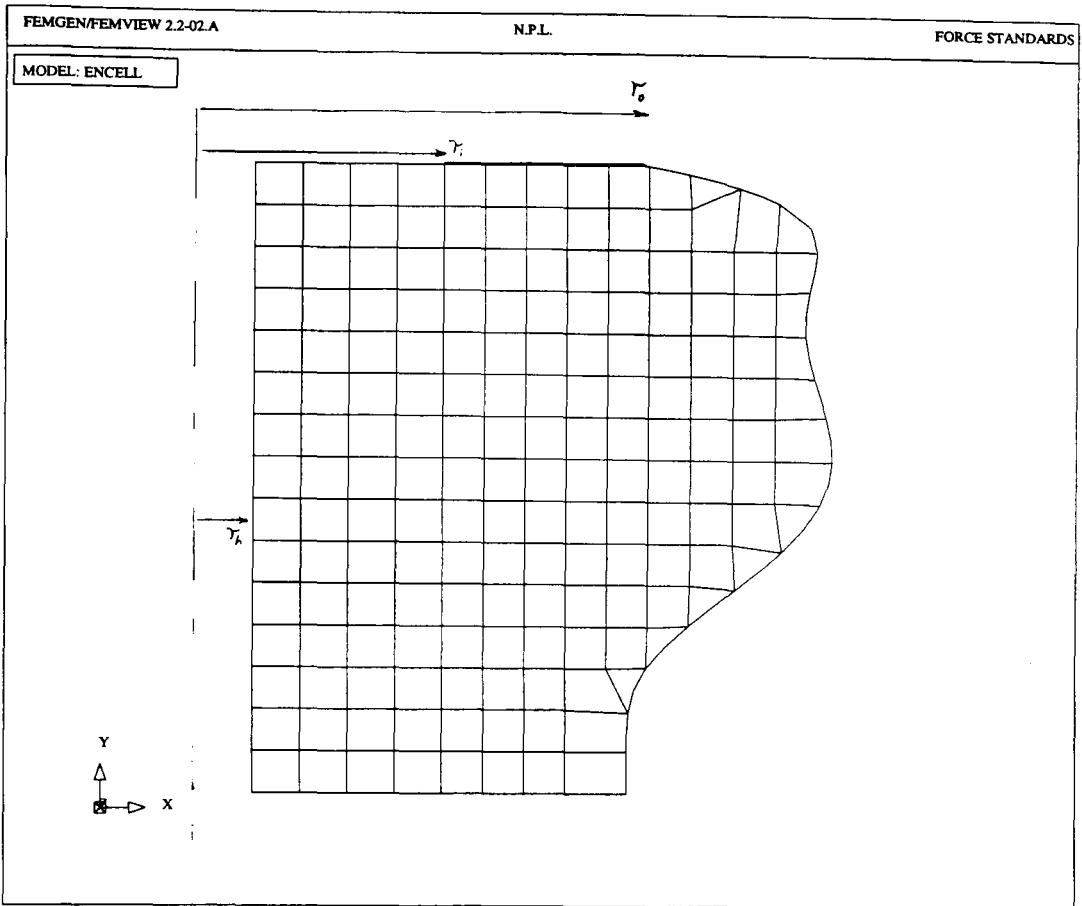


Figure 9.2: Mesh of load cell optimised for EN-immunity

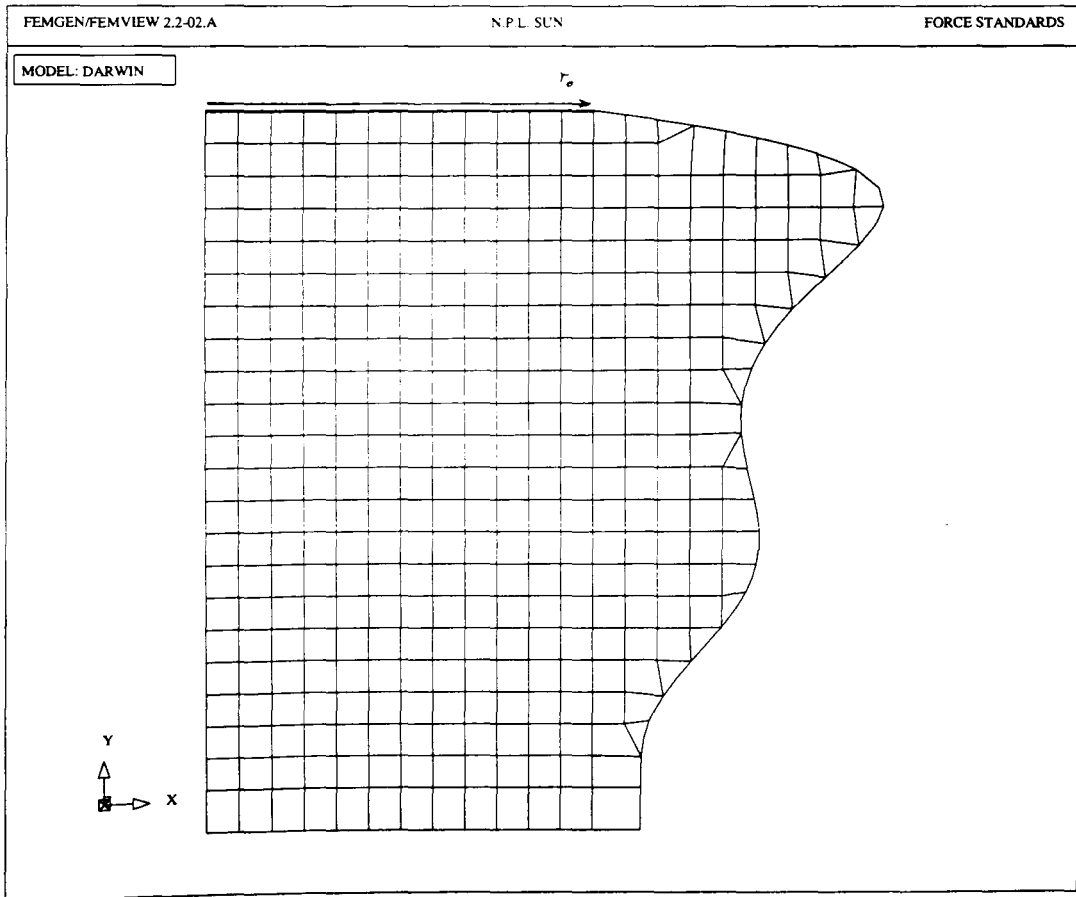


Figure 9.3: Mesh of load cell optimised for PCCU-immunity

this design. The design was named 'Darwin' in recognition of the role played by evolutionary principles in its development.

9.4 End-loading sensitivity of 3 MN load cells with solid and hollow circular cylindrical elements

In order to provide a comparison for evaluating the Darwin design, the EN-immunity and PCCU immunity values of 3 MN load cells of plain and hollow cylindrical shape were calculated. While it is rare for load cells to have such simple shapes, the results illustrate the effect of varying aspect ratio and internal radius.

The radii of the cylinders were adjusted such that both the hollow and solid cylinders were of the same cross-sectional area as the mid-plane of the Darwin design. All designs therefore give an output of approximately 2 mV/V. The FE calculated fitness measures are presented against aspect ratio in figures 9.4 and 9.5. The solid lines show the fitness of solid cylinders. The four broken lines represent hollow cylinders of internal bore radii: $0.2r_o$, $0.4r_o$, $0.6r_o$ and $0.8r_o$, where r_o is the radius of the solid cylinders. The aspect ratio for these hollow cells are also referred to the solid cylinder radius (i.e. aspect ratio=height/ $2r_o$). The horizontal dotted lines in figure 9.4 denote the limits for the four EN 10002-3 classifications.

9.4.1 EN immunity of circular cylinders

The curves in figure 9.4 show the variation of the EN-immunity of 3 MN cylindrical load cells with aspect ratio and hole radius. Each curve displays a low aspect ratio and a high aspect ratio peak. It can be seen no one hole diameter is superior over the whole range, rather the optimum hole size varies with aspect ratio. An interesting feature is the peak of the solid cylinder curve at aspect ratio 1.3. A solid cylinder of this aspect ratio is predicted to have a EN-immunity superior to any other cylindrical load cell of aspect ratio less than 2.4. The results indicate that such a low-profile design would satisfy the bearing pad test requirements for class 1.

9.4.2 PCCU-immunity of circular cylinders

The values of PCCU-immunity calculated for solid and hollow cylinders are plotted in figure 9.5. Comparison with figure 9.4 reveals the effect of variation in the contact coefficient of friction. It is apparent that including load cases with zero contact friction in the fitness measure has a significant effect on the relative merits of solid and hollow cylinders. The change in contact friction has a disproportionate effect on the hollow load cells. This results in the solid cylinders having equal or superior PCCU-immunity

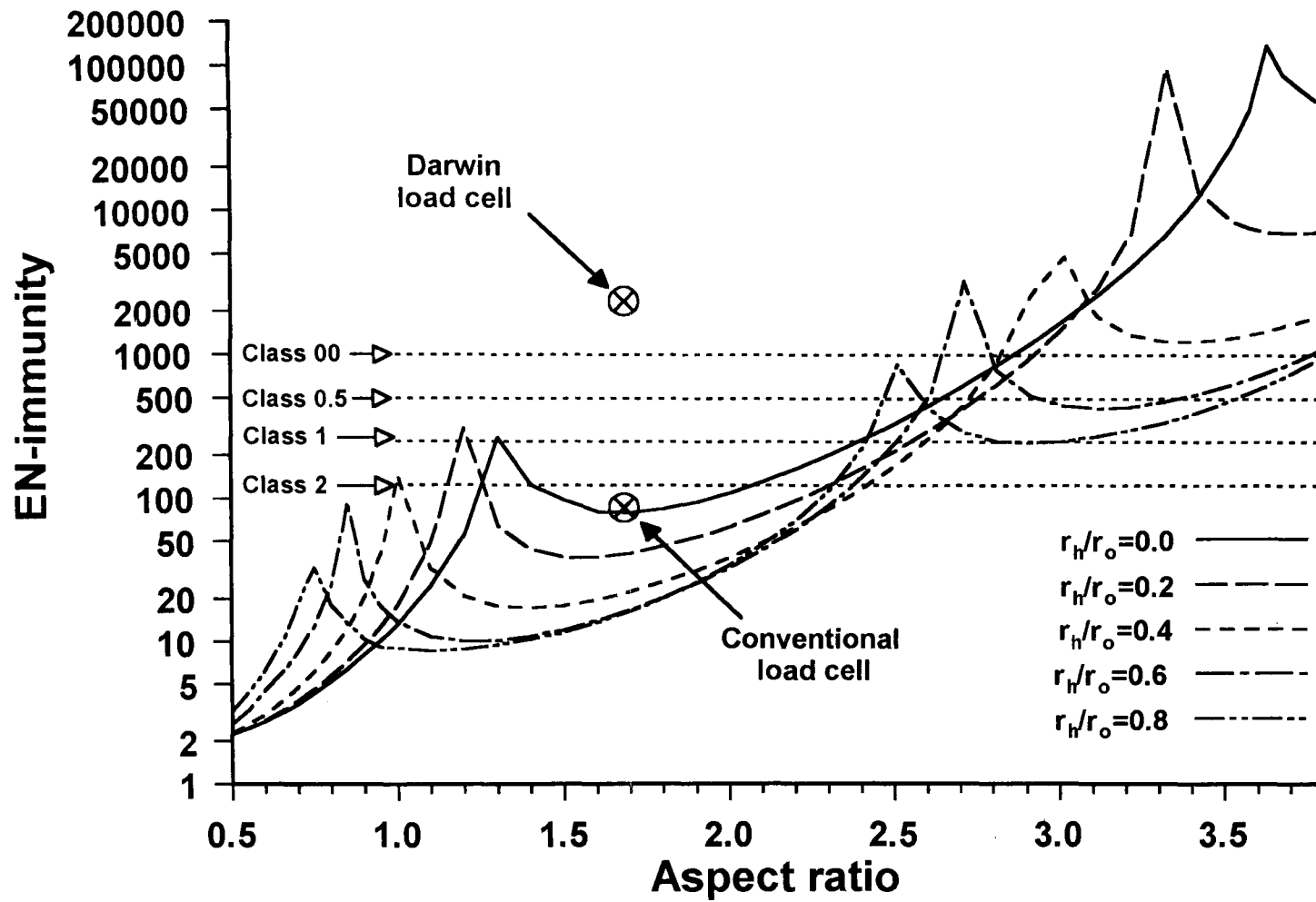


Figure 9.4: Comparison of EN-immunity of cylindrical, Darwin and conventional load cell designs

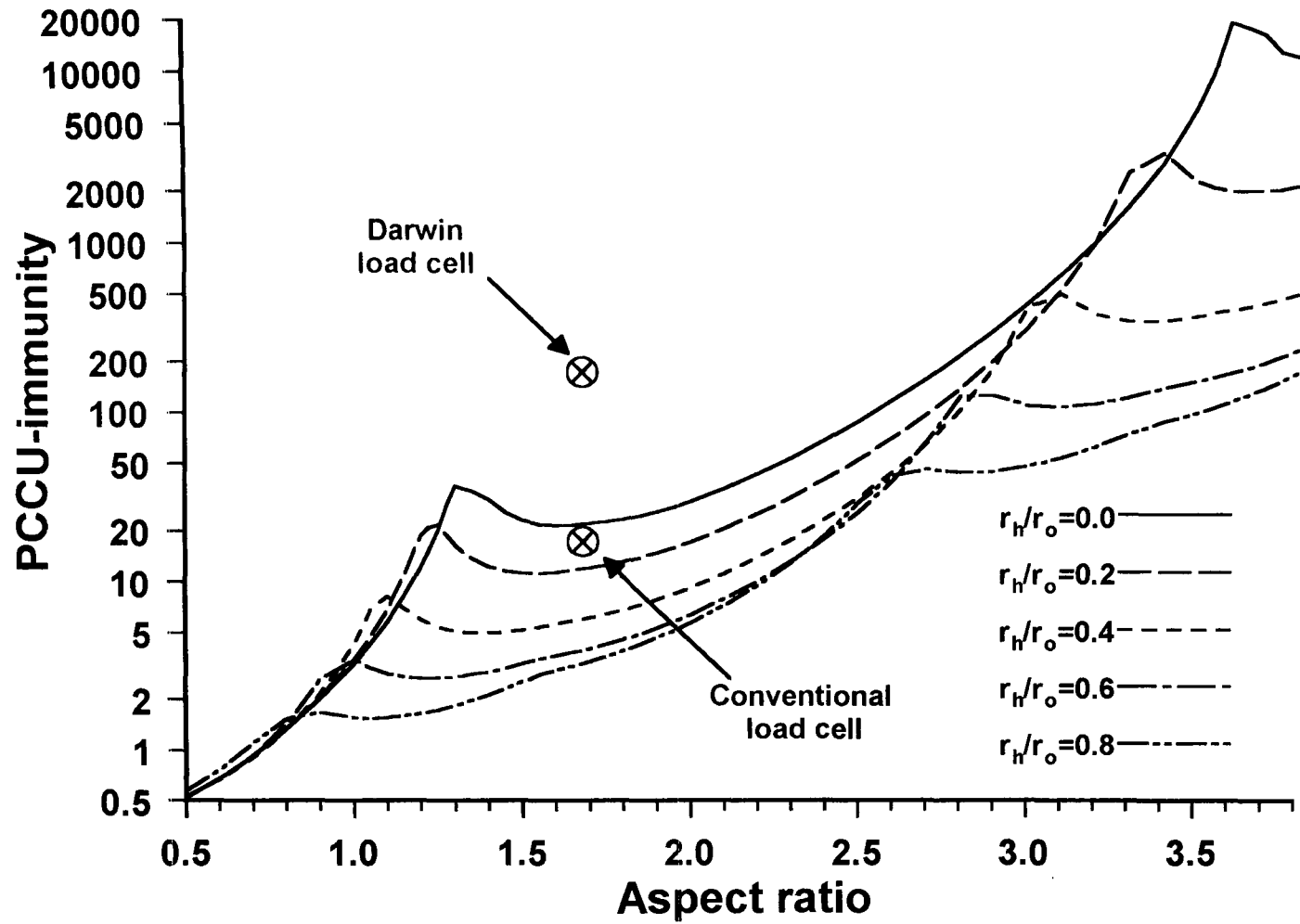


Figure 9.5: Comparison of PCCU-immunity of cylindrical, Darwin and conventional load cell designs

values throughout almost the entire range of aspect ratios. Like the EN-immunity, the solid cylinder PCCU-immunity peaks at an aspect ratio of approximately 1.3.

9.4.3 Comparison of Darwin design with cylindrical load cells

The calculated values of EN-immunity and PCCU-immunity for the Darwin load cell have been marked on figures 9.4 and 9.5.

It can be seen from figure 9.4 that the Darwin load cell design is predicted to easily pass the bearing pad test requirements of class 00. The Darwin design has an EN-immunity 52 times that of a solid cylinder of equal aspect ratio and an EN-immunity higher than any solid or hollow cylindrical design of aspect ratio less than 2.7.

It is apparent from figure 9.5 that the Darwin cell also has lower end-loading sensitivity than equivalent cylindrical load cells, when judged by the PCCU-immunity measure. The Darwin load cell has 4.7 times the PCCU-immunity of an equal aspect ratio solid cylinder. Although smaller than for EN-immunity, the improvement is still significant.

9.5 Conventional 3 MN low-profile load cell

In addition to the above comparison with hollow and solid cylinders, a comparison with a shape, more representative of typical load cell designs, was sought. The 185 mm height of the Darwin load cell compares with 277 mm for a typical class 1 3 MN dial-gauge load column and 320 mm for a typical class 00 column load cell. No existing 3 MN single column load cell design, equal in height to the 'Darwin' load cell, was available to the author. In order to provide a comparison, a design based on the standard NPL 3 MN load cell design was created. The height of the central cylindrical portion of the standard design was reduced, in order to alter the overall height from the 320 mm of the standard design to the 185 mm height of the Darwin load cell. The manually generated finite element mesh of the resulting 3 MN load cell design is illustrated in figure 9.6. Although created especially for this study, this design is not unlike many commercial low-profile load cells. The EN-immunity and PCCU-immunity values were calculated for this conventional design and are indicated on figures 9.4 and 9.5.

The EN-immunity value of 87 is only slightly above the solid cylinder curve. It is perhaps surprising that this conventional load cell design has an end-loading sensitivity which is only a slight improvement over a solid cylinder of the same height.

MODEL: NORMAL

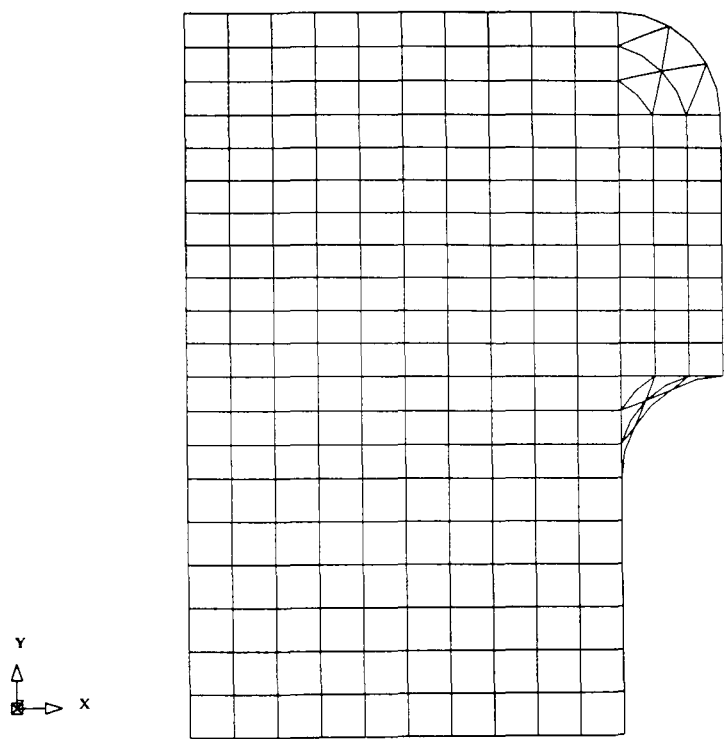


Figure 9.6 Mesh of low-profile load cell of conventional design

Perhaps the PCCU-immunity value of 17 is even more surprising, being below the value for a solid cylinder. This implies that at this aspect ratio a solid cylinder is less sensitive to end-loading conditions than a load cell of conventional shape.

9.5.1 Comparison of the Darwin and conventional designs

The Darwin design is calculated to have an EN-immunity 26 times that of the conventional design and a PCCU-immunity 10.5 times that of the conventional load cell design.

In order to illustrate this reduced end-loading sensitivity, full field plots of bridge strain were made. Figures 9.7 to 9.10 show the bridge strain in the conventional load cell design for the uniform, convex, concave and plane load cases. Figures 9.11 to 9.14 show the bridge strain in the Darwin load cell design over the same load cases. Although the strain contours of the two sets of plots cover different ranges, both represent equal strain intervals. Changes in colour in each plot therefore represent equal strain changes.

Applying uniform loading to the conventional load cell results in a very uniform bridge strain over the gauged area, as indicated by the extent of the green contour in figure 9.7. However, changes of the end-loading conditions results in variation in the bridge strain in the gauged area, indicated by the variation of colour from orange to blue between figures 9.9 and 9.10.

It is apparent from figure 9.11 that the strain over the gauged area of the Darwin load cell is much less uniform than in the case of the conventional load cell. However, in contrast to the conventional load cell, the strain pattern in the gauged area shows little variation over the four load cases.

9.6 Manufacture of the prototype Darwin load cell

The computational results predicted that the Darwin load cell design would be superior to conventional load cell designs. However to prove the design it was necessary to manufacture, gauge and test a prototype load cell. A steel load cell of the Darwin shape was therefore manufactured.

9.6.1 Machining

The grinding of the end faces of the load cell was a simple machining exercise. However, generating the lateral surface was less straight forward. One option

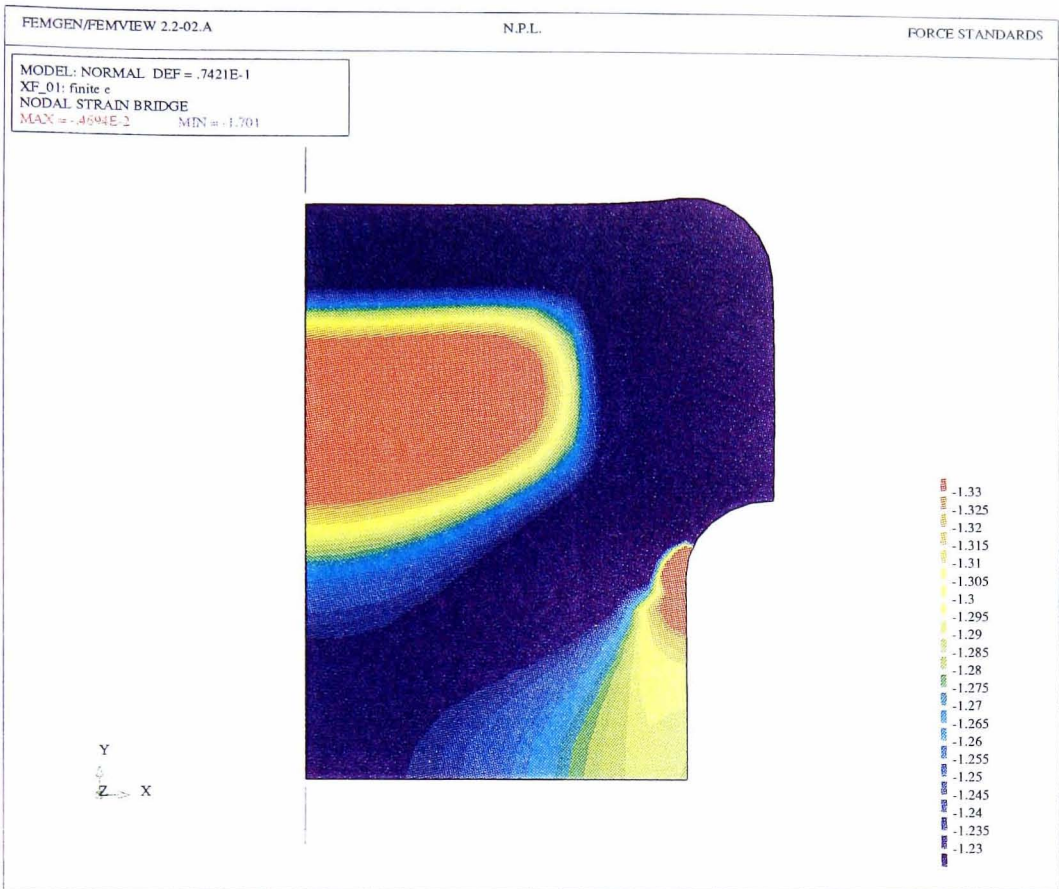


Figure 9.7: Contours of bridge strain in conventional load cell: Uniform pressure: No friction

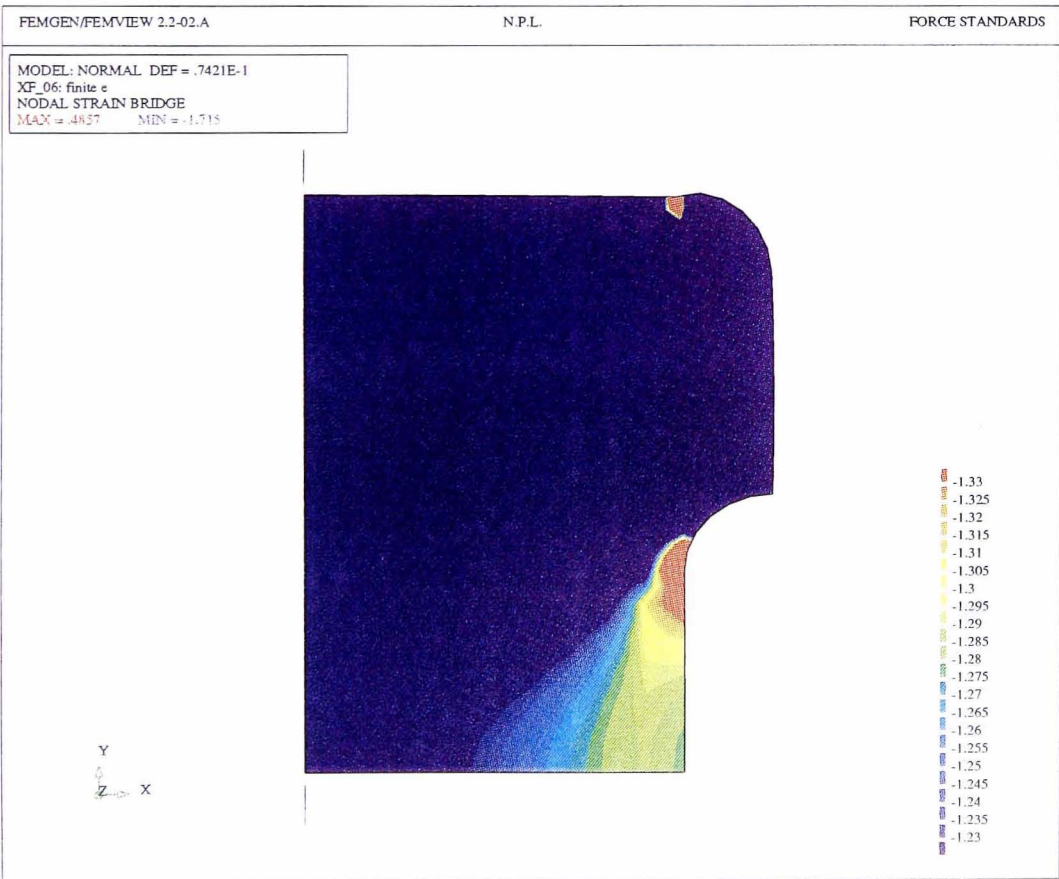


Figure 9.8: Contours of bridge strain in conventional load cell: Plane pad: Friction=0.3

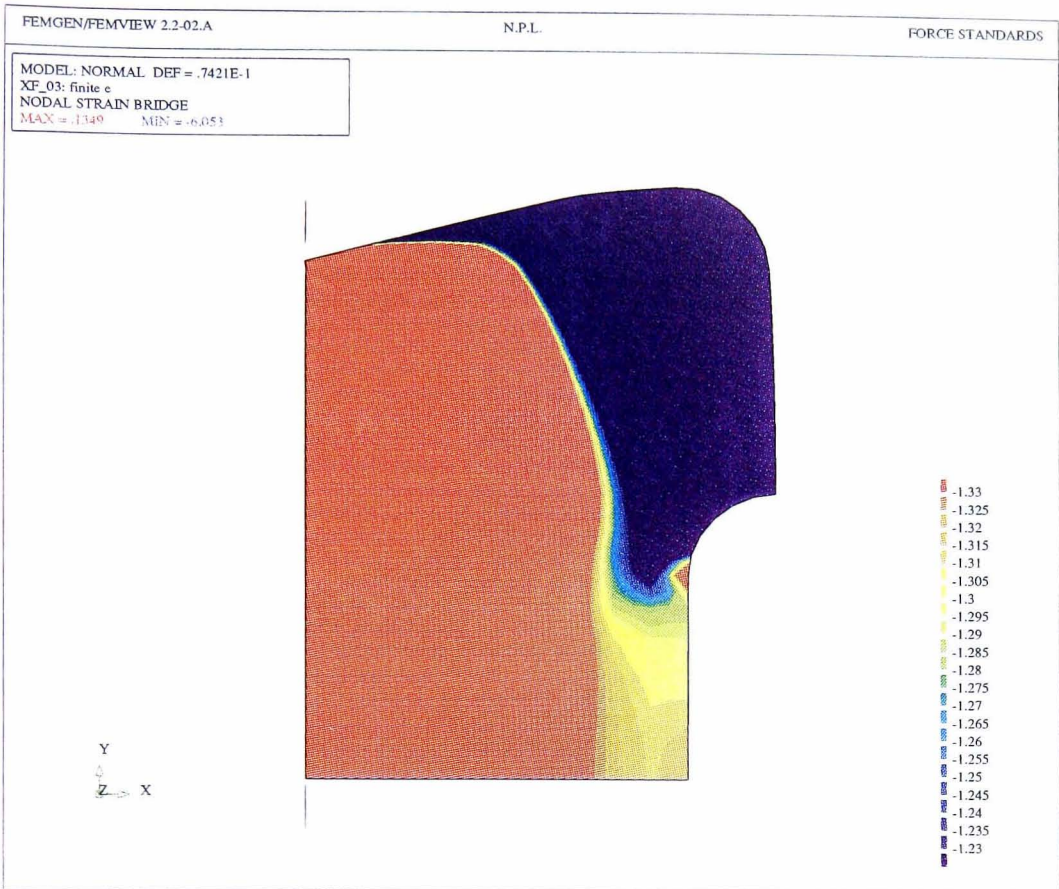


Figure 9.9: Contours of bridge strain in conventional load cell: Convex pad: Friction=0.3

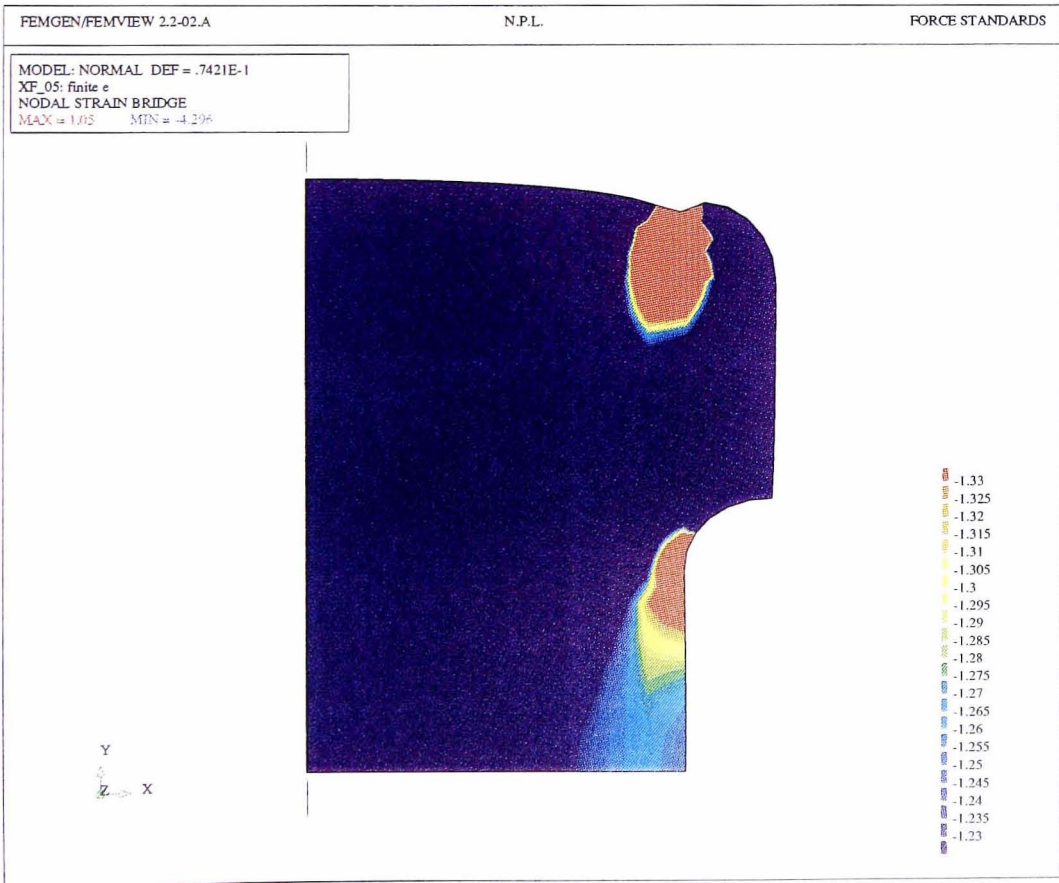


Figure 9.10: Contours of bridge strain in conventional load cell: Concave pad: Friction=0.3

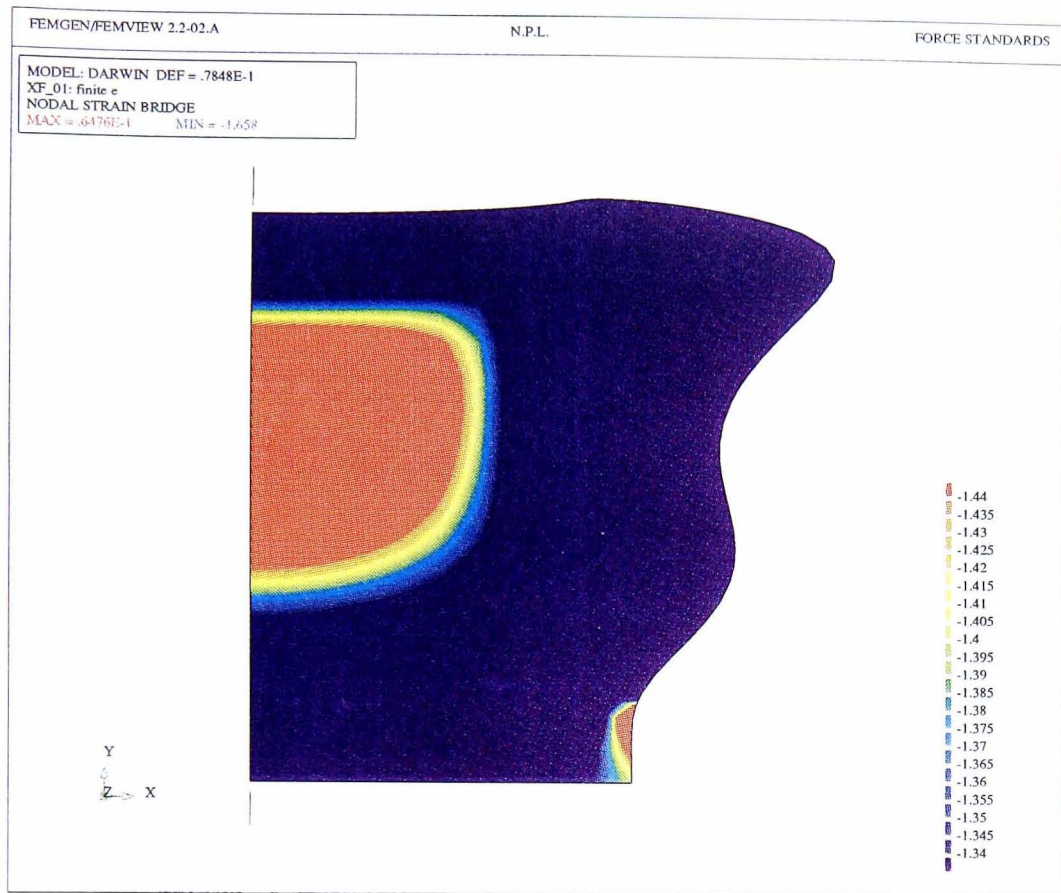


Figure 9.11: Contours of bridge strain in GA optimised load cell: Uniform pressure: No friction

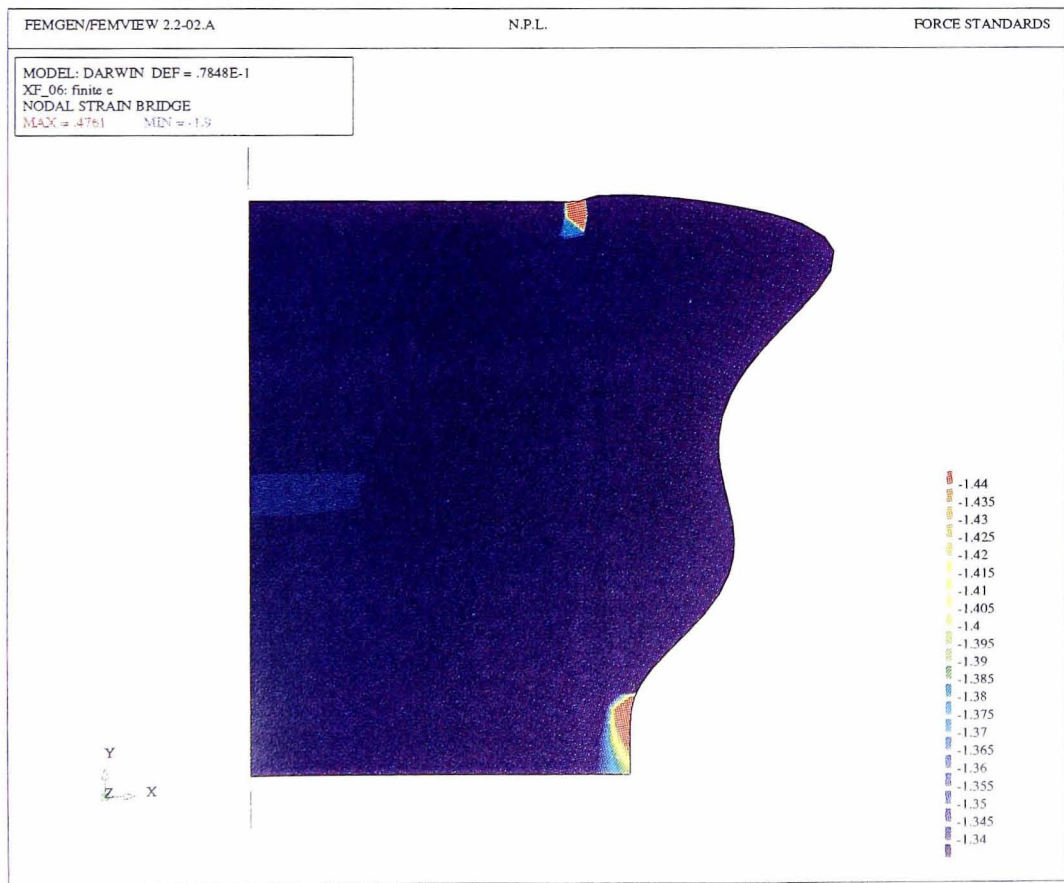


Figure 9.12: Contours of bridge strain in GA optimised load cell: Plane pad: Friction=0.3

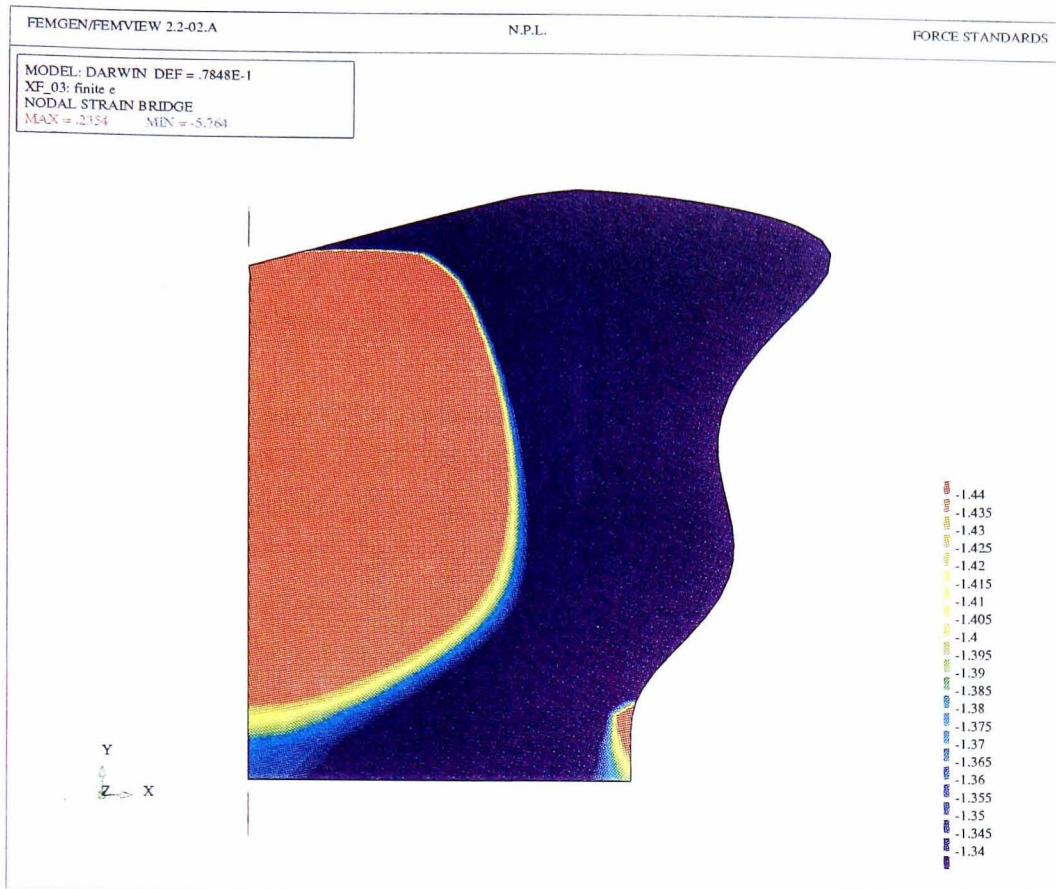


Figure 9.13: Contours of bridge strain in GA optimised load cell: Convex pad: Friction=0.3

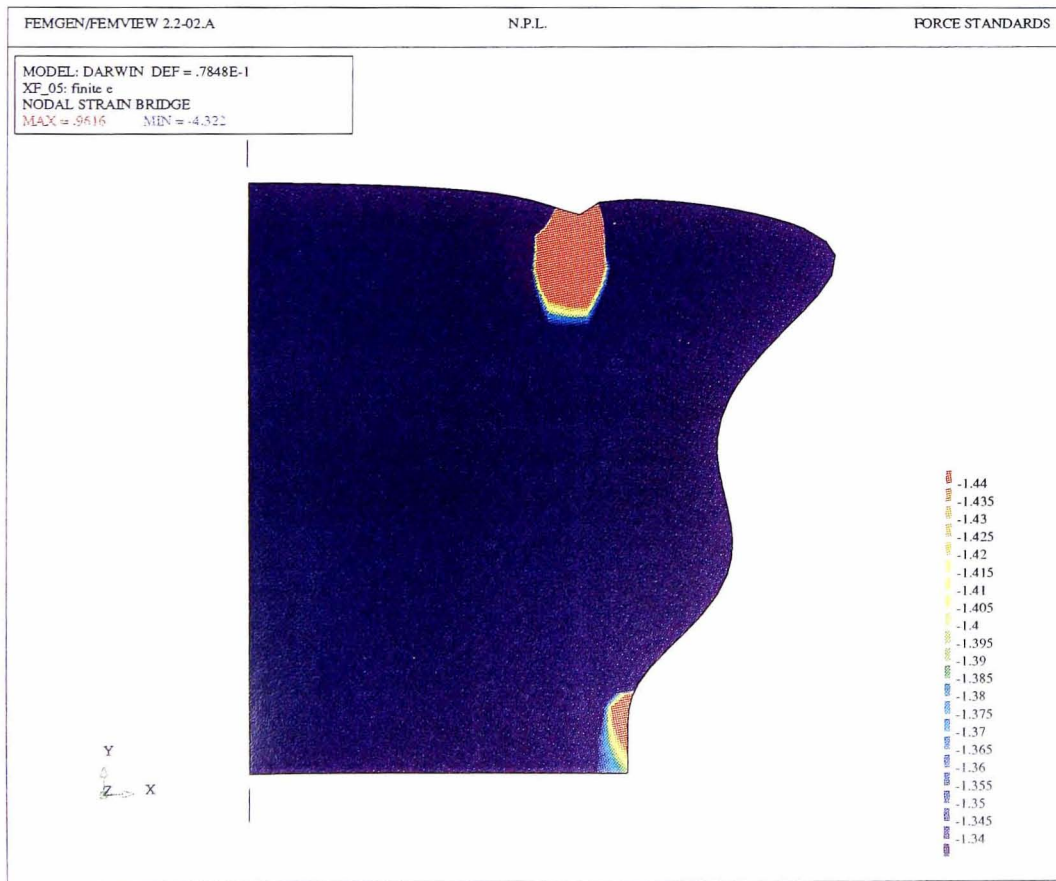


Figure 9.14: Contours of bridge strain in GA optimised load cell: Concave pad: Friction=0.3

considered was to use a two stage machining process. The billet would first be rough machined on an NC lathe, leaving an allowance for distortion during heat treatment. Following heat treatment, the billet would be machined to its final dimensions on an NC grinder. Machine time on NC lathes is moderately expensive, while NC grinding is extremely costly. This option although practicable was judged to be very expensive. A cheaper solution was therefore sought.

In an attempt to avoid the expense of NC grinding, the feasibility of machining the billet to net shape on an NC lathe in a single stage was assessed. Following heat treatment, the surface would then be polished, leaving the distortion due to heat treatment uncorrected. Tests on the computer model indicated that in order to obtain the high end-loading immunity, the lateral surface would have to be accurate to approximately 0.1 mm. Distortions due to conventional heat treatment could easily result in errors of this order. However, heat treatment under vacuum results in the production of much less scale and distortion. Although more expensive than conventional heat-treatment, it was concluded that use of vacuum heat treatment would allow the machining of the billet to net shape on an NC lathe, resulting in an overall saving.

Few machines can generate the lateral Bézier curve surface directly. However, all NC machines can generate straight lines. The Bézier curve was therefore approximated as a series of straight line segments between vertices. Forty seven vertices were spaced such that areas of high curvature were approximated by short segments with longer segments used elsewhere. The vertices were chosen such that the maximum departure between the Bézier curve and its straight line approximation was 0.02 mm. A tolerance of ± 0.05 mm on radius was specified for the NC turning leaving a 0.03 mm allowance for heat-treatment distortion.

Although the original intention was to use an NC lathe, machine availability resulted in the adoption of an alternative approach. The table of vertices was used to program a numerically controlled spark erosion machine to create a 2-D template of the lateral surface profile. A copy lathe was then used to transfer the profile from this template to the metal billet. Following heat-treatment the lateral surface of the billet was polished to blend in the vertices and remove scale. To complete the machining, the top and bottom surface of the billet were ground perpendicular to the billet axis.

Before manufacturing the steel element, an aluminium test-piece was manufactured using the same method, less the heat-treatment. The test-piece was measured on a co-ordinate measuring machine to determine whether the correct dimensions had

been achieved. While most dimensions were found to be within tolerance, an error, gradually increasing with height was observed. This was found to result from excessive temperature rise during turning. It was judged that provision of an additional flow of coolant during the machining process would cure the problem, and allow a steel billet to be manufactured to the correct dimensions.

Using the method described above, an element was manufactured from 826M40 steel. The billet was turned in the 'T' condition, before being vacuum quenched to 'Z' condition (hardness approximately 60R_C). Dimensional measurements indicated that the machined lateral surface was well within the target 0.1 mm tolerance.

9.6.2 Strain gauging

Although NPL manufactured load cells normally have bridges of eight or sixteen gauges a four gauge full-bridge was applied to the load cell billet. This cheaper option was considered acceptable as the prototype was to be used solely for the assessment of sensitivity to axisymmetric load cases. BLH FAE-25S-35-S6 gauges were used. These have a ¼" square active grid area, as specified in the optimisation. HBM EP310, hot curing epoxy adhesive was used to bond the gauges. Abradable resistors were used to balance the bridge zero and adjust its temperature coefficient of zero. Span compensation resistors were judged to be unnecessary as the load cell would be used in a temperature controlled environment, and only comparative results were required. The gauges were protected with a layer of RTV silicone compound only. It was considered unnecessary to add either additional protection or a case to the prototype. The finished prototype load cell is shown in plate 9.1.

9.7 Testing of the prototype load cell

In order to test the prototype load cell, a standard EN10002-3 bearing pad test was carried out at both the maximum load of 3 MN and at the 300 kN minimum load. The 300 kN tests were carried out in the NPL 1.2 MN deadweight force standard machine and the 3 MN tests in the NPL 5 MN hydraulic amplification force standard machine. In each case the load was applied to the top of the load cell via a ball seat unit placed on a plane pad. The load cell was supported on either a plane, convex or concave pad as required by the test. Each of the pads used had a radius of 88 mm ($=1.6r_0$).

The load cell was energised at 10 volts by a precision DC supply. The output was taken to a Solartron 7066 DVM with a resolution of 0.1 μ V. In the standard bearing pad test, each load is applied three times per bearing pad. In order to improve the accuracy of the tests, the load was applied five times, the load cell rotated 180° and



Plate 9.1: The prototype Darwin load cell

applied a further five times. Mean output differences were calculated from each of the ten load applications.

9.7.1 Bearing pad test results

The results of the bearing pad test are given in table 9.4.

Lower pad profile	Mean output difference at 300 kN (μV)	Mean output difference 3 MN (μV)
Plane	2230.6	22172.7
Convex	2229.5	22179.9
Concave	2230.4	22165.1

Table 9.4: Bearing pad test results for Darwin cell design

The relative departures from the plane loading case are presented in table 9.5 together with the EN10002-3 class 00 limits. The results from FE simulations, calculated for a contact pad radius of $1.6r_c$, are also given.

	300 kN		3 MN	
	Convex	Concave	Convex	Concave
Class 00 limit	$\pm 0.10\%$	$\pm 0.10\%$	$\pm 0.05\%$	$\pm 0.05\%$
FE simulation	-0.03%	-0.04%	+0.00%	+0.01%
Measured	-0.05%	-0.01%	+0.03%	-0.03%

Table 9.5: Relative deviation from output on plane pad

While not exact, the agreement between the FE and experimental results is reasonable given the accuracy limitations of both the FE simulation and the measurements. In particular it should be noted that the differences between the results at 3 MN are of the same order as the repeatability of the hydraulic force standard machine used at this force.

The experimental results certainly confirm the low sensitivity to end-loading conditions predicted by the FE simulation. It can be seen that the prototype load cell easily satisfies the class 00 limits of the EN10002-3 bearing pad test.

9.8 Conclusions

A Program for the Optimisation of the Geometry of (column) Load cell Elements, **POGLE**, has been developed. The program combines the routines for contact modelling, automatic meshing, and genetic algorithms described in previous chapters.

The **POGLE** program has been used to develop a new low-profile 3 MN load cell of radical design. A prototype of this 'Darwin' load cell design has been manufactured and tested. The test results confirm the program's prediction that the Darwin design would have a much lower end-loading sensitivity than conventional low-profile load cell designs. Successful development of the 3 MN load cell design has demonstrated the feasibility of optimising the shape of load cells using a combination of finite element analysis and genetic algorithm optimisation.

CONCLUSIONS AND PROPOSALS FOR FURTHER WORK

10.1 Conclusions

The work presented in this thesis concerned the analysis of the effect of end-loading conditions on column strain gauge load cells.

A preliminary analysis determined the relationship between the bridge output, the number of equispaced strain gauges in the bridge, and the angular frequencies of the contact stress distributions. This analysis concluded that most transfer standard column load cell designs should be insensitive to all but the axisymmetric component of the contact stresses.

An analysis based on Prokopov's solution for a semi-infinite circular cylinder loaded over its free end demonstrated that the relationship between aspect ratio and end-loading sensitivity is more complex than had been indicated by most of the previous studies.

Experimental measurements of strains in a finite cylinder have shown good agreement with the analytic results for loading without shear stress. However, the experimental results indicate that the radial shear stresses that arise in common loading conditions have significant effects on the load cell output.

A finite element program has been developed and tested against 'benchmark' problems. The program has the ability to model infinite domains and frictional contact. The results from using the program to model the experimental contact conditions were found to be in excellent agreement with the measured values.

By combining genetic algorithm routines with the finite element program, a Program for Optimising the Geometry of column Load cell Elements, **POGLE**, was developed. This program can be used to find load cell geometries with minimum end-loading sensitivities as defined by appropriate numerical measures. As a demonstration of the use of this program, optimisations of the geometry of 3 MN load cells were carried out

with two different measures of end-loading sensitivity, named EN-immunity and PCCU-immunity.

The radical shape predicted by the POGLE program to have the maximum PCCU-immunity was manufactured and tested. This 'Darwin' design was found to meet the EN-10002-3 bearing pad test requirements for a Class 00 device over the range 300 kN to 3 MN. The load cell has an overall height of only 185 mm, far less than any previous design meeting this requirement. The extent of the improvement is illustrated in figure 10.1 which compares the PCCU-immunity of the Darwin load cell design with that of solid cylinders of various aspect ratio.

The author believes that the work presented in this thesis has demonstrated that computational methods can be used to design improved load cells. Development of such novel designs using traditional methods would be impossible.

10.2 Proposals for further work

The author believes that there is much potential in the development of new load cell designs using a combination of FE and GA techniques. The following areas for further work are therefore proposed:

The present version of the POGLE program is not user friendly, design parameters being altered by editing a header file and re-compiling. The addition of a proper user interface would allow the program to be used as a general design tool.

The Darwin load cell design has demonstrated the potential for improved performance from POGLE optimised designs. The author intends to use the program to develop a range of load cells of various capacities. Already the program has been used to develop a low-profile 2 MN load cell and a hollow load cell for monitoring the tension in the hangers of a suspension bridge.

The contact algorithm should be capable of modelling contact during load reversal. Minor modifications to the existing routines would allow the prediction of the component of hysteresis due to reversal of the friction forces at the contact surface. The objective function of the optimisation could be modified so as to include a contribution which is a function of this hysteresis

The **POGLE** program optimises column load cells only. An approach, similar to that presented in this thesis, could be used to develop bar tension load cells with low sensitivity to variations in the depth of engagement of threaded adaptors.

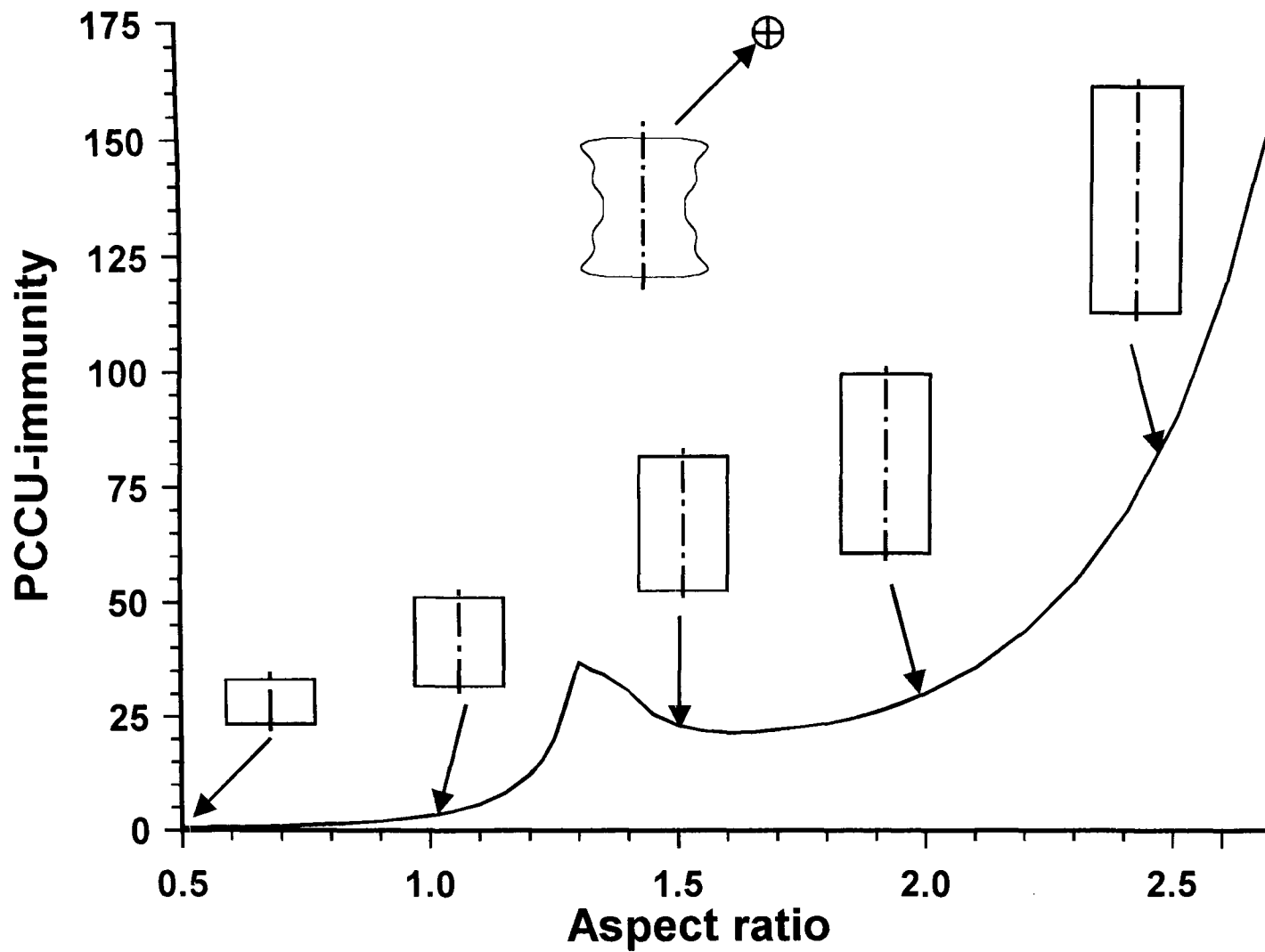


Figure 10.1: Comparison of PCCU immunity of Darwin and solid cylindrical load cells

References and bibliography

- Abdullah F, & Erdem U, (1978), Mathematical modelling and design of a shear force cell transducer, *VDI-Berichte*, **312**, 149-155
- Abdullah F & Li C W, (1983), Finite element modelling of load cell billets, *Weighing and force measurements in trade and industry*, Inst. Meas. & Control, London, England
- Anderson D L, & Ungless R L, (1977), Infinite finite elements, *Int. Symp. Innovative Num. Anal. Appl. Eng. Sci.*, France
- Barbato G, Desogus S, Zompì A, & Levi R, (1980), Load-cell design development by numerical and experimental methods, *4th SESA International Congress on Experimental Mechanics*, Boston, Massachusetts, USA
- Barlow J, (1976), Optimal stress locations in finite element models, *Int. J. for Num. Meth. in Eng.*, **10**, 243-251
- Baumgartner A, Burkhardt S, & Mattheck C, (1991), The kill-option: A powerful method to prepare engineering low weight design proposals, *Mechanical behaviour of materials IV*, 639-642, Pergamon Press, Oxford, England
- Bettess P, (1977), Infinite elements, *Int. J. Num. Meth. Eng.*, **11**, 53-64
- Bettess P, & Bettess J A, (1984), Infinite elements for static problems, *Eng. Comput.*, **1**, 4-16
- Boussinesq J, (1985), Application de potentials à l'étude de l'équilibre et des mouvements des solides élastiques, Gauthier-Villars, Paris, France
- Braibant V, & Fleury C, (1984), Shape optimal design using B-splines, *Comp. Meth. in Appl. Mechanics and Eng.*, **44**, 247-267
- Bray A, (1972), The influence of contact stresses on the characteristics of a load cell, *VDI-Berichte*, **176**, 43-49

- BS1610 Materials testing machines and force verification equipment, Part 2: Specification for the grading of equipment used for the forces applied by materials testing machines, British Standards Institute, Milton Keynes, England
- BS EN10002 Metallic materials, Tensile testing, Part 3: Calibration of force proving instruments used for the verification of uniaxial testing machines. British Standards Institute, Milton Keynes, England
- BSSM Strain measurement reference book [1979], British Society for Strain Measurement, Newcastle-upon-Tyne, England
- Chow Y K, & Smith I M, (1981), Static and periodic infinite solid elements, *Int. J. Num. Meth. Eng.*, **17**, 503-526
- Chree C, (1889), The equations of an isotropic elastic solid in polar and cylindrical bodies, *Trans. Cambridge. Phil. Soc.*, **14**, 250
- Debnam R C, & Jenkins R F, (1972), The influence of end loading conditions on the performance of strain gauge load cells, *VDI-Berichte*, Nr **176**, 53-60
- Debnam RC & Weiringa H, (1974), An intercomparison of force standard machines, *VDI-Berichte* Nr. **212**, p41-47
- De Jong K A, (1975), An analysis of the behavior of a class of genetic adaptive systems, *Dissertation Abstracts International*, **36(10)**, 5140B
- Dhingra A K, & Lee B H, (1994), A genetic algorithm approach to single and multiobjective structural optimization with discrete-continuous variables, *Int. J. for Num. Meth. in Eng.*, **37**, 4059-4080
- DIN 51233 - Materials testing machines; compression testing machines, *Deutsches Institut für Normung e.V.*, Berlin, Germany
- DIN 51301 - Verification of materials testing machines with the aid of static force measuring devices, *Deutsches Institut für Normung e.V.*, Berlin, Germany
- Femview 2.2, Femsys Ltd, Leicester, England

- Feucht W, (1970), in report of discussion on Hild K, (1970), Einige Untersuchungen über den Einfluß der Krafteinleitung auf die Veformung von Fraftmeßgeräten, *VDI-Berichte*, Nr 137, 71-74
- Filon L N G, (1902), On the elastic equilibrium of circular cylinders under practical systems of load, *Phil. Trans. Roy. Soc. (Ser. A)*, **198**, 147
- Forrest S, (1993), Genetic algorithms: Principles of natural selection applied to computation, *Science*, **261**, 872-878
- Francavilla A, & Zienkiewicz O C, (1975), A note on numerical computation of elastic contact problems, *Int. J. Num. Meth. Eng.*, **9**, 913-924
- Gerald C F, (1978), Applied numerical analysis, second edition, Addison-Wesley, Reading, Massachusetts, USA
- Goldberg D E, (1989), Genetic algorithms in search, optimization & machine learning, Addison Wesley, New York, USA
- Goodier J N, (1937), *Phil. Mag.*, ser 7, **24**, 325
- Haftka R T, & Grandhi R V, (1986), Structural shape optimisation - A survey, *Comp. Meth. in Appl. Mechanics and Eng.*, **57**, 91-106
- Hajela P, & Lin C-Y, (1992), Genetic search strategies in multicriterion optimal design, *Structural Optimisation*, **4**, 99-107
- HBM, Hottinger Baldwin Messtechnik GmbH, Darmstadt, Germany
- Hinton E, & Campbell J S, (1974), Local and global smoothing of discontinuous finite element functions using the least squares method, *Int. J. for Num. Meth. in Eng.*, **8**, 461-480
- Hogan C O, (1989), Recent developments concerning Saint-Venant's principle: an update, *Appl. Mech. Rev.*, **42** No 11, 295-303
- Holland J H, (1975), Adaption in natural and artificial systems, MIT Press, Cambridge, Massachusetts, USA
- Holland J H, (1992), Genetic algorithms, *Scientific American*, July 1992, 44-50
- Horgan C O, & Knowles J K (1983), Recent developments concerning Saint-Venant's principle, *Advances in applied mechanics*, **23**, 179-269

- Jenkins R F, (1979), The limitations of strain gauge load cells used as force transfer standards, *Proceedings of the 2nd Conference on Weighing and Force Measurement, Weightech 81*, Harrogate UK, Inst. Meas. & Control, London, England
- Jenkins R F, & Debnam R C, (1982), An intercomparison of force standard machines at the National Bureau of Standards, USA and the National Physical Laboratory, *NPL Report MOM 61*, National Physical Laboratory, Teddington, England
- Kasper M, (1992), Shape optimization by evolution strategy, *IEEE Trans. on Magnetics*, **28**, No. 2, 1556-1560
- Kela A, Saxena M, & Perucchio R, (1987), A heirarchical structure for automatic meshing and adaptive FEM analysis, *Eng. Comput.*, **4**, 104-111
- Khadem R, & O'Conner J J, (1969), Axial compression of an elastic circular cylinder in contact with two identical elastic half spaces, *Int. J. of Eng. Science*, **7** No 8, 785-800
- Kikuchi N, Chung K Y, Torigaki T, & Taylor T E, (1986), Adaptive finite element methods for shape optimization of linearly elastic structures, *Comp. Meth. in Appl. Mechanics and Eng.*, **57**, 67-89
- Kirkpatrick S, Gelatt C D, & Vecchi M P, (1983), Optimization by simulated annealing, *Science*, **220**, 671-678
- Klemm J L, & Little R W M, The semi-infinite elastic cylinder under self-equilibrated end loading, *SIAM J. Appl. Math.*, **19**, No 4, 712-729
- Knott A J & Robinson G M, (1990), An intercomparison of force standards between NPL and TNO-IWECO, *12th IMEKO TC3 conference*, Szeged, Hungary, 67-77
- Knowles J K (1966), On Saint-Venant's Principle in the two-dimensional linear theory of elasticity, *Arch. Ration. Mech. Anal.*, **21**, 1-22
- Kuipers M, (1953), Numerical calculation of the end-effect of cylinders, used as measuring element in load cells, *Appl. Sci. Res. A*, **4**, 337-360
- Leinonen H T, (1988), Experiments and analysis of force transmission in force transducers to improve their characteristics, *Measurement*, **6**, 81-86

- Leinonen, H T, & Keinanen H A, (1989), Comparisons of the numerical and experimental data of a multi-component force transducer developed by utilising the finite element method, *Australasian Instrumentation and Measurement Conference 1989*, Adelaide, Australia
- Little R W M, & Childs S B, (1967), Elastostatic boundary region in solid cylinders, *Quart. Appl. Math.*, **25**, 261-274
- Love A E H, (1944), A treatise on the mathematical theory of elasticity, 4th edition, Dover, New York, USA
- Lur'e A I, (1964), Three-dimensional problems of the theory of elasticity, Interscience, New York, USA
- Lynn P P, & Hadid H, (1981), Infinite elements with $1/r^n$ type decay, *Int. J. Num. Meth. Eng.*, **17**, 347-355
- Mattheck C, & Burkhardt S, (1990), A new method of structural shape optimization based on biological growth, *Int. J. Fatigue*, **12**, No. 3, 185-190
- McLachlan N W, (1934), Bessel functions for engineers, Oxford University Press, Oxford, England
- Micro-Measurements Catalog 500, Measurements Group, Raleigh, North Carolina, USA
- Mitchell R A, Woolley R M, & Fisher C R, (1971), Formulation and experimental verification of an axisymmetric finite-element structural analysis, *J. of Res. of the National Bureau of Standards*, **75C**, Nos 3 & 4, 155-163
- NAG Finite Element Library, NAG Ltd, Oxford, England
- NAG Fortran Library Mk 15, Numerical Algorithms Group, Oxford, England
- NAFEMS, (1986), A Finite Element Primer, National Agency for Finite Elements and Standards, East Kilbride, Scotland
- NAFEMS, (1989), The Standard NAFEMS Benchmarks, National Agency for Finite Elements and Standards, East Kilbride, Scotland
- Ohte S, (1973), Finite element analysis of elastic contact problems, *Bull. of JSME*, **16**, No. 95, 797-804

- Olukoko O A, Becker A A, & Fenner R T, (1993), Three benchmark examples for frictional modelling using finite element and boundary element methods, *J. of Strain Analysis*, **28**, No 4, 293-301
- PAFEC FE, Pafec Ltd, Nottingham, England
- Pascoe S K, Mottershead J E, & Hellen T K, (1989), A comparison of finite element techniques for contact stress analysis, *Modern practice in stress and vibration analysis*, Editor J E Mottershead, Pergamon press, Oxford, England
- Pochhammer L, (1876), Beitrag zur thoerie der biegunng des kreiszylinders, *J. reine u. angew Math.*, **81**, 33
- Power L D, & Childs S B, (1971), Axisymmetric stresses and displacements in a finite circular bar, *Int. J. Eng. Sci.*, **9**, 241-255
- Prokopov V K, (1948), Dissertation, Leningrad Politekhnic Institute.
- Prokopov V K, (1950), The axisymmetric problem of the theory of elasticity for the isotropic cylinder, *Trudy Leningrad Politekhn. Inst.*, **2**
- Rohrbach C, (1970), Einige gesichtspunkte zur präzisions-kraftmessung und -wägung mit dehnungs-meßstreifen, *VDI-Berichte*, Nr **137**, 5-10
- Sachdeva T D, & Ramakrishnan C V, (1981), A finite element solution for the two-dimensional elastic contact problems with friction, *Int. J. Num. Meth. Eng.*, **17**, 1257-1271
- Saint-Venant A-J-C B de (1856), Mémoire sur le flexion des prismes, *J. Math. Pures Appl.* 1 (Ser. 2), 89-189
- Saint-Venant A-J-C B de (1856), Mémoire sur le torsion des prismes, *Mémoires présentés pars divers Savants a l'Academie des Sciences de l'institute Imperial de France* **14**, 253-560
- Schnack E, (1988), Structural Optimisation, *Proceedings of the IUTAM symposium*, 299-306, Kluwer Academic Publishers
- Schnack E, & Iancu G, (1991), Gradientless computer methods in shape designing, Structural Systems and Industrial Applications, *Computer Aided Optimum Design of Structures '91, Optimization of Structural Systems and Industrial Applications*, 363-76

- Shyy Y K, Fleury C, & Izadpanah K, (1988), Shape optimal design using high-order elements, *Comp. Meth. in Appl. Mechanics and Eng.*, **71**, 99-116
- Stefanescu D-M, (1988), Study of S-shaped flexible elements of force transducers instrumented with strain gages using the finite element method, *Proc. of 11th World congress of IMEKO*, Houston, Texas, USA, 591- 598.
- Steklov V A, (1891), On the equilibrium of elastic cylindrical bodies, *Soobsch. Kharkov'skogo, matematicheskogo oshchestva*.
- Sternberg E, (1954), On Saint-Venant's principle, *Quart. of Appl. Math.*, **11**, 393-402
- Sundin K G, & Jonsson M, (1985), A stiff and compact impact-force transducer based on strain measurement, *Experimental Mechanics*, **25**, No 1, 48-53
- Timoshenko S P, & Goodier J N, (1982), Theory of elasticity, 3rd edition, McGraw Hill, New York, USA
- Toupin R A, (1965), Saint-Venant's principle, *Arch. Rational Mech. Anal*, **18**, 83-96
- Von Mises R, (1945), On Saint-Venant's principle, *Bull. Amer. Math. Soc.*, **51**, 555-562
- Williams D C, (1983), The effect of non-uniform loading on a cylindrical load cell billet, *MOM Technical Note No. 40*, National Physical Laboratory, Teddington, England
- Zanaboni (1937), Dimostrazione generale del principio del de Saint-Venant, *Atti. Acc. Naz. Lincei*, **25**, 117-120
- Zienkiewicz O C, (1977), The finite element method, 3rd edition, McGraw-Hill, London, England
- Zienkiewicz O C, Emson C, & Bettess P, (1983), A novel boundary infinite element, *Int. J. Num. Meth. Eng.*, **19**, 393-404